APPLICATION OF TRANSIENT ELECTROMAGNETIC FIELDS TO RADAR TARGET DISCRIMINATION

By

John Edwin Ross, III

A DISSERTATION

Submitted to
Michigan State University
in partial fulfillment of the requirements
for the degree of

DOCTOR OF PHILOSOPHY

Department of Electrical Engineering

1992

ABSTRACT

APPLICATION OF TRANSIENT ELECTROMAGNETIC FIELDS TO RADAR TARGET DISCRIMINATION

By

John Edwin Ross, III

This dissertation addresses several topics associated with non-cooperative radar target discrimination using the E-pulse and S-pulse methods. An automated discrimination scheme based on the E-pulse and S-pulse is presented. The performance of this scheme is evaluated for the case of wire targets in the presence of random noise. The applicability of the automated discrimination scheme in a multiple target environment is evaluated.

In a multiple target environment interactions between targets must be considered. The behavior of the Singularity Expansion Method (SEM) modes of a system of targets are investigated. Approximate methods for calculation of SEM system mode frequencies are presented. The transient response of a system of wires is constructed using a Class I SEM expansion and compared to results obtained using Fourier inversion of moment method calculations. It is seen that SEM system modes are non-physical prior to the onset of system late-time. The automated discrimination procedure is evaluated for a system of two parallel wires and the results interpreted using the correct physical meaning of the SEM system modes.

Accurate transient measurements are essential for implementation of an automated discrimination scheme for complicated targets. Transient measurements can be made directly in the time domain or synthesized from swept frequency measurements using the

inverse Fourier transform. A calibration method capable of removing systematic errors inherent in the measurement system and background clutter is presented. Verification is accomplished by measurement of canonical targets such as spheres and wires as well as a wire stick aircraft model.

The calibration scheme is used for experimental study of several topics. The response of a system of parallel wires is measured and compared to theoretical predictions. The amount of late-time energy available for discrimination is evaluated for realistic aircraft models. Discrimination of realistic aircraft models is demonstrated using experimental data. It is experimentally demonstrated that coupling between aircraft adversely affects discrimination.

In Loving Memory of My Grandmother

Dorothea R. Stine

October 14, 1901 - May 8, 1992

ACKNOWLEDGMENTS

I would like to express my sincerest appreciation to Dr. D.P. Nyquist. Your encouragement to continue my graduate studies at Michigan State University and your teaching and guidance during my research will long be remembered. I am also indebted to Dr. K.M. Chen. Thank you for affording me the opportunity to work in an outstanding environment and for your deep concern and guidance. To Dr. Byron Drachman, thank you for participating as a member of my guidance committee. I am especially grateful to Dr. E.J. Rothwell, the finest thesis advisor one can imagine. Your enthusiasm, encouragement and expert technical advice will not be forgotten.

I also want to thank my fellow graduate student Ponniah Ilavarasan whose bright smile and persona has brightened many cloudy Michigan days. It has been a great pleasure to work and learn with you.

To my mother and father I want to express my appreciation for their constant encouragement and for always being there for me.

Finally, to my wife Linda, no amount of thanks for your constant love and encouragement would be too much. It's over, let's get on with life.

Table of Contents

List of Tables

List of Figures

Chapter 1

Introduction

This dissertation is concerned with the application of transient electromagnetic waves to the detection and identification of remote objects with an Ultra-Wide-Band (UWB) or impulse radar system. Before proceeding further it is useful to put some of the common terminology in context.

The bandwidth of a radar system can be defined in an several ways. In an absolute sense, the spectral bandwidth W of the transmitted waveform is specified as

$$W = f_h - f_l \tag{1.1}$$

where f_h and f_l are the highest and lowest frequency components passed completely from the transmitter to the receiver. Bandwidth can also be expressed in a relative sense as

$$B = \frac{W}{f_c} \tag{1.2}$$

where the center frequency f_c is defined as

$$f_c = \frac{f_h + f_l}{2} \tag{1.3}$$

The term "narrow band" refers to systems that have a fractional bandwidth B of less than 3% and usually less than 1%. Systems with a bandwidth of 10% are considered wideband. An UWB system on the other hand has a fractional bandwidth greater than 25% [1,2].

Conventional radars are narrow-band systems used to detect the presence or absence of a target, measure a target's speed, or measure a target's position. An impulse radar is a UWB radar system that uses very short duration pulses to achieve a high range resolution. UWB radars can also be designed using a Frequency Modulated Continuous Wave (FM-CW) or with a spread spectrum or noise type modulation [3].

The term "high resolution radar" is also commonly used to describe a radar system that provides superior resolution of target features. The exact type of technology is ambiguous unless the purpose of the radar is specified. For mapping radars, the term "high resolution" usually refers to a system that can resolve small areas on the ground using Synthetic Aperture Radar (SAR) techniques. For airplane detection and tracking radars, the term "high resolution" refers to the range resolution and the ability to resolve specific scattering centers along the fuselage and wings of an aircraft. It should be pointed out that the range resolution ΔR of any radar is dependent only on the absolute bandwidth W of the system [4] as

$$\Delta R = \frac{cW}{2}. \tag{1.4}$$

Hence, a narrow-band system operating at a center frequency of 100 GHz with a bandwidth of 2 GHz has the same range resolution as an ultra-wide band impulse radar using the frequency range from 100 Mhz to 2.1 GHz. Thus, the term "high resolution" does not necessarily imply a UWB radar system.

During the past 10 years, interest in UWB radar has risen dramatically and nearly every major meeting of electromagnetics, microwave and radar workers has sessions devoted to topics related to UWB technology [5,6]. The UWB radar has the potential

for extracting more information from a target echo than just its speed and location. Specifically, it is believed that UWB radars have the potential for identifying the size and shape of a target. It has also been suggested that the UWB radar might have better detection performance than conventional radars when the class of target to be detected is known [7].

Much of the work presented in this dissertation is concerned with the application of UWB radar for non-cooperative target recognition. Though there are a number of schemes under investigation for identifying a target from its radar return, this work focuses on resonance based methods. The natural resonances of a target are inherently useful for target discrimination since the natural frequencies are dependent only on the geometry of the target and not on the shape of the incident waveform or the orientation of the target with respect to the incident wave. The aspect independence of the natural frequencies allows for identification of complicated targets whose orientation is usually unknown. A successful method of discrimination based on the target natural frequencies is embodied in the Extinction pulse (E-pulse) or Single-mode extraction pulse (S-pulse) methods [8,9,10].

Chapter 2 reviews some of the previous work on the E-pulse and S-pulse scheme. Several advances in automating the discrimination scheme are presented. The performance of the automated scheme for single thin-wire targets in the presence of noise is evaluated using theoretical scattering data. This analysis serves as a baseline for comparison for other performance evaluations.

The problem of discrimination when more than one target is present is more difficult. When two or more targets are sufficiently separated in down range, the target

responses can be treated separately and the discrimination process applied as if there is only a single target. These cases are discussed and analyzed in Chapter 2.

In some cases the targets may be too close together to apply range separation. This case is more complicated since mutual interaction between targets can significantly change the scattering response. Much effort was focused on evaluating the effect of the mutual interactions on the E-pulse and S-pulse discrimination scheme. One effect of the mutual interactions is to shift the natural frequencies of the group of targets away from the natural frequencies of the individual targets. Chapter 3 is devoted to evaluating the shifting phenomena and obtaining a better understanding of transient coupling phenomena. It is seen that more than just the shift of natural frequencies must be considered for a proper understanding of the effect of mutual interactions on the transient response and on the E-pulse and S-pulse discrimination performance.

Chapter 4 presents an analysis of coupling on the E-pulse and S-pulse discrimination schemes using theoretically generated thin wire data. The discrimination results are interpreted according to the physical insight gained in Chapter 3.

To implement the E-pulse and S-pulse discrimination scheme, the natural frequencies of the targets must be accurately extracted from a measured transient response. Unfortunately, all current mode extraction procedures are sensitive to noise and systematic errors in the measured data. Until recently, extraction procedures have been prone to yielding natural frequencies with a non-physical positive damping coefficient when the data is corrupted. This may be about to change with the advent of a new method to constrain the natural frequencies to physically meaningful ranges recently introduced by Ilavarasan [11]. In any case, the measurements must be of extremely

high quality. Further, very little is currently known of the early-time response of complicated targets to impulse excitation. Thus accurate transient measurements are essential in understanding and using information contained in the early-time portion of the response. For these reasons, a great deal of effort was focused on developing and implementing a practical transient scattering measurement system.

Chapter 5 describes in detail procedures developed and used to obtain accurate transient scattering measurements at Michigan State University during the course of this research. A calibration procedure is presented that can be used to eliminate most systematic errors from both time domain measurements and measurements performed in the frequency domain with a frequency sweeping vector network analyzer. The calibration is verified by measurement of canonical targets.

Chapter 6 presents numerical and experimental results associated with this research. The experimental verification of the transient coupling effects discussed in Chapter 3 is presented using a series of measurements of coupled thin wires. The effect of resistive losses on the response of a system of parallel wires excited in the transmission line mode is discussed. A wire stick airplane model is measured in several orientations to illustrate the capability of the measurement system to accurately measure a complicated target whose response can be theoretically calculated. The amount of energy available for discrimination that is present in the late-time of a target response is discussed using data from realistic scale model aircraft. The effect of coupling on discrimination of realistic aircraft models is explored using experimentally derived data. Finally, measurements of the early-time of several targets are presented.

Chapter 2

Target Discrimination Using E-Pulses and S-Pulses

2.1 Introduction

Though there has been considerable work published on radar target discrimination using the E-pulse and S-pulse technique [12,13,14], there has been a continual evolutionary improvement in the application of E-pulses and S-pulses in an automated target discrimination scheme. This chapter briefly presents the E-pulse and S-pulse discrimination scheme as implemented at Michigan State University. Some of the improvements are probably useful only in a laboratory demonstration of the discrimination scheme, however, many of the problems present in the laboratory environment are likely to be even more difficult to solve in a practical implementation of the discrimination scheme.

The first portion of the chapter briefly reviews the theoretical foundations of the E-pulse and S-pulse discrimination method. Quantification of the discrimination is discussed and problems involved in the automated decision making process are addressed. Then, the performance of the automated scheme is evaluated for theoretical thin wire scattering data in the presence of noise. Finally, the difficulties encountered in a multiple target environment are discussed.

2.2 Review of E-Pulse and S-Pulse Discrimination

The E and S pulse method of target discrimination is based on the singularity expansion method (SEM) representation of scattered electromagnetic fields first advanced by Baum [15] in 1971. According to this theory, the transient currents and fields in late-time can be expressed as a natural mode series

$$r(t) = \sum_{n=1}^{N} a_n \exp(\sigma_n t) \cos(\omega_n t + \phi_n) \qquad t > T_l \tag{2.1}$$

where $s_n = \sigma_n + j\omega_n$ is the aspect independent natural frequency of the n^{th} target mode, a_n and ϕ_n are aspect dependent modal amplitudes and phases, and T_l is the aspect dependent beginning of late-time. Marin later proved the validity of this expression for the case of finite sized perfectly conducting bodies of arbitrary shape [16].

The E-pulse waveform $e(t)$ for a particular target is defined [9] such that

$$e(t) * r(t) \equiv 0 \qquad t > T_l + T_e \tag{2.2}$$

where T_e is the duration of $e(t)$, and $r(t)$ can be the response of the target from any aspect angle. This definition implies that

$$E(s) \equiv \mathcal{L}\{e(t)\} \equiv 0 \qquad \text{for } s = s_n \text{ and } s = s_n^*; \quad n = 1,2,3,...N \tag{2.3}$$

where the s_n are natural-mode frequencies of the target.

To effect target discrimination using E-pulses, the response from an unknown target $v(t)$ is convolved with each of the E-pulses in a database. The convolved waveforms are denoted $c_e(t) = e(t) * v(t)$. If $E(s)$ has zeros at all natural frequencies present in the late-time portion of $v(t)$, then $c_e(t) = 0$ in the late-time. If $E(s)$ does not

contain zeros at all natural frequencies in the late-time portion of $v(t)$, then $c_e(t) \neq 0$ in the late-time [9]. Thus, the target producing $v(t)$ is associated with the E-pulse that yields zero in late-time after convolution with $v(t)$.

The sine S-pulse waveform $s_s^i(t)$ for the i^{th} mode of a particular target is defined by

$$s_s^i(t) * r(t) \equiv b_i \exp(\sigma_i t) \sin(\omega_i t + \theta_i) \qquad t > T_l + T_s \tag{2.4}$$

where b_i and θ_i are aspect dependent amplitudes and phases. The cosine S-pulse waveform $s_c^i(t)$ for the i^{th} mode of a particular target is defined by

$$s_c^i(t) * r(t) \equiv c_i \exp(\sigma_i t) \cos(\omega_i t + \phi_i) \qquad t > T_l + T_s \tag{2.5}$$

where c_i and ϕ_i are aspect dependent amplitudes and phases, T_s is the duration of the sine and cosine S-pulses and $r(t)$ can be the response of the target from any aspect angle. The spectral interpretation for these definitions is

$$S^i(s) \equiv \mathcal{L}\{s^i(t)\} \equiv 0 \qquad for\ s = s_n\ and\ s = s_n^*;\ n = 1,2,3,\ldots,N;\ \ n \neq i \tag{2.6}$$

In addition, these definitions require $S_s^i(s_i) = -S_s^{i^*}(s_i)$ and $S_c^i(s_i) = S_c^{i^*}(s_i)$. The unknown aspect dependent phases θ_i and ϕ_i cause difficulty in quantifying discrimination when only a sine or only a cosine S-pulse is used. To circumvent this problem, a quadrature sum of a cosine and sine S-pulse $\tilde{s}^i(t) = s_c^i(t) - j s_s^i(t)$ is defined. When the quadrature sum S-pulse is convolved with a response waveform $r(t)$ the following result is obtained

$$\tilde{s}^i(t) * r(t) = b_i \exp(-j\theta_i) \exp(\sigma_i t - j\omega_i t) \qquad t > T_l + T_s \tag{2.7}$$

Application of the Fourier transform results in

$$\mathcal{F}\{\tilde{s}^i(t) * r(t)\} = b_i e^{-j\theta_i} \int_0^{W_e} e^{s_i^* t} e^{-j\omega t} dt = b_i e^{-j\theta_i} \left\{ \frac{e^{(s_i^* - \omega)W_e} - 1}{(s_i^* - \omega)} \right\} \equiv F(\omega) \tag{2.8}$$

where W_e is the duration of an observation window. It is clear that the frequency variation of $|\mathcal{F}\{\tilde{s}^i(t) * r(t)\}|$ is aspect independent.

2.3 Quantification and Automation of Discrimination

The automation of the E-pulse and S-pulse discrimination method was originally pioneered by Rothwell and Ilavarasan [17, 18]. Automated discrimination requires a measure of the amount of signal present in the late-time of $c_e(t)$ for each E-pulse. Thus, the E-pulse Discrimination Number (EDN) can be defined as

$$EDN = \left[\int_{T_L}^{T_L + W_e} c_e^2(t)\, dt \right] \left[\int_0^{T_e} e^2(t)\, dt \right]^{-1} \tag{2.9}$$

The EDN is a measure of the deviation from the expected value of zero late-time energy. The choice of the window duration is usually based on the duration of the target response and the Signal-to-Noise Ratio (SNR) present in the measurement of an unknown target. Note that the late-time energy of $c_e(t)$ is normalized by the E-pulse energy. To use the EDN for automated discrimination, the EDN is calculated for each E-pulse in the data base. If the target producing $v(t)$ has been cataloged with an E-pulse in the database then the EDN for that E-pulse is zero while all other E-pulses yield a non-zero EDN. In

actual practice, noise and inaccuracies in the estimates of the target natural frequencies used to construct the E-pulses prevent the EDN from precisely vanishing when the E-pulse is matched to the target producing the response. Thus, the target is identified by the E-pulse yielding the minimum EDN. As a quantitative measure of the differences in the EDN values computed for all E-pulses in the database the E-pulse Discrimination Ratio (EDR) can be defined as

$$EDR\,(dB) \;=\; 10.0 \log_{10} \left\{ \frac{EDN}{\min(EDN)} \right\} \tag{2.10}$$

Therefore, the E-pulse yielding the smallest EDN has an EDR of 0 dB, while the EDR produced by the other E-pulses is greater.

The S-pulse discrimination scheme is similar to the E-pulse discrimination scheme. In this case the convolved waveforms are denoted $c_s(t) = \tilde{s}^t(t) * v(t)$. The target is identified by the S-pulse that causes the late-time portion of $c_s(t)$ to be a damped sinusoid with a known complex frequency s_i. The S-pulse corresponding to the target response produces a convolution whose late-time spectrum matches the spectrum of $F(\omega)$ to within a constant. To assign a numerical value to the quality of this match Schwartz's inequality

$$\frac{\left\{\int f(x)\, g(x)\, dx\right\}^2}{\int f^2(x)\, dx \int g^2(x)\, dx} \quad \begin{cases} < 1 \\ = 1;\ \text{iff } f(x) = k g(x);\ k = const \end{cases} \tag{2.11}$$

where $f(x)$ and $g(x)$ are real functions is used to define the S-pulse Discrimination Number (SDN)

$$SDN = 1 - \left[\int_{\omega_s}^{\omega_e} |C_s(\omega)||F(\omega)|\,d\omega\right]^2 \left[\int_{\omega_s}^{\omega_e} |C_s(\omega)|^2\,d\omega \int_{\omega_s}^{\omega_e} |F(\omega)|^2\,d\omega\right]^{-1} \quad (2.12)$$

where $C_s(\omega)$ is the Fourier spectrum of $c_s(t) = \tilde{s}^t(t) * v(t)$, $F(\omega)$ is the Fourier spectrum of the expected single mode signal taken over the finite duration W_e as defined in (2.8), and ω is the radian frequency. The integration limits ω_s and ω_e are determined by the bandwidth of the measurement system. The SDN is a measure of the error from the expected single mode spectrum. From the Schwartz inequality it can be seen that the SDN is zero if the spectrum of the late-time portion of $c_s(t)$ matches the expected single mode spectrum to within a constant. As in the case of E-pulse discrimination, each of the quadrature S-pulses in the database are convolved with the response waveform $v(t)$. For each convolution, the SDN is calculated. The target is identified by the quadrature S-pulse that yields the smallest SDN. To quantify the differences in the SDN for different quadrature S-pulses used in the discrimination we define the S-pulse Discrimination Ratio (SDR) as

$$SDR = 10.0 \log_{10}\left\{\frac{SDN}{\min(SDN)}\right\} \quad (2.13)$$

Therefore, the SDR of the correct target is 0 dB, while the SDR of all other targets is greater than 0 dB. If the method is working properly, the EDR and SDR values approach infinity for E-pulses and S-pulses not associated with the target in the response. In most applications, noise in the measurement system and inaccuracies in estimates of target natural frequencies prevent the EDN and SDN from being zero when the E-pulses and S-pulses match the target producing $v(t)$.

To apply the discrimination scheme, the beginning of the late-time T_l for the unknown target response $v(t)$ must be estimated. For most targets of interest, the start of late-time can be computed based on the maximal one-way transit time of the target T_{tr}, the effective pulse duration used in the measurement system T_p, and an estimate of when the wave strikes the leading edge of the target T_b. For the usual case of back-scattering measurements

$$T_l = T_b + T_p + 2T_{tr} \tag{2.14}$$

The target data base contains a value for T_p as well as values of T_{tr} for each target. Thus, only T_b must be estimated from the response data.

For this analysis a computer model of a threshold detector is used to determine T_b. The point at which $v(t)$ is greater than a threshold voltage V_T is taken to be T_b. The threshold voltage V_T must be set small enough to detect weak signals, but large enough limit the false alarm rate to an acceptable level. For Gaussian noise, the mean time between false alarms T_{fa} for a given V_T is given by [4] as

$$T_{fa} = \frac{1}{B_{IF}} \exp \frac{V_T^2}{2\psi_0} \tag{2.15}$$

where B_{IF} is the IF bandwidth of the measurement system, and ψ_0 is the mean-square value of the noise voltage. For the analysis to be presented in the next section, the threshold voltage was chosen so that $V_T = 8\sqrt{\psi_0}$. This resulted in $T_{fa} = 21.36$ hours for the 1.022 GHz bandwidth used. Note that the determination of T_b is essential for proper operation of the automated discrimination scheme. As such, it may require a vastly more

sophisticated method to accurately estimate T_l in actual practice than the simple threshold detector used in this analysis.

It should be pointed out that the problem of E-pulse and S-pulse synthesis has not been pursued in this work. Though the synthesis problem has already been extensively investigated by Rothwell [9] and further refined by Ilavarasan [19], there is still a great deal of work necessary in this area. For the purposes of this research however, it is sufficient to say, that synthesis of the E-pulse and S-pulse requires knowledge of the target natural frequencies. Unfortunately, the natural frequencies can be accurately calculated for only a few simple geometries. Thus, the natural frequencies of practical targets such as missiles and airplanes must be extracted from measured transient scattering data. It should also be mentioned that there are ways to construct E-pulses directly from the transient response and the natural frequencies obtained as a by product [20]. The problem of extraction of the natural frequencies is also very difficult and requires more research in both the measurement technology and the extraction procedures. For the latest in the extraction procedure consult Ilavarasan [19].

2.4 Performance of Automated Discrimination Scheme

This section describes the application of the automated E-pulse and S-pulse discrimination scheme to theoretical scattering data for thin wires. Scattering data was generated using a frequency domain method-of-moments solution as described in Appendix A. A Galerkin technique employing piecewise sinusoidal basis functions and thin-wire approximations was used. The back-scattering responses of wires of length 0.80, 0.85, 0.90, 0.95, 1.00, 1.05, 1.10, 1.15, and 1.20 meters were calculated for

length-to-radius ratios (l/a values) of 100, 200, 400, and 800. The complex field values were calculated at 512 equally spaced frequencies between 0.002 GHz and 1.024 GHz. These results were subsequently inverse Fourier transformed using a fast Fourier transform (FFT) to obtain the transient response. A Gaussian pulse was used for the incident wave $p(t)$. The temporal variation is given by

$$p(t) = \exp(\frac{-4t^2}{\tau^2}) \tag{2.16}$$

where $\tau = 1$ ns was chosen to give a pulse width of approximately 2 ns between the 2% of maximum points.

Calculations were performed for all wires at both broadside-incidence orientation and 45 degrees off broadside. The wire natural frequencies were extracted from the calculated data using a hybrid E-pulse/least squares method [21] as would be done in the case of measured responses. In this case, the extracted natural frequencies were found to be very close to those computed from a singularity expansion method (SEM) formulation as described in Chapter 3 and Appendix B. The E-pulses and quadrature S-pulses were synthesized for each of the wire lengths and l/a values. To simulate noise encountered in a practical implementation, the calculated transient responses were corrupted by adding varying amounts of Gaussian noise. The automated discrimination process was applied to the noisy data.

In transient analysis, the usual Continuous-Wave (CW) definition of SNR is inappropriate. It is more useful to interpret the SNR within a specified time window, the choice of which affects the SNR value. For this analysis the window duration W_d was

chosen as the minimum duration window that contains 99% of the total energy in the noise free data. The ratio of the signal energy to the noise energy within this window is

$$SNR\ (dB) = 10.0 \log_{10} \left\{ \frac{\int_{W_d} v^2(t)dt}{\psi_0 W_d} \right\} \tag{2.17}$$

where $v(t)$ is the noise free signal. A zero-mean Gaussian white noise model is used throughout the analysis. To illustrate the level of noise corruption used in the analysis, several examples are shown. Figure 2.1 shows the noise free back-scattering response of a broadside 1.00 m wire with l/a = 800. Figure 2.2 shows the same response with noise added to provide a SNR of 30 dB. Figure 2.3 shows the same response with noise added to provide a SNR of 5 dB.

To test the sensitivity of the E-pulse method to SNR and differences in target dimensions, the E-pulses for all wires with l/a = 800 were used to discriminate the response of a 1.00 m wire with l/a = 800. The response waveform was corrupted with varying amounts of noise with the SNR varying from 5 dB to 30 dB. EDR values for each of these noisy signals were computed. Figure 2.4 shows the results of this test when the 1.00 m wire is in the broadside orientation. If the 1.00 m wire is identified correctly the EDR of the 1.00 m wire E-pulse is zero. This is the case for all values of SNR computed. As expected, the EDR is largest for all wrong target E-pulses when the SNR is high. When the SNR is low, the EDR for all wrong target E-pulses is less. Also, E-pulses for targets similar to the 1.00 m wire (ie. 0.95 m and 1.05 m) provide smaller EDR values than E-pulses for targets significantly different from the 1.00 m wire (ie. 0.80 m and 1.20 m). Figure 2.5 shows a similar result when the response is from the

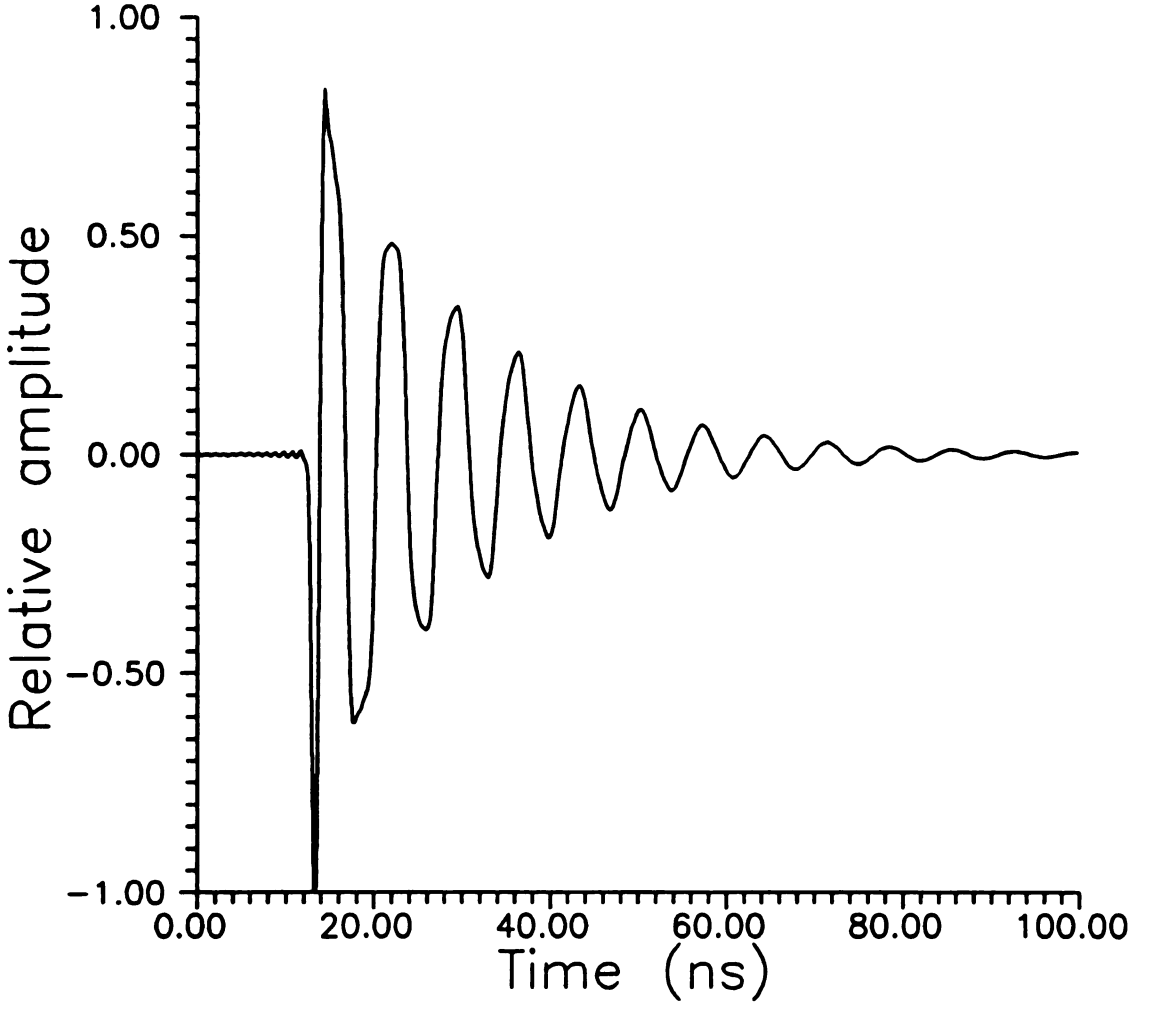

Figure 2.1 Noise free back-scattering response of 1.00 m (l/a = 800) oriented at broadside.

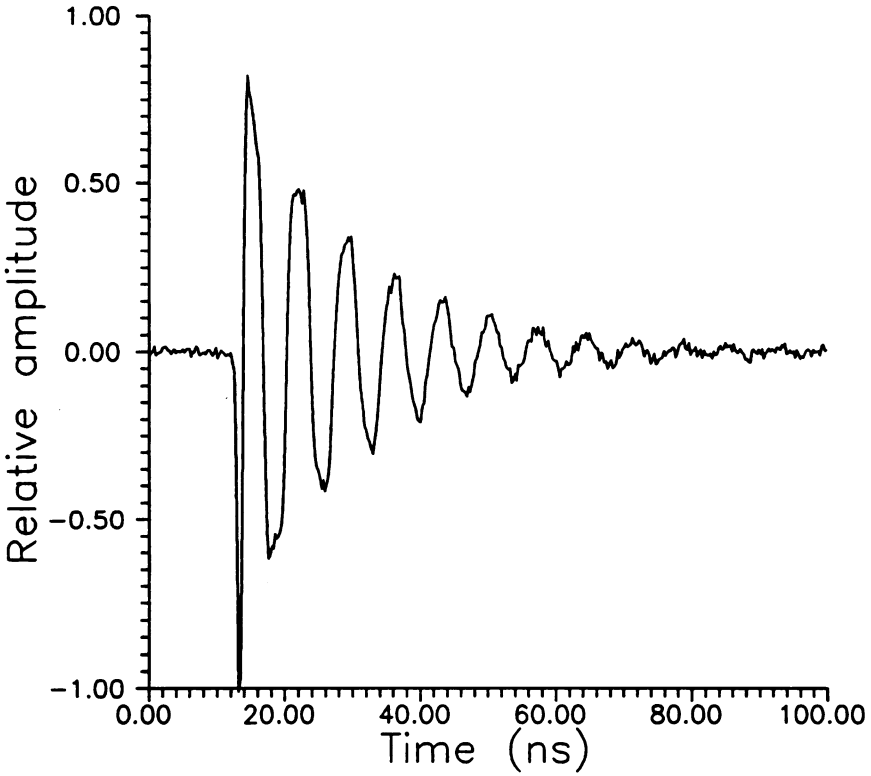

Figure 2.2 Back-scattering response of 1.00 m wire (l/a = 800) oriented at broadside with SNR of 30 dB.

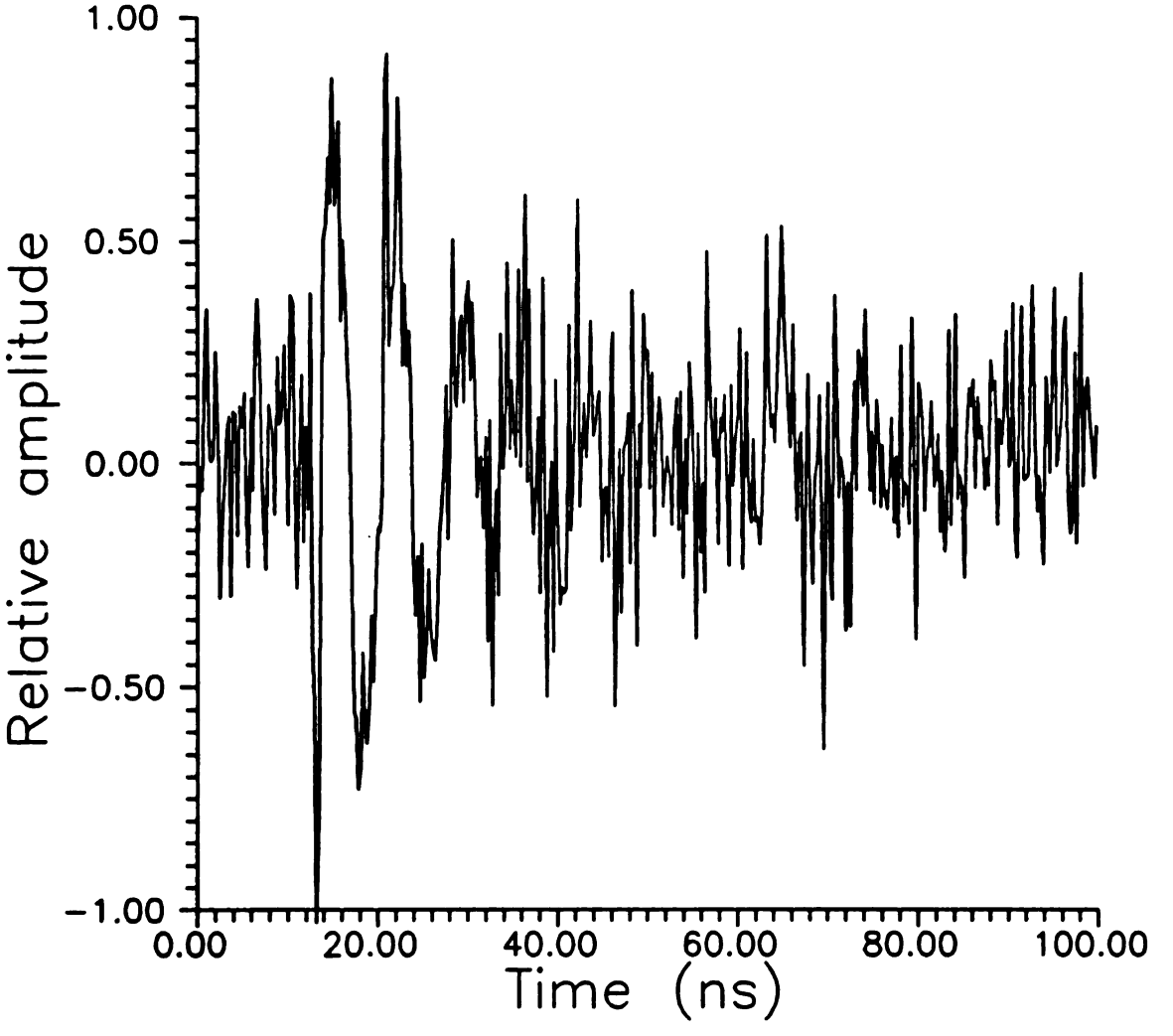

Figure 2.3 Back-scattering response of 1.00 m wire (l/a = 800) oriented at broadside with SNR of 5 dB.

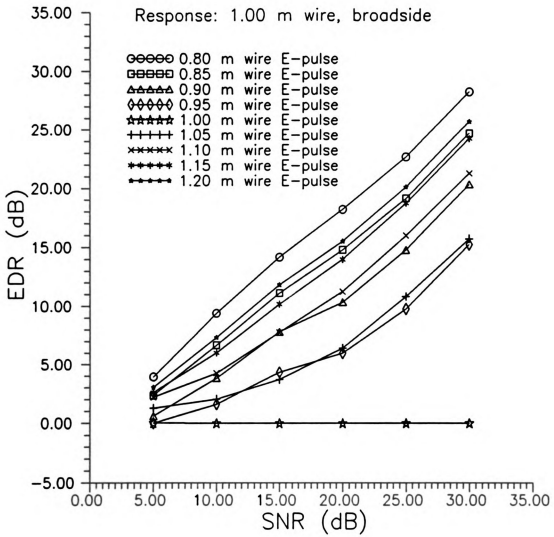

Figure 2.4 EDR values computed for response of 1.00 m wire (l/a = 800) oriented at broadside.

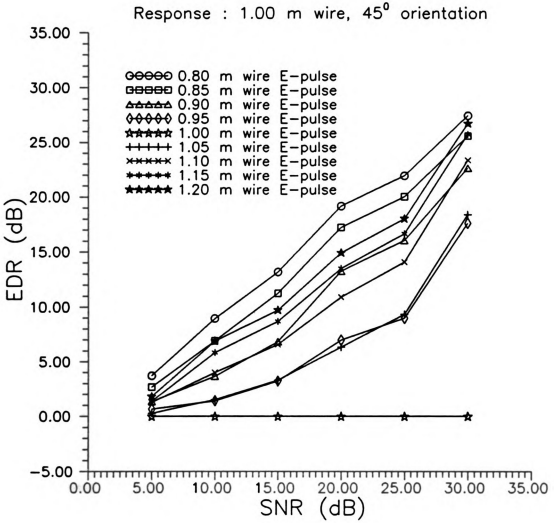

Figure 2.5 EDR values computed for response of 1.00 m wire (l/a = 800) oriented 45 degrees from broadside.

1.00 m wire in the 45 degree orientation. This illustrates the aspect independence of the E-pulse method.

It is interesting to determine if the effectiveness of target discrimination using E-pulses and S-pulses is a function of target Q. Note that thinner wires (those with higher l/a ratios) have higher Q values. Thus, several tests were run using wires of different thickness. Wires with l/a values of 100, 200, 400, and 800 were used. The evaluation proceeds as follows: The E-pulses for all wires (l = 0.80, 0.85, 0.90, 0.95, 1.00, 1.05, 1.10, 1.15, 1.20) with l/a = 100 were used to discriminate a 1.00 m wire with l/a = 100. Similarly, the E-pulses for all wires with l/a = 200 were used to discriminate a 1.00 m wire with l/a = 200. This process was repeated for the cases of l/a = 400 and l/a = 800. In each case, 1.00 m wire was oriented at broadside and the EDR of the E-pulses corresponding to wires that are $\pm 10\%$ (ie. wires of length 0.90 m and 1.10 m) were calculated. The minimum of the two EDR values was plotted vs SNR for each of the l/a cases. Figure 2.6 shows that wires with l/a = 800 have higher minimum EDR values for a given SNR than thicker wires. This effect is seen for other aspect angles as shown in Figure 2.7 where the wire is oriented 45 degrees from broadside.

The same tests were performed for the case of S-pulse discrimination. Figure 2.8 shows the results when using quadrature S-pulses based on the first fundamental resonance frequency of the wires with l/a = 800. Again, $v(t)$ is chosen as the broadside response of a 1.00 m wire with l/a = 800. The SDR results are similar to those obtained using the E-pulse method, however, the SDR values are significantly larger than the EDR for all values of SNR. Figure 2.9 indicates that S-pulses based on the second resonance frequency do not yield large SDR values regardless of SNR. This is due to the fact that

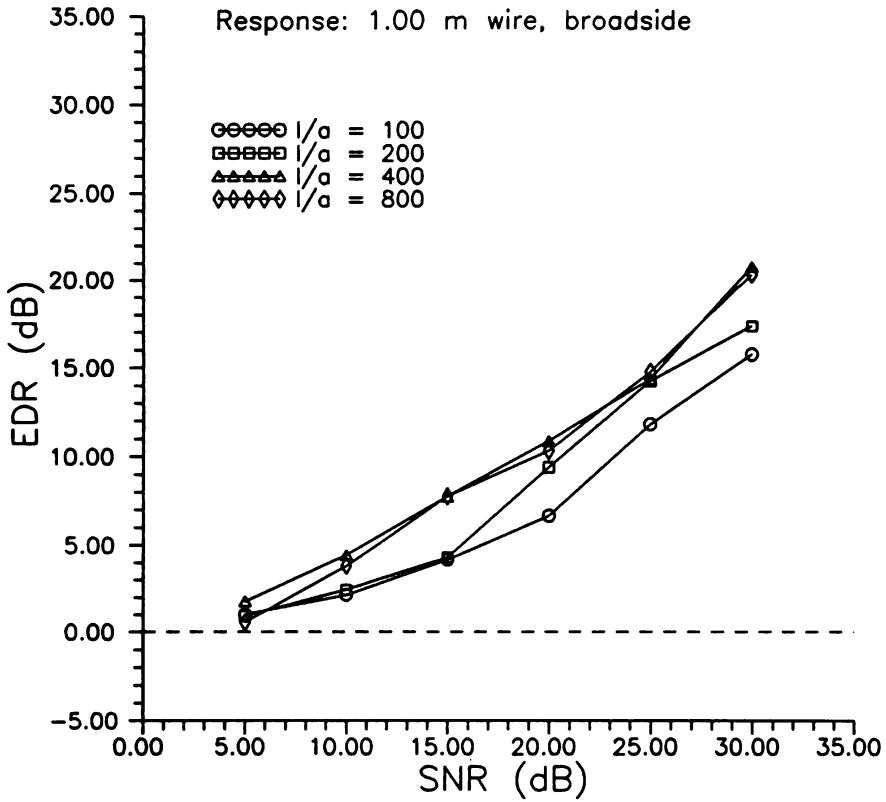

Figure 2.6 Minimum EDR values computed for 0.90 m and 1.10 m wire E-pulses for response of 1.00 m wire oriented at broadside.

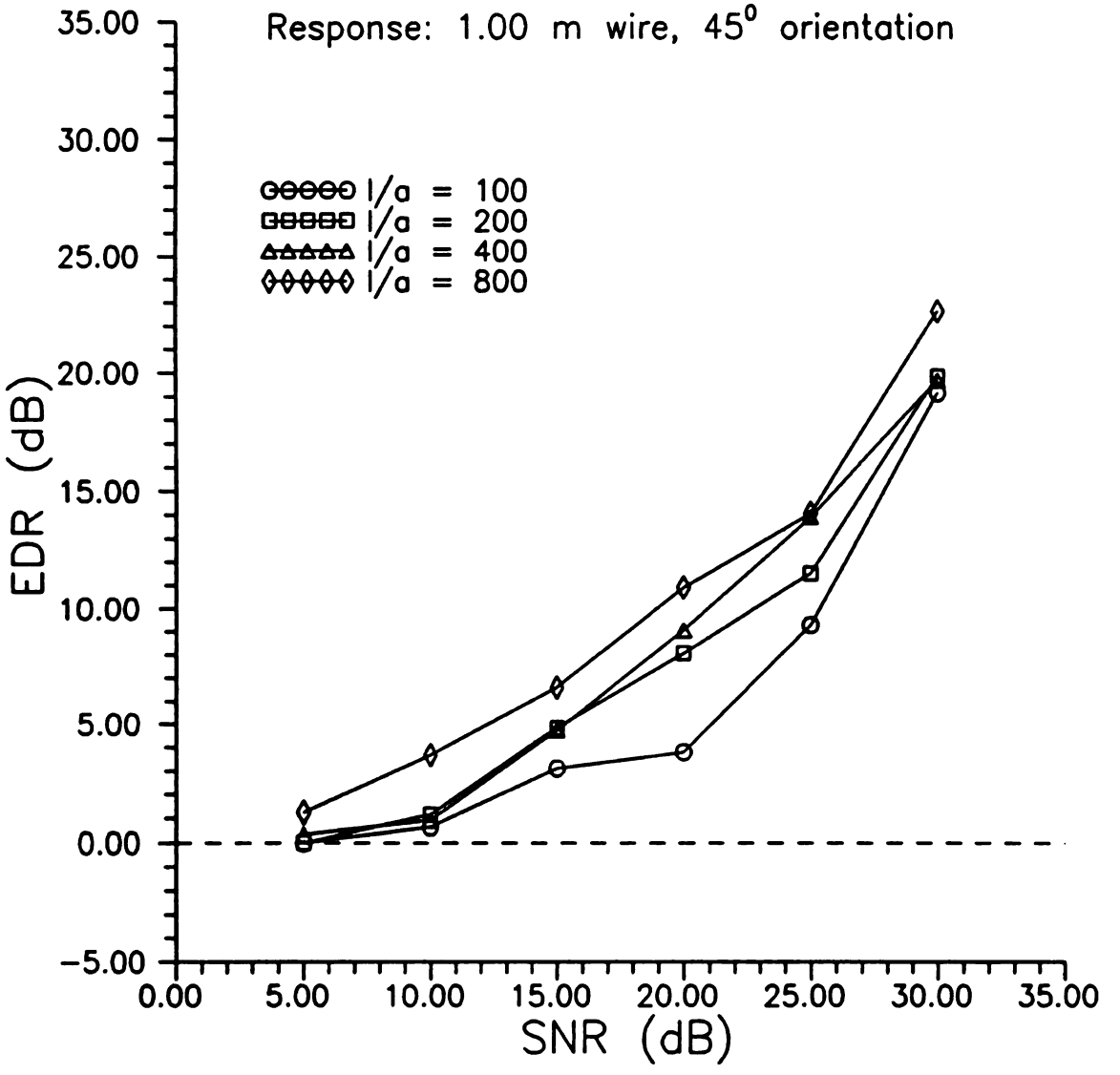

Figure 2.7 Minimum EDR values computed for 0.90 m and 1.10 m wire E-pulses for response from 1.00 m wire oriented 45 degrees from broadside.

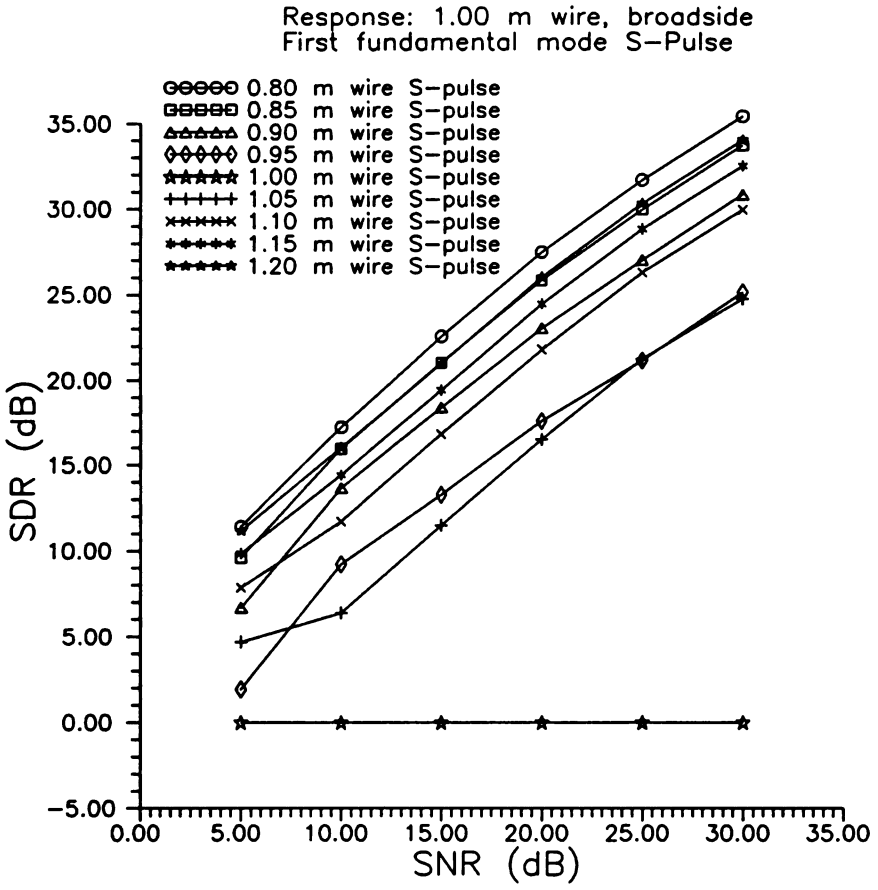

Figure 2.8 SDR values computed for first mode S-Pulses for response of 1.00 m wire (l/a = 800) oriented at broadside.

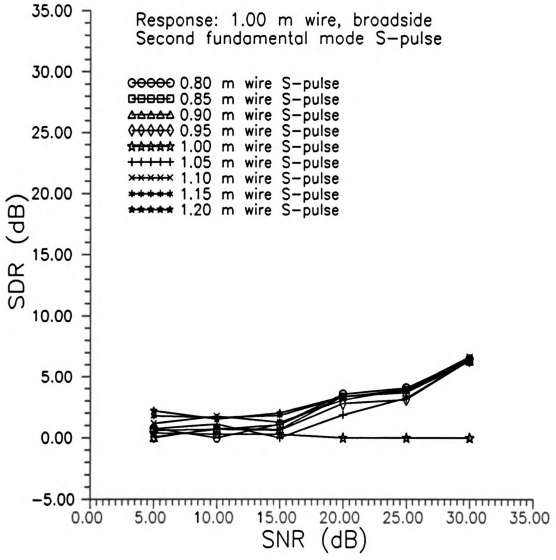

Figure 2.9 SDR values computed for second mode S-pulse for response from 1.00 m wire (l/a = 800) oriented at broadside.

the second resonance of the 1.00 m wire is excited for broadside incidence. Thus, the expected mode must be present in the response waveform for the S-pulse method to work effectively. Figure 2.10 shows that the second mode S-pulse can be used effectively for the case of 45 degree orientation since the second mode is strongly excited.

The effect of target Q is evaluated for S-pulse discrimination as was done previously in the case of E-pulse discrimination. Figure 2.11 shows the results when using first mode S-pulses for the broadside response of the 1.00 m wire. The results are consistent with the E-pulse results except that the SDR values are larger than the EDR values. Further evidence of this phenomenon is shown in Figure 2.12 for the case of second mode S-pulses and a response from a 1.00 m wire at 45 degree orientation.

This section has presented an automated discrimination scheme based on the E-pulse and S-pulse methods. The scheme can be readily applied in applications where many targets are considered and a computer is used to make the discrimination decisions. The performance of the discrimination scheme is evaluated for thin wire targets in the presence of Gaussian random noise.

Several conclusions can be made from the numerical results. For the cases considered, the S-pulse discrimination scheme is successful in situations where the targets are $\pm 10\%$ different in length even when the SNR is only 10 dB, while the E-pulse scheme is successful where the targets are $\pm 10\%$ different in length with an SNR of 15 dB. Also, the discrimination is better for higher Q targets with both the E-pulse and S-pulse schemes. Discrimination of very similar targets whose natural frequencies are also similar requires higher values of SNR to obtain a given EDR or SDR value. On the other hand, for targets that are vastly different in size and shape (with natural frequencies that

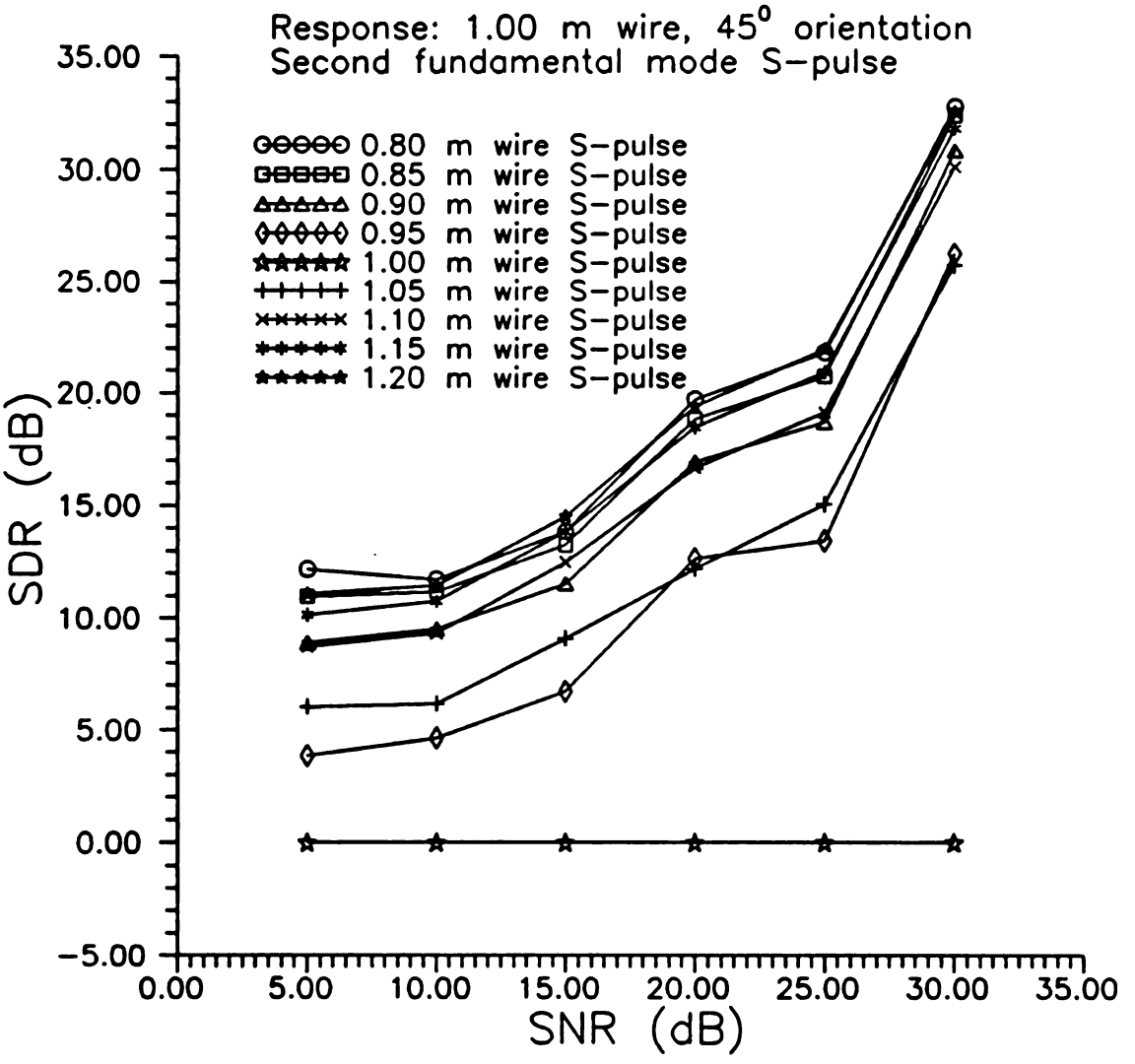

Figure 2.10 SDR values computed for second mode S-pulse for response of 1.00 m wire (l/a = 800) oriented 45 degrees from broadside.

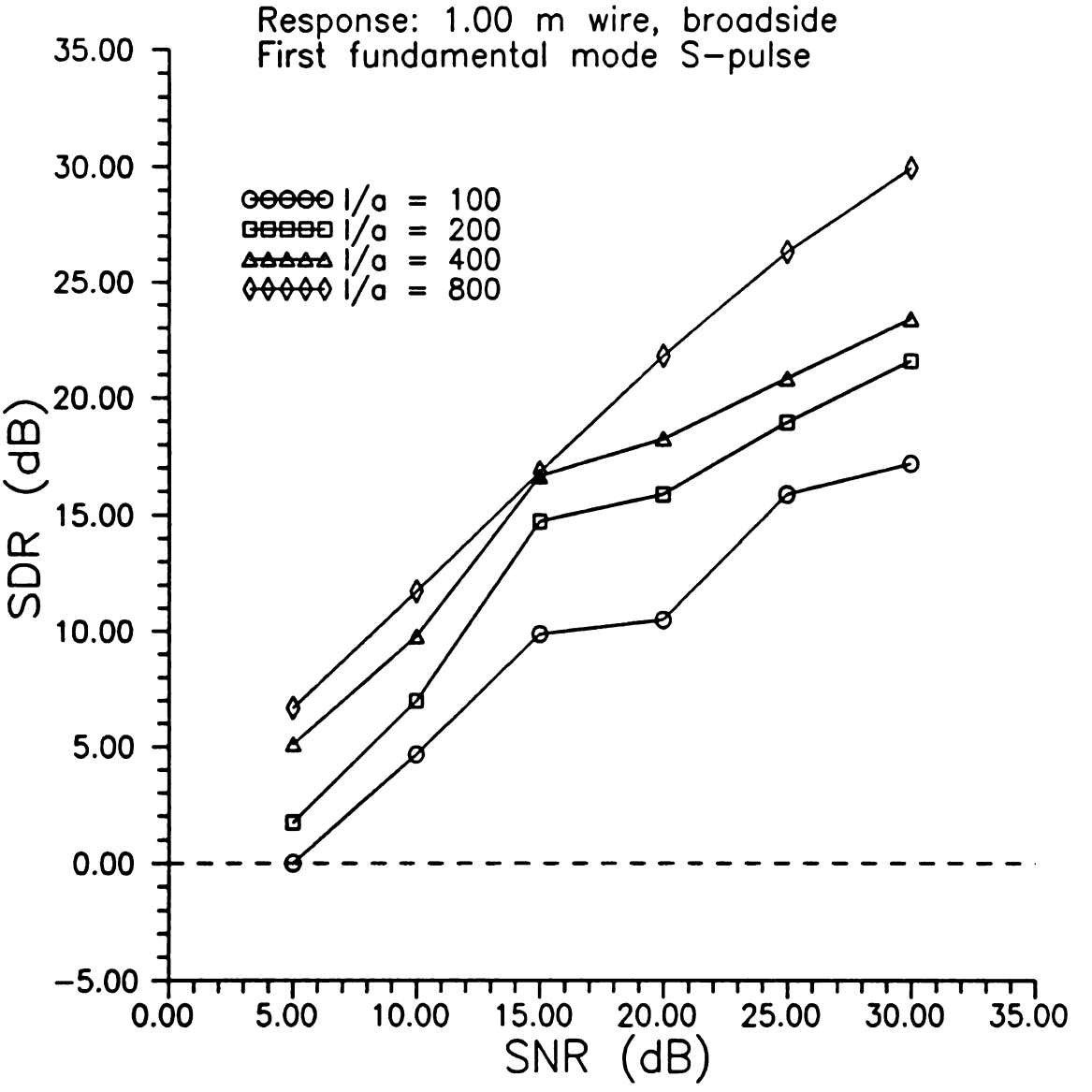

Figure 2.11 Minimum SDR values computed for S-pulses for 0.90 m and 1.10 m wires using response of 1.00 m wire oriented at broadside.

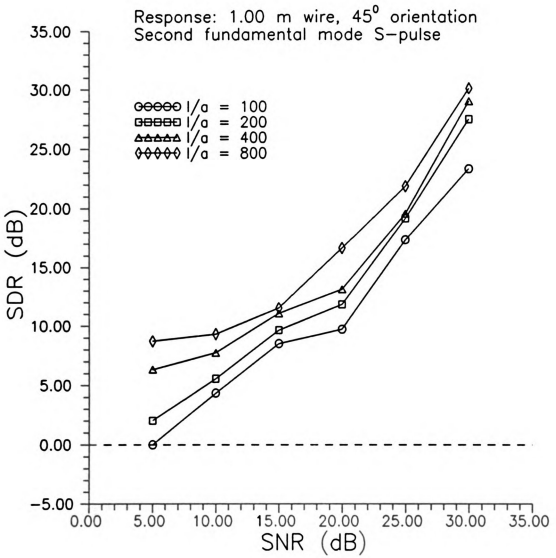

Figure 2.12 Minimum SDR values computed for second mode S-pulses for 0.90 m and 1.10 m wires using response from a 1.00 m wire oriented 45 degrees from broadside.

are also vastly different) it should be possible to obtain a sufficient EDR or SDR value for discrimination even in a low SNR environment.

For systems design, curves such as those presented in this section could be generated for a group of targets. The transmitter, receiver, and antenna requirements could then be estimated based on the desired discrimination level and SNR environment.

2.5 Multiple Target Discrimination

The applicability of the E-pulse and S-pulse method to a waveform where there is only a single target response has been well documented [9, 22]. The case where the waveform may contain more than one target response is more difficult and has not yet been adequately addressed. This section qualitatively addresses some of the problems associated with the multiple target situation. The analysis in this section assumes that the targets are electrically uncoupled. The case when the targets are electrically coupled is significantly more complicated and is the subject of Chapter 3 and 4. Since the number of possible configurations for a multiple target system can become very large and complicated, the analysis here of this section is limited to the simpler case of two targets.

Assuming a mono-static radar, the geometry of a two target situation is diagramed in Figure 2.13. As shown in the diagram, target 1 is located at $\vec{r}_1$ and target 2 is located at $\vec{r}_2$ relative to the antenna. There are several distinct situations with regard to the locations of the targets.

First, let $|\vec{r}_2| = |\vec{r}_1| + \epsilon$ so that the response from target 1 appears first while the response from target 2 is delayed by $t_d = 2\epsilon/c$ from the start of the target 1 response.

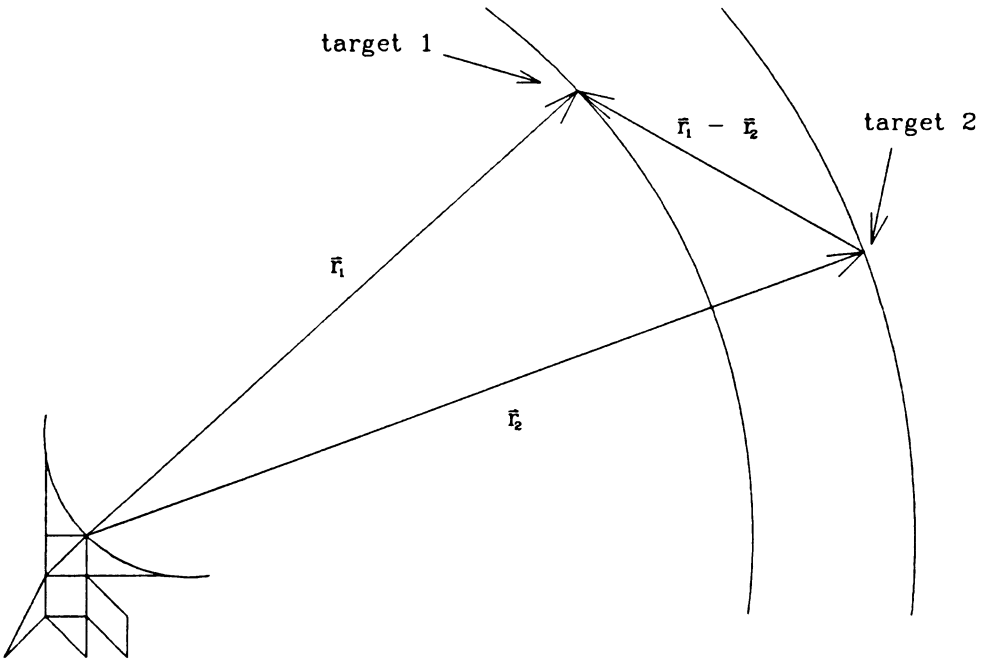

Figure 2.13 Geometry for two target discrimination problem.

Then consider the case when $|\vec{r}_2 - \vec{r}_1|$ is very large so that multiple interactions between the targets are sufficiently delayed and diminished that the targets can be considered isolated. The exact distance at which this approximation is valid depends on the size and type of targets, the incident field waveform, and receiver bandwidth. The received waveform $v(t)$ can then be written as the superposition of two responses

$$v(t) = v_1(t) + v_2(t) \tag{2.18}$$

where $v_1(t)$ and $v_2(t)$ are the responses from targets 1 and 2 assuming that the targets are independent and hence uncoupled. Now, the discrimination procedure can be applied easily if the response from target 1 is significantly diminished prior to the response of target 2 and

$$t_d > W_e + T_p + T_{e_{max}} + 2T_{tr_{max}} \tag{2.19}$$

where W_e is the observation window, T_p is the pulse width, $T_{e_{max}}$ is the maximum E-pulse duration in the database and $T_{tr_{max}}$ is the maximum transit time in the database. In this situation, the response of target 1 is distinctly separated in time from the response of target 2 and the response of target 1 that is present during the late-time interval of target 2 is assumed to be negligible. A slightly more difficult case occurs when

$$T_p + T_{e_{max}} + 2T_{tr_{max}} < t_d < W + T_p + T_{e_{max}} + 2T_{tr_{max}} \tag{2.20}$$

in which case the target responses overlap. In this case, discrimination proceeds as follows: First, identify the response from target 1 by applying the method with a reduced observation window W_e sufficient to prevent inclusion of the target 2 response. With target 1 identified, compute the convolution $w(t) = v(t) * e_1(t)$. Note that the convolution

operation eliminates any overlap of the resonance response of target 1 onto the response of target 2. The discrimination procedure can then be applied to the waveform $w(t)$ as usual except that the start of late-time for target 2 T_{l_2} is

$$T_{l_2} = T_{b_2} + T_{e_1} + T_p + 2T_{tr} + T_e \tag{2.21}$$

where T_{b_2} is the beginning of the response from target 2, T_{e_1} is the E-pulse duration for target 1, and T_{tr} and T_e are the transit time and assumed E-pulse duration of target 2. Unfortunately, if the modes excited in target 2 are degenerate with the modes of target 1 the method fails since the late-time of target 2 is zero in the $w(t)$ waveform. This is not as bad as it seems since at least one of the targets is identified and the identity of the second target is limited to a smaller number of possible choices.

As a graphical example of the preceding process, consider the response shown in Figure 2.14. Targets 1 and 2 are simulated with wires of length 0.90 m and 1.20 m with $l/a = 200$. The start of the response from the 1.20 m wire is delayed 25 ns from the start of the response from the 0.90 m wire. After convolving this waveform with the E-pulse for a 0.90 m wire the waveform shown in Figure 2.15 is obtained. The modes of target 1 are annihilated indicating that discrimination can be effected for target 1. Next, this waveform is convolved with the E-pulse for the 1.20 m wire. The resulting waveform is shown in Figure 2.16. Note that the late-time of target 2 is nearly zero in this waveform indicating that discrimination can be effected.

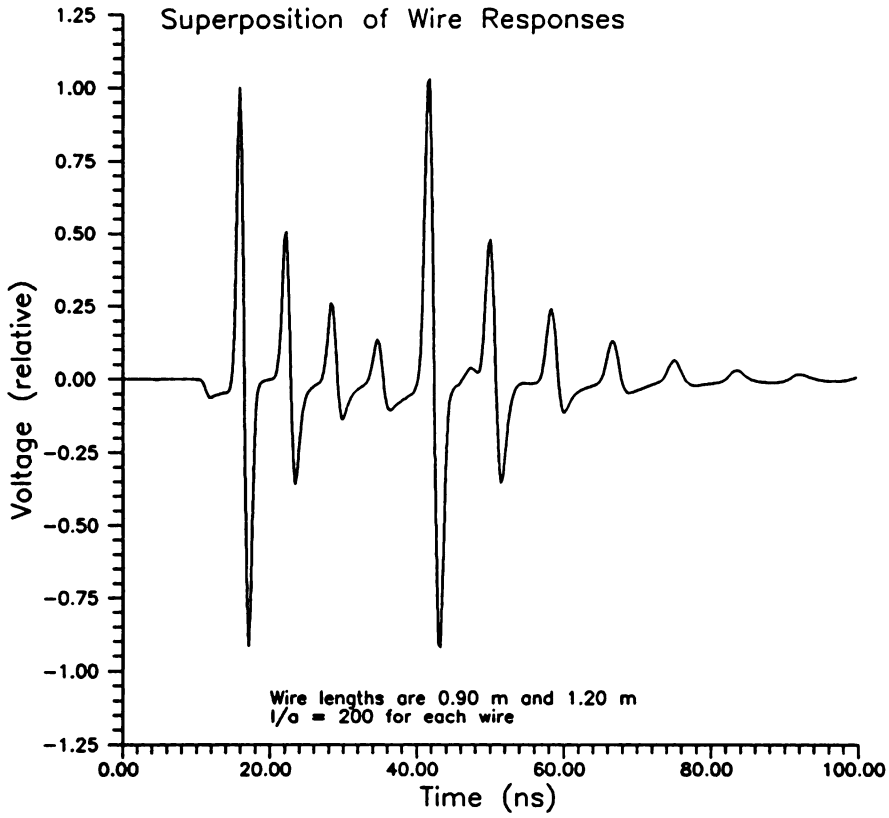

Figure 2.14 Waveform produced by superposition of response from wires of length 0.90 m and 1.20 m with $l/a = 200$. The response of the 1.20 m wire is delayed 25 ns from the start of the 0.90 m wire.

Next, consider the case of small time delays when

$$t_d < T_p + T_{e_{max}} + 2T_{tr_{max}} \tag{2.22}$$

where there is an insufficient window available for evaluation of target 1 separately from target 2. By linearity, the late-time of the received waveform $v(t)$ is composed of the natural frequencies contained in $v_1(t)$ and $v_2(t)$. This suggests that discrimination can be accomplished by successively convolving the waveform with combinations of E-pulses since

$$c_{e_{12}}(t) = v(t) * e_1(t) * e_2(t) = 0 \qquad t \geq T_l + T_{e_1} + T_{e_2} \tag{2.23}$$

when the E-pulses $e_1(t)$ and $e_2(t)$ match the targets producing the waveform. Note that T_l must be chosen as the point after which both target 1 and target 2 are in late-time. The evaluation of the EDN must be limited to the late-time portion of the convolved waveform. This could lead to inaccurate determination of target 1 depending on the exact spacing of the targets, the Q of target 1 and the transit time of target 2. To implement this scheme, the number of targets and the location of target 2 must be established prior implementing the discrimination process. This information might be obtained by using another radar system capable of resolving the targets. The identity of the targets could then be determined with an impulse radar system using the multiple E-pulse scheme. Alternatively, the impulse radar could be designed with sufficient angular resolution to resolve the targets without need for a secondary tracking radar or even the multiple E-pulse technique. Unfortunately, achieving sufficient angular resolution with an impulse radar will probably be significantly more difficult than with a conventional radar unless great advances are made in the area of highly directive UWB antennas.

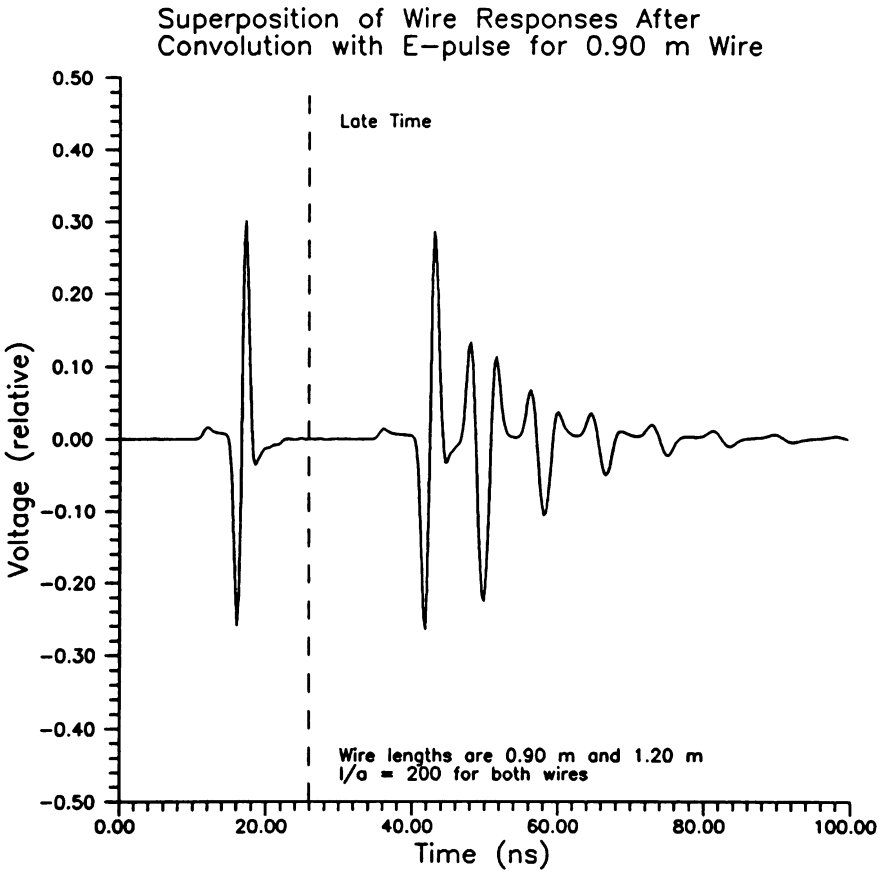

Figure 2.15 Waveform of Figure 2.14 after convolution with E-pulse for 0.90 m wire.

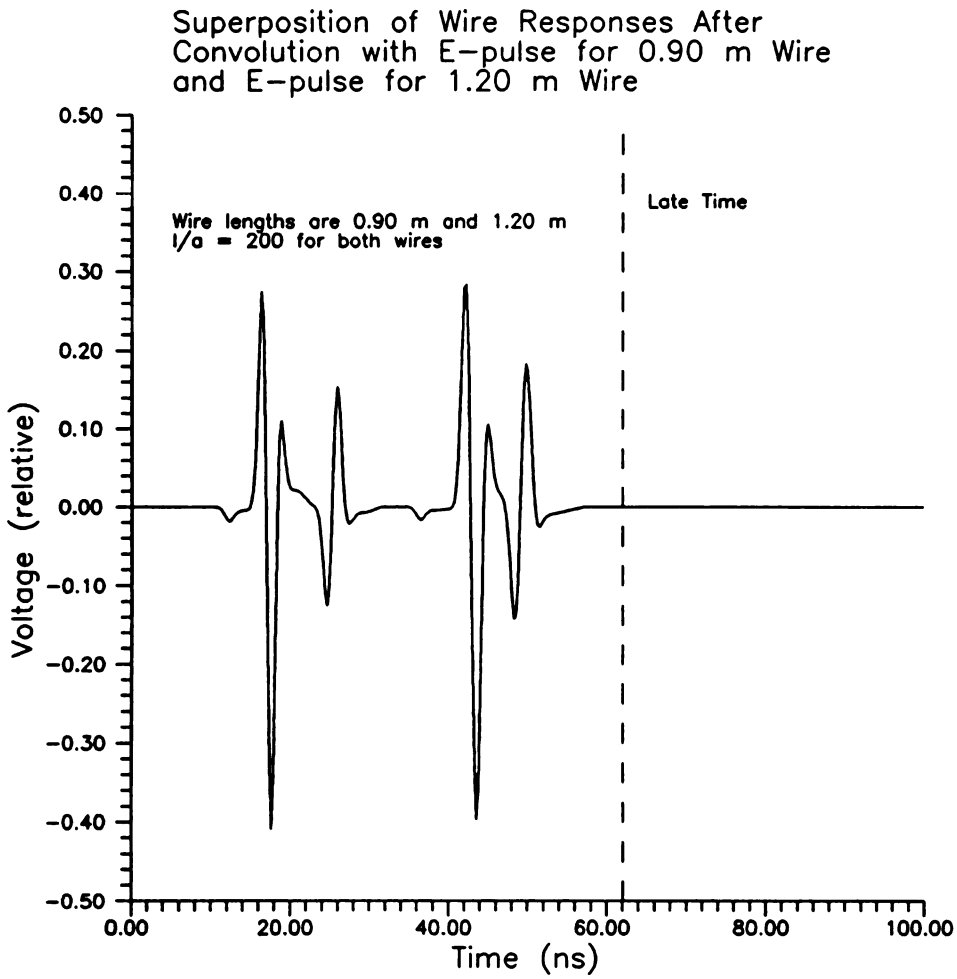

Figure 2.16 Waveform of Figure 2.15 after convolution with E-pulse for 1.20 m wire.

To graphically illustrate the use of multiple E-pulses for discrimination, consider the response shown in Figure 2.17. The targets are the same wires used previously except that the response of the second wire has not been time shifted. Clearly one could not presume to know that there are actually two target responses in this waveform. After convolution of this waveform with the E-pulse for the 0.90 m wire the result as shown in Figure 2.18 is obtained. Note that the response is not zero in the late-time since the modes of the 1.20 m wire were not annihilated by the E-pulse for the 0.90 m wire. Interestingly, it may be possible to determine if there are two targets present by comparing the signal after convolution with the first E-pulse to the expected result of zero. Of course if the targets were identical this method would fail. Next, this waveform is convolved with the E-pulse of the 1.20 m wire. This result is shown in Figure 2.19 and it is clear that all natural modes are eliminated in the late-time.

In applying this method, accurate knowledge of ϵ is essential since the discrimination scheme is predicated on knowing the start of late-time in the measured response. As discussed previously, the start of late-time is estimated based on the start of the response, the maximal transit time of the target, and the pulse width. If the beginning of the response of target 2 is unknown then the estimate of the start of late-time for this target is in error. Unfortunately, even if target 2 is known to be present but ϵ remains unknown, the estimates are such that the discrimination scheme is erroneously be applied to early-time data. This can cause the method to fail since the early-time response is not annihilated by the E-pulse. The best way to avoid this problem is to design the impulse radar with angular resolution to sufficient to minimize the likelihood of encountering this problem. Unfortunately, this does not solve all multiple target

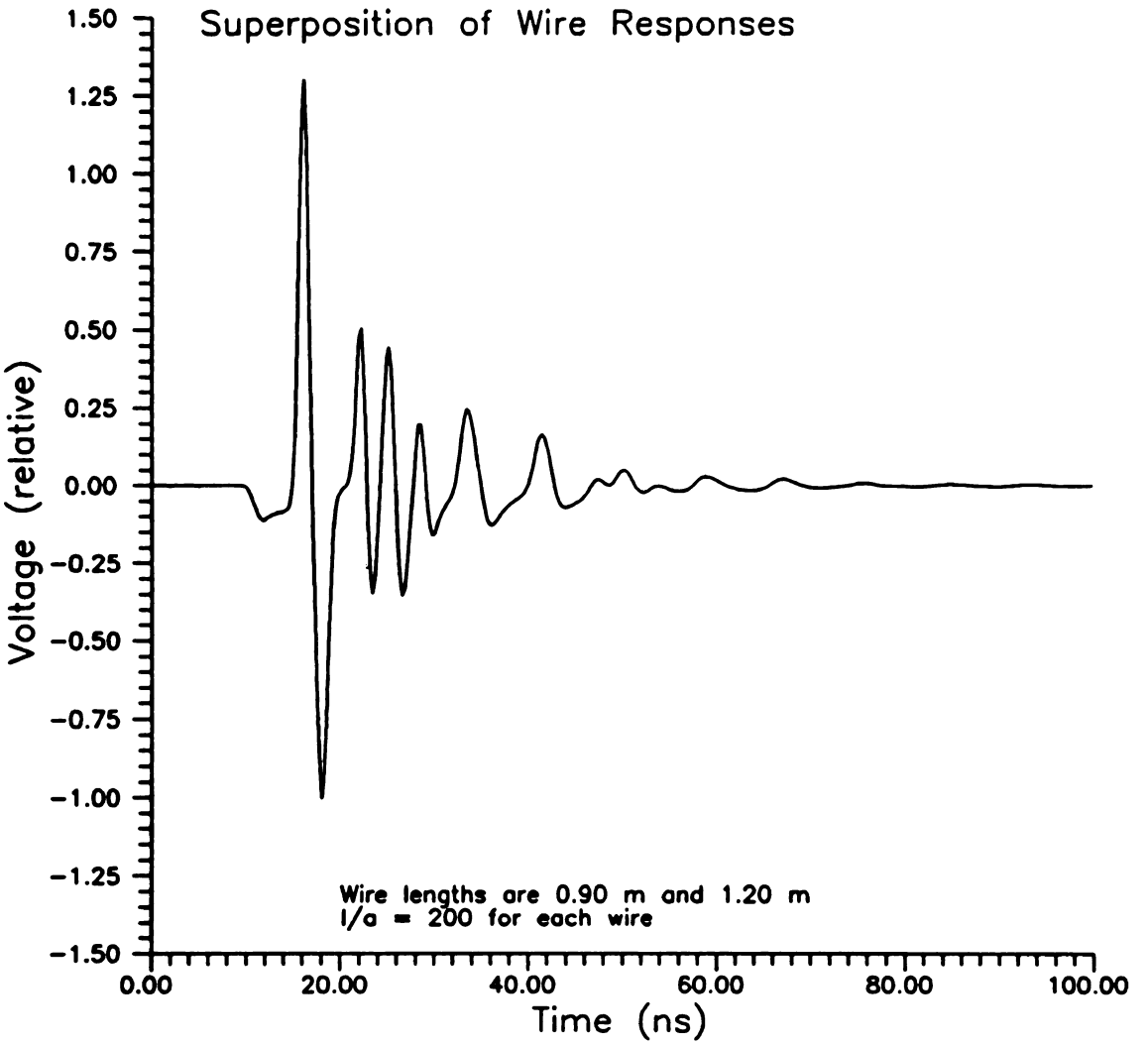

Figure 2.17 Waveform produced by superposition of responses from wires of length 0.90 m and 1.20 m with l/a = 200. The response of the 1.20 m wire is co-temporal with the response of the 0.90 m wire.

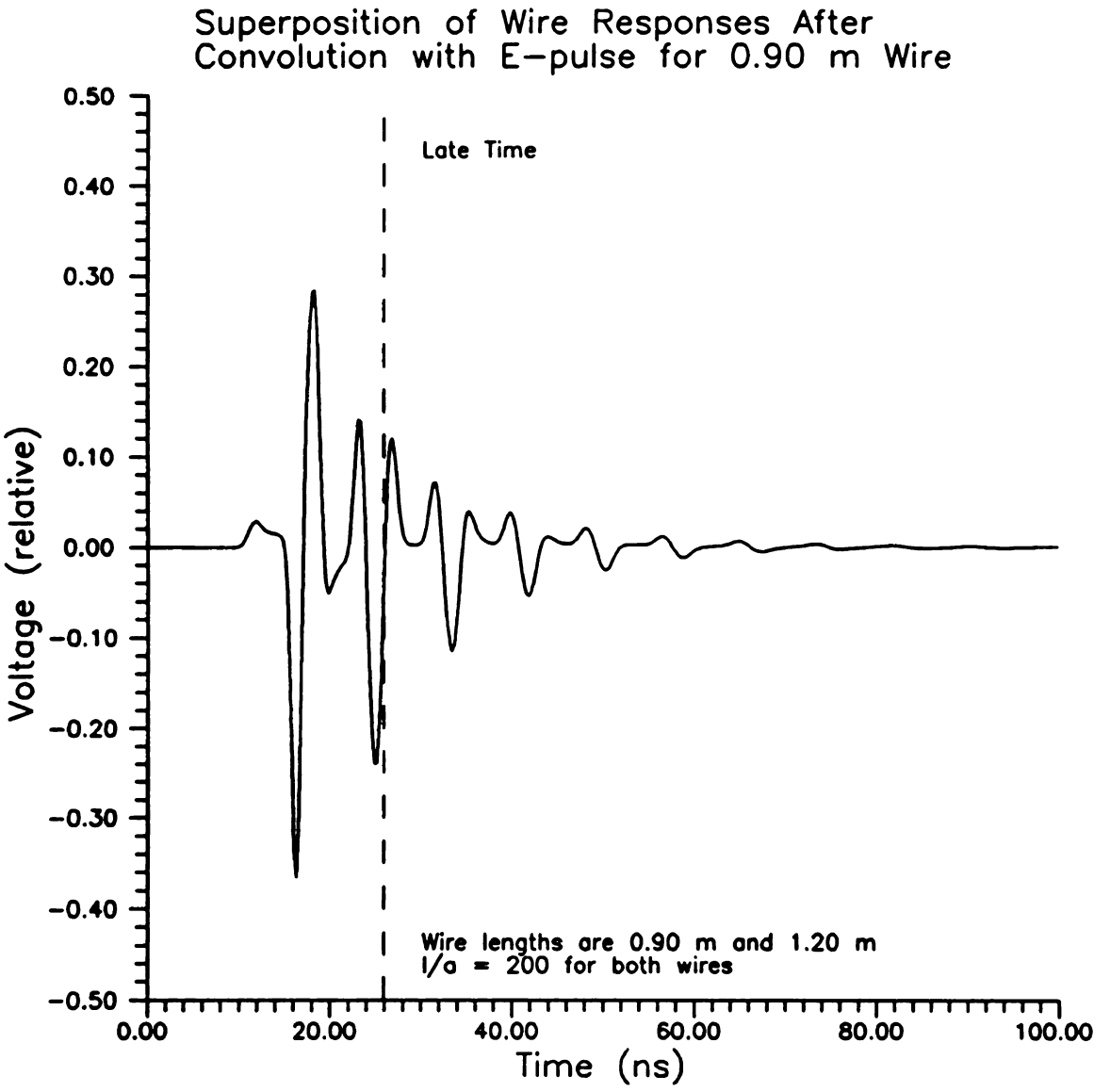

Figure 2.18 Waveform of Figure 2.17 after convolution with the E-pulse for 0.90 m wire.

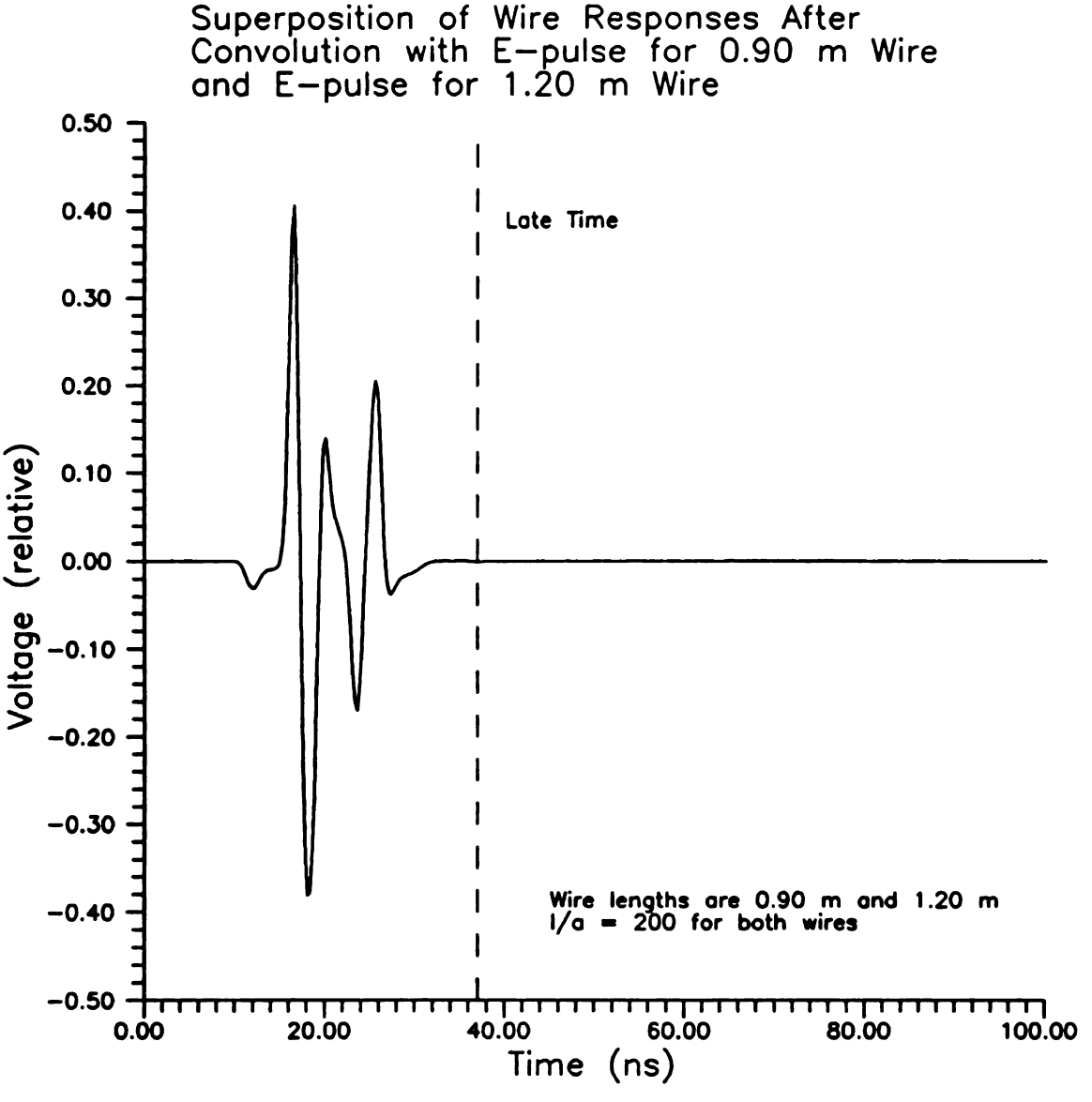

Figure 2.19 Waveform of Figure 2.18 after convolution with the E-pulse for 1.20 m wire.

problems.

The preceding method of using multiple E-pulses relied on the fact that two targets were known to be present and the exact start time of the target 2 response was known. If the number of targets and their positions are not known prior to using the E-pulse and S-pulse method, the discrimination is greatly degraded. To illustrate this point consider the case of two identical targets separated by a small amount in range. To simulate this situation the discrimination scheme was applied to a series of waveforms composed of the responses from two 1.0 m wires with the response from the second wire time shifted by varying amounts. Since the targets are identical, one would hope that the discrimination scheme would choose the 1.0 m wire as the target producing the response even though the discrimination scheme only assumes one target is present in the response. Figure 2.20 shows that for small values of time delay, the response is identified as belonging to the 1.0 m wire. Here the minimum EDR is very large indicating that the method works well. Unfortunately, the EDR decreases sharply when the time delay increases beyond a certain value and the method ultimately fails. The sudden decrease in EDR and failure of the method is due to the presence of the early-time response of the second wire. Since only one target is assumed, the early-time response of the second wire is misconstrued as being the late-time response from the first wire. The S-pulse method yields similar results as shown in Figure 2.21. In both the E-pulse and S-pulse results, the deterioration of the discrimination is not as severe for the 45 degrees orientation as compared to the broadside orientation. This is most likely due to the weaker early-time response of the 45 degree orientation responses as compared to the broadside responses. These curves suggest that discrimination might be possible for

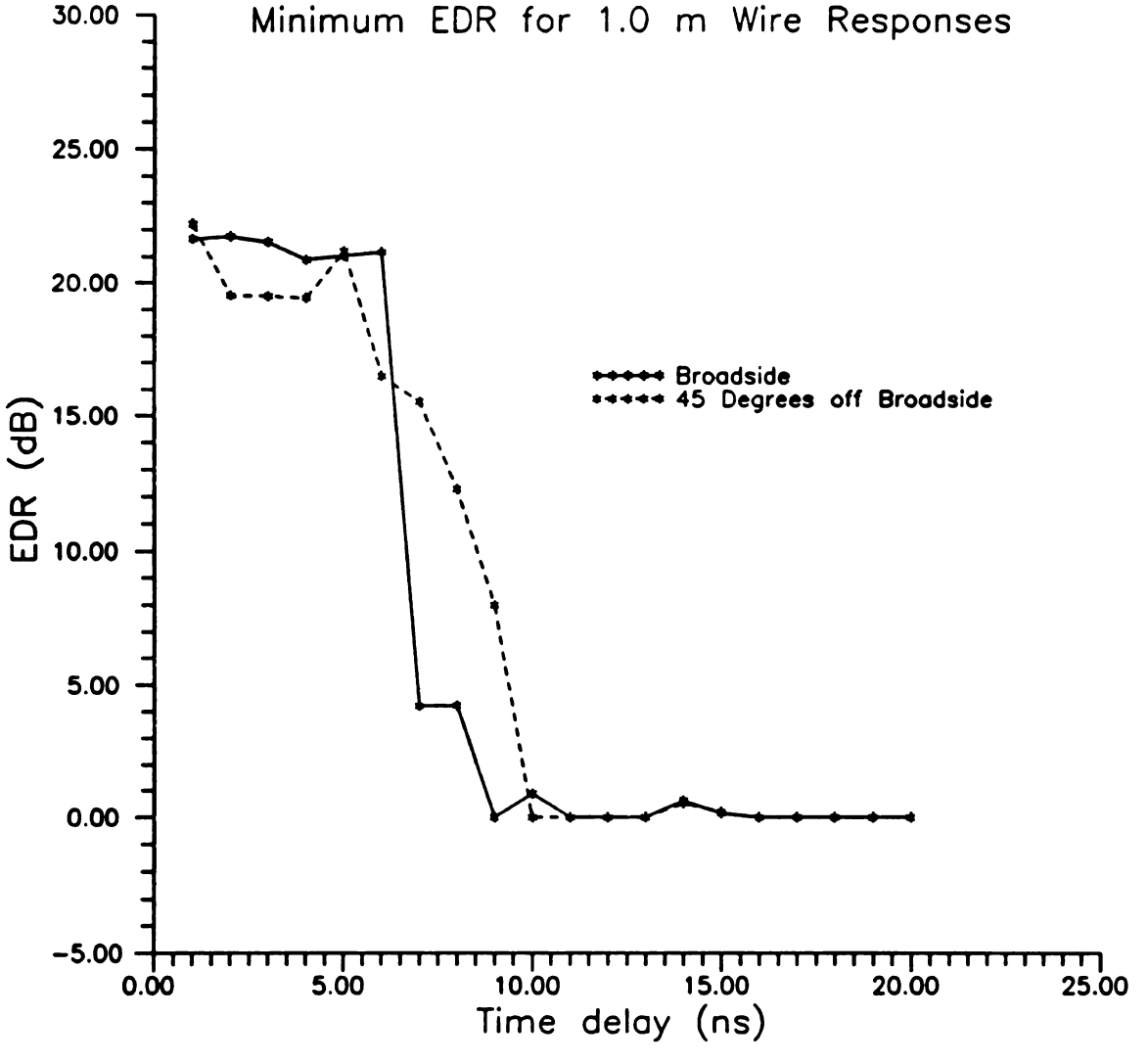

Figure 2.20 Minimum EDR vs time delay when E-pulse method is applied to a response consisting of two 1.0 m wires.

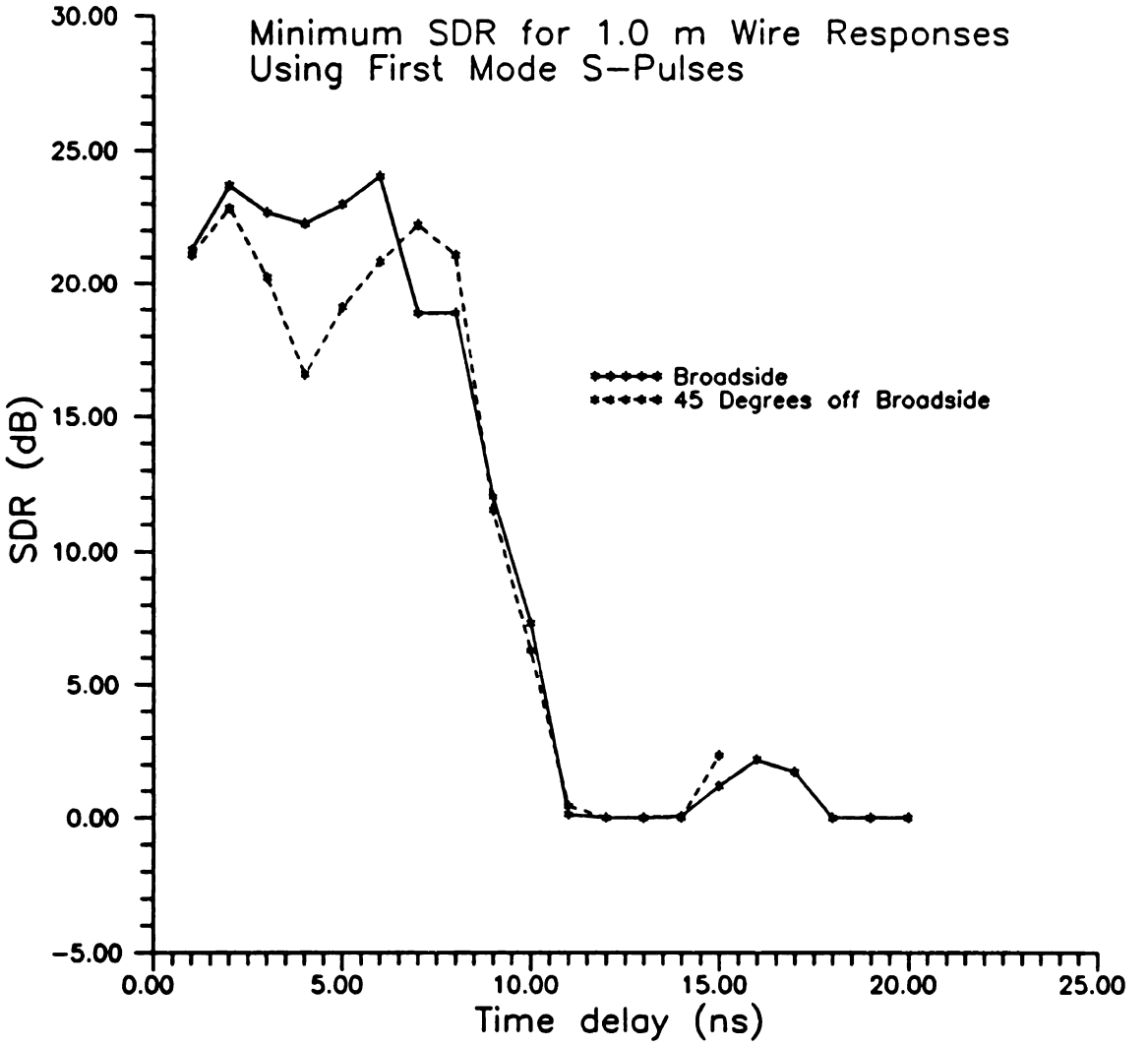

Figure 2.21 Minimum SDR vs time delay when S-pulse method is applied to a waveform containing responses from two 1.0 m wires separated by a time delay.

identical targets if the time delay is not so large as to place significant early-time signal components into the assumed late-time portion of the convolution (assuming no coupling between targets). The curves also show that discrimination is not possible when the targets are identical and have an intermediate range spacing (ie. too large for the early-time portions to be excluded and too small for the targets to be clearly separated in range and identified as two separate targets). The method can also be shown to completely fail when the responses are from different targets and the fact that two targets exist is not known prior to applying the discrimination scheme.

Next, consider the case of two targets closely spaced in both range and cross-range. For the military, this is a very practical situation to consider since aircraft squadrons are routinely flown in closely spaced formations. It is also important in the case of a target flying close to the ground or sea since the target images into the highly conducting surface and electrically appear as two targets. In this situation both ϵ and $|\vec{r}_2 - \vec{r}_1|$ are small and the scattering phenomena becomes very complicated. The first portion of the late-time before the field scattered from target 1 has reached target 2 is simply the superposition of the responses as previously considered. After the field scattered from target 1 has interacted with target 2 and returned to the observer, the received waveform is no longer simply the superposition of responses. The transient interaction among targets and the ground or sea causes some interesting effects. The received waveform can be described by the natural frequencies of the individual (uncoupled) scatterers prior to the interaction, and a different set (coupled) characteristic of the system of scatterers after the interaction has occurred. The system natural frequencies are dependent on the size and shape of the individual scatterers and their

locations and orientations. This problem is extremely important in the case of target discrimination since any change of the natural frequencies has the potential to reduce the effectiveness of the E-pulse and S-pulse discrimination method. The initial course of this research effort was to establish how the natural frequencies of a target are affected by the transient mutual coupling. Chapter 3 presents the analysis used to evaluate this problem and the physical interpretation necessary to understand the transient coupling problem. Chapter 4 evaluates E-pulse and S-pulse discrimination effectiveness for thin wire targets when coupling has been included.

Chapter 3

Transient Coupling

3.1 Introduction

To preface the problems discussed in this chapter, it is useful to highlight some of the relevant literature. Tesche [23] was the first analyze the current induced on a thin wire by a transient field using SEM. In a later paper [24] Tesche examined the far-zone transient response of a linear antenna using SEM. Umashankar, Shumpert and Wilton [25] were the first to perform the SEM analysis of a thin wire parallel to an infinite perfectly conducting ground plane. Later papers by Shumpert and others have considered the special case when the wire is very close to the ground plane [26] and when the ground is lossy [27]. Chuang [28] considers the case of a thin wire at an arbitrary angle located above a perfectly conducting ground. Baum, Shumpert and Riggs consider the perturbation of the SEM poles for an arbitrary object above a perfectly conducting ground plane and present results for the case when the object is a thin wire at an arbitrary angle [29]. Nitch, Baum and Sturm [30] used SEM to evaluate the effect coupling on multi-conductor transmission lines. Also, in the paper by Riley, Davis, and Besieris [31] SEM is applied in the analysis of scattering from a random distribution of scatterers.

Most of the above mentioned papers emphasize the calculation of the SEM mode frequencies for an object above a ground plane. Several papers present plots of the s-plane trajectory of the SEM mode frequencies as the distance above the ground plane is

varied. The trajectory is a complicated spiral-like curve that revolves about the point associated with the natural frequency of the object when it is isolated in free space. Unfortunately, the significance of these natural frequencies within the context of the temporally observed currents and fields is not discussed in these papers. Such an understanding is essential if target discrimination and identification methods based on the SEM mode frequencies are to be properly implemented in practical systems where more than one scatterer may be present. Only this author [32] has investigated the effect of coupling on the performance of the discrimination methods prior to this writing.

The primary shortfall of the above papers is that none discuss the time interval over which the SEM modes of the coupled wire system is valid and how these system modes are related to the modes of the isolated wire. Part of this problem is that several of these papers were published prior to a proper understanding of the use of SEM in the representation of the scattered field response. The use of SEM in describing the scattered field response is discussed by Morgan [33, 34], Pearson [35], Felson [36], Dudley [37], and most recently and most completely by Baum [38]. The essence of their publications is that the Class I SEM pole series expansion with constant coefficients is only valid after the global modes have been established. Prior to this, the SEM pole series must be augmented by some means with terms that result from the inverse transform of an entire function.

There are many means of attempting to determine the entire function contribution. The Class II coupling coefficients first put forth by Baum [39] were an attempt to account for the entire function by expanding the early-time in a series of time modulated damped sinusoids with frequencies identical to those used in the Class I expansion. The

Class II coefficients, however, are non-physical since they attempt to represent the early-time response, which is essentially local information, using a series expansion that is based on global resonances. There are also attempts to augment the class I coefficient expansion using physical optics and other complex beam/ray methods. All of these endeavors are important for future early-time detection and discrimination schemes. However, for present discrimination schemes based on natural resonance frequencies, the analysis must be confined to the portion of the response that can be represented as a Class I pole series expansion.

This chapter attempts to clarify the meaning and significance of the SEM system modes of a group of scatterers in relation to the temporal response of a system at various observation positions and under varying excitations. For simplicity, the case of two thin wires is considered. The theoretical part of the study is presented in this chapter and begins with a general formulation for the SEM mode frequencies, currents and Class I coupling coefficients. The behavior of the SEM mode frequencies and currents for a system of coupled wires are investigated using several methods of varying accuracy and computational efficiency. Then, the SEM Class I coupling coefficients are calculated and the temporal scattered field is evaluated using the SEM approach. The SEM results are compared to the solution obtained via the inverse discrete Fourier transform of frequency domain method-of-moments calculations. Comparisons are also made to the response of a single wire to illustrate how causality is important in the SEM interpretation. The experimental portion of the study is presented in later chapters. The measurement methodology is discussed in Chapter 5 and measured results for systems of coupled wires are presented in Chapter 6.

3.2 General SEM Formulation

The analysis of the SEM mode frequencies begins in a general fashion and is subsequently specialized for various cases of interest. Consider a system of P arbitrarily shaped perfectly conducting scatterers as shown in Figure 3.1. The time varying electric field $\vec{E}^i$ impressed upon the system generates currents $\vec{K}(\vec{r})$ on the surface of the conductors. These currents in turn generate a scattered electric field $\vec{E}^s$ such that the total electric field tangential and upon the surface of the conductors is everywhere zero. Thus,

$$\hat{t}_p \cdot [\vec{E}^i(\vec{r},t) + \vec{E}^s(\vec{r},t)] = 0 \tag{3.1}$$

where $\hat{t}_p$ is a unit vector tangent to the p^{th} scatterer, $\vec{r}$ is the location vector, and t is the time. The double sided Laplace Transform of a time function $f(t)$ is defined as

$$\mathcal{L}_2\{f(t)\} \equiv \int_{-\infty}^{\infty} f(t) e^{-st} dt \tag{3.2}$$

where the transform variable s is the complex frequency. Applying the Laplace transform to (3.1) results in

$$\hat{t}_p \cdot [\vec{E}^i(\vec{r},s) - \vec{E}^s(\vec{r},s)] = 0 \tag{3.3}$$

where the transform domain field quantities are

$$\vec{E}^{i,s}(\vec{r},s) \equiv \mathcal{L}_2\{\vec{E}^{i,s}(\vec{r},t)\} \tag{3.4}$$

In the transform domain, the electric field scattered by a conducting object can be written using the dyadic Green's function formalism as [40]

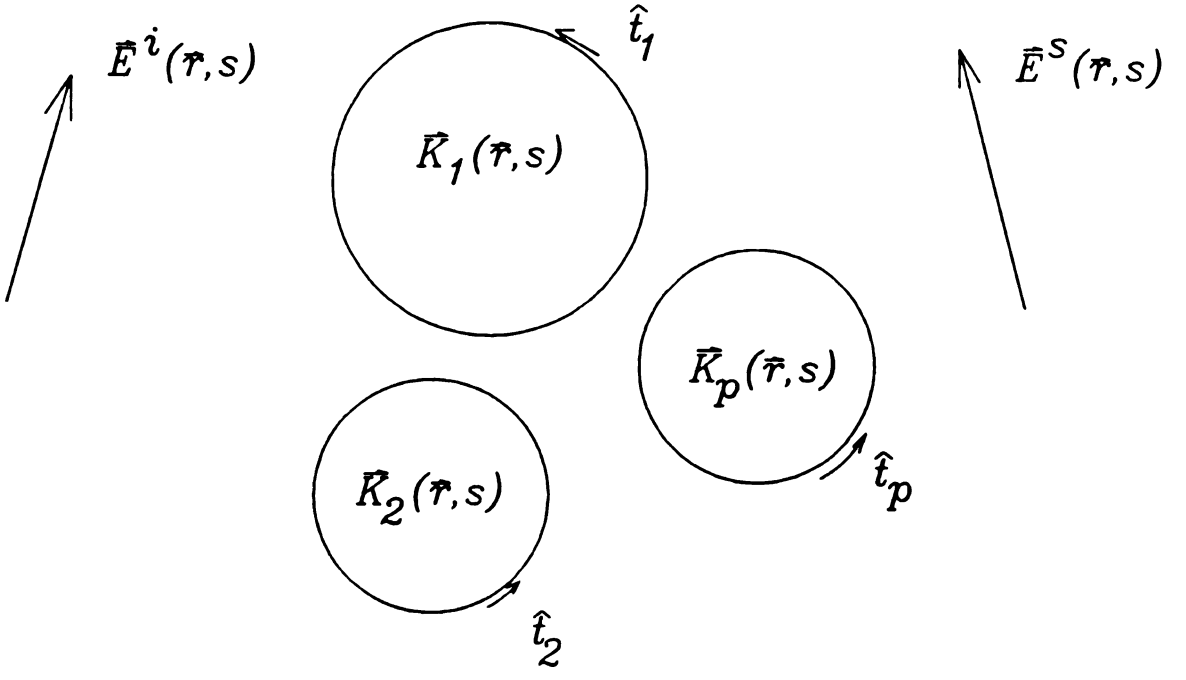

Figure 3.1 System of P perfectly conducting scatterers.

$$\vec{E}^s(\vec{r},s) = \lim_{\delta \to 0} \int_{V_f - V_\delta} \ddot{G}(\vec{r},\vec{r}',s) \cdot \vec{J}(\vec{r}',s)\, dV' + \frac{\ddot{L} \cdot \vec{J}(\vec{r},s)}{s\epsilon_0} \tag{3.5}$$

where $\ddot{G}(\vec{r},\vec{r}')$ is the dyadic Green's function, $\vec{J}(\vec{r}',s)$ is the current density and $\ddot{L}$ is a source dyadic that is dependent only on the geometry of the principle volume V_δ. Since the scatterers are assumed immersed in free space, the free space electric dyadic Green's function is used. It is given by

$$\ddot{G}(\vec{r},\vec{r}',s) = \eta \frac{\gamma}{4\pi} \left(\frac{1}{\gamma^2} \nabla\nabla - \ddot{I} \right) G(\vec{r},\vec{r}',s) \tag{3.6}$$

where the complex wavenumber $\gamma \equiv \frac{s}{c}$ and the scalar Green's function is

$$G(\vec{r},\vec{r}',s) = \frac{\exp(-\gamma |\vec{r}-\vec{r}'|)}{|\vec{r}-\vec{r}'|} \tag{3.7}$$

In the limit of perfectly conducting scatterers, the volume current density $\vec{J}(\vec{r},s)$ is replaced by a surface current density $\vec{K}(\vec{r},s)$ and the integration is carried out over the surface of the scatterer S. Note that $\ddot{L}$ is not specified since it is dependent only on the on the shape of the principle volume V_δ used in the calculation. To simplify notation, a principal value surface integration is implied throughout the rest of this general analysis.

The field from a system of P perfectly conducting scatterers can be written as

$$\vec{E}^s(\vec{r},s) = \sum_{p=1}^{P} \int_{S_p} \ddot{G}(\vec{r},\vec{r}',s) \cdot \vec{K}_p(\vec{r}',s)\, dS' \tag{3.8}$$

The boundary condition (3.3) can be applied everywhere on the surface of each scatterer to obtain a system of electric field integral equations (EFIE),

$$\hat{t}_q \cdot \sum_{p=1}^{P} \int_{S_p} \bar{\bar{G}}(\vec{r},\vec{r}',s) \cdot \vec{K}_p(\vec{r}',s)\, dS' = -\hat{t}_q \cdot \vec{E}^i(\vec{r},s) \qquad \vec{r} \in S_q \qquad q=1,2,\ldots,P \qquad (3.9)$$

From SEM, the late-time portion of the current at any point on the surface of the p^{th} scatterer can be expressed as a sum of exponentially damped sinusoidal waveforms which can be represented as

$$\vec{K}_p(\vec{r},t) = \sum_{\substack{n=-N \\ n\neq 0}}^{N} a_{pn} \vec{K}_{pn}(\vec{r},s_n)\, e^{-s_n t} \qquad (3.10)$$

where a_{pn} is the coupling coefficient for the n^{th} natural mode current $\vec{K}_{pn}(\vec{r},s_n)$ and s_n is the n^{th} complex natural mode frequency of the system of P scatterers. The current thus has the form of a complex pole series in the transform domain. So

$$\vec{K}_p(\vec{r},s) = \sum_{\substack{n=-N \\ n\neq 0}}^{N} \frac{a_{pn}\vec{K}_{pn}(\vec{r},s_n)}{s-s_n} \qquad (3.11)$$

Since the time domain current waveform must be real, one requires that $s_{-n} = s_n^*$ and $a_{pn}K_{pn}(\vec{r},s_n) = \left[a_{p,-n}K_{p,-n}(\vec{r},s_{-n})\right]^*$. Then, substituting (3.11) into (3.9) yields

$$\hat{t}_q \cdot \sum_{p=1}^{P} \sum_{\substack{n=-N \\ n\neq 0}}^{N} \frac{a_{pn}}{s-s_n} \int_{S_p} \bar{\bar{G}}(\vec{r},\vec{r}',s) \cdot \vec{K}_{pn}(\vec{r}',s_n)\, dS' = -\hat{t}_q \cdot \vec{E}^i(\vec{r},s) \qquad \vec{r} \in S_q \qquad q=1,2,\ldots,P \qquad (3.12)$$

The natural solutions are found by solving the equations with $\vec{E}^i(\vec{r},s) = 0$. To guarantee the finiteness of the quantity on the left hand side one must require that

$$\hat{t}_q \cdot \sum_{p=1}^{P} \int_S \ddot{G}(\vec{r},\vec{r}',s_n) \cdot \vec{K}_{pn}(\vec{r}',s_n)\, ds' = 0 \qquad \vec{r} \in S_q \qquad q=1,2,\ldots,P \tag{3.13}$$

This system of homogenous EFIE's defines the natural mode frequencies s_n and the natural mode currents $\vec{K}_{pn}(\vec{r},s_n)$ of the system of scatterers.

To compute the transient currents and fields using the SEM, the current coupling coefficients must be determined. Rewriting inhomogeneous EFIE (3.12) gives

$$\hat{t} \cdot \int_S \ddot{G}(\vec{r},\vec{r}',s) \cdot \sum_{\substack{n=-N \\ n\neq 0}}^{N} \frac{a_n \vec{K}_n(\vec{r},s_n)}{s-s_n}\, dS' = -\hat{t} \cdot \vec{E}^i(\vec{r},s) \qquad \vec{r} \in S \tag{3.14}$$

where, to simplify notation the integration is carried out over the entire collection of P scatterers. Next, replace the operation $\hat{t}\cdot$ by $\vec{K}_m(\vec{r},s_m)\cdot$. Note that $\vec{K}_m(\vec{r})$ is tangent everywhere to the surface. Now, integrate over the entire surface of all scatterers to obtain

$$\sum_{\substack{n=-N \\ n\neq 0}}^{N} \frac{a_n}{s-s_n} \int_S \vec{K}_m(\vec{r},s_m) \cdot \int_S \ddot{G}(\vec{r},\vec{r}',s) \cdot \vec{K}_n(\vec{r}',s_n)\, dS'\, dS = -\int_S \vec{K}_m(\vec{r},s_m) \cdot \vec{E}^i(\vec{r},s)\, dS \tag{3.15}$$

Then, interchange $\vec{r}$ and $\vec{r}'$ and use the reciprocity property of the Green's dyad to rewrite the previous equation as

$$\sum_{\substack{n=-N \\ n\neq 0}}^{N} \frac{a_n}{s-s_n} \int_S \vec{K}_n(\vec{r}',s_n) \cdot \int_S \ddot{G}(\vec{r},\vec{r}',s) \cdot \vec{K}_m(\vec{r},_m)\, dS'\, dS = -\int_S \vec{K}_m(\vec{r},s_m) \cdot \vec{E}^i(\vec{r},s)\, dS \tag{3.16}$$

Taking the limit as s approaches s_n gives

$$\lim_{s\to s_n} \frac{a_n}{s-s_n} \int_S \vec{K}_n(\vec{r}',s_n)\cdot\int_S \ddot{G}(\vec{r},\vec{r}',s)\cdot\vec{K}_n(\vec{r},s_n)\,dS'dS = \lim_{s\to s_n} -\int_S \vec{K}_m(\vec{r},s_n)\cdot\vec{E}^i(\vec{r},s)\,dS \qquad (3.17)$$

where all terms on the left $n \neq m$ are zero by definition of the m^{th} mode frequency (3.13). Using L'hospitals rule on the left and solving for a_n gives

$$a_n = -\frac{1}{c_n}\int_S \vec{K}_n(\vec{r},s_n)\cdot\vec{E}^i(\vec{r},s_n)\,dS \qquad (3.18)$$

where the normalization constant c_n is

$$c_n = \frac{\partial}{\partial s}\int_S \vec{K}_n(\vec{r},s_n)\cdot\int_S \ddot{G}(\vec{r},\vec{r}',s)\cdot\vec{K}_n(\vec{r}',s_n)\,dS'dS\,|_{s\to s_n} \qquad (3.19)$$

3.3 Moment Method Solution

To solve the homogenous EFIE for the natural mode frequencies and currents, the method of moments is usually employed. Since the moment method is widely used, only the outline of the solution method is mentioned here while the details are presented in Appendix B. The case of the EFIE in (3.13) is slightly more difficult than most moment method problems since both the frequency and the current are unknown. To solve the problem, the matrix form of the system of integral equations is obtained by expanding the unknown currents in an appropriate series of basis functions f_m

$$\vec{K}(\vec{r}) = \sum_{m=1}^{M} c_m \vec{f}_m(\vec{r}) \qquad (3.20)$$

Entire domain basis functions such as *sines* and *cosines* or sub-sectional basis functions such as piece-wise sinusoids and pulse functions can be used to represent the current. The

equations are then tested using an appropriate weighting function. The testing operation has the form

$$\int_S \vec{w}_i(\vec{r})\, dS \cdot \tag{3.21}$$

where typical weighting functions w_i include Dirac delta functions, pulse functions and piecewise sinusoids. If the expansion functions are of the same form as the weighting functions then the method is called a Galerkin method. If piecewise sinusoidal basis functions are chosen, the EFIE can be solved easily since there is an exact analytical solution for the field scattered from a thin wire with sinusoidal current as shown in Appendix A. After a sufficient number of weighting functions have been applied, a matrix equation is obtained

$$A(s=s_n)\ c\ =\ 0 \tag{3.22}$$

where the A matrix contains the overlap integrals given by

$$A_{im} = \int_S \vec{w}_i(\vec{r}) \cdot \int_S \ddot{G}(\vec{r},\vec{r}',s) \cdot \vec{f}_m(\vec{r}')\, dS'\, dS \tag{3.23}$$

and the vector c contains the coefficients of the basis functions representing the unknown current. Note that equality holds only if $s=s_n$. The natural frequencies of the system of scatterers can be determined by rooting the determinental equation

$$det\ A(s)\ =\ 0 \tag{3.24}$$

The natural mode currents of the system can be determined to within a multiplicative constant by calculating the null space of the matrix $A(s_n)$.

Rooting of the determinental equation is accomplished numerically. The Mueller method was used for this research [41]. Since even simple structures have a large

number of possible modes, deflation can be used to prevent the search procedure from wasting valuable computer time searching for modes that are already catalogued.

There were several formulations of the moment method solution used in this work. All are based on the assumption that the thin wire approximations are valid. This assumption is appropriate for the class of problems addressed and simplifies the analysis by eliminating the source point singularity. The first formulation uses a Hallen formulation for the problem of a group of vertical monopoles connected to an infinite perfectly conducting ground screen. A pulse function expansion in the current was used along with point matching. A second more general Galerkin formulation based on the EFIE and a current expansion in piecewise sinusoidal basis functions was also used. These approaches are detailed in Appendix B.

3.4 Perturbational Transcendental Solution

A perturbational solution can be obtained for the natural mode frequencies of a group of scatterers by assuming that the modal current distribution on a scatterer in the presence of the ground plane or other similar scatterers is nearly the same as the modal current present on the scatterer when it is isolated in free space. This approximation can be written as

$$\vec{K}_{pn}(\vec{r},s_n) \approx a_{pn}\vec{K}^{o}_{pn}(\vec{r},s^{o}_{pn}) \tag{3.25}$$

where a_{pn} is a constant, $\vec{K}^{o}_{pn}(\vec{r},s^{o}_{pn})$ and s^{o}_{pn} are the modal currents and frequencies of the n^{th} mode of the p^{th} scatterer when it is isolated in free space. Using this approximation, the homogenous EFIE becomes

$$\hat{t}_q \cdot \sum_{p=1}^{P} a_{pn} \int_{S_p} \ddot{G}(\vec{r},\vec{r}',s_n) \cdot \vec{K}_{pn}^{o}(\vec{r}',s_{pn}^{o}) dS' = 0 \qquad \vec{r} \in S_q \quad q=1,2,...,P \tag{3.26}$$

Now, replacing the $\hat{t}_q \cdot$ operation by the weighting function $\int_{S_q} \vec{K}_{pn}^{o}(\vec{r},s_{pn}^{o}) \cdot \{...\} dS$ results in a matrix equation as before. Note that this procedure is essentially a moment method approach employing current expansion with a single term entire domain basis function. The advantage of the perturbational method is that the current is constrained and the numerical root search is simplified and the modes are easier to characterize.

3.5 Approximate Green's Function Solution

A closed form approximate solution for the natural mode frequencies of a simple system of two nearly identical scatterers can be also be obtained. The assumption of nearly degenerate coupling (ie. the resultant system modes are nearly identical to the modes of the isolated scatterers) is used and the Green's function is expanded in a Taylor series about the natural mode frequency of the isolated scatterers. The Green's function is then approximated by retaining only the first two terms in the series expansion. Thus,

$$\ddot{G}(\vec{r},\vec{r}',s) \approx \ddot{G}(\vec{r},\vec{r}',s_{pn}^{o}) + (s-s_{pn}^{o}) \frac{\partial \ddot{G}(\vec{r},\vec{r}',s)}{\partial s} \Big|_{s=s_{pn}^{o}} \tag{3.27}$$

The EFIE then becomes

$$\hat{t}_q \cdot \sum_{p=1}^{P} a_{pn} \int_{S_p} \left\{ \ddot{G}(\vec{r},\vec{r}',s_{pn}^{o}) + (s-s_{pn}^{o}) \frac{\partial \ddot{G}(\vec{r},\vec{r}',s)}{\partial s} \Big|_{s=s_{pn}^{o}} \right\} \cdot \vec{K}_{pn}^{o}(\vec{r}',s_{pn}^{o}) dS' = 0 \qquad \vec{r} \in S_q \tag{3.28}$$

This relation can be simplified by retaining only the leading nonvanishing terms. Note that for $p=q$, the definition of the natural mode currents and frequencies for the isolated bodies requires that

$$\int_{S_p} \ddot{G}(\vec{r},\vec{r}',s_{pn}^o)\cdot\vec{K}_{pn}^o(\vec{r}',s_{pn}^o)\,dS' \triangleq 0 \qquad \vec{r}\in S_p \tag{3.29}$$

For $p\neq q$, assuming that

$$\frac{\partial\ddot{G}(\vec{r},\vec{r}',s)}{\partial s}\Big|_{s=s_{pn}^o} \ll \ddot{G}(\vec{r},\vec{r}',s_{pn}^o) \tag{3.30}$$

gives

$$a_{qn}(s-s_{qn}^o)\hat{t}_q\cdot\int_{S_p}\frac{\partial\ddot{G}(\vec{r},\vec{r}',s)}{\partial s}\Big|_{s=s_{qn}^o}\cdot\vec{K}_{qn}^o(\vec{r}',s_{qn}^o)\,dS' + \sum_{\substack{p=1\\p\neq q}}^{P} a_{pn}\hat{t}_q\cdot\int_{S_p}\ddot{G}(\vec{r},\vec{r}',s_{pn}^o)\cdot\vec{K}_{pn}^o(s_{pn}^o)\,dS' = 0 \tag{3.31}$$

Note that the electric field associated with the n^{th} mode of the p^{th} isolated scatterer is

$$\vec{E}_{pn}^o(\vec{r}) \triangleq \int_{S_p}\ddot{G}(\vec{r},\vec{r}',s_{pn}^o)\cdot\vec{K}_{pn}^o(\vec{r}',s_{pn}^o)\,dS' \qquad \vec{r}\notin S_p \tag{3.32}$$

To convert the EFIE to matrix form, replace $\hat{t}_q\cdot$ with the weighting function

$$\int_{S_q}\vec{K}_{qn}^o(\vec{r},s_{qn}^o)\cdot\{\ldots\}dS \tag{3.33}$$

to get the matrix equation

$$A(s=s_n)c = 0 \tag{3.34}$$

where the elements of the $A(s)$ matrix are

$$a_{pq} = \begin{cases} (s-s_{qn}^{o})\bar{a}_{qq} & q=p \\ \int_{S_q} \vec{K}_{qn}^{o}(\vec{r},s_{qn}^{o}) \cdot \vec{E}_{pn}^{o}(\vec{r})\, dS & q \neq p \end{cases} \tag{3.35}$$

and

$$\bar{a}_{qq} = \int_{S_q} \vec{K}_{qn}^{o}(\vec{r},s_{qn}^{o}) \cdot \int_{S_q} \frac{\partial \vec{G}(\vec{r},\vec{r}',s)}{\partial s}\Big|_{s=s_{qn}^{o}} \cdot \vec{K}_{qn}^{o}(\vec{r}',s_{qn}^{o})\, dS'\, dS \tag{3.36}$$

As with the other methods, the natural frequencies of the system of scatterers are determined by rooting a determinental equation. The special case of only two conducting scatterers results in the determinental equation:

$$\det\begin{pmatrix} (s-s_1^{o})\bar{a}_{11} & a_{12} \\ a_{21} & (s-s_2^{o})\bar{a}_{22} \end{pmatrix} = 0 \tag{3.37}$$

where s_1^{o} and s_2^{o} are the modal frequencies of scatterers 1 and 2 when each is isolated in free space. This determinant has the form of a quadratic equation in s

$$(s-s_1^{o})(s-s_2^{o})\,\bar{a}_{11}\bar{a}_{22} - a_{12}a_{21} = 0 \tag{3.38}$$

The resulting solutions for s are

$$s = \bar{s} \pm \sqrt{\Delta + \delta^2} \tag{3.39}$$

where $\bar{s}$ is the mean of the isolated mode frequencies and Δ is half the difference between the natural mode frequencies

$$\bar{s} \equiv \frac{s_1^{o}+s_2^{o}}{2} \qquad \Delta \triangleq \frac{s_1^{o}-s_2^{o}}{2} \tag{3.40}$$

while δ is a ratio

$$\delta \triangleq \sqrt{\frac{a_{12}a_{21}}{\bar{a}_{11}\bar{a}_{22}}} \tag{3.41}$$

These results imply that the natural frequencies of two nearly identical scatterers are shifted from the natural frequencies of the individual isolated scatterers. Next, consider the case of two identical scatterers. Here $\bar{s} = s^o = s_1^o$ and $\Delta = 0$ so the natural frequency of the system of identical scatterers is

$$s = s_0 \pm \delta \qquad \delta = \frac{a_{12}}{\bar{a}_{11}} \tag{3.42}$$

Thus, in the case of a degeneracy in the modes of the isolated scatterers, the natural frequency of the system of identical scatterers splits into two modes that are shifted from the modes of the isolated scatterer. This is an extremely important result.

3.6 SEM Modes of a Single Thin Wire

This section presents results obtained via the moment method for the SEM mode frequencies and currents of a single thin wire. The analysis of a thin wire is important both for testing and validating the computer programs as well as providing a framework for understanding the more complicated case of two wires considered in later sections. A comparison of the accuracy and convergence of the solutions for the SEM mode frequencies using two different formulations is presented. The first formulation is based on a Galerkin method using piecewise sinusoidal basis functions to solve the EFIE. This method is denoted EFIE-PS. The second formulation is based on the Hallen equation with

a rectangular pulse function expansion and point matching. This method is denoted HALLEN.

Before proceeding further, it is also useful to review some general characteristics of the SEM mode frequencies that have been previously established by Tesche [23] and others. Most importantly, all poles occur in complex conjugate pairs (ie. $s_n=\omega_n + j\omega_n$, $s_{-n}=\omega_n-j\omega_n$). Thus, it is sufficient to search for modes only in the second quadrant of the complex s plane. Further, for thin wires, spheres, infinite cylinders, and other canonical structures, the SEM pole frequencies seem to occur in layers in the complex s plane. An example of this is seen in Figure 3.2. Here, some of the modes of a thin wire of l/a = 200 are plotted. The values shown were computed using the EFIE-PS formulation. The first layer poles lie close to the $j\omega$-axis and occur in roughly integer multiples of $\omega = \pi c/l$. The second layer poles also appear with approximately integer multiplicity but are placed further to the left of $j\omega$-axis than the first layer poles. The third and higher layer poles are even further from the $j\omega$-axis. Because of this layering phenomena, Tesche established a special notation to identify the modes. The modes are denoted $s_{l,n}$, where l denotes the layer number and n denotes the mode number as counted from the σ-axis. This notation is used throughout this document. It has been observed that the late-time transient response of most structures can be adequately described using only the first layer poles since the contribution of poles from the other layers is usually very small due to their much larger negative damping coefficients. Tesche has also shown that the poles of the thin wire migrate to the left as the length-to-radius ratio of the wire is decreased.

When performing numerical analyses with the moment method it is prudent to examine the convergence of the solutions with respect to the number of basis functions

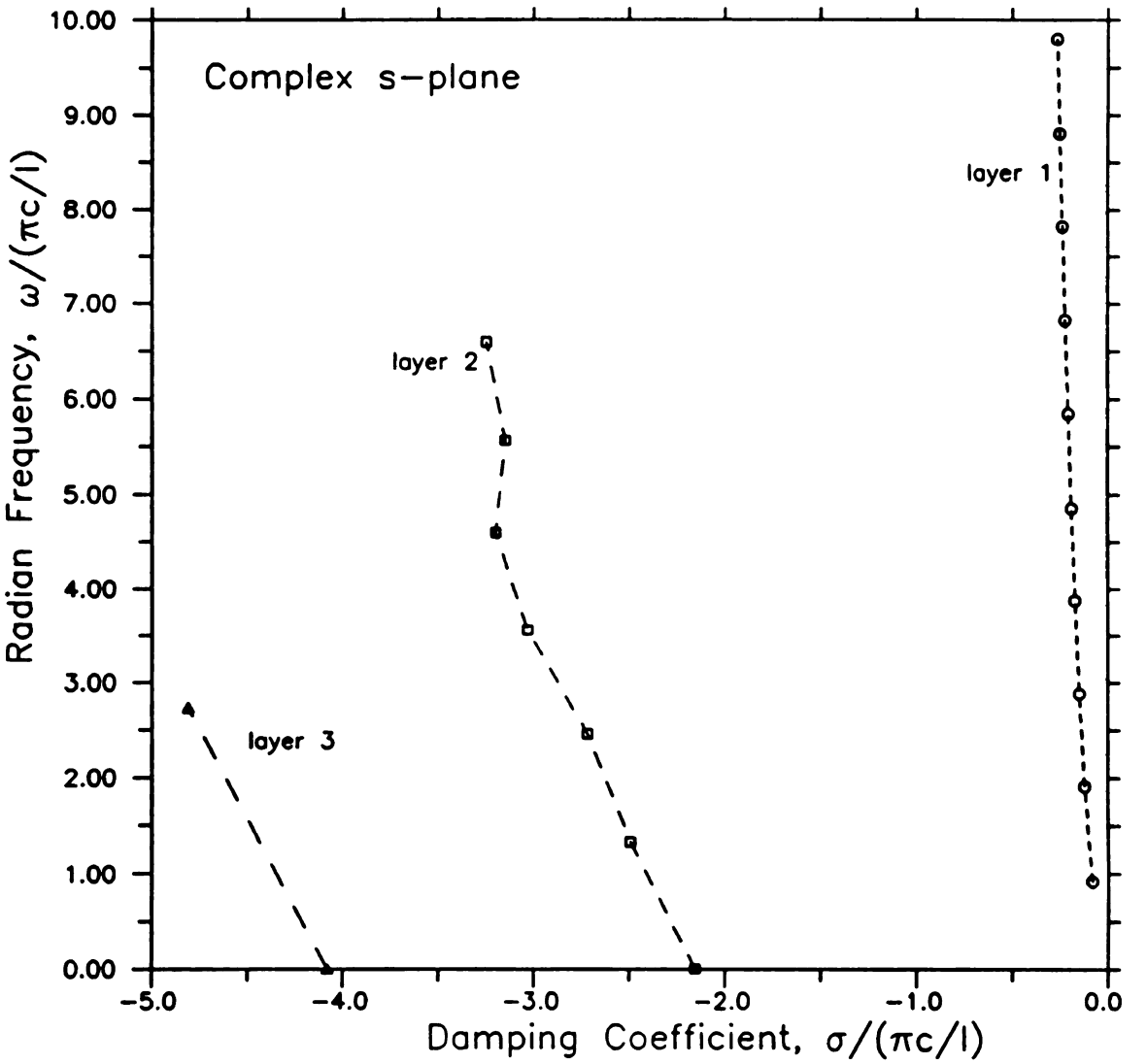

Figure 3.2 Layering of SEM mode frequencies for thin wire ($l/a = 200$).

used in the current expansion. To test the convergence, the case of a unit length wire with $l/a = 200$ was considered. The natural frequency of the lowest order SEM mode was computed for differing numbers of basis functions using both formulations. Figure 3.3 illustrates the convergence of the damping coefficient ω as a function of the number of "segments" per wavelength used in the calculation while Figure 3.4 shows the convergence of the radian frequency ω. From these plots it is evident that the EFIE-PS formulation converges much faster than the HALLEN formulation.

To test the accuracy of the formulations the ten lowest order natural frequencies of a thin wire were computed and compared to the results obtained by Singaraju, Giri, and Baum [41]. The results of this comparison are shown in Table 3.1. The values obtained by Singaraju and those obtained using the EFIE-PS formulation are in agreement to within approximately 1%. The EFIE-PS calculations were performed using segments of length $\lambda/20$. The small differences are most likely due to the different approach taken in the solution and the fact that Singaraju implemented the angular integration over the surface of the wire whereas the author's program neglected integration in the interest of computation speed. The results using the HALLEN formulation are also in agreement with those of Singaraju to within approximately 2%. The HALLEN calculations were performed using segments of length $\lambda/80$. As previously demonstrated, these results are much more sensitive to the size of the segments than the EFIE-PS formulation. Note that natural frequencies of the even modes could not be calculated with the HALLEN formulation since it was specialized to the case of monopoles above an infinite perfectly conducting ground plane. This limitation was accepted in the interest of decreased memory requirements and decreased execution time of the computer program. This

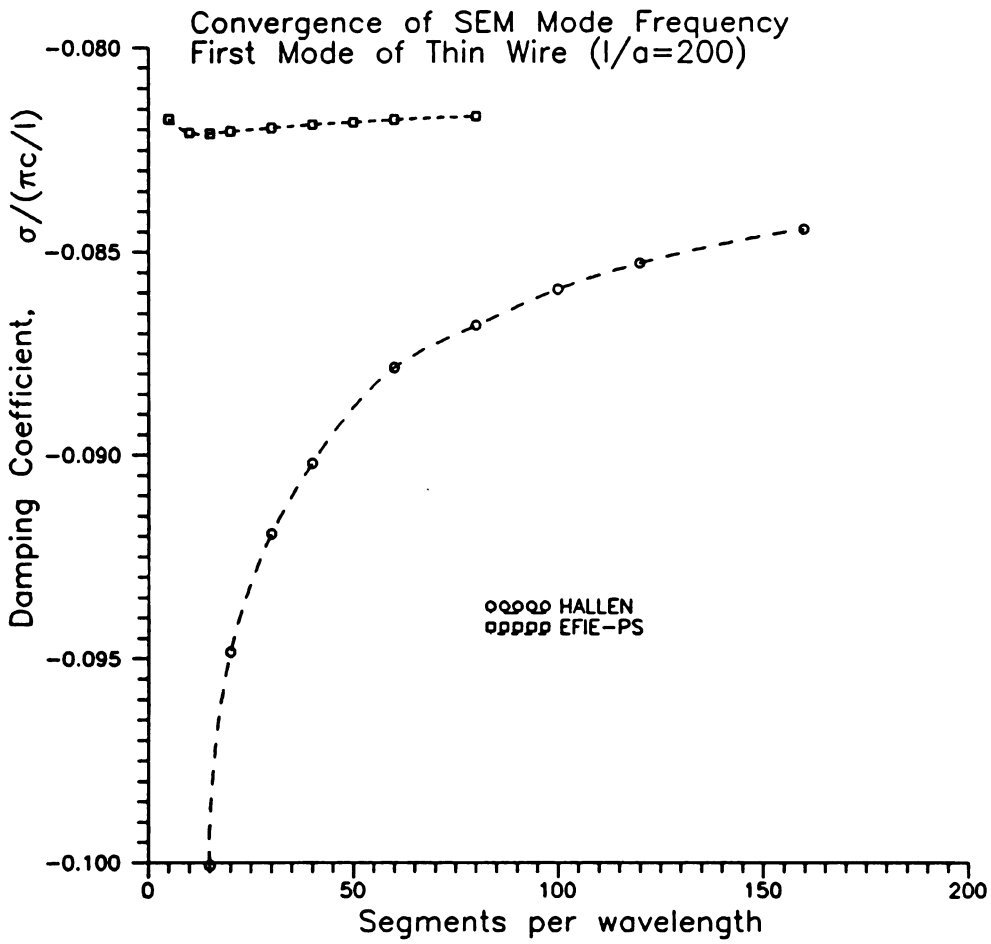

Figure 3.3 Convergence of moment method solutions for damping coefficient.

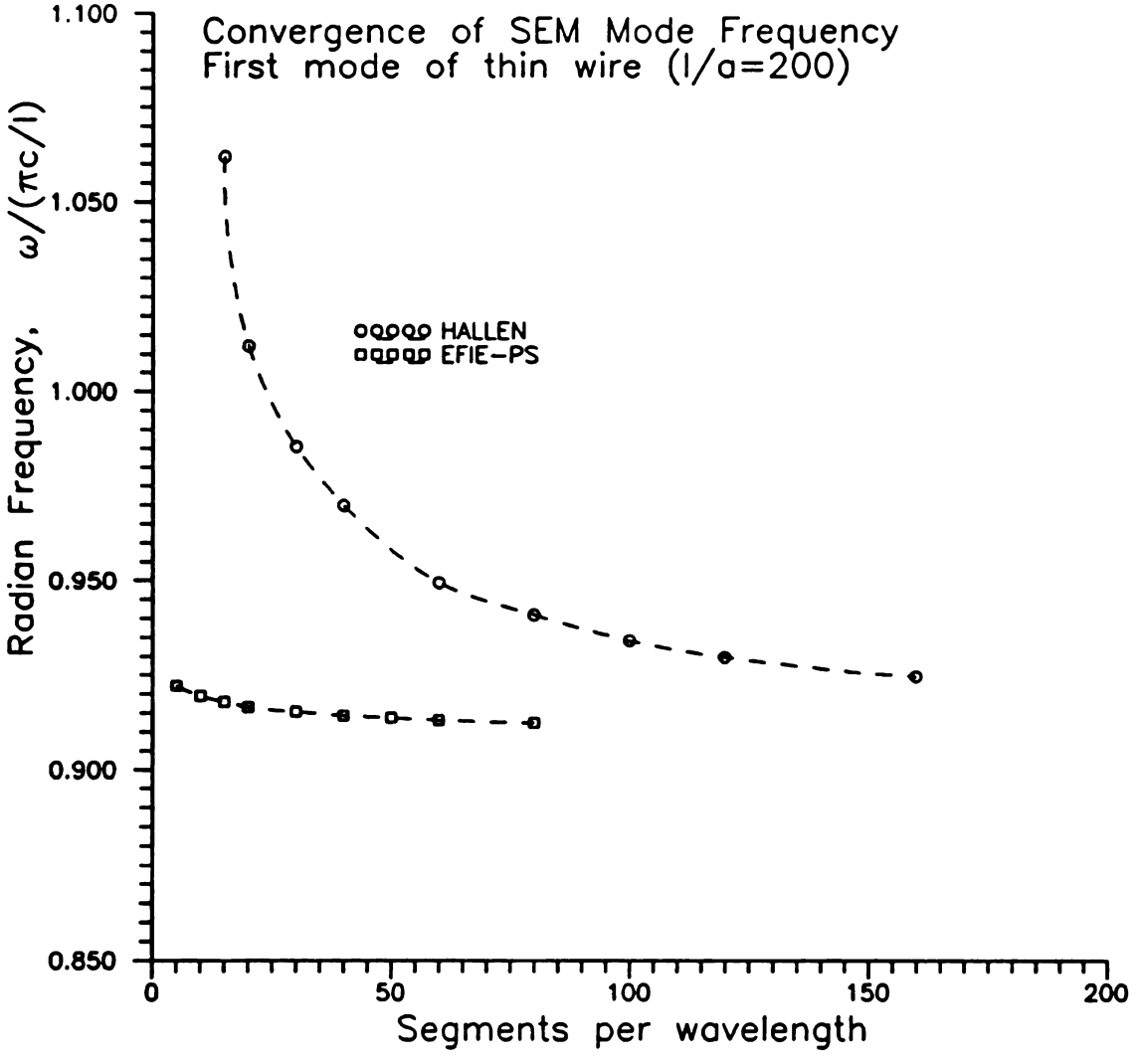

Figure 3.4 Convergence of moment method solutions for radian frequency.

Table 3.1 Comparison of the natural frequencies of a thin wire with l/a = 200 calculated using various moment method formulations.

Natural frequencies of a thin wire $s_n/(\pi c/l)$ for l/a=200.			
	Singaraju, Giri, Baum	EFIE-PS	HALLEN
1	-0.0828+j0.9251	-0.0820+j0.9166	-0.0868+j0.9409
2	-0.1212+j1.912	-0.1207+j1.888	-
3	-0.1491+j2.884	-0.1485+j2.865	-0.1519+j2.886
4	-0.1713+j3.874	-0.1711+j3.845	-
5	-0.1909+j4.854	-0.1905+j4.827	-0.1926+j4.844
6	-0.2080+j5.845	-0.2079+j5.809	-
7	-0.2240+j6.829	-0.2238+j6.792	-0.2288+j6.848
8	-0.2383+j7.821	-0.2385+j7.776	-
9	-0.2522+j8.807	-0.2523+j8.779	-0.2562+j8.815
10	-0.2648+j9.800	-0.2653+j9.766	-

specialization was also useful in the study of the multiple wire case since the number of possible modes was reduced hence making the mode search simpler.

The SEM modal current distributions for a single thin wire are also of interest in this research. As shown previously, the perturbational methods use the current distribution on a single scatterer to estimate the natural frequencies of a group of scatterers. The magnitude of the current as a function of position along the wire z/l for the first principal mode of a thin wire of length l and $l/a = 200$ is shown in Figure 3.5. Note that the HALLEN results are only plotted for one half of the wire length since this program was specialized for monopoles. The phase of the current as a function of position is shown in Figure 3.6. The EFIE-PS results were obtained using segments of length $\lambda/20$ while the HALLEN results were obtained using segments of length $\lambda/80$. The magnitude of the current computed using the moment method is nearly the same as the cosine distribution that is expected for this mode. Figure 3.7 and Figure 3.8 show the current distribution for the second principal mode of the wire. Note that the results for the HALLEN formulation are not available for this mode due to the programming implementation specified previously. The current distribution for third principal mode is available from both programs. The magnitude of the current as a function of position for this mode is shown in Figure 3.9 while the phase is shown in Figure 3.10. In each case, the agreement between the expected cosine variation and the moment method formulations are good.

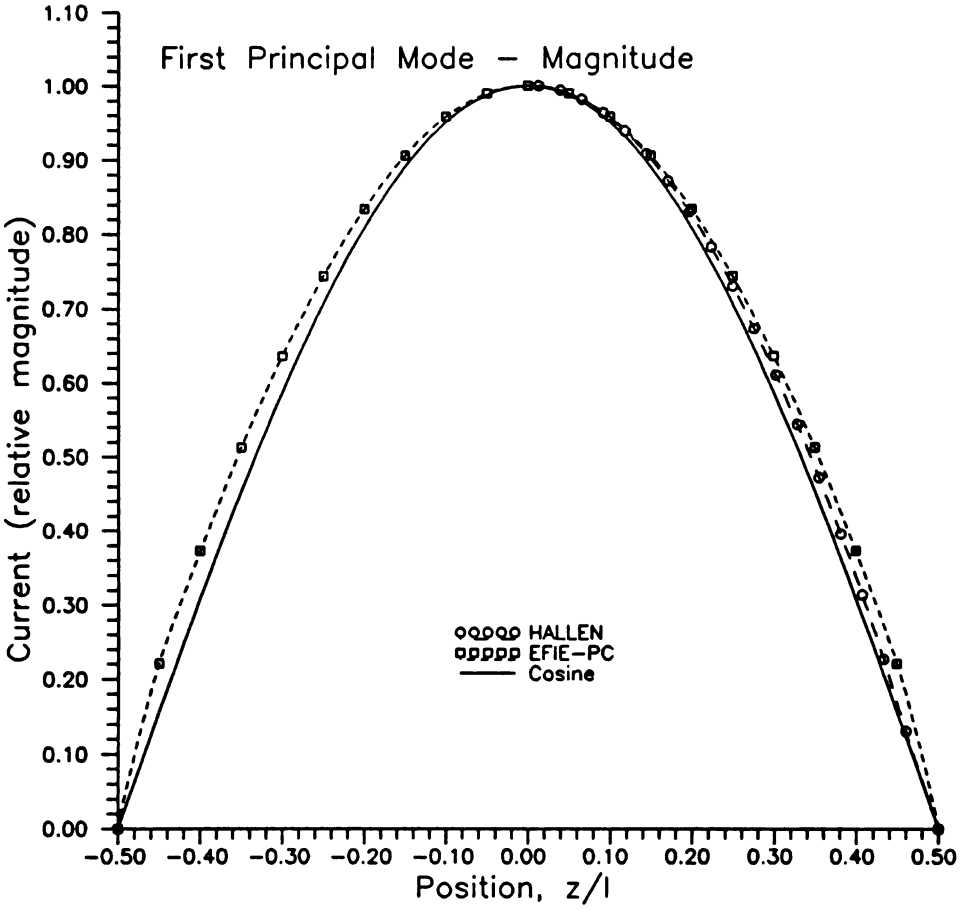

Figure 3.5 Magnitude of current distribution for $s_{1,1}$ mode of wire with $l/a = 200$.

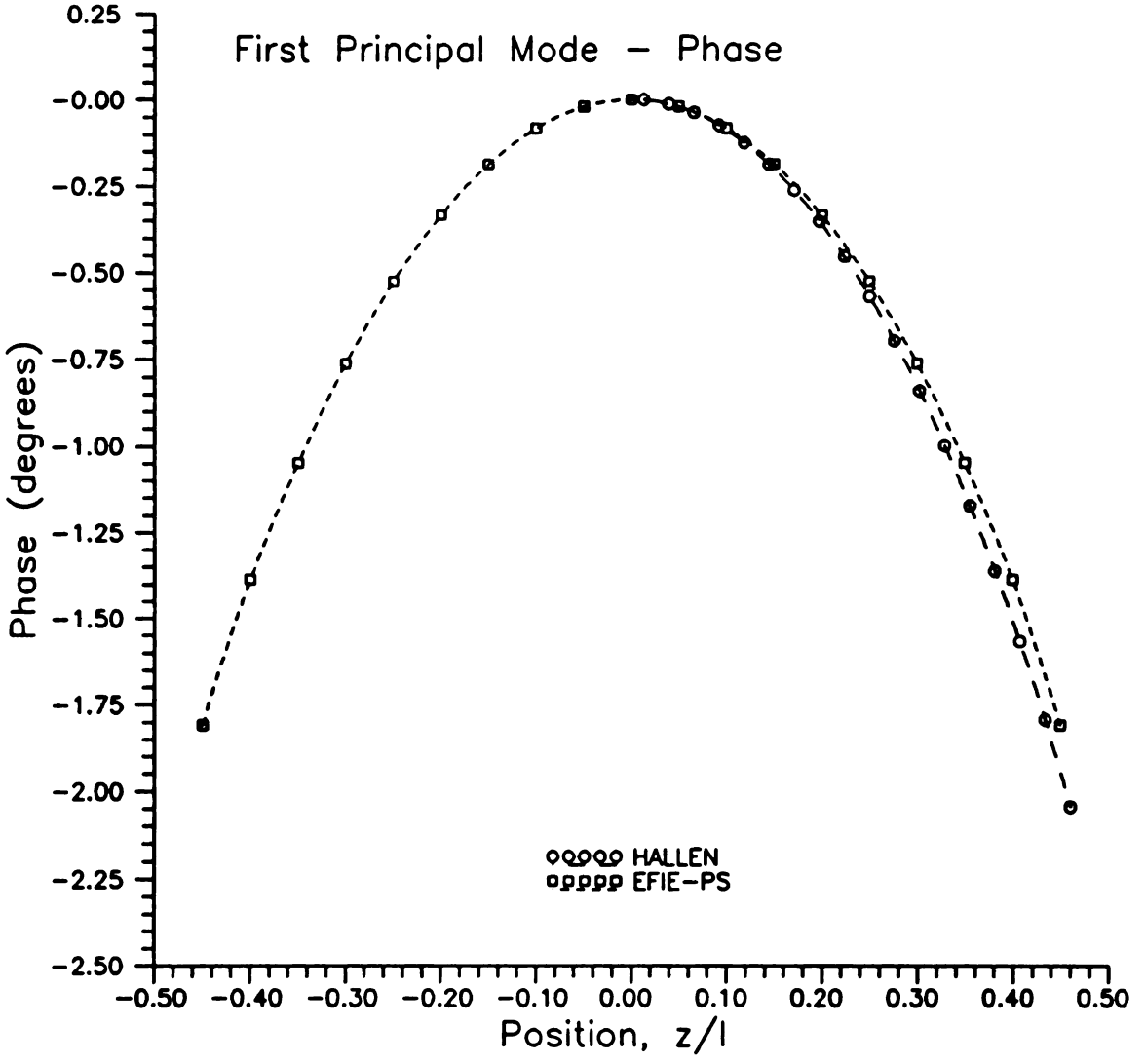

Figure 3.6 Phase of current distribution for $s_{1,1}$ mode of wire with $l/a = 200$.

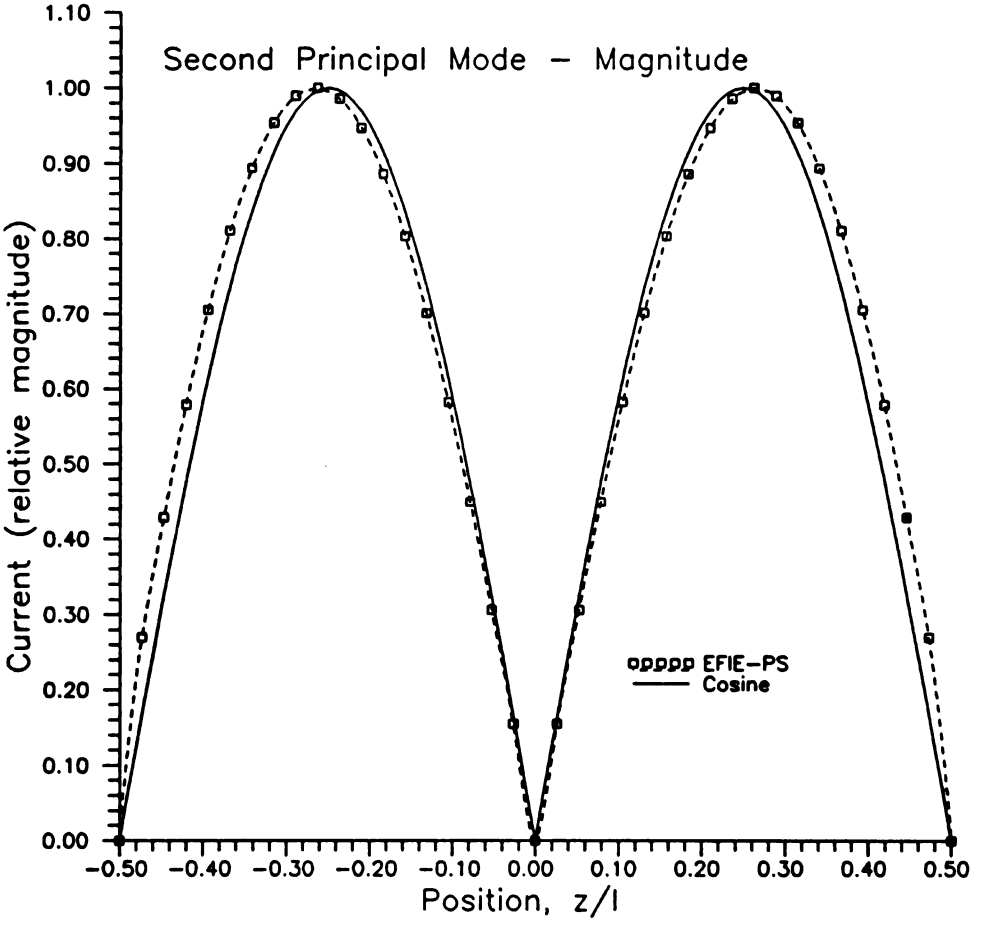

Figure 3.7 Magnitude of current distribution for $s_{1,2}$ mode of wire with $l/a = 200$.

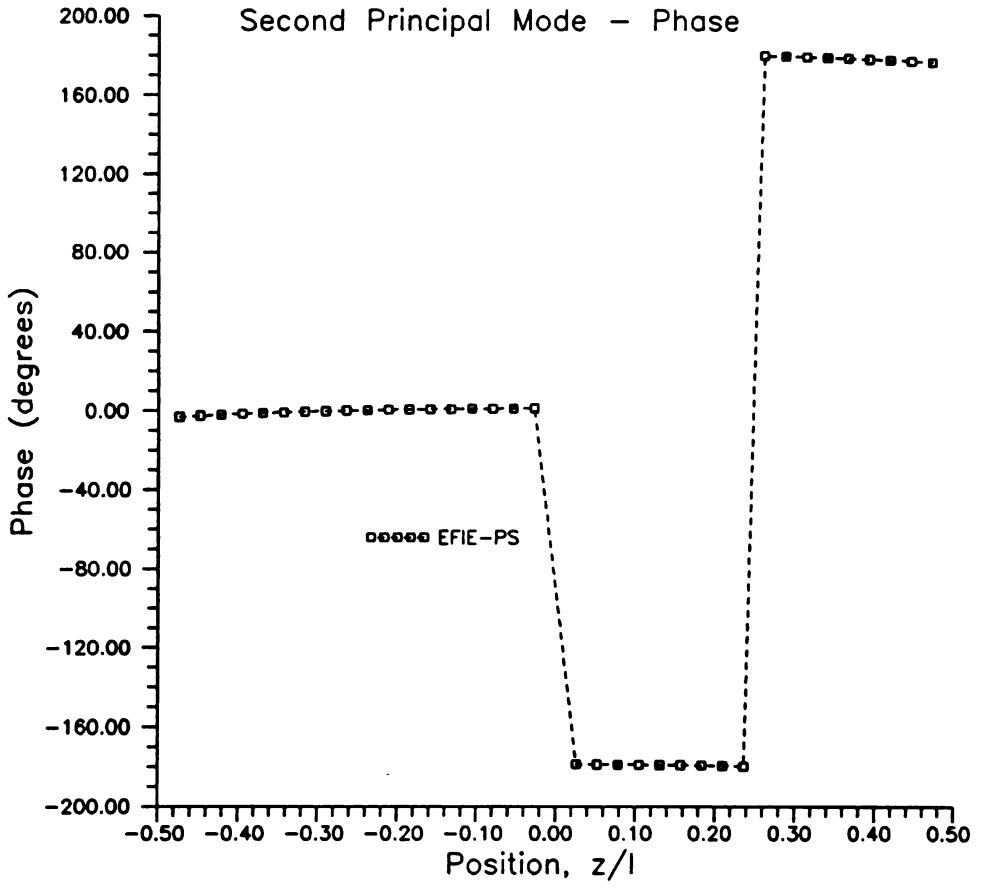

Figure 3.8 Phase of current distribution for $s_{1,3}$ mode of wire with $l/a = 200$.

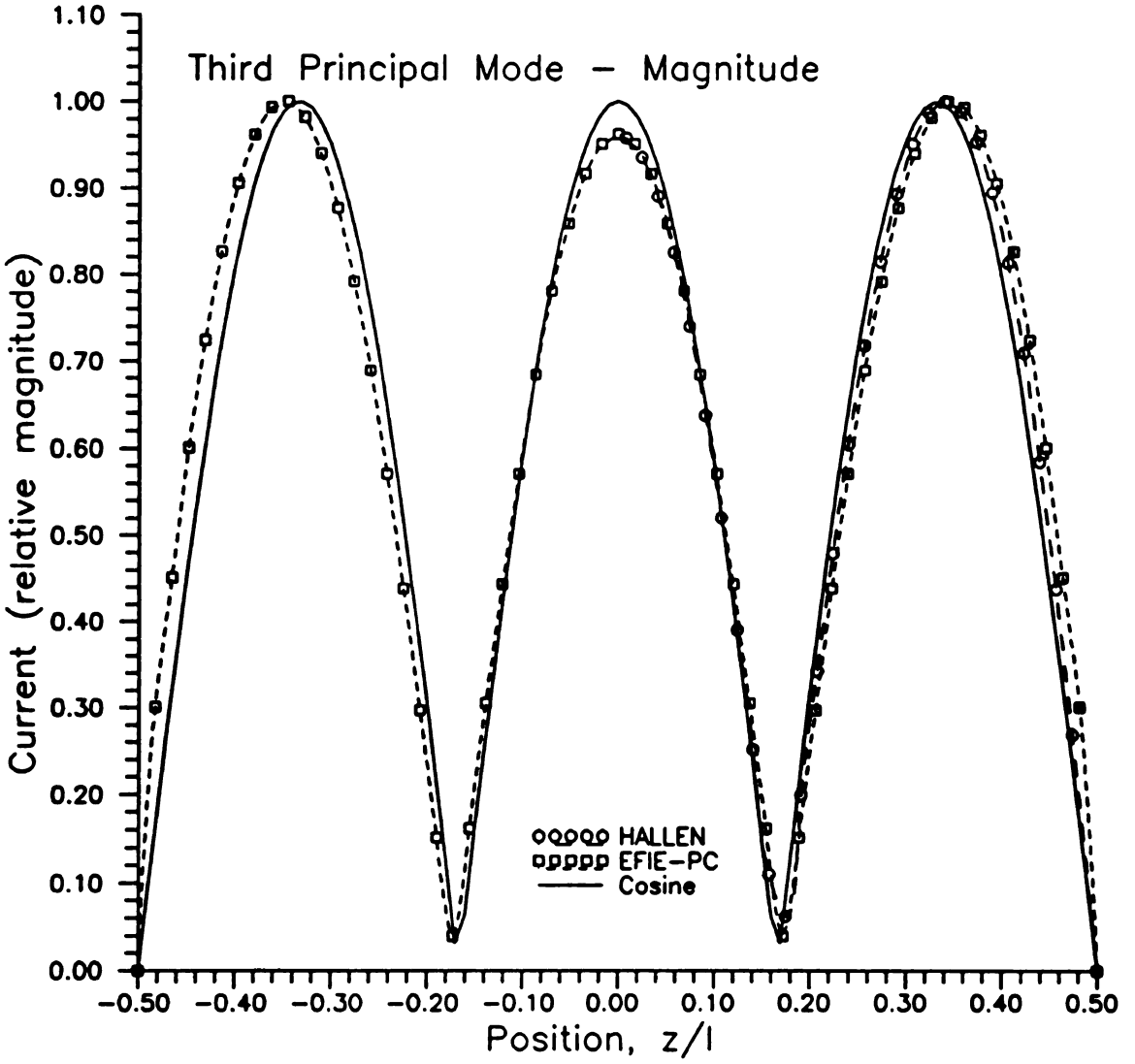

Figure 3.9 Magnitude of current distribution for $s_{1,3}$ mode of wire with $l/a = 200$.

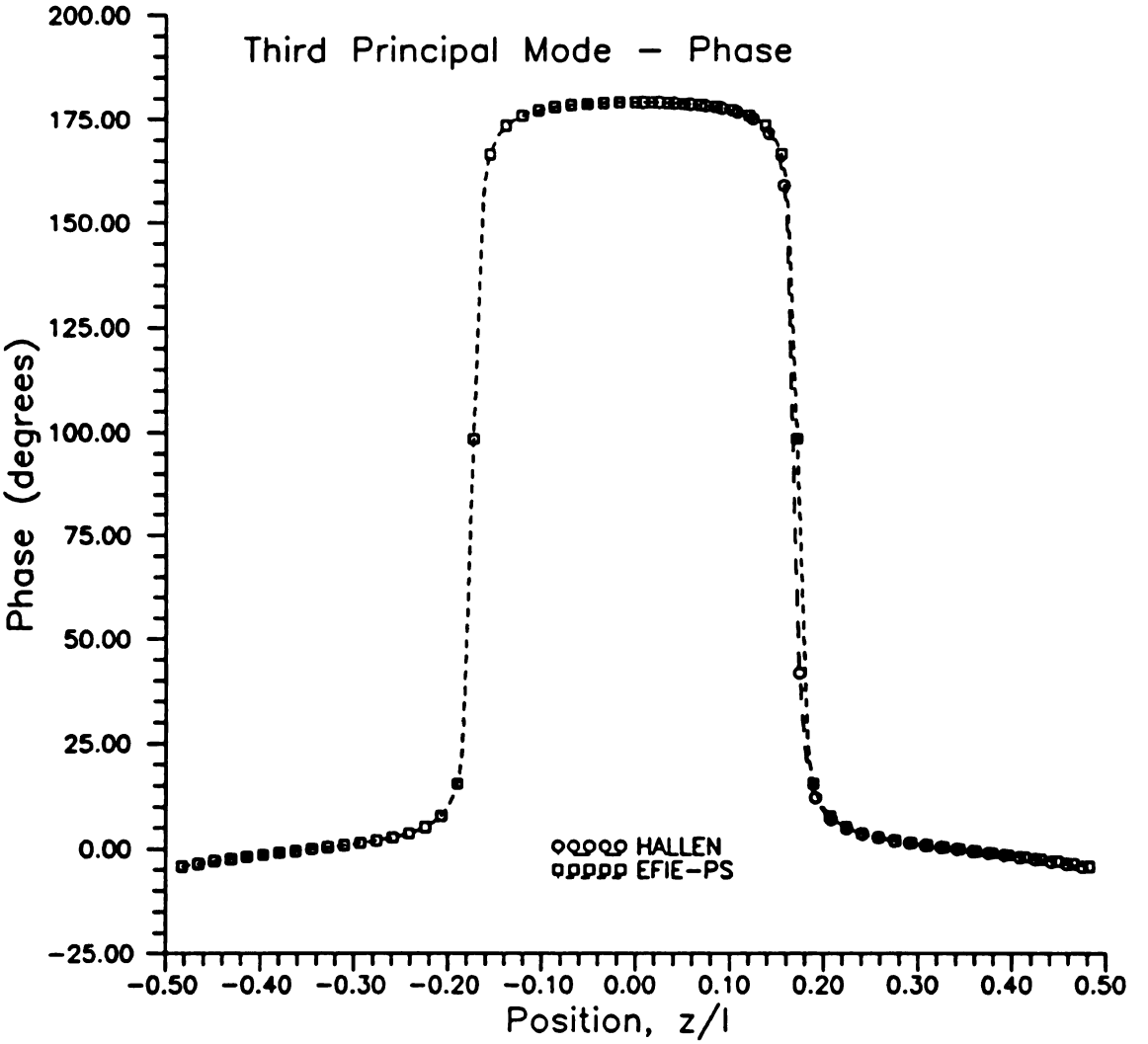

Figure 3.10 Phase of current distribution for $s_{1,3}$ mode of wire with $l/a = 200$.

3.7 SEM Modes of Two Identical Parallel Thin Wires

This section presents an SEM analysis of the problem of two identical thin wire scatterers. The natural mode frequencies of two identical parallel wires are computed using the moment method formulations. Comparisons are made between the moment methods and results available in the literature. The current distributions for a system of wires obtained via the moment method are shown to be in agreement with the current distribution assumed in the approximate analyses for the principal first layer modes.

To begin, the geometry of the problem of two parallel wires of length l radius a and separation distance d is shown in Figure 3.11. The problem of two parallel wires was chosen for several reasons. First, the thin wire is a high Q structure that is easily built, measured, and theoretically modeled. There is also a large body of literature available for the case of wire scatterers and radiators. The case of parallel wires was chosen based on the belief that maximum shifting of modal frequencies would occur for two objects oriented for maximum coupling in the traditional CW sense. For the target discrimination study, it was initially thought that an estimate of the maximum shift likely to be encountered would be sufficient to determine if transient coupling effects would be a factor in the performance of the E-pulse and S-pulse methods.

From the literature and from the perturbational analysis presented in Section 3.4, it is known that when the mode frequencies of two wires are degenerate, the modes of the system of wires splits from the mode frequencies of the isolated objects. Effectively, each mode of the isolated wire is replaced by a pair of modes. One mode is symmetric and the other is antisymmetric based on the direction of current on the wires. If the current is in the same direction for each wire the mode is symmetric. If the current is in

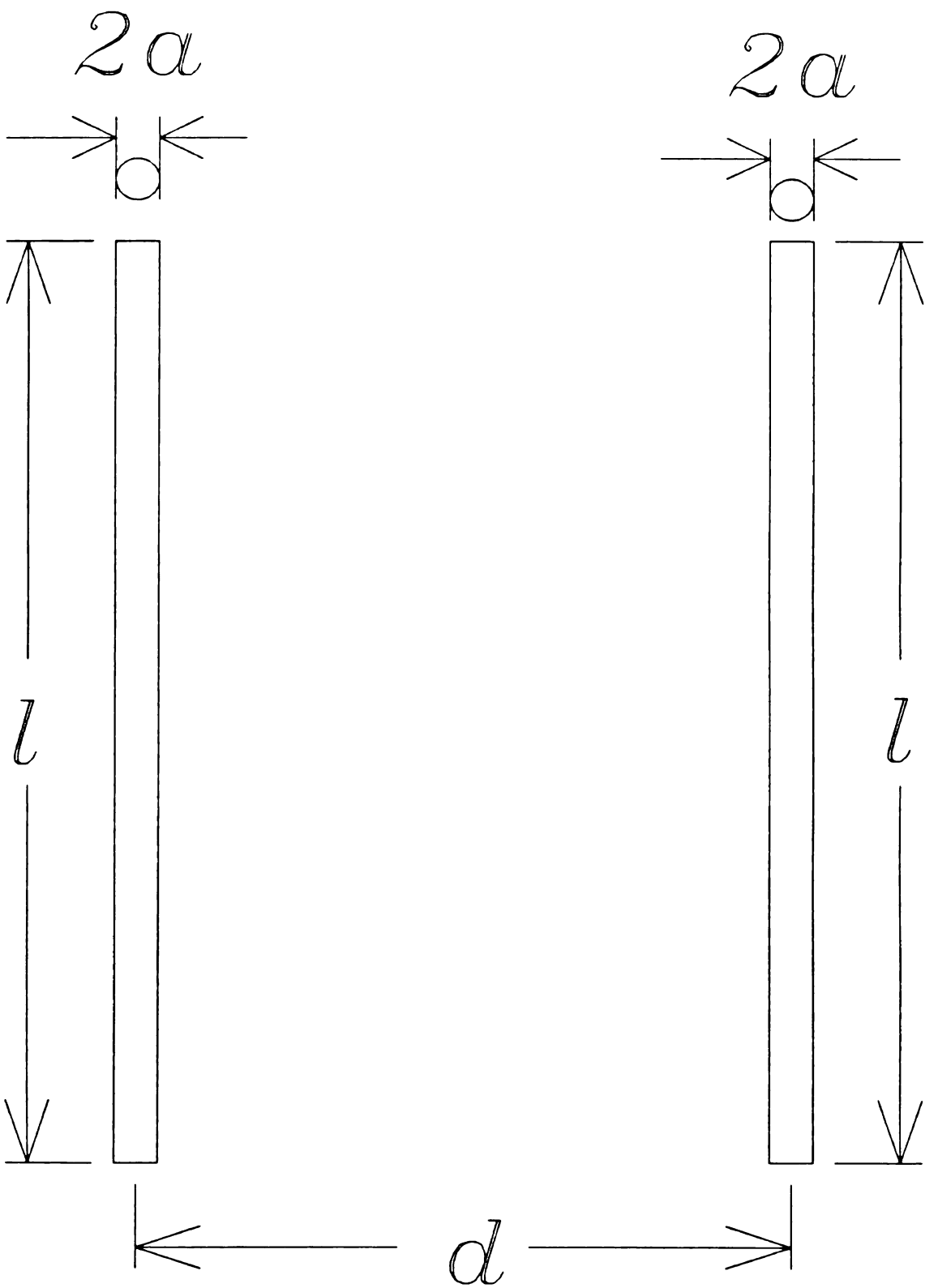

Figure 3.11 Geometry of two parallel thin wire scatterers.

opposite directions the mode is antisymmetric. In the spirit of Tesche's notation, the modes of a two wire system can be denoted as $s_{n,l,a\ or\ s}$, where the subscripts a or s denote either antisymmetric or symmetric modes. In the case of two parallel wires with small separation distance, the $s_{1,1,a}$ mode is also referred to as the transmission line mode.

In the literature concerned with the analysis of parallel wires the natural frequencies are usually plotted as a trajectory in the complex s plane as a function of the separation distance d. The trajectory of the first antisymmetric mode as a function of separation distance is shown in Figure 3.12. The results were computed using the moment method with the HALLEN formulation. For close spacing, the antisymmetric mode has a small damping coefficient σ resulting in a high Q structure. As the separation distance is increased, the pole spirals clockwise about a point near the mode of the isolated wire frequency. However, instead of continuing to spiral toward this point, the mode suddenly begins to move away from the isolated mode frequency and eventually begins moving toward the origin. This behavior has been observed previously by Umashankar and others. This is very puzzling behavior since one would intuitively think that as the separation is increased the mode frequency should tend toward that of the isolated wire. This puzzling behavior is the focus of this chapter. The trajectory of the first symmetric mode as a function of separation distance is shown in Figure 3.13. The Q of this mode is low for small values of separation distance. As the separation distance is increased, the mode frequency spirals clockwise about the isolated mode frequency and eventually moves toward the origin in a manner similar to that of the antisymmetric mode. Indeed, this is peculiar behavior. An even more startling result is shown in Figure 3.14. Here the trajectory of an antisymmetric mode that is originally in the second

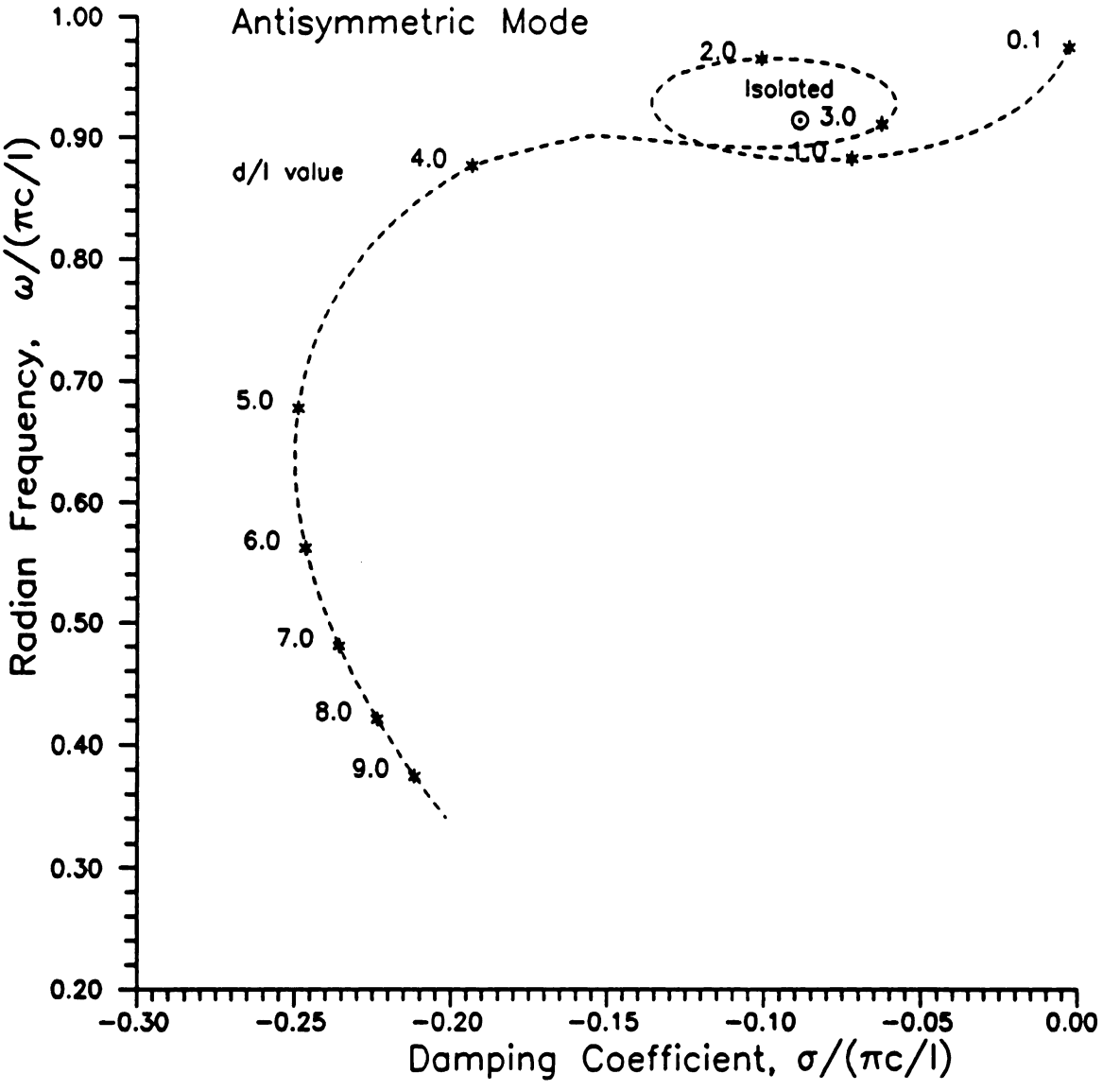

Figure 3.12 Trajectory of lowest order antisymmetric mode of two identical parallel wires (l/a = 200) vs separation distance.

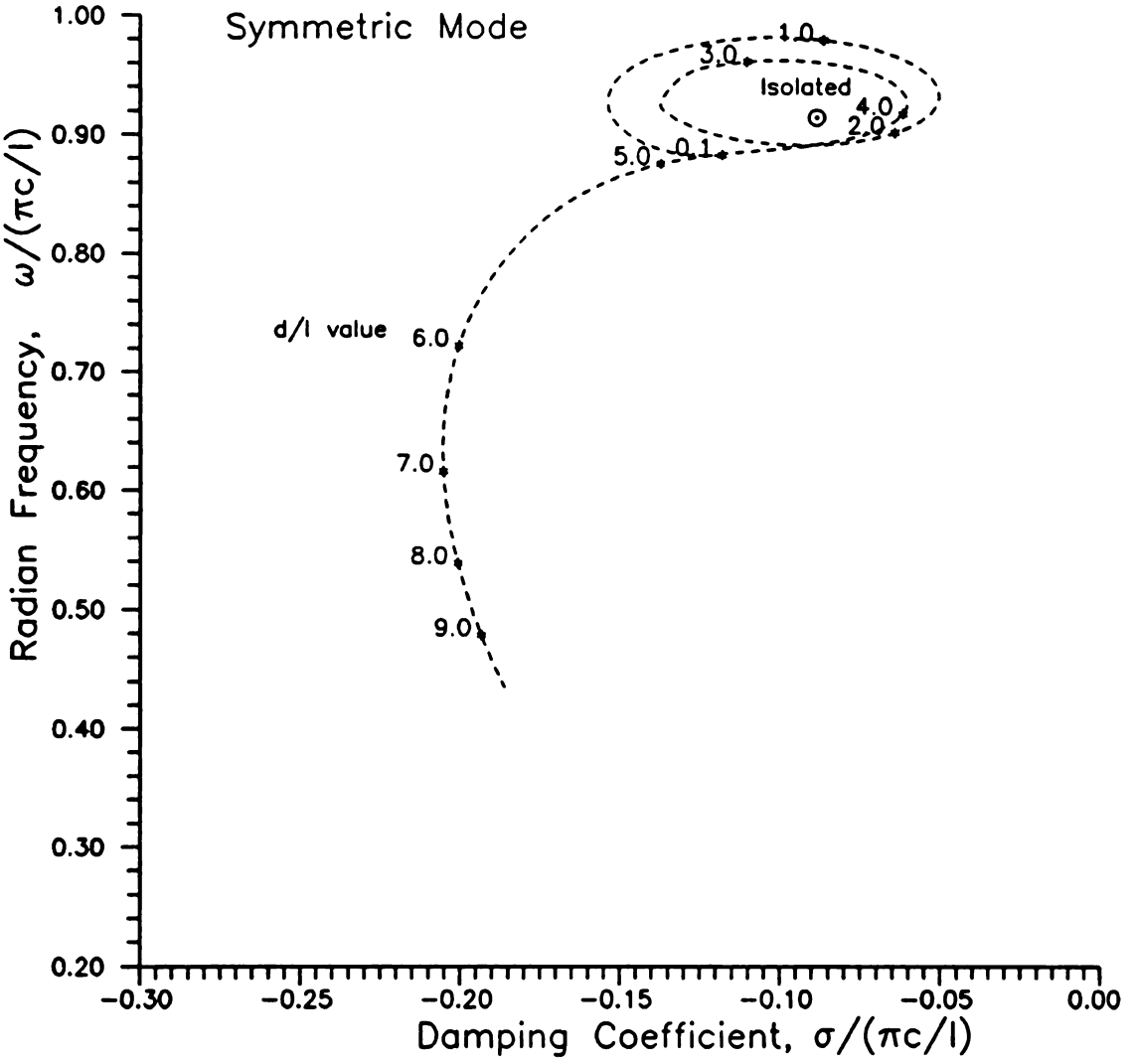

Figure 3.13 Trajectory of first symmetric mode of two identical parallel wires (*l/a* = 200) vs separation distance.

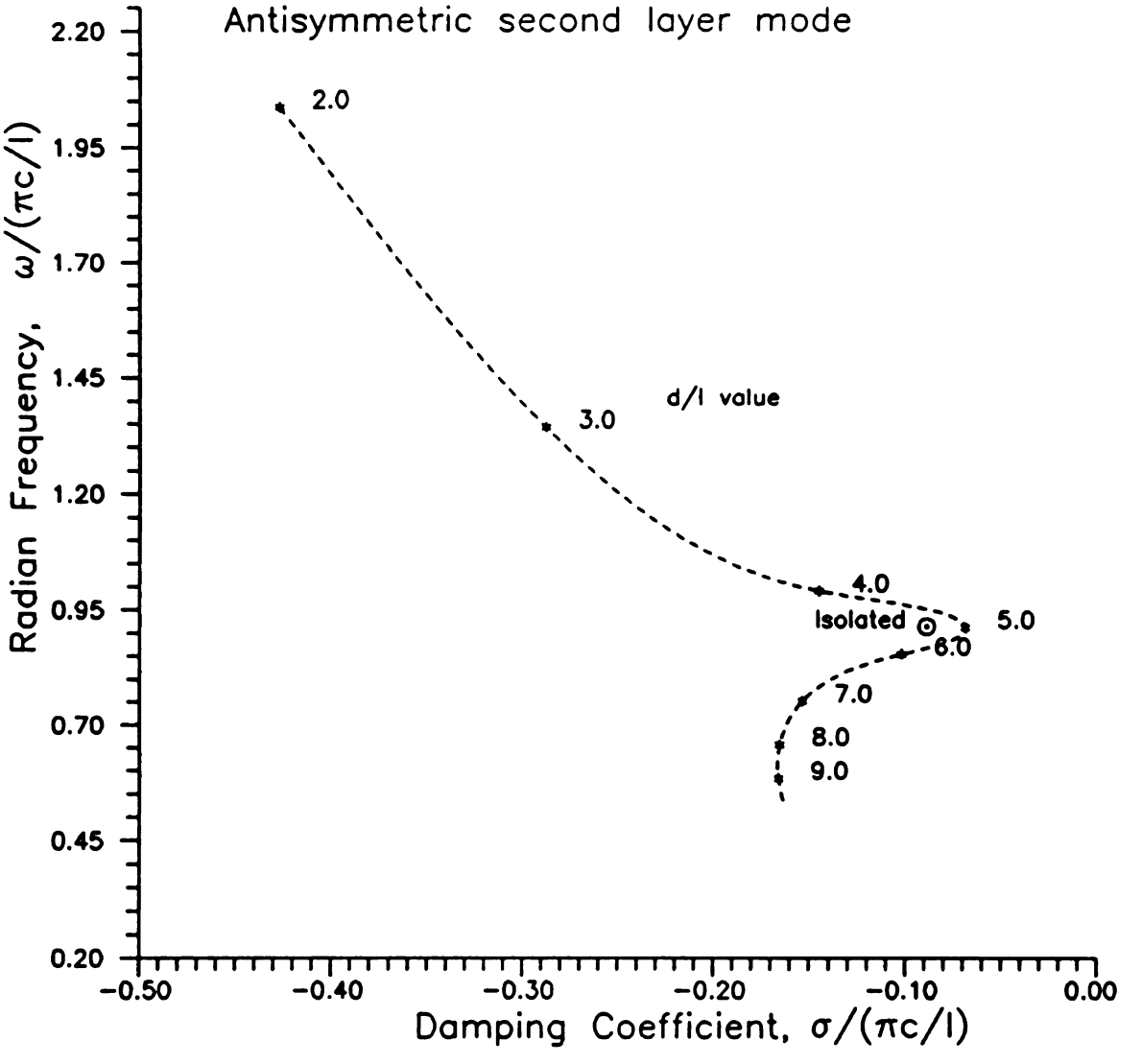

Figure 3.14 Trajectory of antisymmetric mode from second pole layer for two identical parallel wires as a function of separation distance.

layer of poles for small values of separation distance is plotted. It is clear that for small values of separation distance this mode damps very quickly. For larger values of separation distance, the pole moves from the second layer into the first layer near the frequency of the isolated wire. This mode seems to replace the first symmetric mode as it moves away from the isolated pole frequency. A discussion on the significance of this result is deferred until later in this section.

Since the behavior of the SEM mode frequencies is so unusual it is necessary to check the results against those available in the literature before proceeding further. Chuang [27] computed the natural frequencies of two identical wire scatterers using a Hallen formulation similar to the one used here. Figure 3.15 shows the damping coefficient as a function of separation distance for both the symmetric and antisymmetric modes. The HALLEN results are seen to be in agreement with those computed by Chuang. Figure 3.16 shows the radian frequency as a function of separation distance for both the symmetric and antisymmetric modes. Again there is excellent agreement between the HALLEN results and those obtained by Chuang. Note: the point $d=4.0l$ obtained by Chuang for the case of the antisymmetric mode is probably in error. The error most likely resulted from confusion with one of the poles moving in from another layer. Unfortunately, this error causes Chuang to arrive at the wrong conclusion as to the nature of the system modes[1] "as the distance becomes larger and larger, the coupling between the wires decreases, and subsequently the root becomes closer and closer to that of an isolated wire". Chuang's inability to detect the eventual outward spiral is most

[1] Chuang Che-I, "Transient Waveform Synethesis For Radar Target Discrimination," Doctoral Dissertation, Michigan State University, p. 72, 1983.

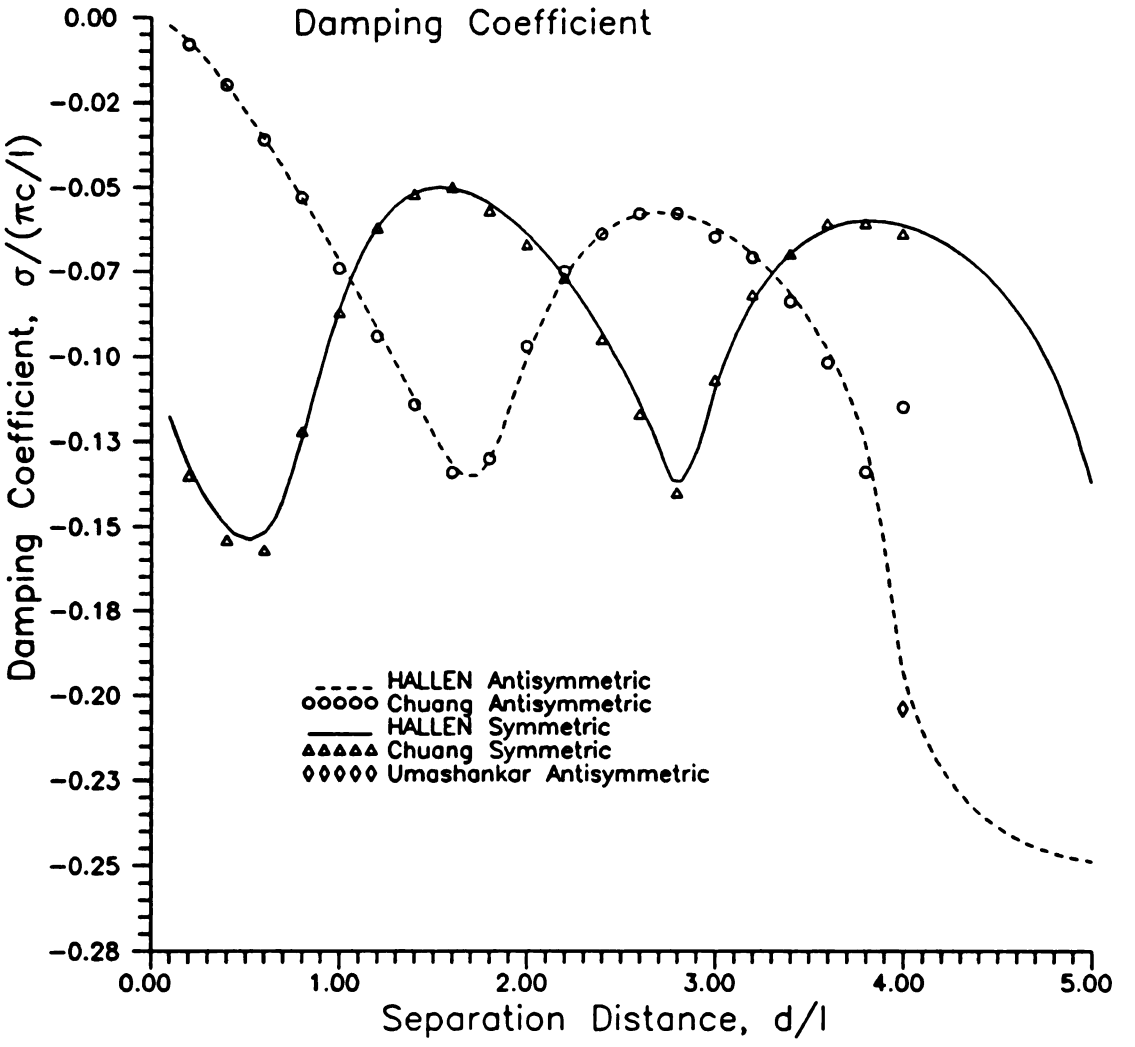

Figure 3.15 Damping coefficient of lowest order principle modes of two identical parallel wires (l/a = 200) vs separation distance.

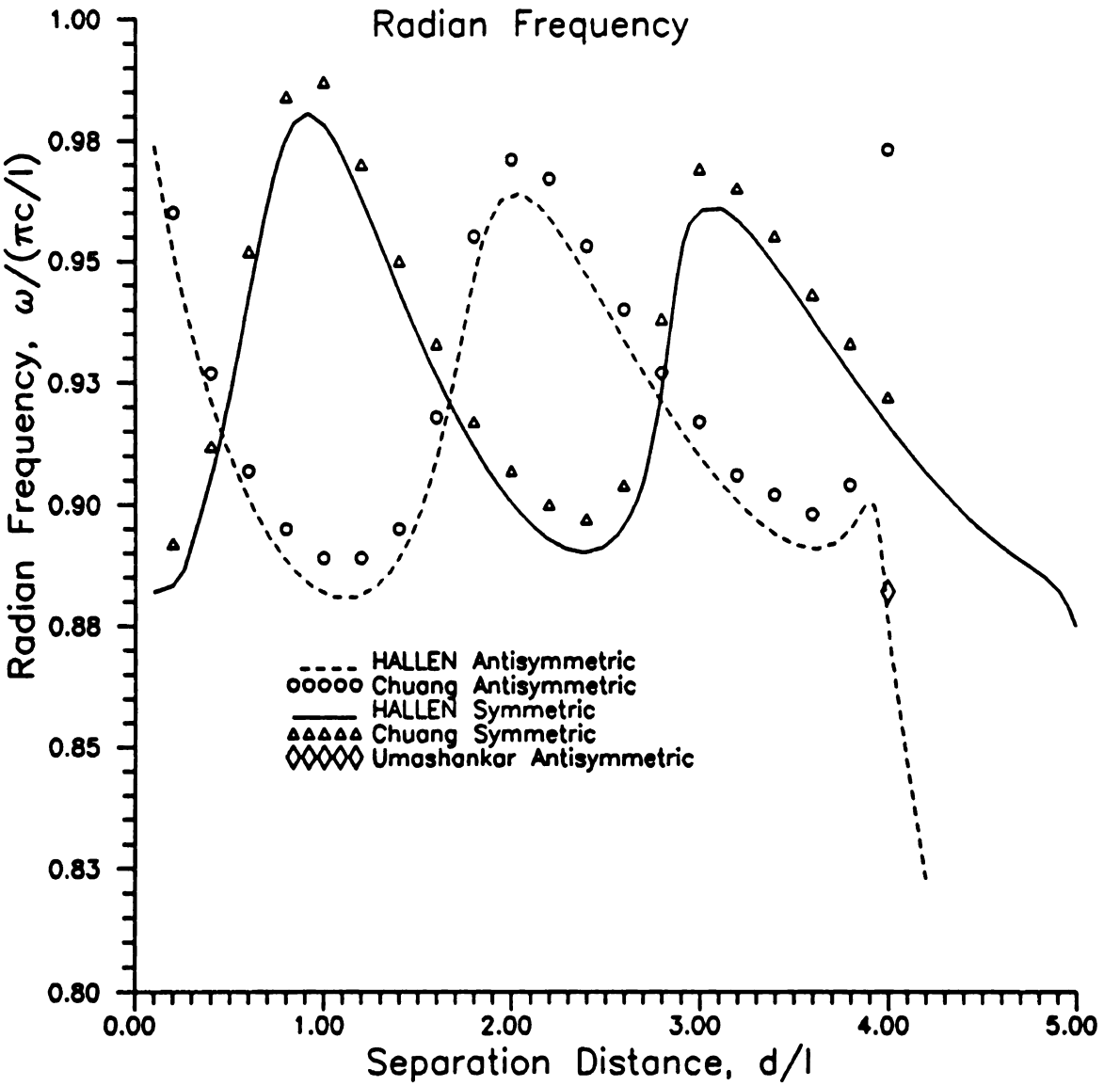

Figure 3.16 Radian frequency of lowest order principle modes of two identical parallel wires (l/a = 200) vs separation distance.

likely due to a large step increment in a tracking algorithm. The fact that the modes should continue to move away from the isolated mode frequency is supported by the results of Ummashankar [24] and data transcribed from this paper is in agreement with the outward spiral results computed by this author using the several different formulations. Another interesting phenomena associated with the spiralling modes is observed when the mode trajectories are computed for a system of wires which have different length-to-radii ratios. Ummashankar and others have empiracally observed that the mode trajectory of thin wires complete more spirals about the isolated mode pole frequency than thicker wires. The trajectory of the antisymmetric mode for $l/a=400$ is shown in Figure 3.17. It is seen that the separation distance at which the mode trajectory breaks from the spiral path about the isolated mode frequency has been increased from approximately $d/l=4$ to $d/l=6$. Even though this phenomena has been observed previously by Umashankar and Baum they provided no physical interpretation of the phenomena. As of this writing there is still no adequate physical interpretation of this phenomena.

Since the behavior of the mode frequencies for the coupled wire system is so complicated, it is useful to examine the SEM mode current distribution associated with the various system modes. One expects the current distribution on the wires to be nearly sinusoidal in order to satisfy the boundary condition of zero current at the ends of the wires. A plot of the magnitude and phase of the current distribution for the first antisymmetric mode for different values of separation distance is shown in Figure 3.18 and Figure 3.19. Only the current on one of the wires is considered since the other wire is identical except for a negative sign as expected for the antisymmetric mode. It is clear

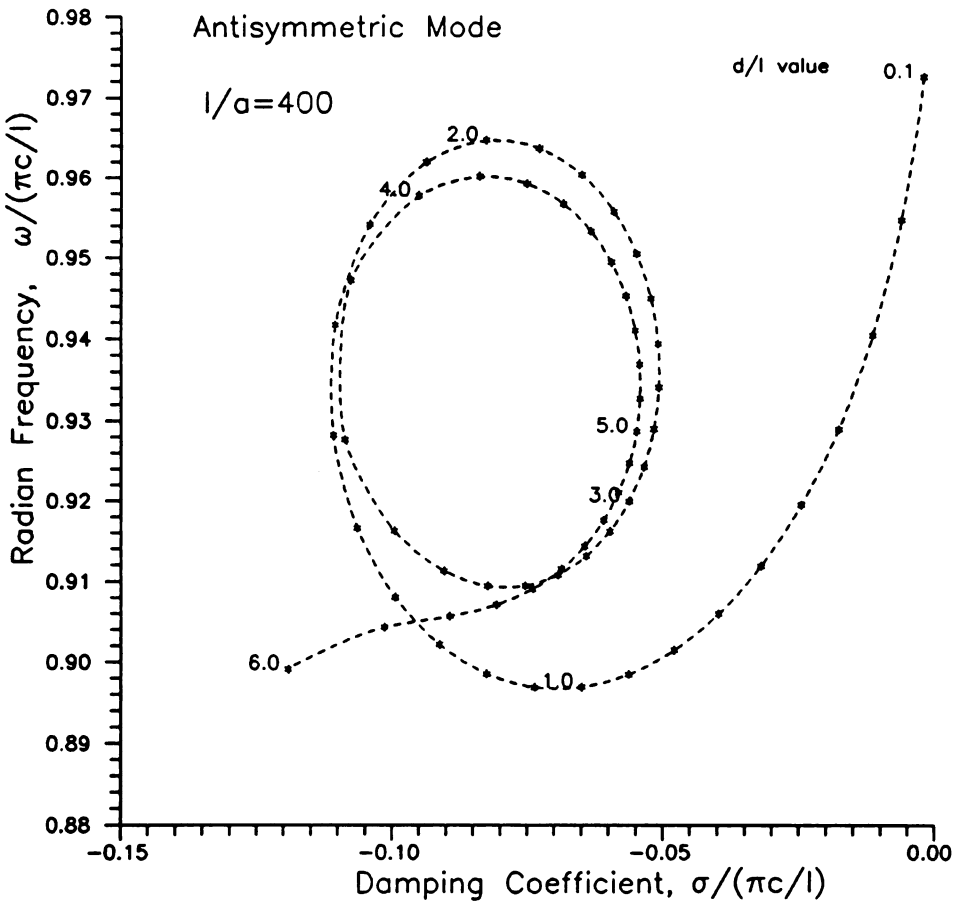

Figure 3.17 Trajectory of lowest order antisymmetric mode of two identical parallel wires (l/a=400) vs separation distance.

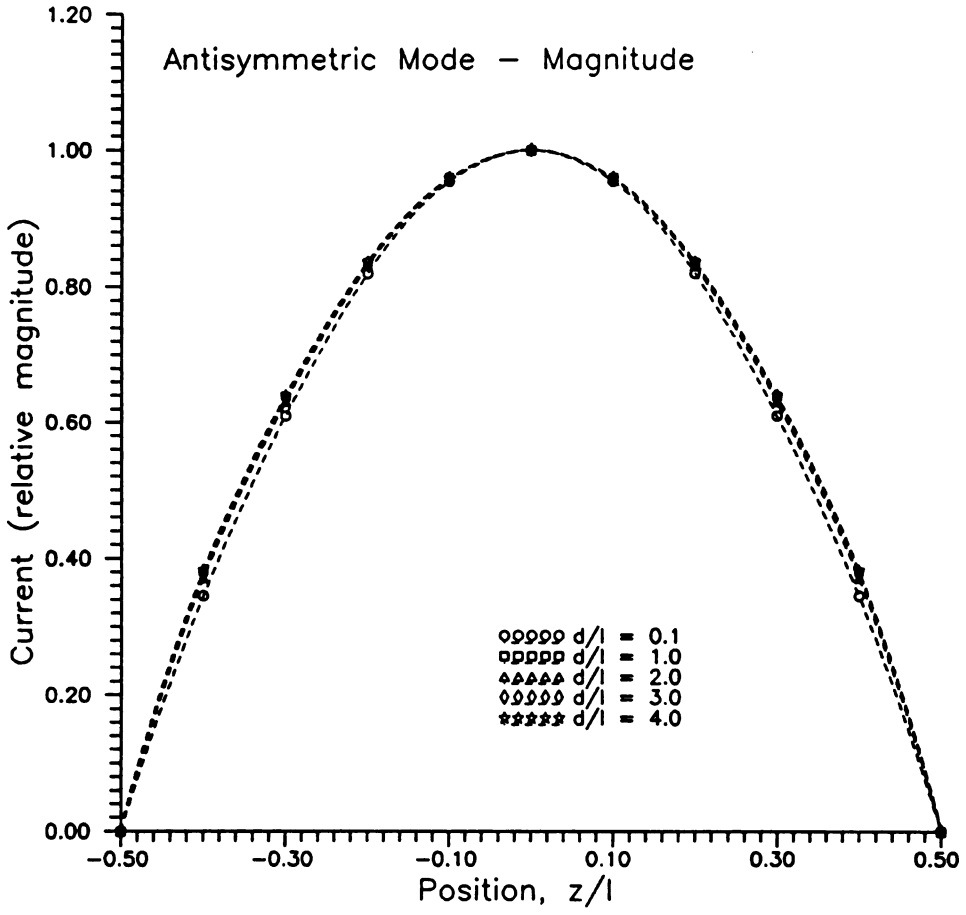

Figure 3.18 Magnitude of current distribution for lowest order antisymmetric mode of two identical parallel wires (l/a = 200) vs separation distance.

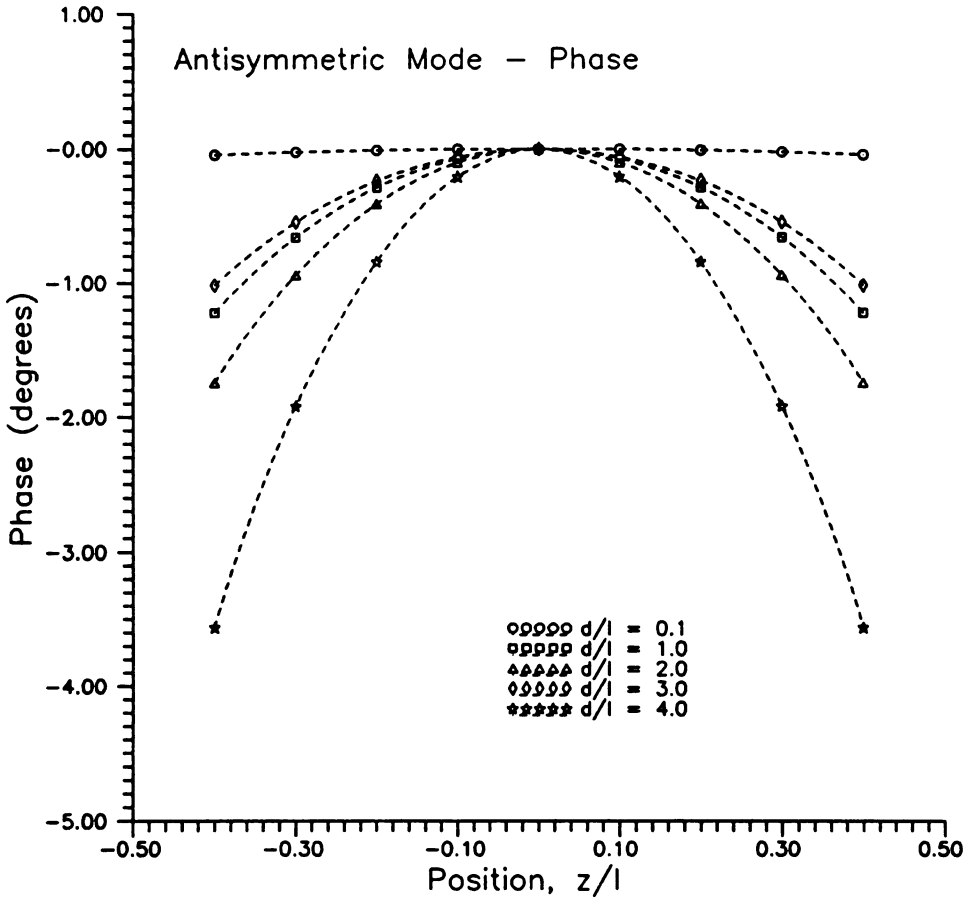

Figure 3.19 Phase of current distribution for lowest order antisymmetric mode of two parallel wires (l/a = 200) vs separation distance.

from these figures that the current is nearly sinusoidal regardless of the separation distance. Similar results are obtained for the magnitude and phase of the symmetric mode current distribution as shown in Figure 3.20 and Figure 3.21.

The next issue concerning the coupled wire systems is the distribution of current present on the modes that migrate from the second layer of poles to the first layer. Figure 3.22 and Figure 3.23 show that the current distribution of the first antisymmetric mode of the second layer changes as a function of separation distance. The amplitude distribution becomes more sinusoidal as the separation distance is increased and the mode frequency moves toward the isolated mode frequency and the jω-axis. The phase difference between the center and ends of the wire is large for small separation distances. As the separation distance is increased, the phase becomes more uniform across the wire which is the opposite of Figure 3.19. This is characteristic of the mode of an isolated wire scatterer. It appears then that as the second layer pole moves closer to the isolated pole, the current distribution becomes more sinusoidal so as to smoothly replace the first layer pole that begins to move away from the pole of the isolated scatterer. It is anticipated that this same effect is present for other poles as they sweep past the poles of the isolated scatterer.

It is important to note that what is referred to as the first principal mode may not in actuality be the $s_{II,a}$ of the configuration for a given spacing. Instead, the mode is tracked from the first principal mode for close spacings.

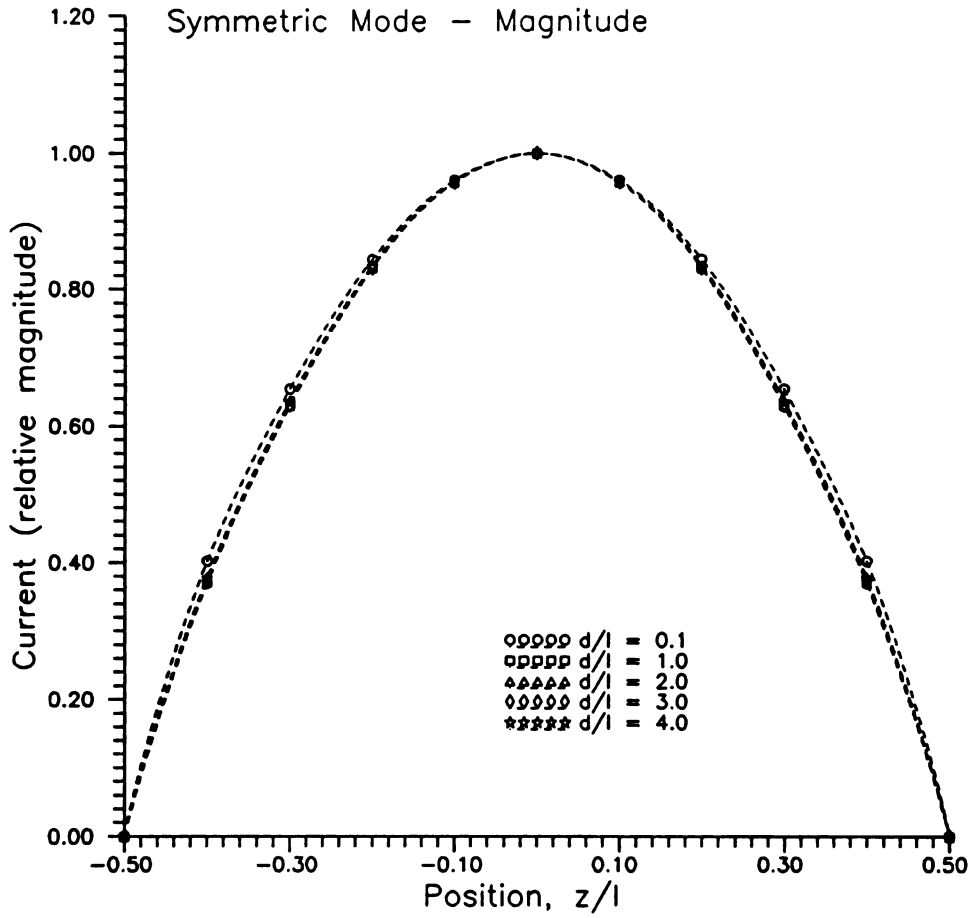

Figure 3.20 Magnitude of current distribution for lowest order symmetric mode of two identical (l/a = 200) parallel wires vs separation distance.

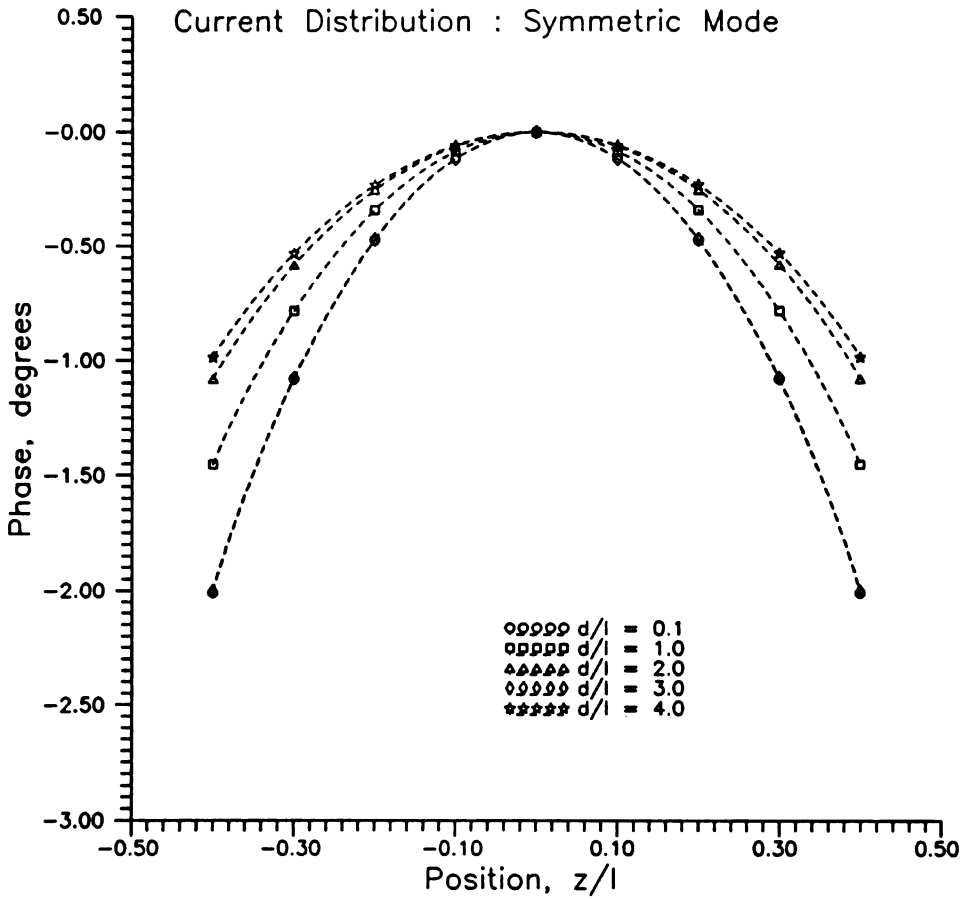

Figure 3.21 Phase of current distribution for lowest order symmetric mode of two identical (l/a = 200) parallel wires vs separation distance.

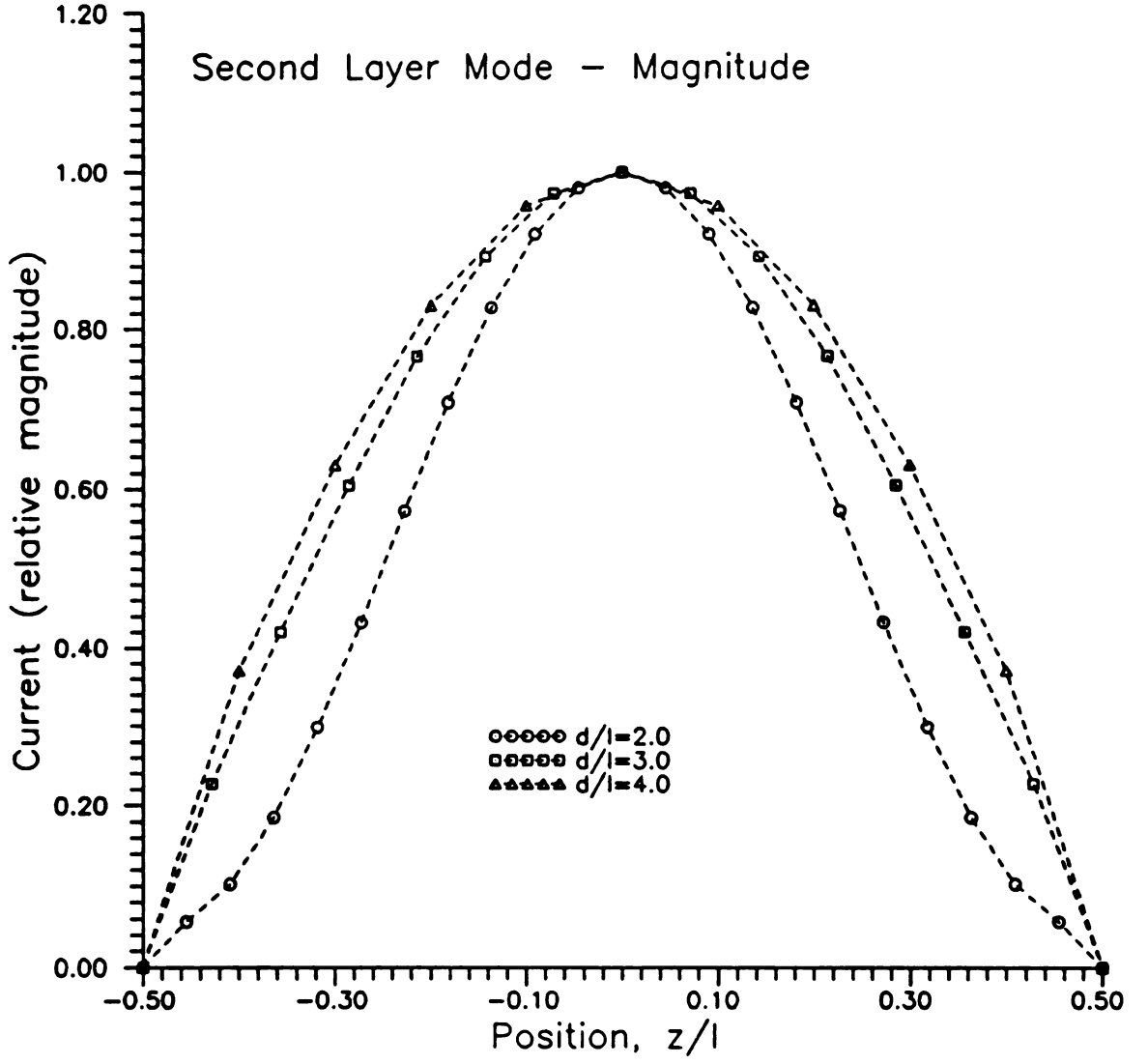

Figure 3.22 Magnitude of current distribution for second layer antisymmetric mode of two identical (l/a=200) parallel wires vs separation.

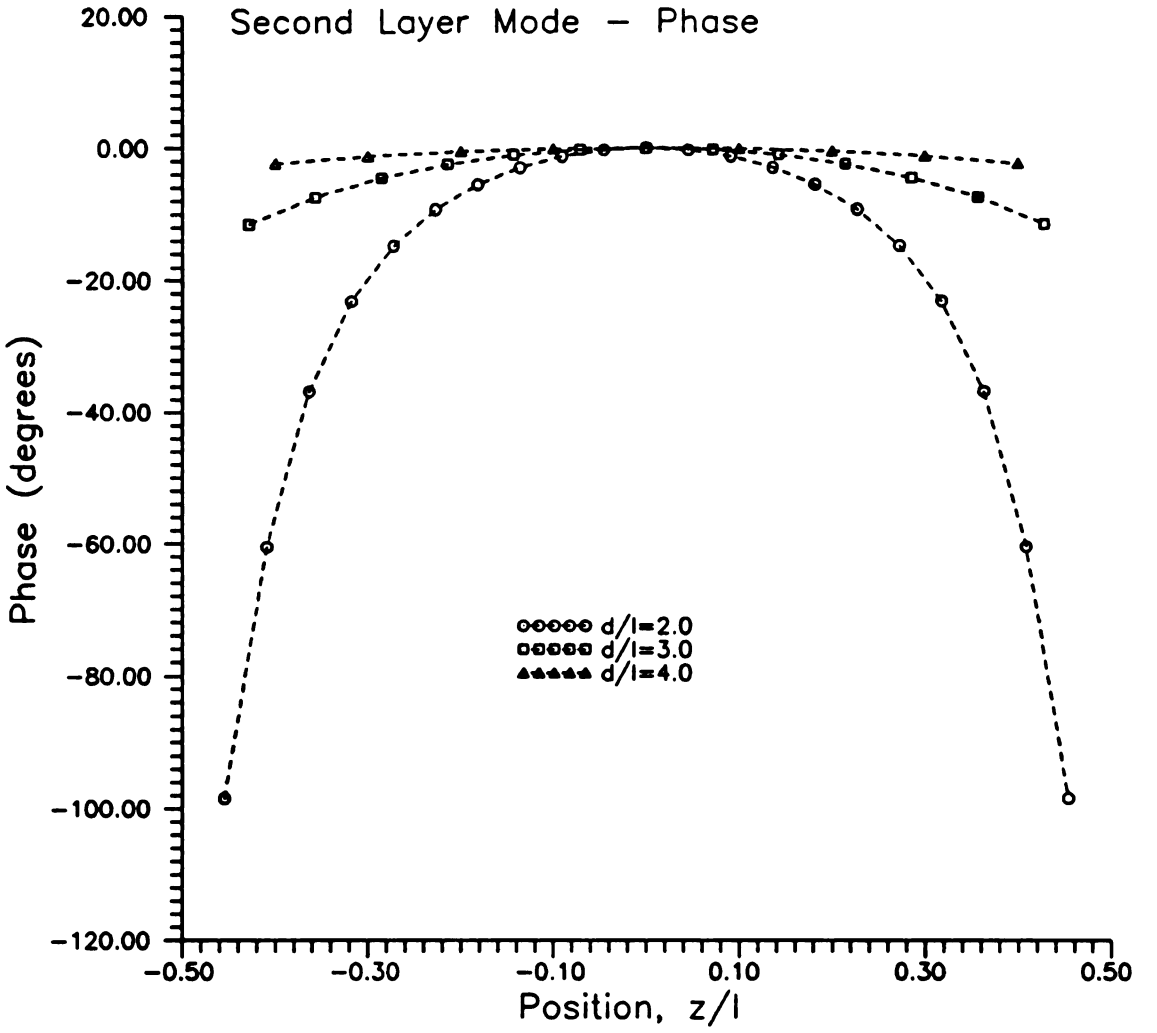

Figure 3.23 Phase of current distribution for second layer antisymmetric mode of two identical (l/a = 200) parallel wires vs separation distance.

3.8 Evaluation of Approximate Methods

This section presents a comparison of the SEM mode frequencies obtained using the moment method to those of the approximate methods outlined in sections 3.4 and 3.5. From the last section, it is apparent that the SEM mode currents for a system of coupled wires is nearly identical to the SEM mode currents of the single wire. This is necessary if either of the approximate methods are to provide accurate results.

To illustrate applicability of the approximate methods to this type of problem, the approximate methods were used to solve for the mode frequencies of the system of two identical parallel wire considered previously. Figure 3.24 and Figure 3.25 show the damping coefficient and radian frequency for the first antisymmetric mode of the system of system of two identical parallel wires as a function of separation distance. Moment method calculations obtained using the HALLEN formulation are shown for comparison. The perturbational results were obtained by using the current distribution calculated from the HALLEN moment method solution for a single wire. The results for the approximate Green's function method were obtained by assuming a sinusoidal current and the Hallen formulation of the integral equation. It is apparent in both plots that the agreement between the moment method and the perturbational method is very good as the separation distance is increased. The approximate Greens function method also provides good results for small separation distances. However, the approximation of the Green's function by only two terms in the Taylor series is apparently invalid for large values of separation distance. The breakdown of this approximation is evidenced in the large error between the approximate method and both the moment method solution as well as the perturbational method that does not approximate the Green's function. It is especially

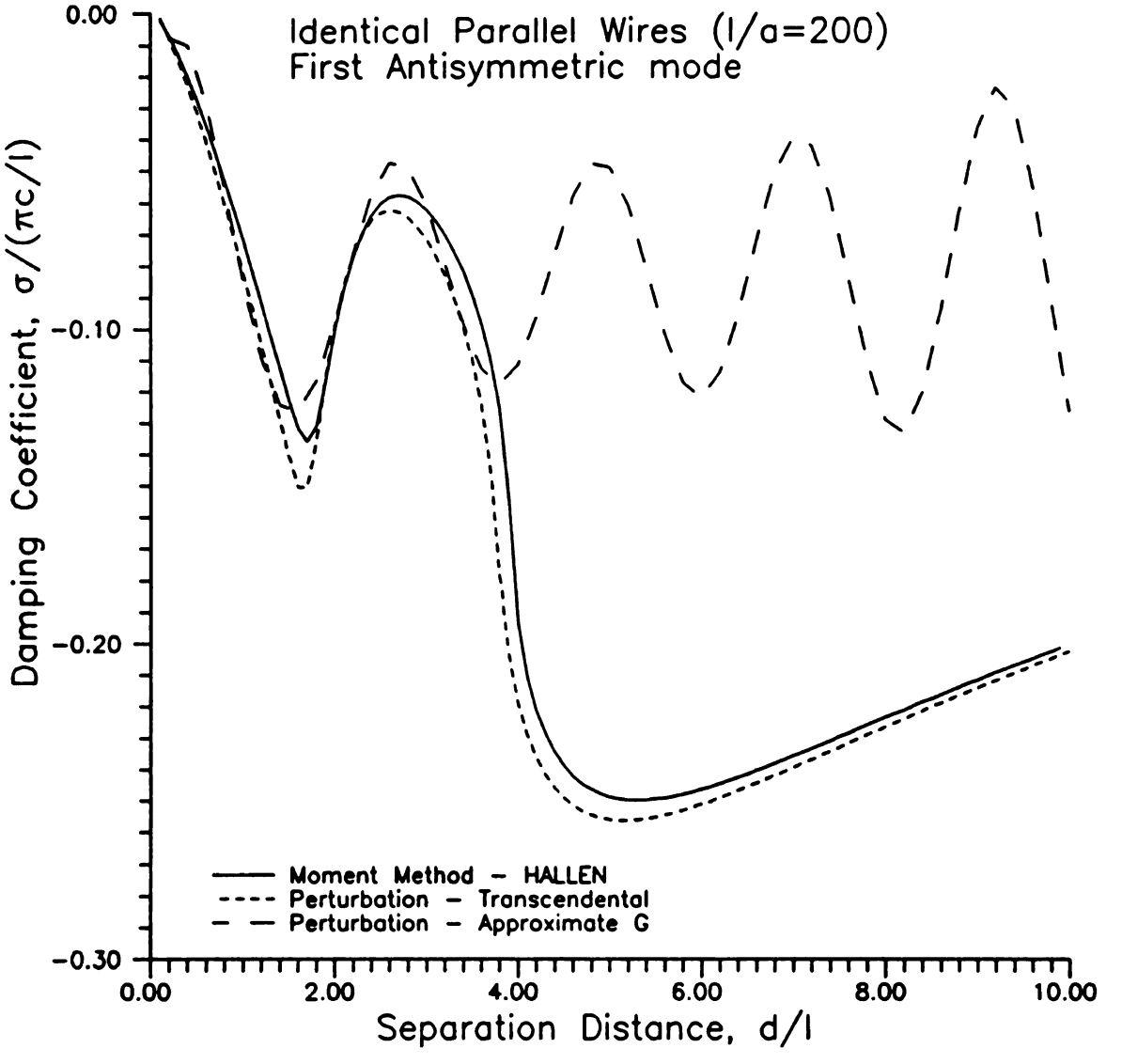

Figure 3.24 Damping coefficient of lowest order antisymmetric mode frequency of two identical parallel wires (l/a = 200) vs separation distance - approximate methods.

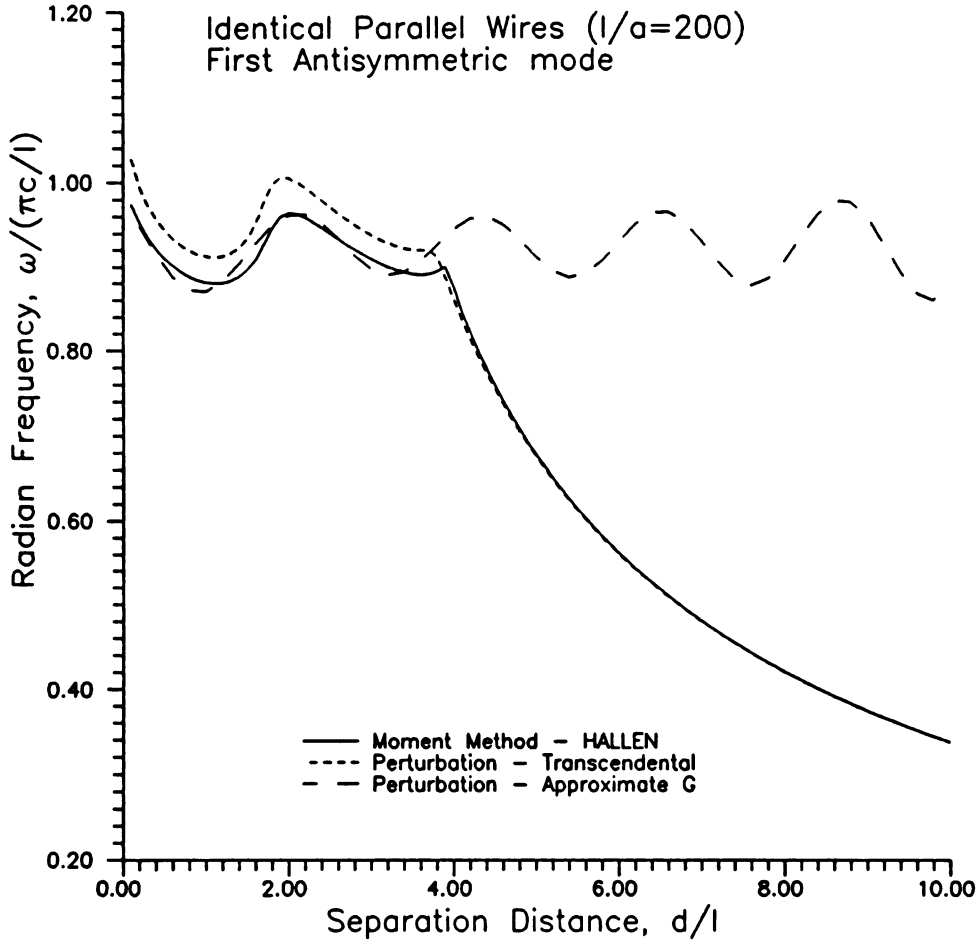

Figure 3.25 Radian frequency of lowest order anti-symmetric mode frequency of two identical parallel wires (l/a = 200) vs separation distance - approximate methods.

interesting to note that the approximation on the Green's function breaks down at the point where the mode breaks away from the spiral path about the isolated mode frequency. Similar effects are observed for the case of the lowest symmetric mode as evidenced by Figure 3.26 and Figure 3.27. Again, the approximation on the current is valid for most all values of separation distance while the approximation on the Green's function is invalid for separation distances greater than approximately 4 wire lengths. It is anticipated that the range of validity for the approximate Green's function method is a function of the wire length-to-radius ratio or effectively the Q of the isolated target mode. This conjecture is based on the previously observed effect of wire radius on the trajectory of the spiral path and the fact that the approximate Green's function method appears to break down for separation distances where the actual mode breaks from the circular path near the isolated mode frequency. The effect can be illustrated by using the case of a wire with $l/a=400$ whose trajectory was previously shown in Figure 3.17. The damping coefficient and radian frequency computed using the approximate Green's function is shown in Figure 3.28 and Figure 3.29. In both cases the approximate Green's function method produces erroneous results for separation distances greater than approximately 6 wire lengths, the same point at which the mode begins to break from the spiral path about the isolated mode frequency. Since the range of validity for lower Q targets is for smaller separation distances, one would expect that this method could be even more limited when dealing with more complicated lower Q structures such as aircraft.

It is conjectured that this same effect allowed Hanson [42] to use the approximate Green's function method to model the currents and radiation from integrated

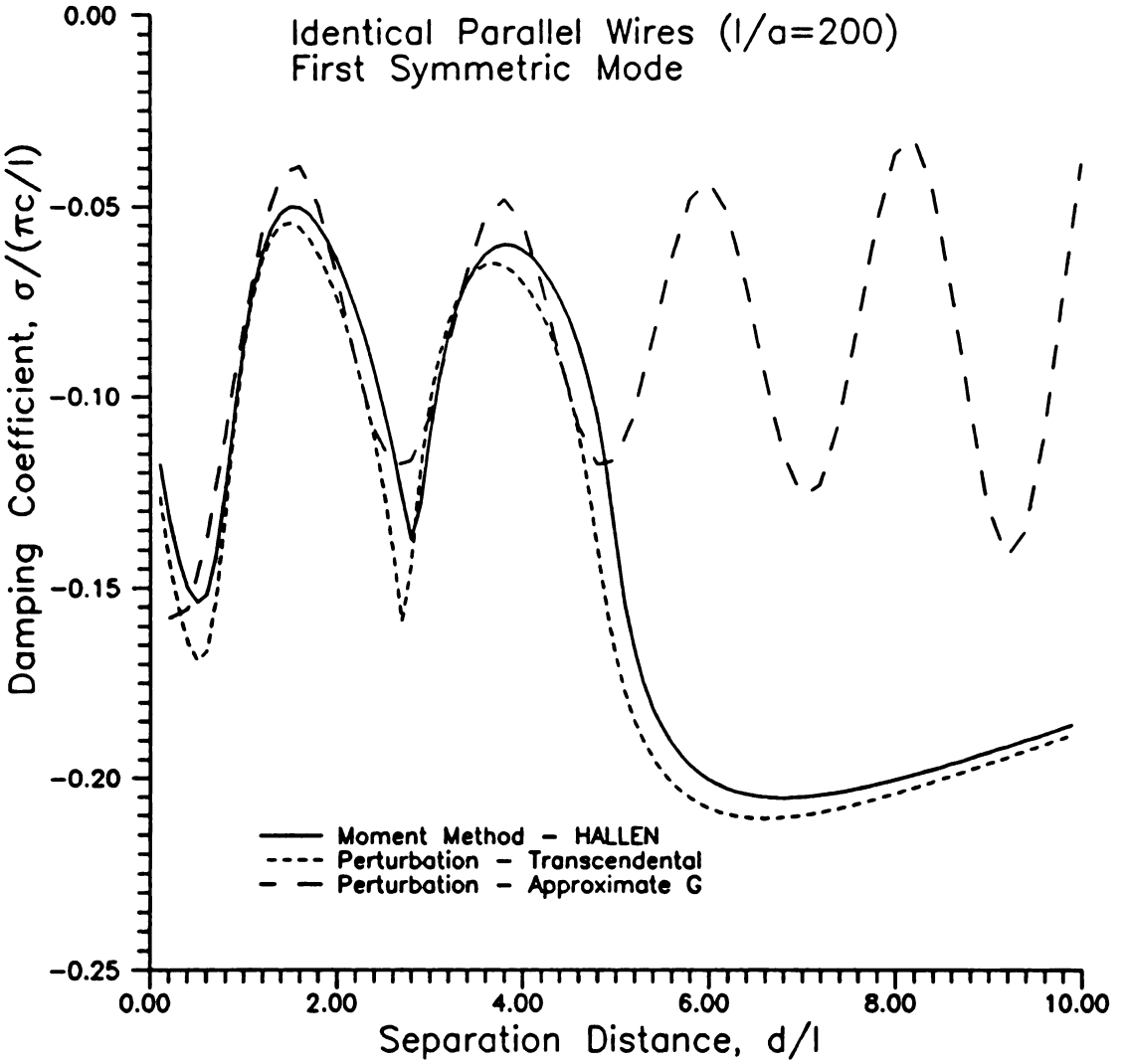

Figure 3.26 Damping coefficient of lowest order symmetric mode of two identical parallel wires (l/a = 200) vs separation distance - approximate methods.

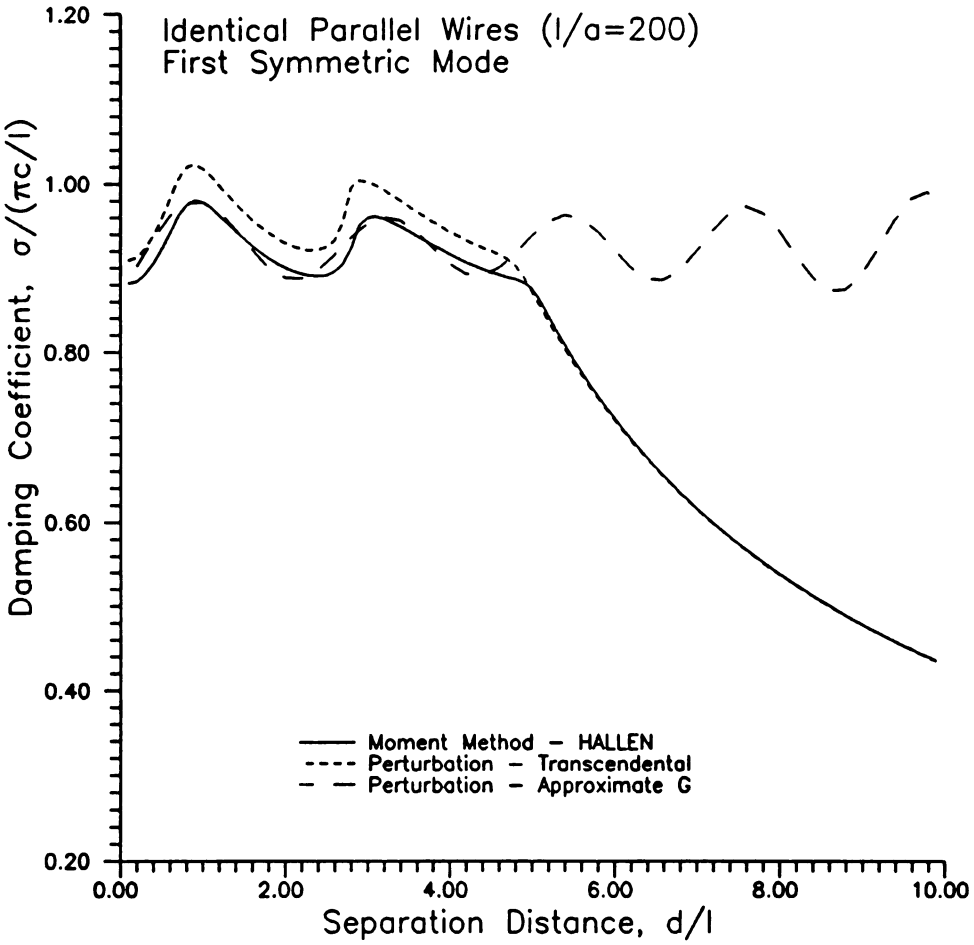

Figure 3.27 Radian frequency of lowest order symmetric mode frequency of two identical parallel wires (l/a = 200) vs separation distance - approximate methods.

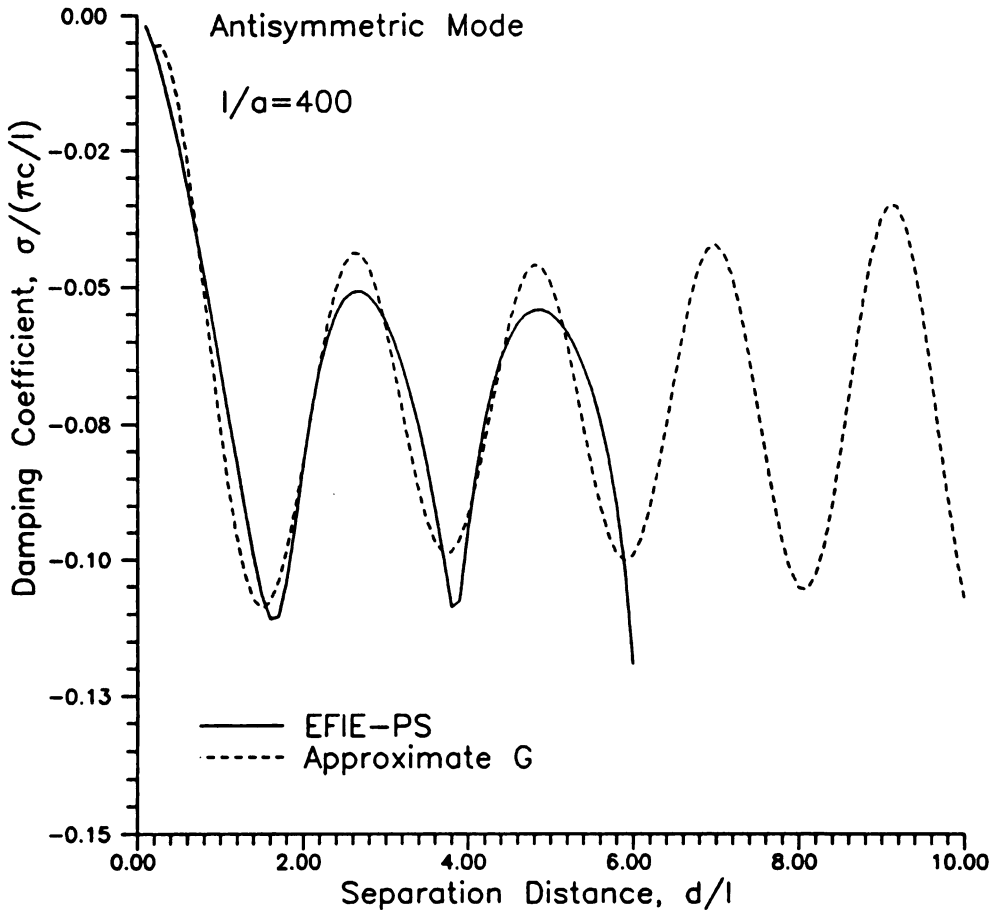

Figure 3.28 Comparison of damping coefficient calculations using the approximate Green's function method for a system of two identical parallel thin wires (l/a = 400).

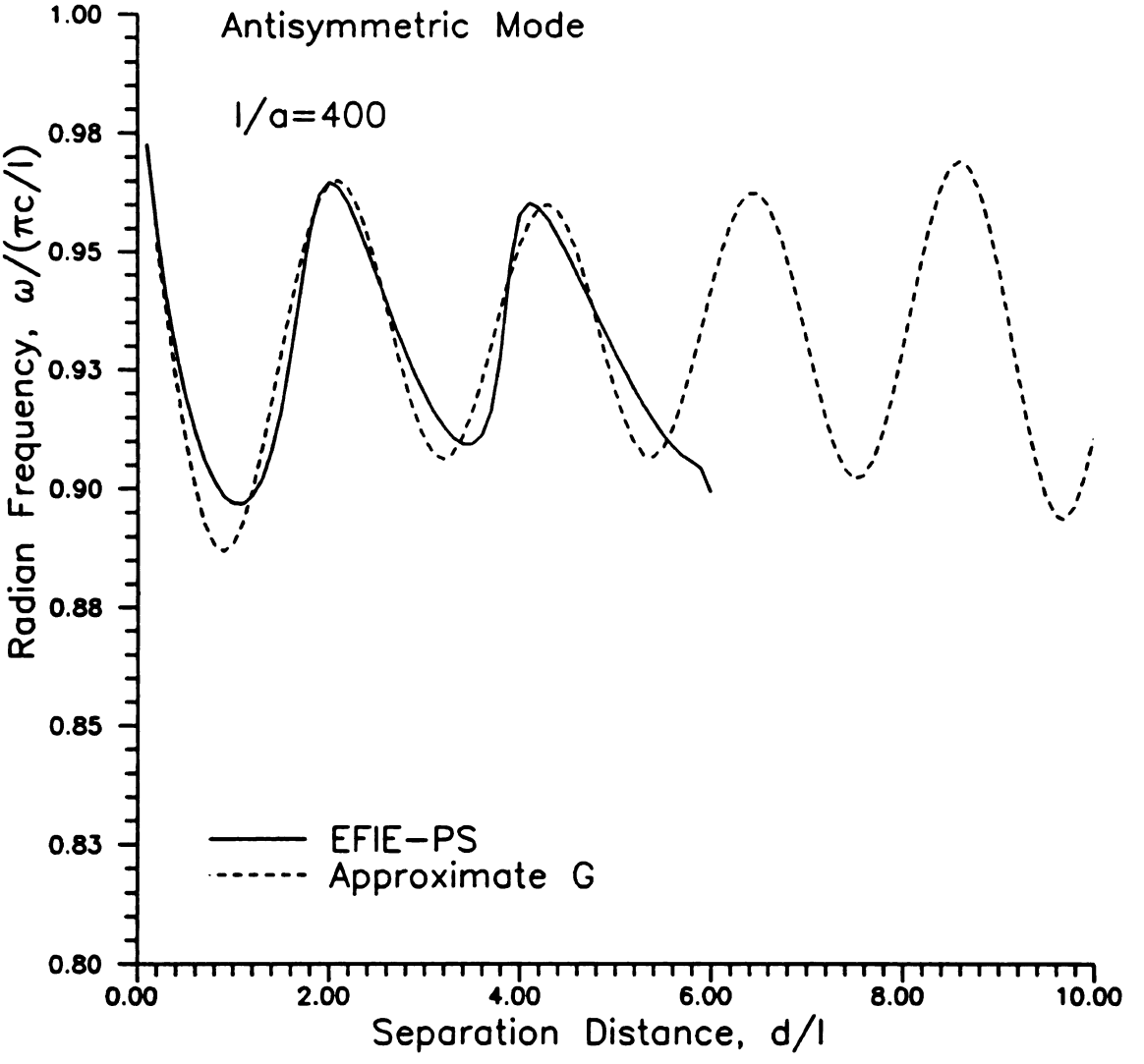

Figure 3.29 Comparison of radian frequency obtained using approximate Green's function method for system of two identical parallel wires (l/a = 400).

circuit dipoles. The dipoles considered were etched onto a thin dielectric film over a perfectly conducting substrate. The close spacing of the dipole and its "image" effectively caused the system of dipoles to work as a transmission line resonator with a very high Q. This high Q allowed the approximate Green's function method to produce good results over the range of distances encountered in the printed circuit environment. One might expect that the method may not yield good results for other types of lower Q elements such as patch antennas. Verification of these conjectures however, is beyond the scope of this work. It should be noted that the solution using the approximate Green's function has been performed for values of separation distance greater than those shown in the plots. It is observed that the solution never spirals back toward the correct result and in fact the predicted mode frequencies spiral outward from the isolated mode pole toward infinity and eventually enters the right half of the complex s-plane.

3.9 Scattered Fields of Two Identical Parallel Wires

To more fully understand the phenomena of transient coupling and the SEM modes of a multiple scatterer system, the transient response of a system of two parallel wires is investigated. The transient response calculated using a SEM Class I formulation is compared to the response obtained by the inverse FFT of frequency domain moment method calculations for both the two wire and one wire scattering problems. The objective of the comparison is to illustrate when the temporal response constructed using the system modes is applicable and to determine which system modes are significant in a Class I SEM expansion.

Calculation of the transient response using the SEM formulation requires calculation of the coupling coefficient and mode fields for all significant modes. The SEM mode frequencies and currents and modal fields were computed using the EFIE-PS formulation. The general formulation for the coupling coefficient is presented in Section 3.2 while specifics of the formulation are contained in Appendix B.

For purposes of comparison, all results presented in this section are effectively band-limited by convolution of the impulse response with a Gaussian pulse of duration $0.6l/c$. The duration is taken as the interval between the 2% of maximum points. The bandwidth of the Gaussian pulse includes first layer SEM modes up to $s_{1,5}$ for the case of a single wire. Since the two wire system has first layer modes that are near the modes of the single wire, the SEM modes up to $s_{1,5,a}$ and $s_{1,5,s}$ are used to construct the transient response.

Since the vast majority of radar implementations are mono-static, only the backscattering response is considered. Excitation is chosen as a plane wave with the impressed electric field parallel to the axis of the wires. These assumptions do not limit the validity of the general conclusions.

To begin the discussion, consider the case of two identical parallel wires ($l/a=200$) that are separated in down range by $d/l=1.0$. The principal layer poles computed for this case along with the normalization constant a for a distance of $100l$ are listed in Table 3.2. The coupling coefficients and modal field strengths for down range separation are shown in Table 3.3. It is clear by examination of the coupling coefficients that the antisymmetric modes are dominant in this configuration. The antisymmetric modes dominate in this configuration since the incident pulse does not excite the wires

Table 3.2 SEM parameters for d/l = 1.00.

Mode	σ x10^9 np/s	ω x10^9 rad/s	Re{C_n x10^{-6}}	Im{C_n x10^{-6}}
1,1,a	-0.0656	0.8274	0.0510	0.1862
1,1,s	-0.0795	0.9158	0.0037	0.1638
1,2,a	-0.1538	1.7977	0.0570	0.2646
1,2,s	-0.0830	1.7707	0.0725	0.3443
1,3,a	-0.1307	2.7143	0.0569	0.4383
1,3,s	-0.1466	2.6985	0.1055	0.4064
1,4,a	-0.1613	3.6447	0.1279	0.4995
1,4,s	-0.1657	3.6159	0.1710	0.5284
1,5,a	-0.1592	4.5425	0.1652	0.6645
1,5,s	-0.1998	4.5705	0.1409	0.5696

Table 3.3 SEM coupling coefficients for down range separation distance d/l=1.00.

Mode	$Re\{A_n\}$	$Im\{A_n\}$	$Re\{E_n\}$	$Im\{E_n\}$
1,1,a	0.038271	-0.13028	-0.33590	1.16595
1,1,s	0.009256	-0.01961	-0.08121	0.16834
1,2,a	1.02×10^{-16}	-7.79×10^{-17}	-9.18×10^{-16}	5.97×10^{-16}
1,2,s	-9.18×10^{-14}	-2.15×10^{-14}	8.15×10^{-13}	1.92×10^{-13}
1,3,a	0.058433	-0.13872	-0.50490	1.24539
1,3,s	0.052523	-0.03116	-0.46391	0.27568
1,4,a	2.88×10^{-14}	4.20×10^{-14}	-2.57×10^{-13}	-3.73×10^{-13}
1,4,s	-2.82×10^{-14}	-1.16×10^{-14}	2.51×10^{-13}	1.03×10^{-13}
1,5,a	0.075527	-0.144720	-0.64593	1.30580
1,5,s	0.069919	-0.043287	-0.61446	0.39014

at the same time and in the same direction. The backscattered field response is shown in Figure 3.30. Note that the moment method calculations for a single wire and the system of wires are identical until the response from the second wire is received and is a clear demonstration that causality is included in the moment method calculations. The response obtained from the SEM formulation using the system modes clearly does not agree with the moment method results until the incident wave has passed the second wire. The point on the graph labeled system late-time indicates the point at which a Class I expansion using the SEM system modes should be valid according to the Baum's criteria [38]. This criteria determines the time at which the scattered field can be represented solely by a convergent Class I SEM expansion with no entire function contribution. Essentially, this criteria states that the scattered field can not be guaranteed to be a convergent Class I expansion until the response from the last excited portion of the scatterer traverses to all points on the scatterer and then to the observer. It is also important to note that the SEM response appears to be accurately represented for this case by using only the first layer system poles.

Next, consider the case when the same wires are separated in cross range by $d/l=1.0$. The coupling coefficients and modal fields for this case are shown in Table 3.4. It is clear from the table that the dominant system modes in this case are symmetric. The strong symmetric mode excitation is the result of the incident field exciting the currents on both wires at the same time and in the same direction. The backscattered field response is shown in Figure 3.31. Again, it is clear that the response from two wires separated in cross range is identical to that of a single wire until the wires have had time to interact. In this case, the SEM results based on the system modes seem to provide a

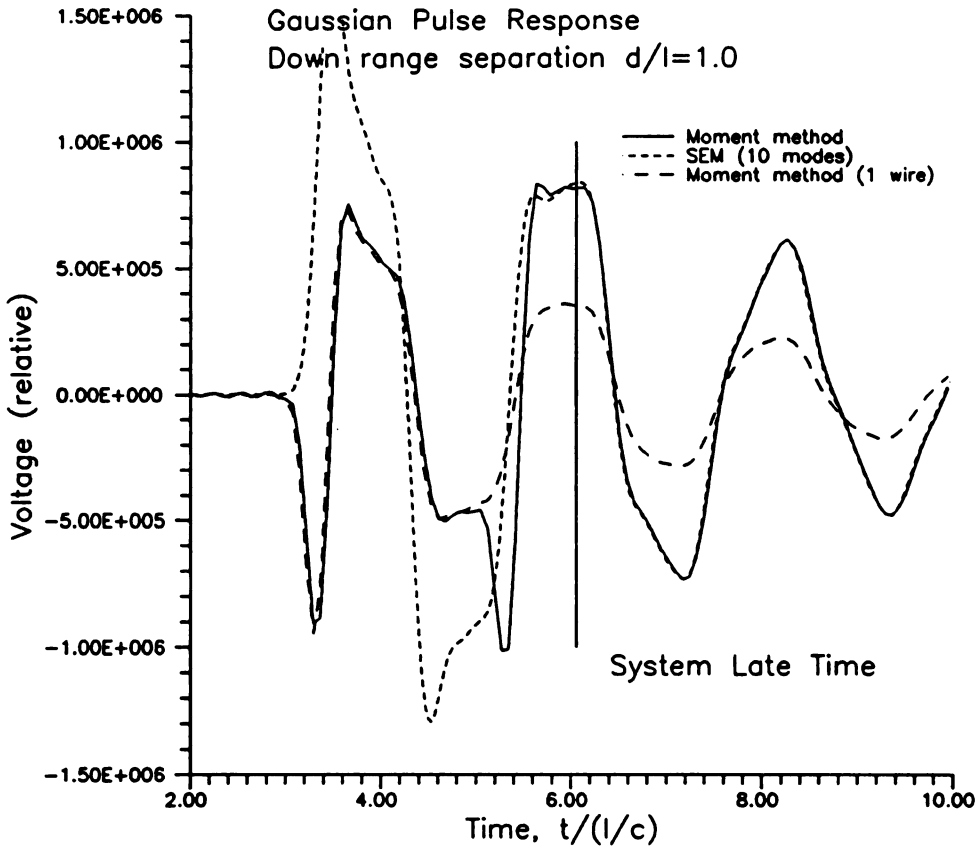

Figure 3.30 Backscattered field response of two identical parallel wires (l/a = 200).

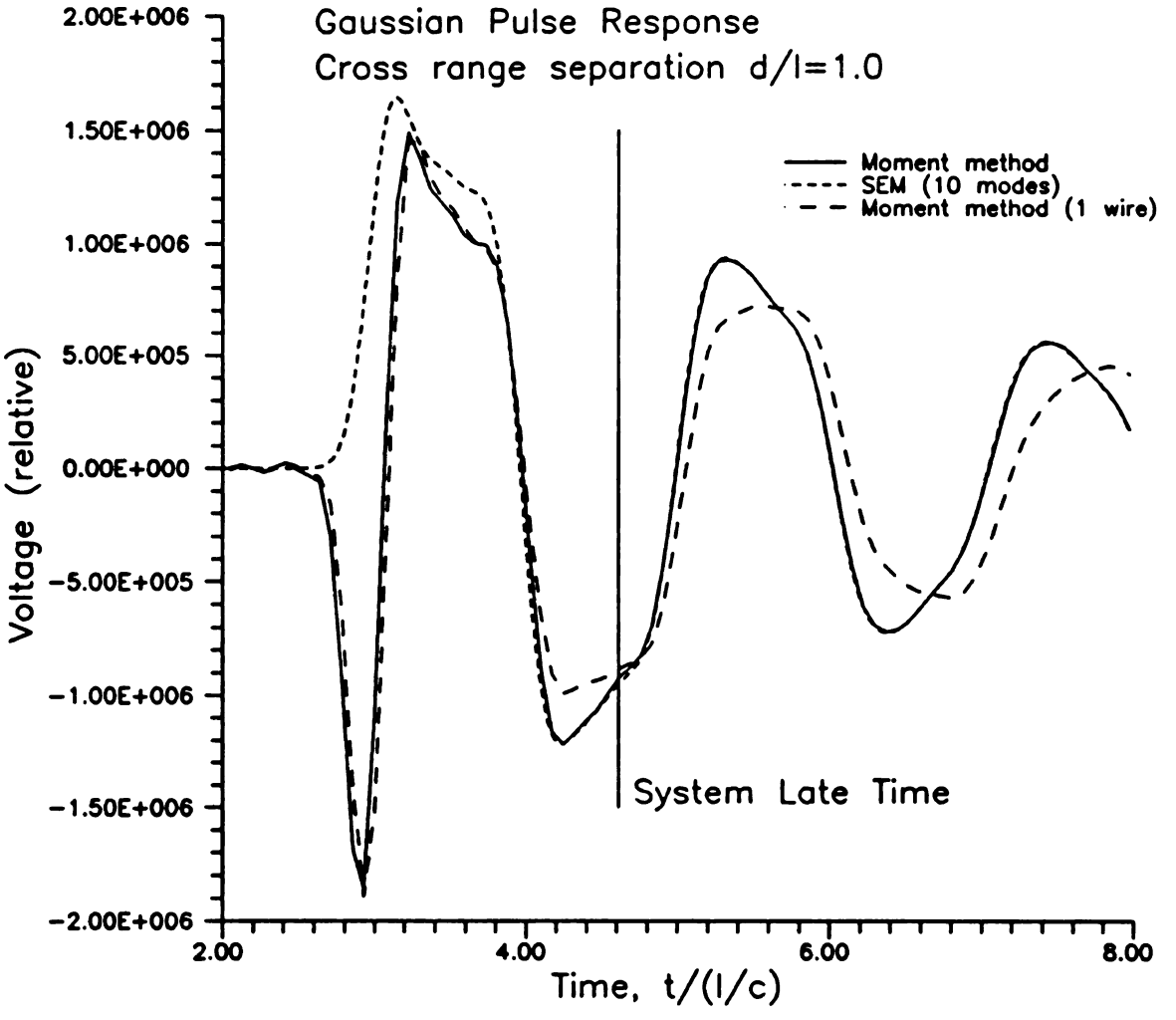

Figure 3.31 Backscattered field response from two identical parallel wires ($l/a = 200$) separated in cross range by $d/l = 1.0$.

Table 3.4 Coupling coefficients and modal fields for cross range separation d/l = 1.0.

Mode	$Re\{A_n\}$	$Im\{A_n\}$	$Re\{E_n\}$	$Im\{E_n\}$
1,1,a	-3.62×10^{-16}	-2.88×10^{-17}	-0.00759	-0.00106
1,1,s	-0.01090	0.135075	0.08388	-1.21551
1,2,a	3.91×10^{-17}	-6.80×10^{-17}	-3.09×10^{-16}	5.53×10^{-16}
1,2,s	-6.53×10^{-14}	1.61×10^{-14}	5.83×10^{-13}	-1.66×10^{-13}
1,3,a	1.66×10^{-11}	8.13×10^{-13}	-0.02407	-0.00450
1,3,s	-0.013574	0.146805	0.07812	-1.32391
1,4,a	2.33×10^{-14}	1.49×10^{-14}	-2.18×10^{-13}	-1.19×10^{-13}
1,4,s	-1.63×10^{-14}	2.98×10^{-15}	1.44×10^{-13}	-3.68×10^{-14}
1,5,a	3.54×10^{-14}	1.31×10^{-15}	-0.04249	-0.00448
1,5,s	-0.021844	0.142170	0.12397	-1.28824

good approximation for times prior to the beginning of system late-time. It is believed that this is purely a case of luck and does not represent physical reality in most cases. The reason for the reasonably good fit of the SEM system modes is that the modes closest to the modes of the isolated scatterers dominate the response. These system modes are thus similar enough to represent the response of the isolated scatterers for a short time span. It is also important to note that only first layer poles are required to accurately represent the system late-time.

Next consider the case when the wires are separated by $d/l=2.0$ in down range. The SEM modes and normalization constants are listed in Table 3.5. The coupling coefficients and modal fields for the down range separation are shown in Table 3.6. As for all down range separations the antisymmetric modes are dominant. The backscattered field response is shown in Figure 3.32. Again, the SEM modes fail to accurately describe events prior to the start of system late-time.

For completeness, consider the case of cross range separation $d/l=2.0$. The coupling coefficients and modal fields for this case are listed in Table 3.7. The backscattered field response is shown in Figure 3.33. This figure gives a better indication of the inapplicability of the system modes prior to the time where the wires have interacted.

Table 3.5 SEM frequencies and normalization constants for $d/l = 2.00$.

Mode	σ x10^9 np/s	ω x10^9 rad/s	Re{C_n x10^{-6}}	Im{C_n x10^{-6}}
1,1,a	-0.0932	0.9022	-0.00994	0.15252
1,1,s	-0.0584	0.8449	0.05516	0.19512
1,2,a	-0.1309	1.7726	0.08644	0.27371
1,2,s	-0.0984	1.7887	0.05349	0.34251
1,3,a	-0.1433	2.7168	0.07154	0.39778
1,3,s	-0.1397	2.6957	0.12998	0.41144
1,4,a	-0.1613	3.6447	0.12794	0.49951
1,4,s	-0.1657	3.6160	0.17101	0.52845
1,5,a	-0.1827	4.5508	0.17241	0.58681
1,5,s	-0.1794	4.5632	0.11768	0.61886

Table 3.6 Coupling coefficients and modal fields for down range separation ***d/l*** = 2.00.

Mode	Re{A_n}	Re{A_n}	Re{E_n}	Im{E_n}
1,1,a	0.037546	-0.049997	-0.32796	0.429997
1,1,s	-0.064562	0.132913	0.56451	-1.18430
1,2,a	-3.29×10^{-16}	2.58×10^{-16}	2.93×10^{-15}	-2.09×10^{-15}
1,2,s	8.36×10^{-17}	3.19×10^{-16}	-8.35×10^{-16}	-2.68×10^{-15}
1,3,a	0.13674	-0.046731	-1.19751	0.41143
1,3,s	0.11905	-0.152031	-1.03267	1.13636
1,4,a	1.90×10^{-14}	8.82×10^{-14}	-1.67×10^{-13}	-7.77×10^{-13}
1,4,s	-3.42×10^{-14}	-4.39×10^{-14}	3.01×10^{-13}	3.86×10^{-13}
1,5,a	0.22144	0.024776	-1.94584	-0.00036
1,5,s	-0.17575	0.14929	1.52140	-1.35941

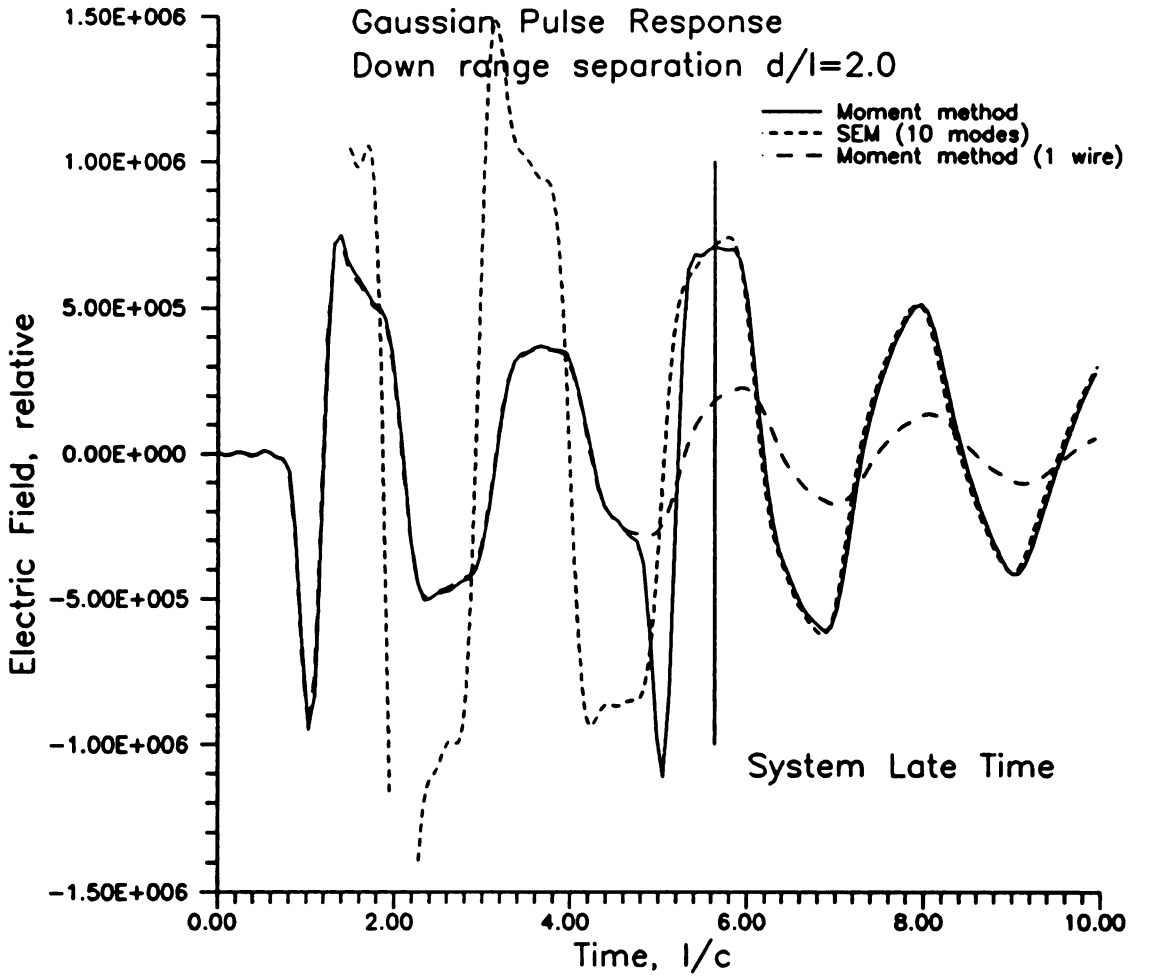

Figure 3.32 Backscattered field response of two identical parallel wires (l/a = 200) separated by d/l = 2.0 in down range.

Table 3.7 Coupling coefficients and modal fields for cross range separation d/l = 2.0.

Mode	$Re\{A_n\}$	$Im\{A_n\}$	$Re\{E_n\}$	$Im\{E_n\}$
1,1,a	3.05×10^{-15}	3.19×10^{-16}	0.035973	0.005850
1,1,s	-0.008085	0.12532	0.036107	-1.12952
1,2,a	2.94×10^{-17}	2.22×10^{-16}	-4.93×10^{-16}	-1.79×10^{-15}
1,2,s	1.18×10^{-16}	1.01×10^{-16}	-1.43×10^{-15}	-7.45×10^{-16}
1,3,a	1.05×10^{-14}	5.46×10^{-16}	0.11914	0.014623
1,3,s	0.003837	-0.11769	-0.074618	1.05670
1,4,a	2.33×10^{-14}	1.49×10^{-14}	-2.38×10^{-13}	-7.15×10^{-14}
1,4,s	-1.63x10-14	2.89×10^{-15}	1.37×10^{-13}	-6.70×10^{-14}
1,5,a	-1.36×10^{-11}	-5.54×10^{-13}	0.19929	0.020386
1,5,s	-0.011935	0.115884	-0.07532	-1.03891

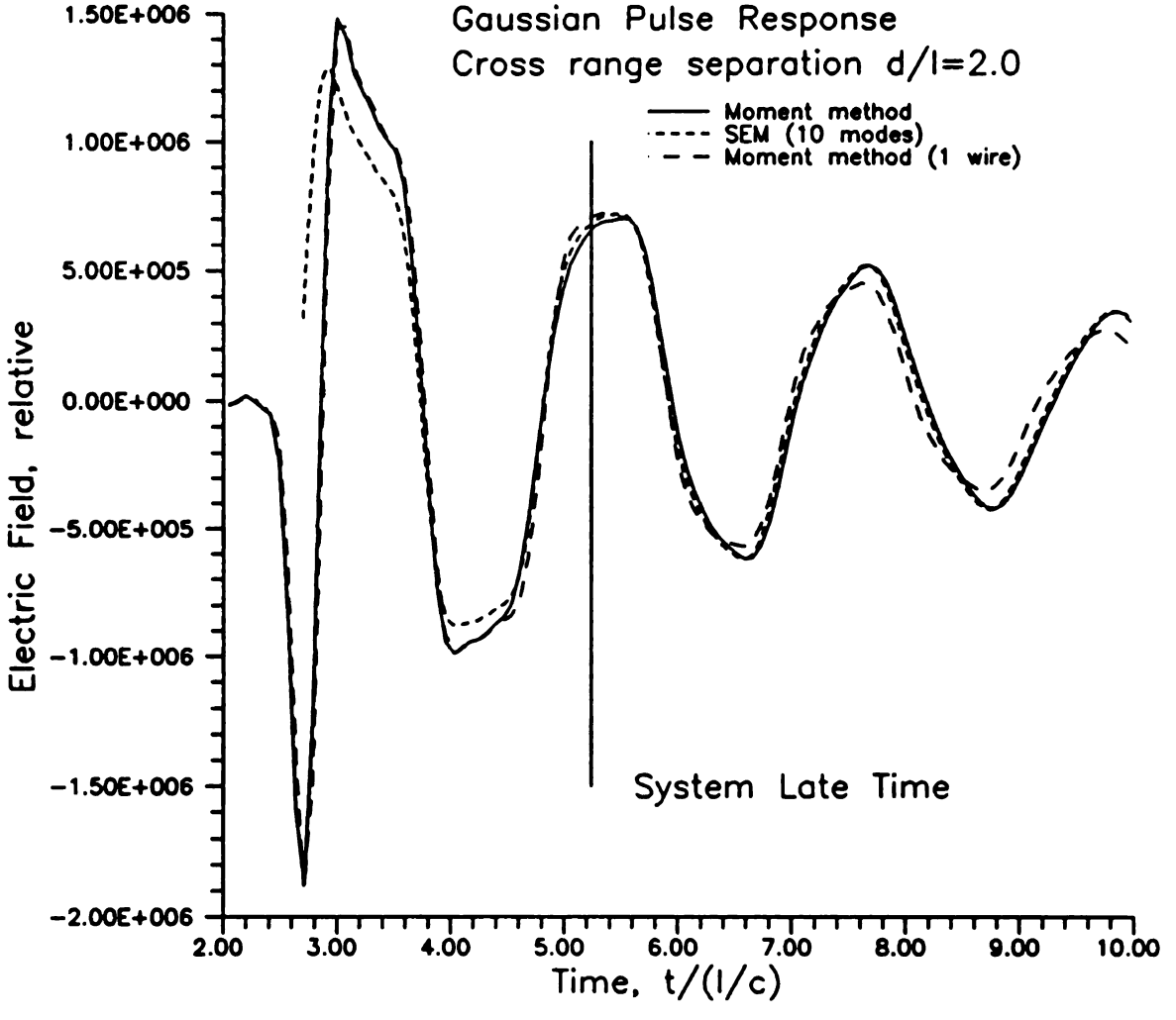

Figure 3.33 Backscattered field response of two identical parallel wires (l/a = 200) separated in cross range (d/l = 2.0).

3.10 Scattered Fields of Two Parallel Wires of Different Length

Another interesting case is backscattering from wires of different length. The case of wires of length 1.00 m and 0.80 m is considered. The wires are parallel and axially separated by 1.00 m. The GMC pulse from the previous section is used to smooth the transient data.

The results for down range separation (the wave strikes the 0.80 m wire first) are shown in Figure 3.34. It is again clear the agreement between the SEM calculation and the moment method are good for times after the pulse has left both targets. For early-time, the SEM mode series does not represent physical reality.

The results for cross range separation are shown in Figure 3.35. Here it is again demonstrated that the Class I expansion in system modes provides a reasonably good fit for times prior to the onset of system late-time even though they strictly do not apply there. Baum has already demonstrated that the Class I series does not converge during this time, however, a limited number of poles may represent approximately over a limited time span the response.

3.11 Summary

This Chapter presents the SEM analysis of coupled wire targets. The variation of the SEM system modes has been studied both from the standpoint of a parameter variation and interpreted using the transient backscatter response. It is seen that as separation distance is increased that the poles spiral about the isolated mode frequency. The poles eventually move to the left away from the isolated mode frequency and are

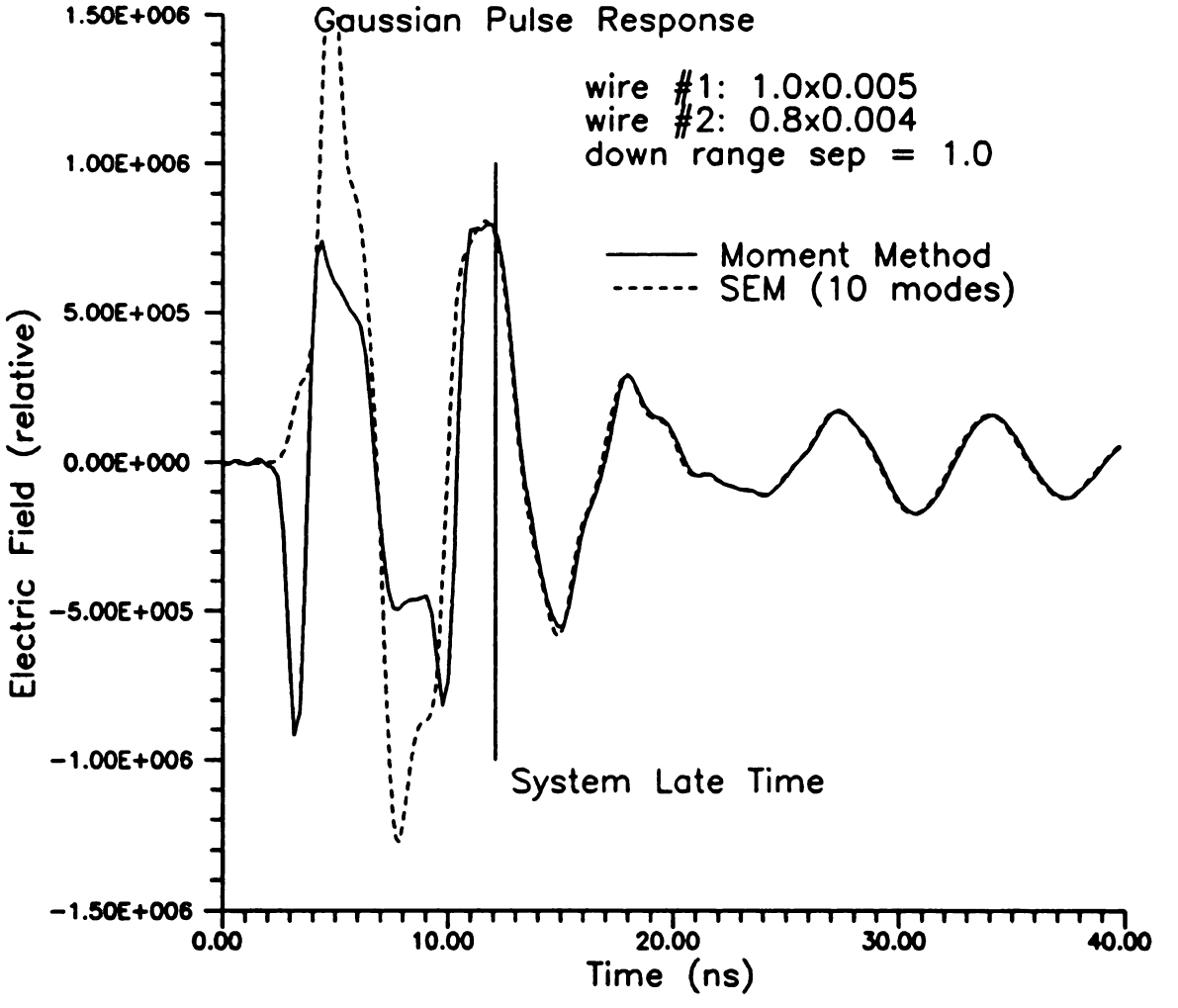

Figure 3.34 Backscatter response of system of two different length wires (1.0m and 0.8m) separated in down range (1.0m).

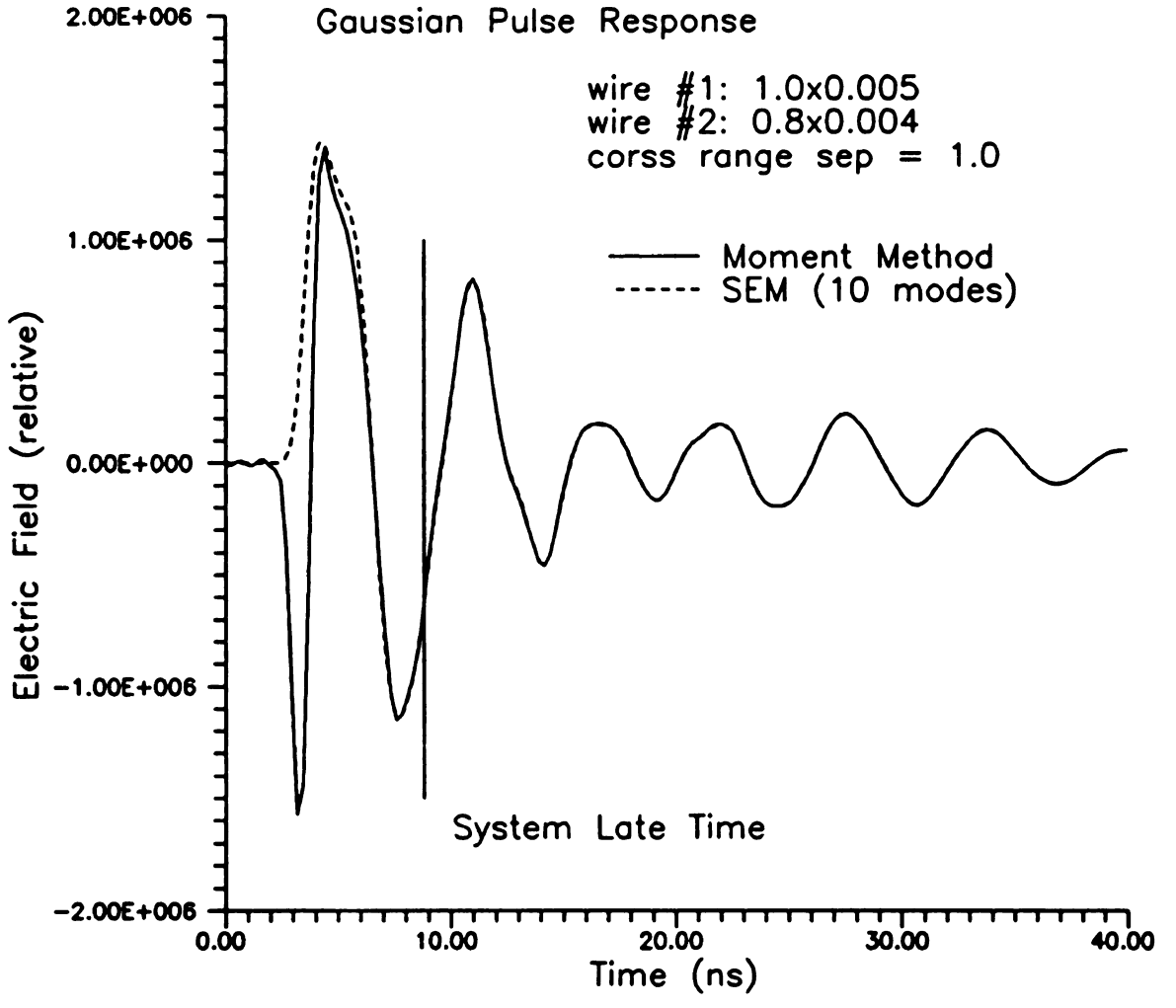

Figure 3.35 Backscatter response of system of different length (1.0m and 0.8m) using SEM and moment method.

replaced by other poles that migrate from the left. The current distribution of the dominant SEM system modes is nearly sinusoidal. It is seen that the current distribution of the second layer poles become more sinusoidal as they migrate toward the poles of the isolated scatterer. These poles dominate the transient response when they are near to the poles of the isolated scatterers. It is demonstrated that the transient response of the system of wires can be represented by the SEM system modes only in the late-time of the system. Some portions of the response of the system prior to the onset of system late-time can be represented by a Class I expansion in the SEM modes of the isolated scatterers. This is an important observation and demonstrates the concept of a sub-resonance which may be useful in discrimination for some classes of targets.

This chapter also presents approximate formulations for the SEM mode frequencies of nearly identical bodies. These approximate methods were shown to provide good results if used within limits imposed by their approximations.

Chapter 4

Discrimination of Coupled Wires

4.1 Introduction

This chapter elaborates on the problem of discrimination using E-pulses and S-pulses in a multiple targets situation as discussed in Chapter 2. The special case of two parallel wires is considered and the discrimination results are interpreted using the physical picture obtained in Chapter 3. The transient scattered field response from two parallel wires is obtained via the inverse Fourier transform of frequency domain moment method calculations as discussed in Chapter 2 and detailed in Appendix A. Since the effect of noise on discrimination has already been investigated in Chapter 2, this chapter deals strictly with noise free data.

4.2 Cross Range Separation

This section describes the application of the E-pulse and S-pulse discrimination method to theoretically generated transient scattering data for a system of two identical parallel wires separated in cross range.

To investigate the effect of coupling on discrimination, the response of a system of two identical parallel 1.0m wires ($l/a=200$) is computed for different values of cross range separation distance. These responses are then discriminated using 9 different E-pulses constructed for isolated wires of lengths 0.80m, 0.85m, 0.90m, 0.95m, 1.00m,

1.05m, 1.10m, 1.15m, 1.20m. The l/a is chosen as 200 for each of the isolated wires. Note that in this analysis the discrimination process assumes that there is only one target present. Thus, the start of late-time is estimated based only on the maximal two-way transit times of the wires. The EDR values obtained for various values of separation distance are shown in Figure 4.1. It can be seen from this graph that the discrimination levels are a function of the separation distance. More importantly, the discrimination method gives the wrong result for some values of separation distance. As a reminder, the target with an EDR of zero is the target selected by the discrimination procedure. To more clearly show this effect, the EDR values of wires of length 0.95m, 1.00m, and 1.05m are shown in Figure 4.2. In this figure it is seen that for $d/l < 0.3$, the 1.05m wire is incorrectly chosen since the EDR for the 1.05m wire E-pulse is zero. The 0.95m and 1.05m wire E-pulses however provide small EDR values. When the separation distance is between 0.3 and 0.6 the 1.00m wire is correctly chosen. When the separation distance is between 0.7 and 1.3, the 0.95m wire is chosen as the correct target. To interpret these results it is useful to refer to Figure 3.16. This figure shows the variation of the radian frequency of the symmetric system mode as a function of separation distance. It is clear that for d/l between 0.7 and 1.3 that the frequency of this mode is significantly higher than the frequency used for constructing the 1.00m E-pulse. In fact, these frequencies are very nearly the same as the ones used for the 0.95m E-pulse. Moreover, for $d/l < 0.3$, the frequencies are closer to those of the 1.05m wire than the 1.00m wire. While for d/l in the 0.3 to 0.7 range, the radian frequency of the system of wires is similar to the 1.00m wire and the discrimination process selects the 1.00m wire as the correct target. Thus, oscillations of the system mode frequency about the mode of

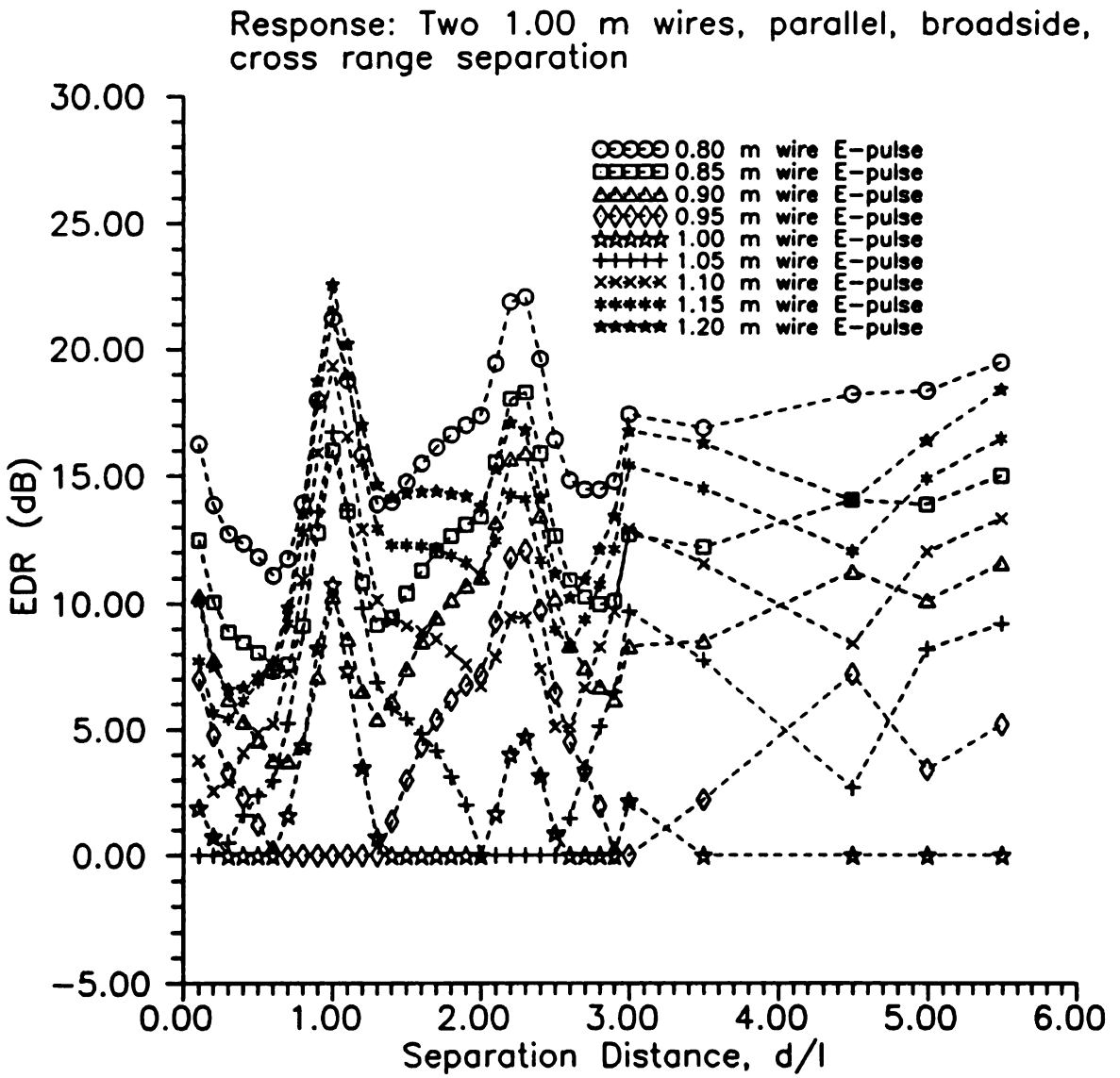

Figure 4.1 Variation of EDR vs cross range separation distance for two parallel 1.00 m wires (l/a=200).

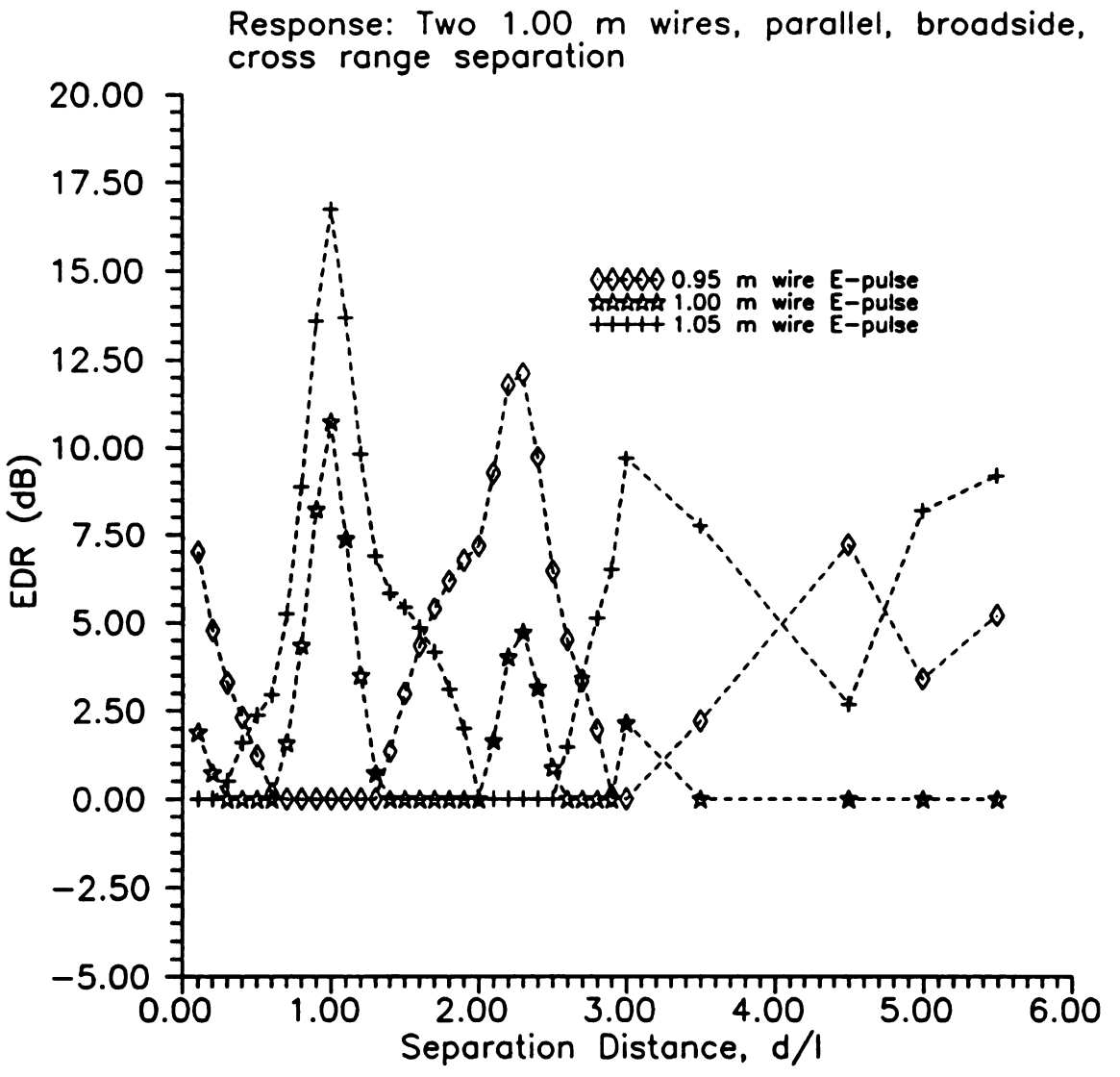

Figure 4.2 Variation of EDR vs cross range separation distance two parallel 1.0m wires (l/a=200).

the isolated 1.00m wire natural frequency result in the discrimination procedure incorrectly identifying the target. The results shown in Figure 4.3 illustrate that the first mode S-pulse is affected in the same manner as the E-pulse. Thus, coupling between identical parallel wires separated in only in cross range causes the response to appear similar to that of wires that are approximately 5% different. This causes the both the E-pulse and S-pulse discrimination scheme to fail for some values of separation distance and reduces the discrimination levels for most values of separation distance. It is seen that discrimination is still possible even for small separations distances provided that the targets are at least 10% different in length. It is also seen that discrimination improves as the separation distance is increased. The discrimination scheme provides the correct result for most cases for $d/l > 4$ even for wires that are only 5% different in length. It is expected that the discrimination continues to improve as separation distance is increased. This is due to two different effects that were observed in Chapter 3. First, as the separation distance is increased the response of the system is dominated by the SEM modes closest to the first layer modes of the isolated scatterer. Secondly, as the separation distance is increased the interactions between wires is sufficiently delayed and the discrimination is effectively performed only on the isolated wire response. If the delay between wire interactions is larger than the observation window W_e, the targets can be considered as isolated as far as the discrimination process is concerned. The simulation performed here used a window duration appropriate for the discrimination of a single wire target. This choice is appropriate if it is not known beforehand that two targets are present. Unfortunately, the observed reduction of discrimination level for the high SNR theoretical data leads to the conclusion that discrimination of similar targets

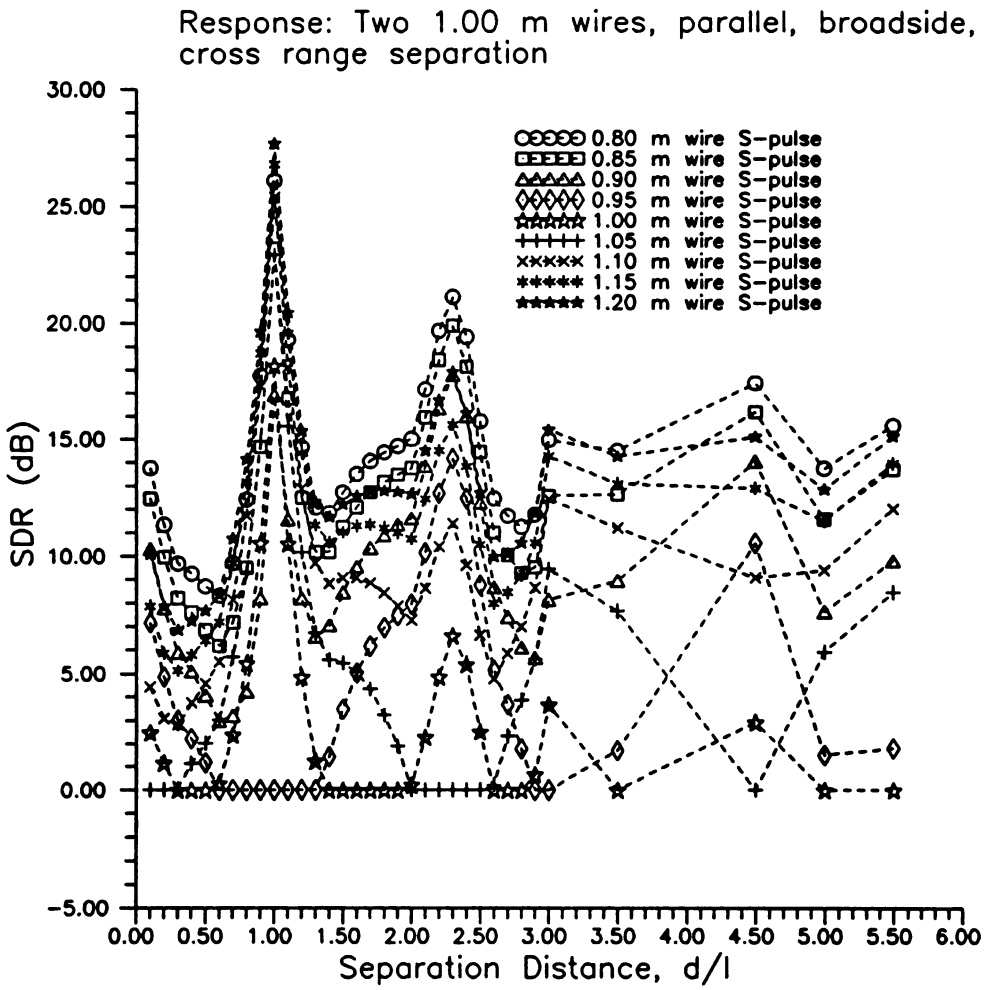

Figure 4.3 Variation of SDR vs cross range separation for two parallel 1.0m wires (l/a=200).

is difficult if there is more than one target and the targets are separated in cross range.

4.3 Down Range Separation

This section considers the case of E-pulse and S-pulse discrimination of two identical parallel wires separated in down range. This case is similar to the time shifting of two wire responses previously discussed in Chapter 2 except the effect of coupling is included to make the analysis more accurate when the targets are not separated by large distances in cross range. This assumption was was required in Chapter 2 to meet the meet the criteria that the wires are electrically uncoupled.

The effect of coupling on the EDR values for down range separation is shown in Figure 4.4. It is clear in almost all cases that the effectiveness of discrimination is severely degraded for all values of separation distance shown. It is especially unfortunate that the EDR values are severely reduced for close spacing since it was shown previously that discrimination could be accomplished for close spacing in down range provided that the targets were effectively uncoupled by a large cross range separation. Overall, an effect similar to the cross range results are obtained with respect to the variation of the discrimination levels with separation distance. In this case however, the response of the system is dominated by the antisymmetric mode for most values of separation distance. Also, the strong early-time contribution from the second wire tends to obscure the physical picture of the simpler case of cross range separation. The early-time contribution also prevents the discrimination from improving for larger separation distances as was observed for the case of cross range separation. Unfortunately, the S-pulse method yields similar results as evidenced by the plot in Figure 4.5. Thus, for down range separation

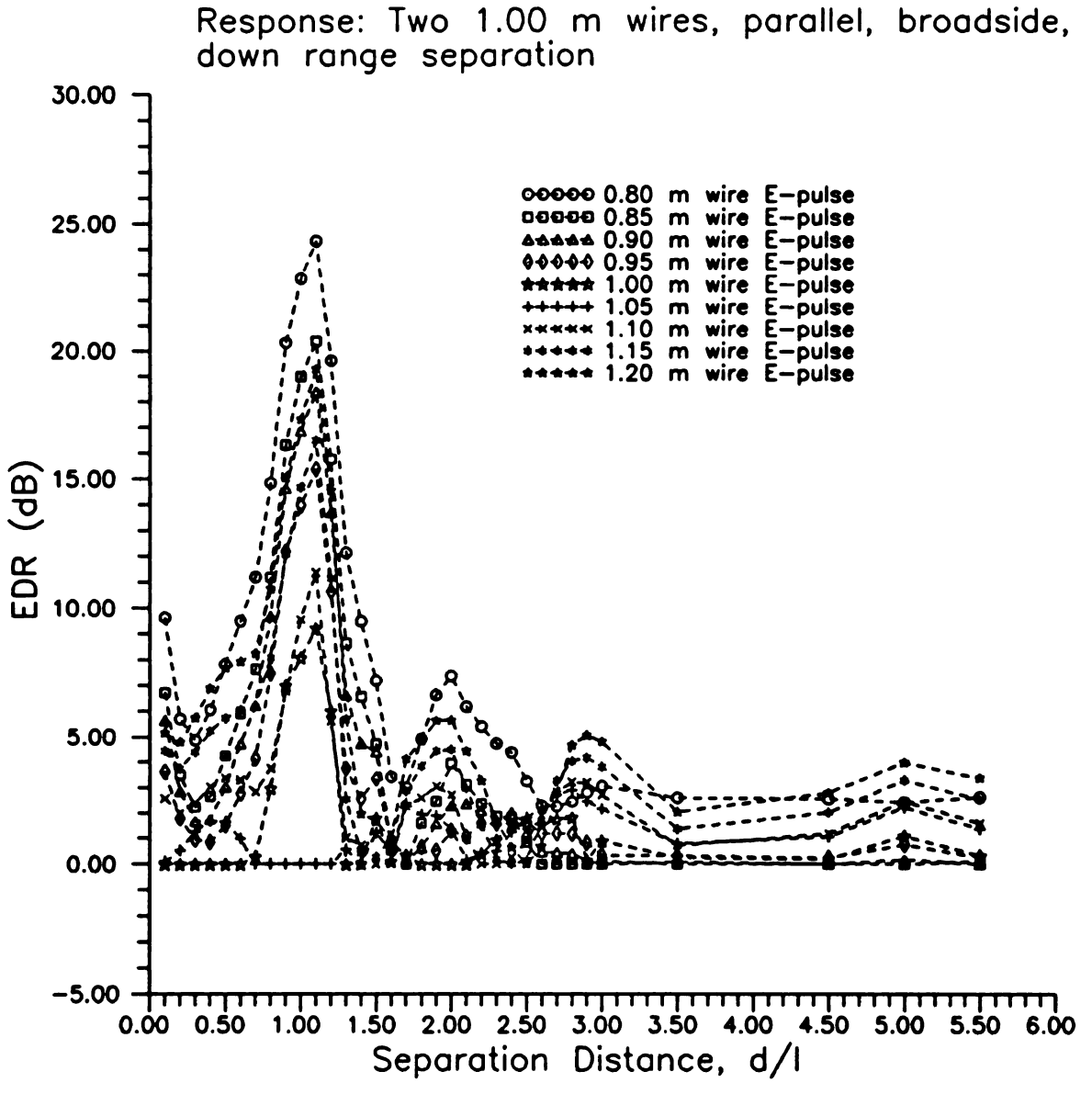

Figure 4.4 Variation of EDR vs down range separation distance for two parallel 1.0m wires (l/a=200).

it is observed that the discrimination is severely degraded for all values of separation distance. For close spacing, the degradation is due only to the effect of coupling, while for greater separation distances, the degradation is primarily due to the presence of the early-time response from the second target. It now seems that an effective countermeasure for the E-pulse and S-pulse methods is to fly aircraft in a close V formation to cause both coupling among aircraft and to intersperse early-time effects into the late-time response of the leading aircraft. This method will probably also be effective even for lower Q targets and targets that are dissimilar since the principle of corrupting the late-time response with early-time data will still be present.

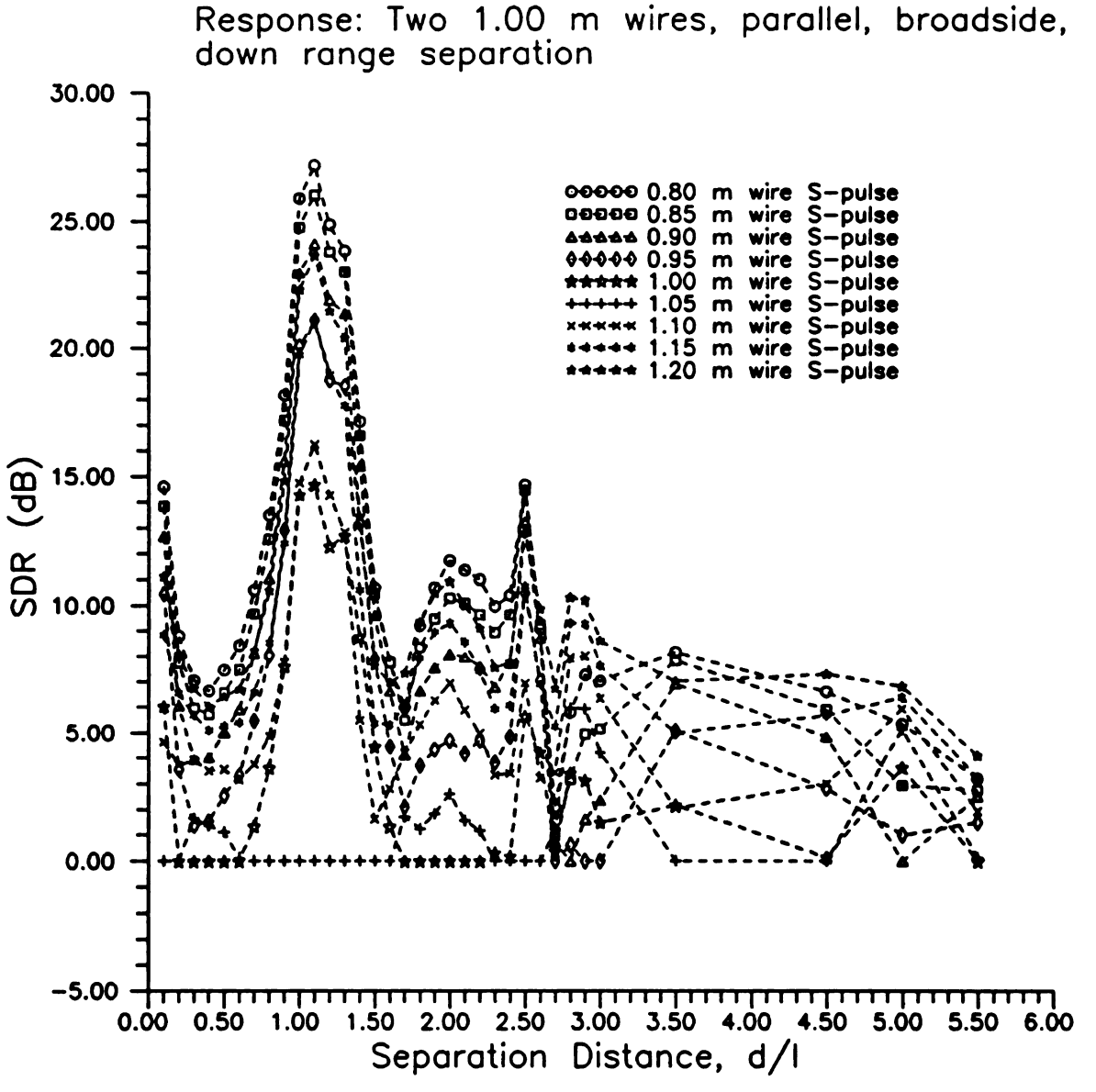

Figure 4.5 Variation of SDR vs down range separation distance for two parallel 1.0m wires (l/a=200).

Chapter 5

Transient Measurements

5.1 Introduction

As discussed previously, accurate measurement of the late-time portion of the transient response of a complicated scatterer is essential for implementation of the E/S-pulse discrimination method. Extraction of complex modal frequencies from measured data with good accuracy is difficult [9]. There have been many papers written concerning mode extraction and spectral estimation. The performance of all extraction methods is degraded with the addition of random noise to the desired waveform. Typically, signal-to-noise ratios on the order of 10 to 15 dB are required for accurate mode extraction. Transient measurements of this quality are difficult to achieve for the ten-to-one bandwidth desired. It has been shown that mode extraction is sensitive to additive random noise [9], but qualitative assessment of the effect of other types of systematic errors in the data have not been performed. However, it is safe to surmise that the effects of non-random noise and distortion of the measured waveform may be detrimental to the accuracy of the mode extraction. Usually, the performance degradation manifests itself in the shifting of the extracted modal frequencies from their true values and the addition of extraneous non-physical modes induced by the measurement system or extraction procedure. The extraneous modes prevent accurate extraction of target modes.

Extraneous modes are especially troublesome when the extraction procedure requires an initial guess as to the number of actual modes contained in the data.

The early-time portion of the transient response is receiving more attention for use in detection and target identification. Analysis of the early-time response of complicated targets using current theoretical and numerical models is difficult and time consuming despite the advanced computer technology available today. Thus, the accurate measurement of the early-time response of a target is important for the advancement of any early-time detection or discrimination schemes using complicated targets. The capability to make accurate transient measurements is also necessary in the verification of current and future numerical models.

This chapter describes two different schemes for performing transient measurements. The first scheme uses traditional time domain reflectometry methods while the second scheme uses a Fourier synthesis approach. The advantages and disadvantages of the schemes are discussed. A method of calibration and deconvolution of the measurement system response is presented along with examples of measured spectral and temporal responses. Characteristics of various calibration targets are discussed. Theoretical expressions for bi-static scattering from a conducting sphere are presented. Examples of scattered field measurements obtained using different methods and calibration standards illustrate the level of fidelity obtainable using different schemes after calibration. The equipment used in the experiments is described in Appendix C.

5.2 Time Domain Systems

Traditionally, transient measurements have been performed directly in the time domain [43,44,45]. The principal component of a time domain system is a wide-band oscilloscope, usually of the digital sampling type. The most important part of the sampling oscilloscope is the sampling head. The rise time specification for the sampling head sets the effective bandwidth of the oscilloscope. The second important component is a very stable pulse generator. The pulse output should be of short duration and have a high peak voltage. The pulse repetition rate should be relatively high to provide good performance. Also required is a wide-band transmitting antenna and a wide-band probe or receiving antenna. The antennas and probes are usually mounted inside an anechoic chamber or over a large conducting ground screen. An example of a time domain measurement system using separate receive and transmit antennas inside an anechoic chamber is shown in Figure 5.1. Recently, the performance of anechoic chamber systems have been enhanced by using several transmit antennas along with power dividers and amplifiers [46]. Methods such as these increase the usable bandwidth and signal-to-noise-ratio of the system. It is also possible to construct a time domain system that uses a single antenna for both transmit and receive as shown in Figure 5.2. However, the unavailability of suitable wide-band circulators limits the usefulness of this approach. A version of this one antenna system was tested during this research. A wide-band (0.5-1.5 GHz) 20 dB directional coupler was used in place of the circulator. The results were disappointing due to the attenuation and distortion induced by the coupler. The use of a wide-band transmit-receive switch in place of the circulator would also be possible, but, the author has not tested this configuration.

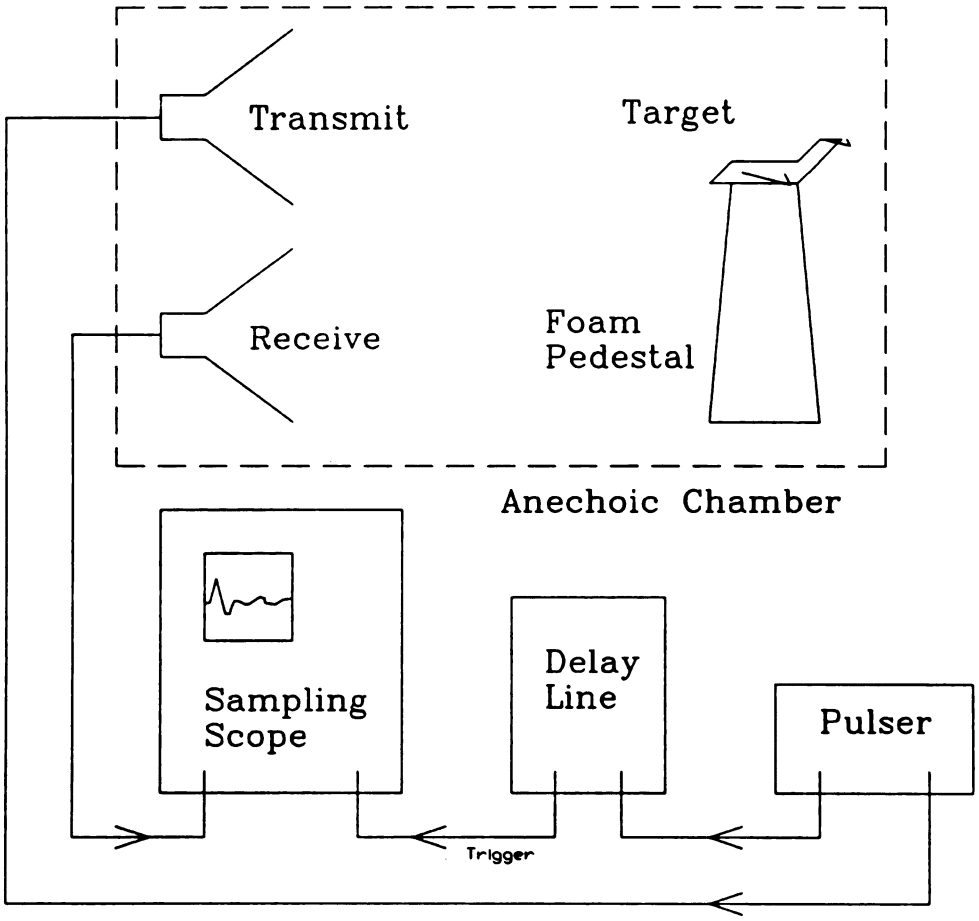

Figure 5.1 Dual antenna free-field time domain transient measurement system.

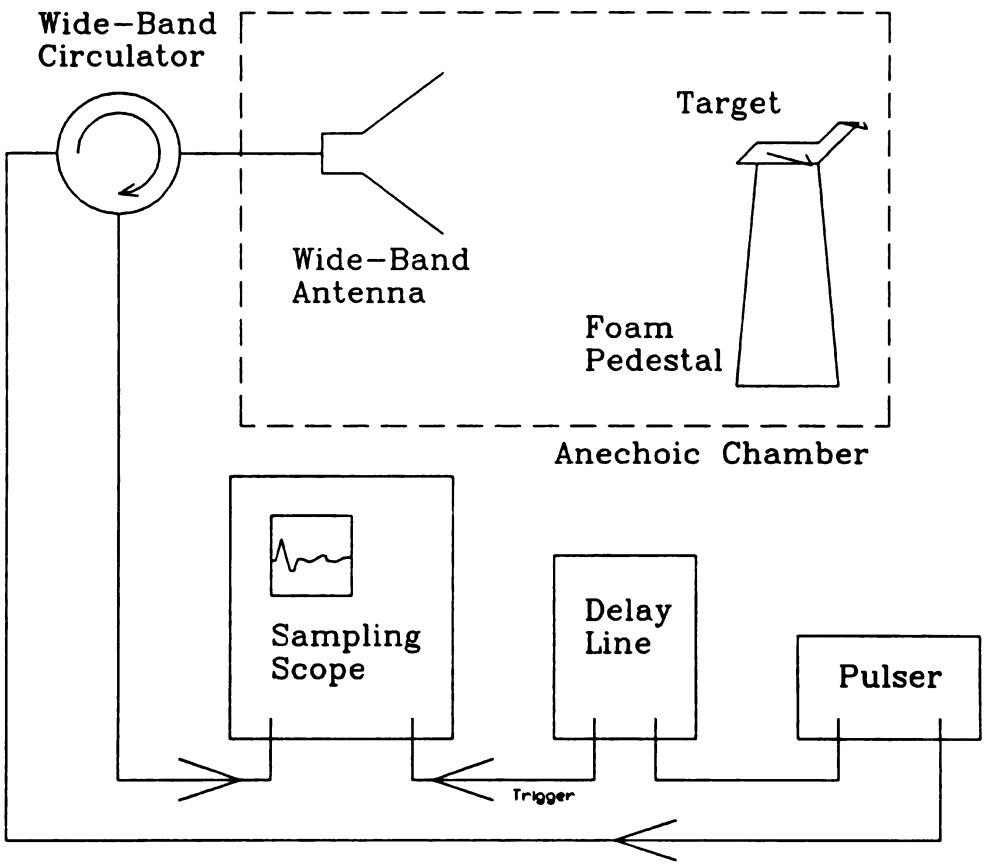

Figure 5.2 Single antenna free-field time domain transient measurement system.

Direct time domain transient measurements have several inherent advantages over continuous wave measurements. The most important advantages are associated with time gating and the speed of the measurements. Time domain systems have the ability to easily reject extraneous reflections. Common sources of these extraneous reflections are the walls of the anechoic chamber, the antenna support structures, and the edges of the ground screen. The extraneous reflections can only be gated out if the measurement system has been properly designed and the target has been properly placed.

Another advantage of the time domain system is that the measurements are direct. In some modern ultra wide-band oscilloscopes the waveform is recorded completely and instantaneously after transmitting only one pulse. This type of measurement has no limitations concerning the linearity and/or time invariance of the target. Digital sampling oscilloscopes require transmission of several hundred pulses to acquire a waveform. This requirement still allows for non-linearities in the target, but the target must not change position or size within the waveform acquisition time. Digital averaging of many waveforms is usually employed to reduce random noise in the final measurement. Averaging requires more time but the process is still relatively fast. Typically, a 512 point waveform using 100 waveform averages is acquired in under 30 seconds with the Michigan State University system.

Unfortunately, time domain systems also suffer from several inherent disadvantages. The most important limitations being limited dynamic range and stability. Most waveform processing oscilloscopes measure the voltage in discrete steps with an analog-to-digital (A-D) converter. The finite word size used in A-D converters leads to truncation error. An A-D converter with N bits can represent 2^N different voltage values.

Assuming a uniform digitization, the measurement cannot be more accurate than one part in 2^N. This leads to a dynamic range of 2^N. A 10 bit converter provides about 30 dB dynamic range. This is not very good if a deconvolution procedure, as described later, is to be employed. It should be noted that waveform averaging can be employed to extend the dynamic range of measurements that are limited by the word length used in the A-D converter. The extent to which averaging can improve scattering measurements depends on the stability of the pulse generator and triggering circuitry.

A problem inherent in all systems, but particularly troublesome in time domain measurement systems, is equipment stability. Stability of the oscilloscope and pulse generator is limited. Slight variations in pulse generator output and noise in the time base circuitry of the oscilloscope lead to timing jitter. The overall effect is to produce a slight time shift from one measurement to another. In situations where the background clutter must be subtracted from the target measurement this effect induces a systematic error that is approximately proportional to the derivative of the background clutter. For systems where the clutter is large this causes great difficulty with mode extraction.

For cases where the time domain system is not located in a sealed anechoic chamber there is a problem of reception of extraneous signals. The wide bandwidth required for good fidelity in the transient measurement unfortunately provides equally good fidelity for reception of television, radio, computer emissions and other types of undesired signals. This characteristic of time domain systems limits their effectiveness if there is insufficient transmitter power. In the case of the transient scattering range at Michigan State University, the extraneous signals do not seem to be significant since it is located inside a metal building.

Finally, the shape of the pulse waveform is not adjustable in most time domain systems. The effectiveness of short pulses from the generator is usually limited by the relatively long duration of the system impulse response. The calibration and deconvolution scheme described later can be employed to eliminate this distortion. However, the stability, dynamic range, and pulse bandwidth of most time domain systems are usually insufficient to effectively use this scheme.

5.3 Frequency Domain Systems

Recently, the application of computer control to high quality solid state microwave equipment has resulted in a new generation of automated vector network analyzers. Vector network analyzers are capable of measuring both the magnitude and phase of the S-parameters of two port networks over a very wide frequency range. This capability gives the vector network analyzer the ability to synthesize the transient response of a target via the inverse discrete Fourier transform. The extremely wide dynamic range of vector network analyzers allows frequency domain deconvolution of the transmit-receive system response from the target measurement with good results. The wide frequency sweep allows for synthesis of very short duration pulses provided the deconvolution procedure is done accurately. A typical free-field dual antenna frequency domain measurement system using a network analyzer is shown in Figure 5.3. With a dual antenna configuration, the transmit port is chosen as port 1 and the received signal is directed into port 2 of the analyzer. A measurement of S_{21} then provides a measure of scattering from port 1 to port 2 from both the scatterer and the environment. The measurement parameter S_{12} can be selected to reverse the situation. This is useful for bi-

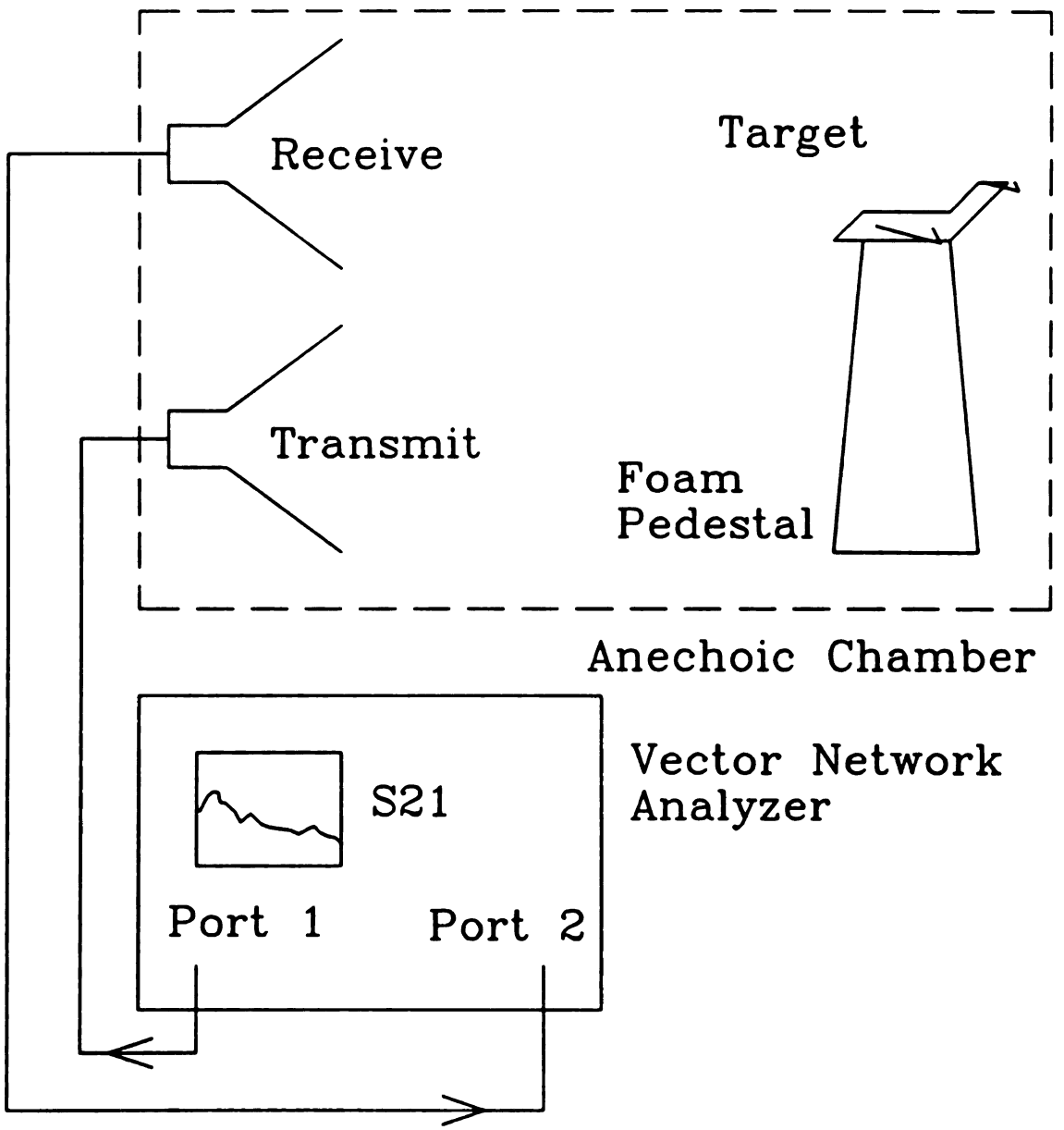

Figure 5.3 Dual antenna free-field frequency domain transient measurement system.

static measurements since the target can be positioned once and two different illumination angles obtained. In a dual antenna configuration amplifiers can be added to both the transmit and receive channels to help boost the dynamic range of the measurements. Of course, this results in the loss of the bi-static advantage. Some researchers have also added a frequency up-converter on the transmit channel and a reciprocal frequency down-converter on the receive channel to increase the bandwidth of the network analyzer systems into the millimeter-wave portion of the spectrum [47]. Such additions provide range resolution for narrow band remote sensing applications but have yet to be used in ultra-wide band measurements.

A frequency domain transient scattering system employing the network analyzer and a single antenna for both transmit and receive is shown in Figure 5.4. Here, port 1 of the analyzer is connected to the antenna without using any amplifier stages. By measuring S_{11}, the reflection from the target can be made with a single antenna. A single antenna system is very attractive since one is usually interested in a backscatter measurement which is difficult to approximate in small anechoic chambers with two antennas. Further, the interactions of a two antenna system are much greater than a single antenna system. Unfortunately, the use of a single antenna system is limited by the large reflections that occur within the antenna itself. The scattered field due to a target only a few meters away is usually many dB lower than the antenna feed point reflection. The target component is actually beyond the measurement accuracy of the network analyzer for the TEM horns used in the MSU system in most instances.

There are several limitations to the use of a network analyzer for transient measurements. The first limitation is characteristic of all frequency domain systems. The

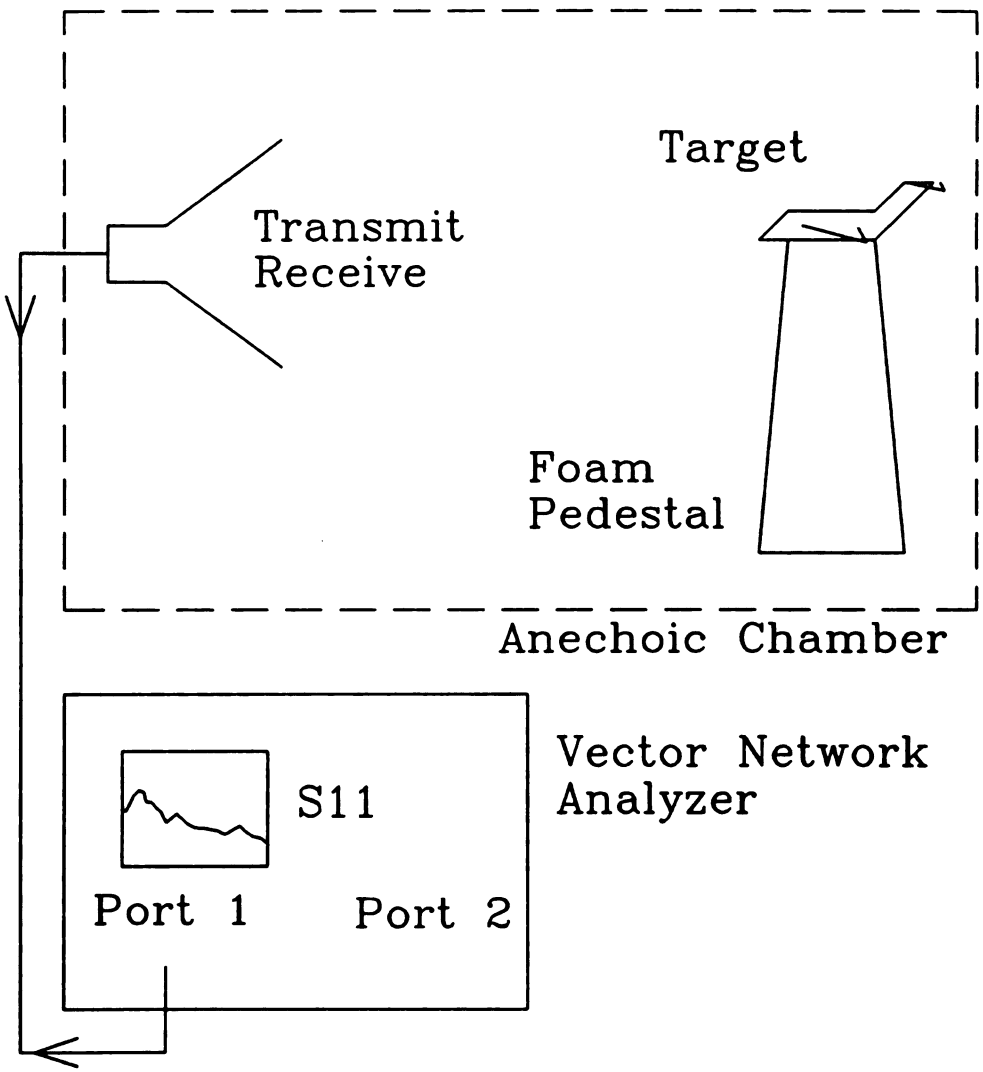

Figure 5.4 Single antenna free-field frequency domain transient measurement system.

target must be linear and time invariant for the inverse transform of the frequency domain measurements to represent the actual transient response. The second limitation is due to limitations of the equipment typically available. The measurement of the S-parameter at several hundred different frequencies takes slightly longer than the time domain systems. Typically, the time required to measure 401 frequency points between 400 Mhz and 4.4 Ghz with an averaging factor of 10 and an IF bandwidth set to 30 Hz is about 2.5 minutes. Finally, the use of time gating, while still allowed is somewhat limited.

To synthesize the transient response from data measured in the frequency domain care must be used in selecting the number of points N, and the bandwidth B, used in the measurement. Of fundamental importance is the sampling rate of the frequency domain measurement f_s

$$f_s = \frac{N-1}{B} \quad . \tag{5.1}$$

To use the frequency domain approach all transient events must be diminished to the noise level within a duration equal to the sampling rate f_s. Otherwise, transient events that occur after $t = f_s$ overlaps onto the responses at $t = t - m f_s$, where m is an integer. This effect is referred to as alaising and is well understood in the usual sense of sampling a band limited signal in the time domain where the sampling rate must larger than twice the highest frequency contained in the signal.

This sampling interval constraint limits the use of the network analyzer system when the antennas are not inside an anechoic chamber. This is one of the reasons that attempts to use a single antenna system employing the conical antenna on the MSU

ground screen were not successful. The reflections from the edges of the ground screen and the laboratory ceiling caused alaising.

It should be noted that just as the time domain system allows direct gating of the extraneous reflections, the frequency domain system allows gating of extraneous frequency components from the measurement. This may seem of little consequence until one realizes that some of the strongest signals received in the time domain system are due to frequency components are contaminated from multi-path effects or are merely direct antenna-to-antenna coupling. In time domain systems, the oscilloscope vertical amplifier gain must be set to prevent clipping of these large undesired signal components. This results in fewer bits of resolution for the smaller desired signal components and reduces the dynamic range.

5.4 Calibration Procedure

To take full advantage of the pulse bandwidth of a time domain system or the wide frequency sweep available with a network analyzer, the clutter and system transfer function must be removed from the measurement. There are many methods for deconvolution in the literature, but the process is in general very sensitive to noise and somewhat ill-conditioned [48]. Thus, to make effective use of deconvolution, the original data must be as accurate and noise free as possible. If the signals are measured in the time domain, deconvolution can be performed directly in the time domain if the system impulse response is known [49]. This procedure has been applied in time domain systems that use a ground screen and a vertical electric field probe.

A method to obtain the system impulse response and perform deconvolution in the frequency domain is detailed in this section. The method is similar to that used by Morgan [45]. The method can be applied to data obtained in the frequency domain or time domain with the obvious limitations incurred in the dynamic range, stability and bandwidth for the case of the time domain system. It is assumed throughout the following development that all data is sampled and discrete transforms are implied.

The objective of any calibration procedure is to determine and remove any repeatable systematic errors from the raw measurement. In the case of transient measurement systems these errors are associated with anechoic chamber clutter, antennas, transmission lines, and probes as shown in Figure 5.5. The first step in the calibration procedure is to measure the empty chamber or ground plane. This is called the background measurement and can be modeled by

$$R^b(f) = S(f)\{H_a(f)+H_c(f)\} + N^b(f) \tag{5.2}$$

Here $H_a(f)$ models the transfer function of the direct coupling from the transmit antenna to the receive antenna, $H_c(f)$ models the transfer function of the coupling from the transmit antenna to receive antenna via the anechoic chamber, antenna supports, and target mount. $N^b(f)$ is random noise and $S(f)$ is the system transfer function

$$S(f) = H_r(f)\,H_t(f)\,E(f) \tag{5.3}$$

where $H_r(f)$ and $H_t(f)$ are the transfer functions of the receive and transmit antennas from the transmission line into the free-field environment while $E(f)$ represents the spectral content of the pulse or CW source. The next step is to measure a known calibration target. Calibration targets are discussed more extensively in the next section. The

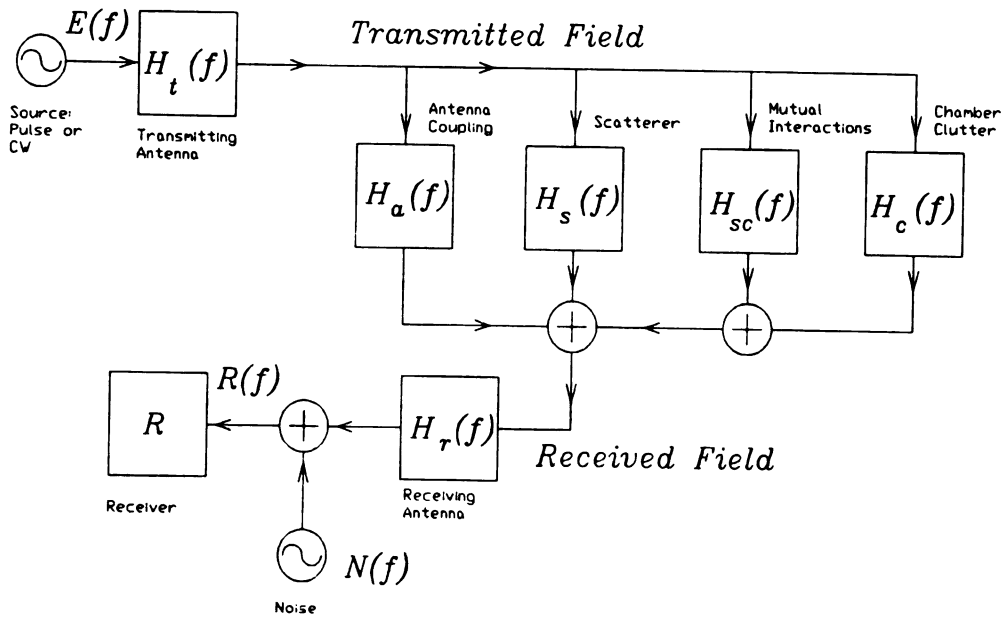

Figure 5.5 Measurement system block diagram.

calibration target measurement gives

$$R^{c+b}(f) = S(f)\{H_a(f) + H_c(f) + H_s^c(f) + H_{sc}^c(f)\} + N^{c+b}(f) \tag{5.4}$$

where $N^{c+b}(f)$ is random noise, $H_s^c(f)$ is the transfer function of the calibrator target which is assumed to be known, and $H_{sc}^c(f)$ is the transfer function of the interaction of the calibration target with the anechoic chamber. Note that the interaction term is causal in the time domain; it cannot not occur prior to the time required for the wave scattered from the target to reach the chamber walls and return to the receive antenna. Note also that the interaction term is represented here as an additive effect.

The next step is to measure the desired target, giving

$$R^{t+b}(f) = S(f)\{H_a(f) + H_c(f) + H_s^t(f) + H_{sc}^t(f)\} + N^{t+b}(f) \tag{5.5}$$

where $N^{t+b}(f)$ is random noise, $H_s^t(f)$ is the transfer function of the unknown target and $H_{SC}^T(f)$ is the transfer function due to the interaction of the unknown target with the anechoic chamber. Again, this term is causal in the time domain.

Next, the background measurement is subtracted from the measurement of the calibration target and the unknown target. Note that in actual practice, the background is measured more than once and the subtraction is performed immediately in the oscilloscope or in the computer just prior to saving the raw data to disk. Measuring the background and performing the subtraction for each measurement in this fashion reduces the time between measurements and minimizes the effect of equipment instabilities. Subtracting gives

$$\begin{aligned} R^c(f) &= R^{c+b}(f) - R^b(f) \\ R^t(f) &= R^{t+b}(f) - R^b(f) \end{aligned} \tag{5.6}$$

The clutter free calibration and desired target measurements are thus obtained:

$$\begin{aligned} R^c(f) &= S(f)\{H_s^c(f) + H_{sc}^c(f)\} + N^c(f) \\ R^t(f) &= S(f)\{H_s^t(f) + H_{sc}^t(f)\} + N^t(f) \end{aligned} \tag{5.7}$$

The noise terms are as

$$\begin{aligned} N^c(f) &= N^{c+b}(f) - N^b(f) \\ N_t(f) &= N^{t+b}(f) - N^b(f) \end{aligned} \tag{5.8}$$

The next step in the calibration depends on the quality of the anechoic chamber. If the anechoic chamber is of very high quality, then the interaction terms are small and can be neglected along with the noise terms giving

$$\begin{aligned} R^c(f) &= S(f) H_s^c(f) \\ R^t(f) &= S(f) H_s^t(f) \end{aligned} \tag{5.9}$$

Now, solving for $S(f)$ in terms of the known calibration target transfer function gives

$$S(f) = \frac{R^c(f)}{H_s^c(f)} \tag{5.10}$$

Next, computing the unknown target transfer function leads to

$$H_s^t(f) = \frac{R^t(f)}{S(f)} \tag{5.11}$$

For anechoic chambers of lesser quality, the interactions terms can be too large to be neglected. To solve this problem, $R^c(f)$ can be transformed to the time domain and windowing can be used to eliminate any interaction terms that are sufficiently delayed beyond the end of the calibration target response. To help visualize the response of the calibration target and the interaction terms in time refer to Figure 5.6. Again the noise terms are neglected.

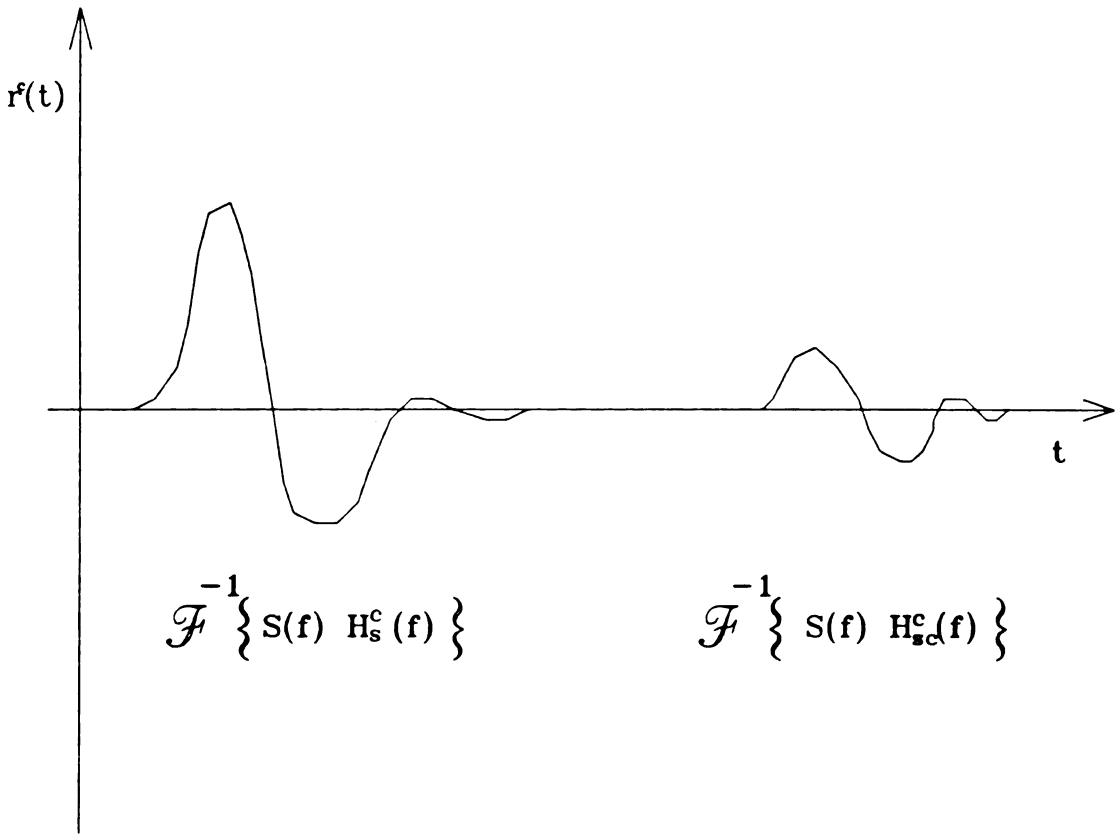

Figure 5.6 Temporal response of clutter-free calibration target measurement.

Define the time response of the calibration measurement as

$$r^c(t) = \mathcal{F}^{-1}\{R^c(f)\} \tag{5.12}$$

Multiply by a window function $w(t)$ to exclude interaction terms

$$r^{cw}(t) = r^c(t)\, w(t) \tag{5.13}$$

If $w(t)$ is defined properly (all of the interaction terms are excluded), and if $\mathcal{F}^{-1}\{S(f)H_s^c(f)\}$ is approximately time limited and not truncated by the window function the following approximation is valid:

$$R^{cw}(f) = S(f)H_s^c(f) \tag{5.14}$$

where $R^{cw}(f) = \mathcal{F}\{r^{cw}(t)\}$. Then, the system transfer function $S(f)$ can be obtained as

$$S(f) = \frac{R^{cw}(f)}{H_s^c(f)} \tag{5.15}$$

Thus, from (5.6)

$$H_s^t(f) + H_{sc}^t(f) = \frac{R^t(f)}{S(f)} \tag{5.16}$$

Finally to isolate $H_s^t(f)$ the inverse Fourier transform is applied to obtain

$$H_s^t(t) + H_{sc}^t(t) = \mathcal{F}^{-1}\left\{\frac{R^t(f)}{S(f)}\right\} \tag{5.17}$$

If the target impulse response is approximately time limited, and the interaction term is causal and delayed beyond the end of the target impulse response, then the target impulse response can be isolated using time gating as before.

5.5 Weighting Functions

Before moving on to other topics, the subject of weighting functions and FFT's must be addressed. Weighting functions are used to eliminate the effect an edge discontinuity has on a spectrum or time response after transformation. It is not the purpose of this work to expound upon all possible weighting functions. It is important to be aware of what effect the choice of weighting function has on the outcome of the calibration. The choice of weighting function is subjective and varies according to the emphasis of the data.

For this research three weighting functions were used extensively. The most often used weighting function was the rectangle function. This function is well known and was used primarily to eliminate interaction terms from the calibration measurement. The second function used was the Gaussian Modulated Cosine (GMC). This weighting function is versatile since the center frequency and spectral width can be adjusted independently. The GMC waveform is given by

$$w_{gc}(t) = \cos(\pi f_c) \exp(-\pi(t/\tau)^2) \tag{5.18}$$

and its corresponding spectrum is

$$W_{gc}(f) = \tau \{\exp(-\pi(f-f_c)\tau^2) + \exp(-\pi(f+f_c)\tau^2)\} \tag{5.19}$$

where f_c is the frequency of the cosine and τ is the shape factor.

The Double-Gaussian (DG) weighting function was also used in the research. A DG waveform is obtained by adding two Gaussian waveforms with different shape factors and amplitudes. The amplitude factors are usually adjusted to give a waveform with zero mean. The spectral content of the zero DC DG waveform is

$$W_{dg}(f) = \sqrt{\frac{\pi}{\alpha_1}}\, a_1 \exp(-\frac{(\pi f)^2}{\alpha_1}) - \sqrt{\frac{\pi}{\alpha_2}}\, a_2 \exp(-\frac{(\pi f)^2}{\alpha_2}) \qquad (5.20)$$

where

$$\alpha_1 = \frac{\pi}{\tau_1^2} \qquad \alpha_2 = \frac{\pi}{\tau_2^2} \qquad (5.21)$$

and

$$a_1 = \frac{\sqrt{\alpha_1}}{\sqrt{\alpha_1} - \sqrt{\alpha_2}} \qquad a_2 = \frac{\sqrt{\alpha_2}}{\sqrt{\alpha_1} - \sqrt{\alpha_2}} \qquad (5.22)$$

The spectrum of the DG waveform used most often in the dissertation research is shown in Figure 5.7. This spectrum works well for the bandwidths typically used in the low band configuration of the frequency domain measurement system. The shape factors used for this research are

$$\tau_1 = 0.25x10^{-9}\ s \qquad \tau_2 = 0.5x10^{-9}\ s \qquad (5.23)$$

The equivalent DG temporal response is shown in Figure 5.8.

5.6 Calibration Targets

There are a number of objects suitable as calibration targets for various applications [50]. A calibration target for a transient measurement system must have a frequency response that is known in both magnitude and phase over a very wide range of frequencies. Ideally, the response is not be a function of aspect angle or highly resonant. The response should be large compared to the clutter to give high signal-to-nose ratios in the calibration measurement. For radars that use the same linear

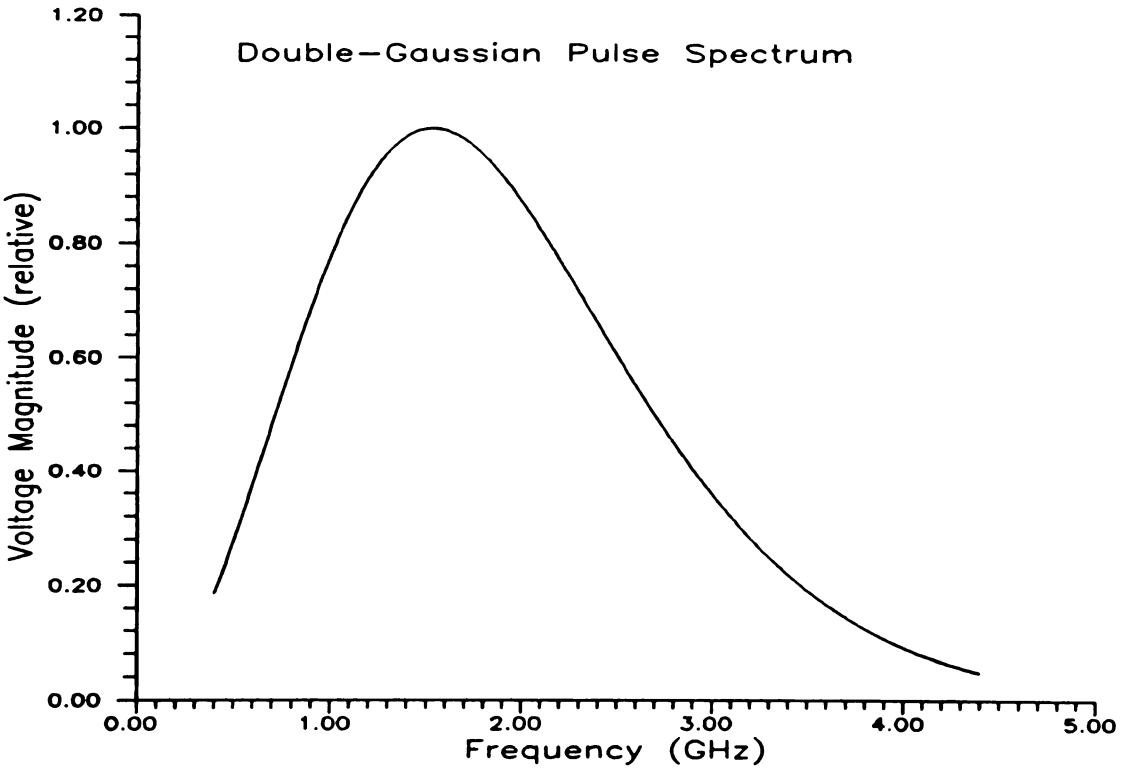

Figure 5.7 Double-Gaussian pulse spectrum.

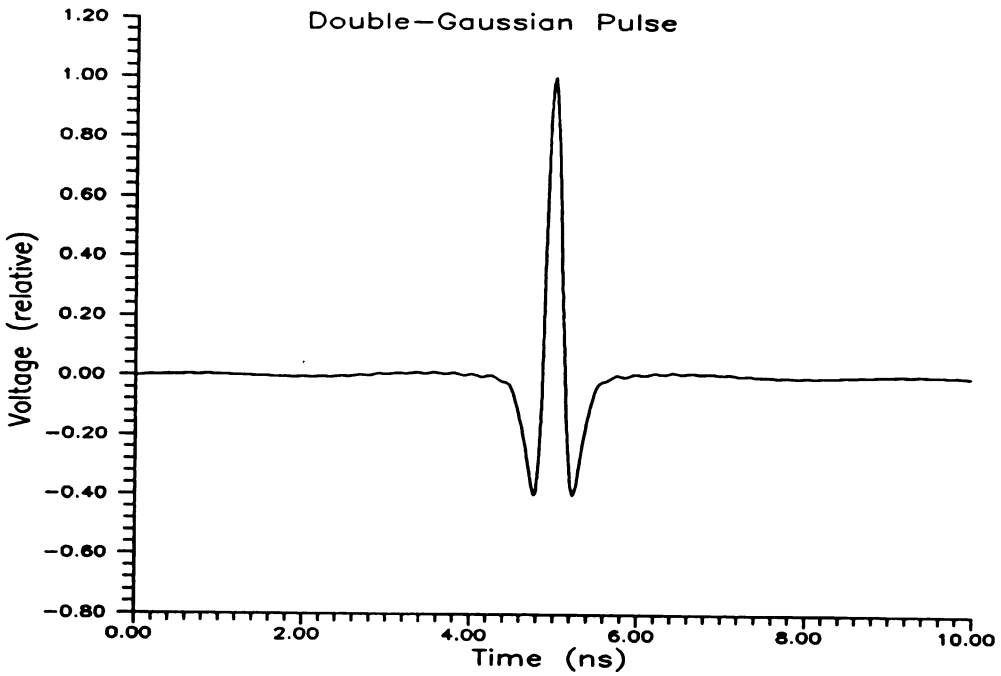

Figure 5.8 Double-Gaussian pulse.

polarization for both transmit and receive, a metal calibration sphere is the most common calibration target. For polarimetric radars, a metal sphere is used for the like polarized components while the cross-polarized components require a target that depolarizes the incident field. Ideally, the target return should provide both horizontal and vertical field components that are approximately the same strength. A common depolarizing target is a thin wire or an array of thin wires oriented at a 45 degree angle with respect to the incident electric field vector. There are other calibration targets in use; however, many of them are suitable only for an amplitude calibration. This is not a problem for (CW) radar cross section (RCS) measurements where phase is not important. However, for time domain systems the phase information is necessary. The metal sphere and thin-wire were used as calibrators in this research and are discussed in this section.

The sphere is a canonical structure in electromagnetics. Scattering from a sphere was first solved by Mie in 1908 [51]. Since then, the analysis of sphere scattering has appeared in many graduate electromagnetics texts such as Stratton [52] and Harrington [53]. The notation used in course notes by Chen [54] is presented here.

Consider a plane electromagnetic wave incident on a perfectly conducting sphere as shown in Figure 5.9. The incident field is assumed to have only an $\hat{x}$ component and is propagating in the $\hat{z}$-direction. Thus

$$\vec{E}^{inc}(\vec{r}) = \hat{x}\, E_0 \exp(-jkz) \tag{5.24}$$

The exact scattered field without far-zone approximations can be written as

$$\vec{E}^{s}(\vec{r}) = -E_0 \sum_{n=1}^{\infty} (-j)^n \frac{2n+1}{n(n+1)} \left\{ a_n \vec{M}_{o1n}^{(4)}(\theta,\phi,R) + j\, b_n \vec{N}_{e1n}^{(4)}(\theta,\phi,R) \right\} \tag{5.25}$$

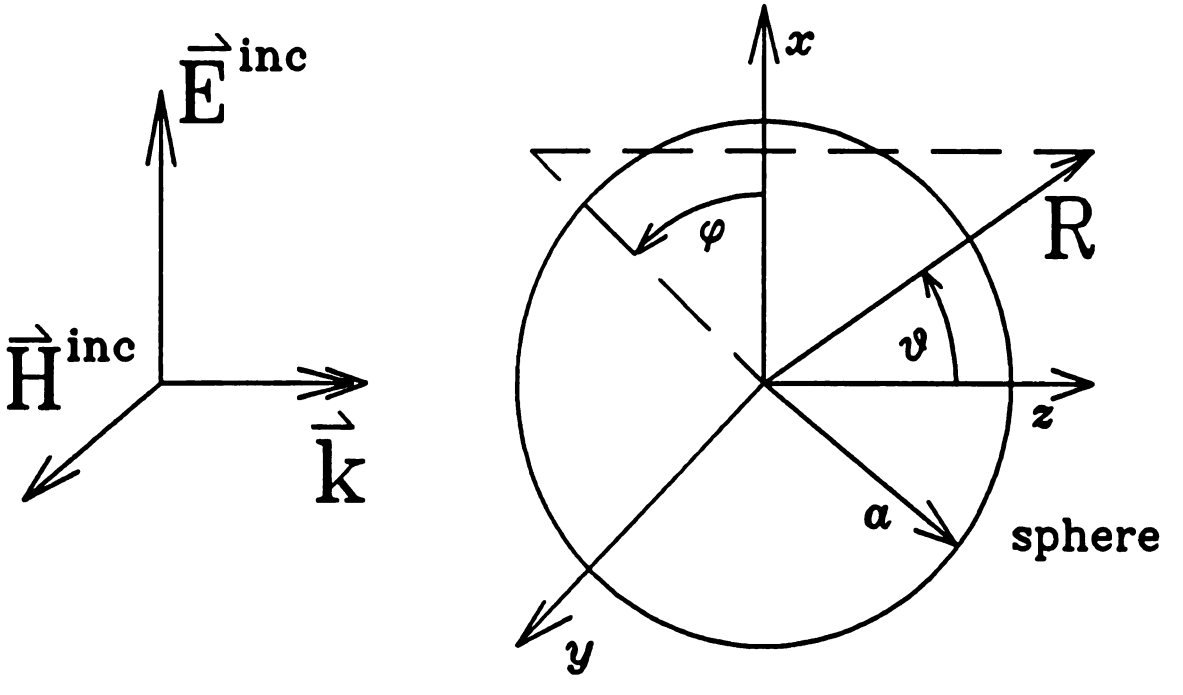

Figure 5.9 Geometry for sphere scattering problem.

where, the spherical vector wave functions are given as

$$\vec{M}^{(i)}_{\substack{e\\o}mn}(\theta,\phi,R) = \mp\frac{m}{\sin\theta} z_n^{(i)}(kR)\, P_n^m(\cos\theta) \begin{Bmatrix}\sin m\phi\\ \cos m\phi\end{Bmatrix} \hat{\theta} - z_n^{(i)}(kR)\left[\frac{\partial}{\partial\theta} P_n^m(\cos\theta)\right]\begin{Bmatrix}\cos m\phi\\ \sin m\phi\end{Bmatrix}\hat{\phi} \tag{5.26}$$

$$\vec{N}^{(i)}_{\substack{e\\o}mn}(\theta,\phi,R) = \frac{n(n+1)}{kR} z_n^{(i)}(kR)\, P_n^m(\cos\theta)\begin{Bmatrix}\cos m\phi\\ \sin m\phi\end{Bmatrix}\hat{R} + \frac{1}{kR}\frac{\partial}{\partial R}\left[R z_n^{(i)}(kR)\right]\left[\frac{\partial}{\partial\theta} P_n^m(\cos\theta)\right]\begin{Bmatrix}\cos m\phi\\ \sin m\phi\end{Bmatrix}\hat{\theta} \pm \frac{m}{kR\sin\theta}\frac{\partial}{\partial R}\left[R z_n^{(i)}(kR)\right] P_n^m(\cos\theta)\begin{Bmatrix}\sin m\phi\\ \cos m\phi\end{Bmatrix}\hat{\phi} \tag{5.27}$$

where $P_n^m(\cos\theta)$ represents the associated Legendre polynomials and the $z_n^{(i)}(kR)$ represents the various kinds of spherical bessel functions.

$$z_n^{(1)}(kR) = j_n(kR), \quad z_n^{(2)}(kR) = y_n(kR)$$
$$z_n^{(3)}(kR) = h_n^{(1)}(kR), \quad z_n^{(4)}(kR) = h_n^{(2)}(kR) \tag{5.28}$$

The spherical wave expansion coefficients are given as

$$a_n = \frac{j_n(ka)}{h_n^{(2)}(ka)} \qquad b_n = \frac{\frac{\partial}{\partial R}(R j_n(kR))|_{R=a}}{\frac{\partial}{\partial R}(R h_n^{(2)}(kR))|_{R=a}} \tag{5.29}$$

The spherical vector wave functions can be approximated in the far-zone ($kR >> 1$) as

$$\vec{M}^{(4)}_{oln}(\theta,\phi,R) \sim \frac{j^{n+1}}{kR}\exp(-jkR)\left\{\frac{P_n^1(\cos\theta)}{\sin\theta}\cos\phi\,\hat{\theta} - \left(\frac{\partial}{\partial\theta} P_n^1(\cos\theta)\right)\sin\phi\,\hat{\phi}\right\} \tag{5.30}$$

$$\vec{N}^{(4)}_{eln}(\theta,\phi,R) \sim (-j)\frac{j^{n+1}}{kR}\exp(-jkR)\left\{\left(\frac{\partial}{\partial\theta} P_n^1(\cos\theta)\right)\cos\phi\,\hat{\theta} - \frac{P_n^1(\cos\theta)}{\sin\theta}\sin\phi\,\hat{\phi}\right\} \tag{5.31}$$

The far-zone scattered electric field can then be written as

$$E_\theta^s(\vec{r}) = -j E_0 \frac{\exp(-jkR)}{kR} \sum_{n=1}^{\infty} \frac{2n+1}{n(n+1)} \left\{ a_n \frac{P_n^1(\cos\theta)}{\sin\theta} + b_n \left(\frac{\partial}{\partial\theta} P_n^1(\cos\theta) \right) \right\} \cos\phi \qquad (5.32)$$

$$E_\phi^s(\vec{r}) = j E_0 \frac{\exp(-jkR)}{kR} \sum_{n=1}^{\infty} \frac{2n+1}{n(n+1)} \left\{ a_n \left(\frac{\partial}{\partial\theta} P_n^1(\cos) \right) + b_n \frac{P_n^1(\cos\theta)}{\sin\theta} \right\} \sin\phi \qquad (5.33)$$

For the back-scatter case, the following relations are useful in the evaluation of the Mie series:

$$P_n^1(\cos\theta)\,|_{\theta=\pi} = -\frac{(-1)^n}{2} n(n+1) \qquad \frac{\partial}{\partial\theta} P_n^1(\cos\theta)\,|_{\theta=\pi} = \frac{(-1)^n}{2} n(n+1) \qquad (5.34)$$

The evaluation of the previous expressions to obtain the response of the sphere is numerically difficult and there has been considerable work on the evaluation of the series [55]. The introduction of personal computers based on 32 bit microprocessors and efficient hardware floating point units has greatly reduced the cost of performing computations such as the Mie series evaluation. Availability of such computer power allows the programmer to spend less time on code development and still have a program which provides useful and accurate results in less time than was possible only a few years ago. The expressions shown in (5.32) and (5.33) were programmed with the use of widely available generalized Bessel function subroutines. Most routines used in the program were written or modified by Anton Tijus of the University of Delft, Netherlands. These routines are very accurate and efficient.

To test the validity of the program results, the special case of back-scattering was considered. The result showing the normalized back-scattered electric field versus

normalized frequency for a perfectly conducting sphere a distance of 10 sphere radii away is shown in Figure 5.10. Here the first sphere resonance

$$f_0 = \frac{c}{2\pi a} \tag{5.35}$$

is used as a normalization. Note that most authors plot the back-scattering RCS instead of electric field. The field is presented in this thesis since the calibration procedures require the field values. The relationship between normalized electric field and back-scattering RCS is given by

$$\sigma_b = 4\pi R^2 \left\{ \frac{|E^s(\theta=\pi)|}{|E^{inc}|} \right\}^2 \tag{5.36}$$

The back-scattering RCS of a sphere in the high frequency limit is the area the sphere projects onto a plane that is parallel to the incident wavefront:

$$\sigma_b = \pi a^2 \tag{5.37}$$

Thus, for the case of a unit radius sphere the normalized scattered field at a distance of 10 sphere radii is

$$\begin{aligned} \frac{|E^s(\theta=\pi)|}{|E^{inc}|} &= \frac{1}{2R} \\ &= 0.05 \quad \textit{for } R=10a \end{aligned} \tag{5.38}$$

The curve in Figure 5.10 approaches this limiting value for high frequencies. According to Skolnik [4] the RCS of a conducting sphere at the first resonance is approximately 5.6 dB larger than the RCS of the sphere in the optical limit. To use this number as a check of the results in Figure 5.10 the normalized scattered field at resonance due to a sphere 10 radii away is calculated as

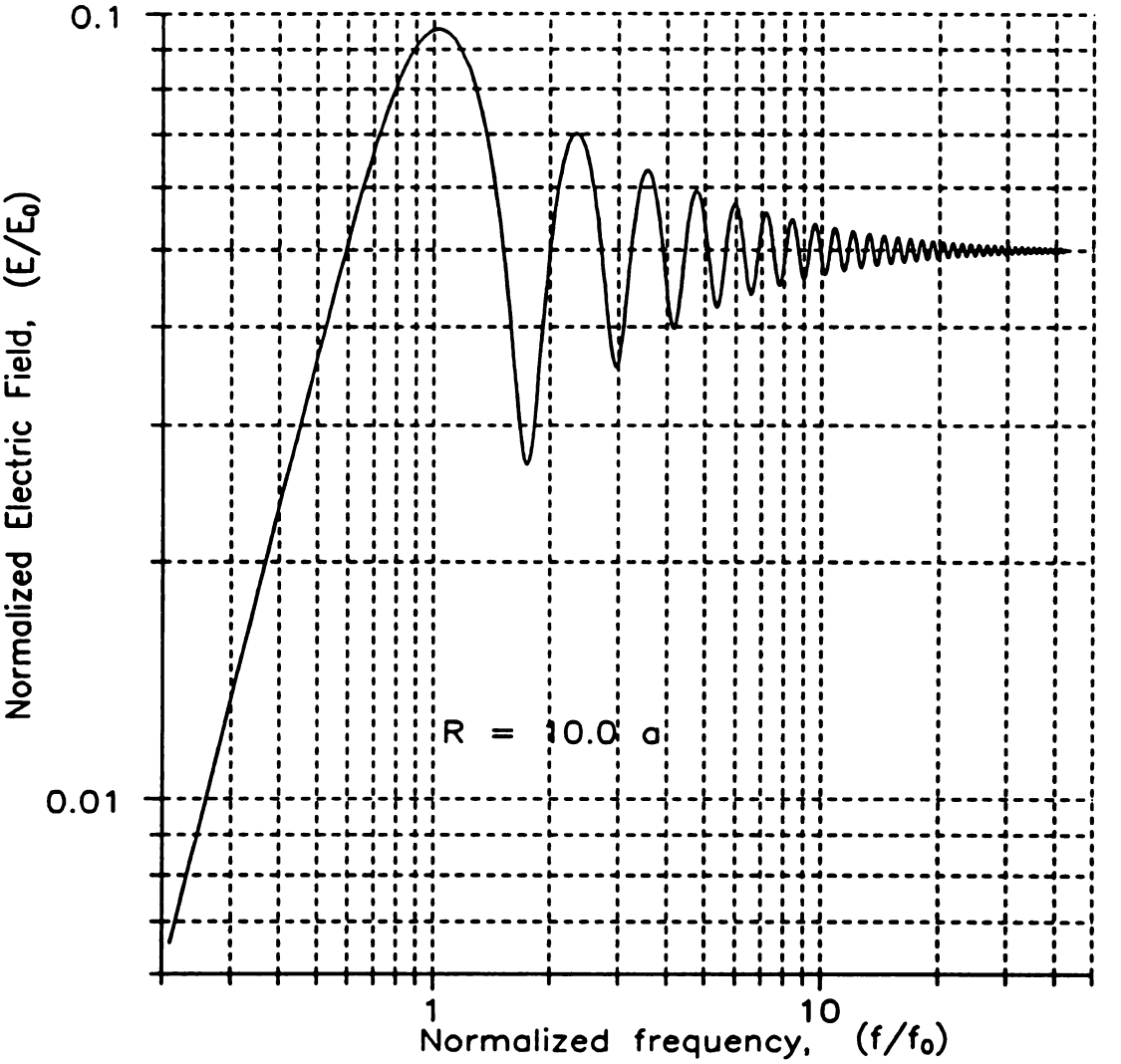

Figure 5.10 Frequency response of a perfectly conducting sphere in back-scatter configuration.

$$\frac{E^s(\theta=\pi)}{E^{inc}} = \frac{0.9527}{R} = 0.09527 \quad for\ R=10a \tag{5.39}$$

The results in Figure 5.10 are in agreement with these calculations.

The transient field response versus normalized time of a sphere in the back-scatter configuration is shown in Figure 5.11. The transient response was synthesized by applying a GMC weighting function to the spectrum previously shown and then applying an inverse FFT. The GMC had a center frequency of 0 Hz and a damping factor of $\tau = 0.025\ t_0$. The strong specular reflection is followed by the well known creeping waves. Since the second creeping wave is very small the scale was magnified in Figure 5.12 to show the second creeping wave.

The thin wire was also used as a calibration target in this research. The thin-wire has been extensively studied in the literature. Although the scattering properties of a thin-wire cannot be expressed in closed form as in the case of the sphere, it is well understood and can be numerically modeled. For purposes of this research the thin-wire was modeled using the method of moments. A Galerkin method was employed using piece-wise sinusoidal sub-sectional basis functions. The details of this formulation are described in Appendix A.

There are several difficulties encountered when using a wire for calibration over an ultra-wide bandwidth. One of these difficulties is that the thin-wire response is a function of orientation angle. This aspect dependency is not a problem in the theoretical formulation, but it can become difficult to place the wire on the styrofoam support inside the anechoic chamber in exactly the same position in a repeatable fashion. Any

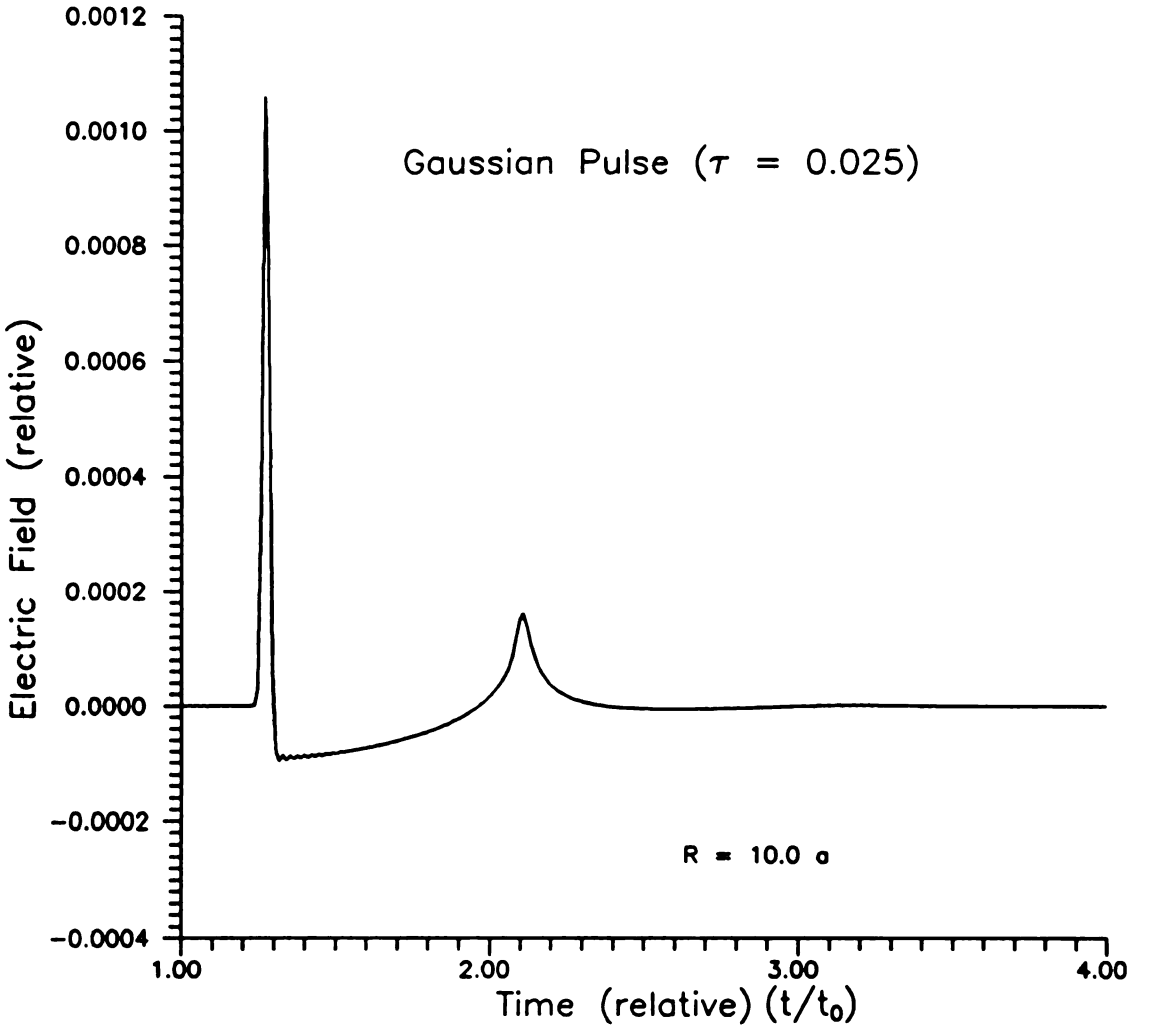

Figure 5.11 Gaussian pulse response of a perfectly conducting sphere in back-scatter configuration.

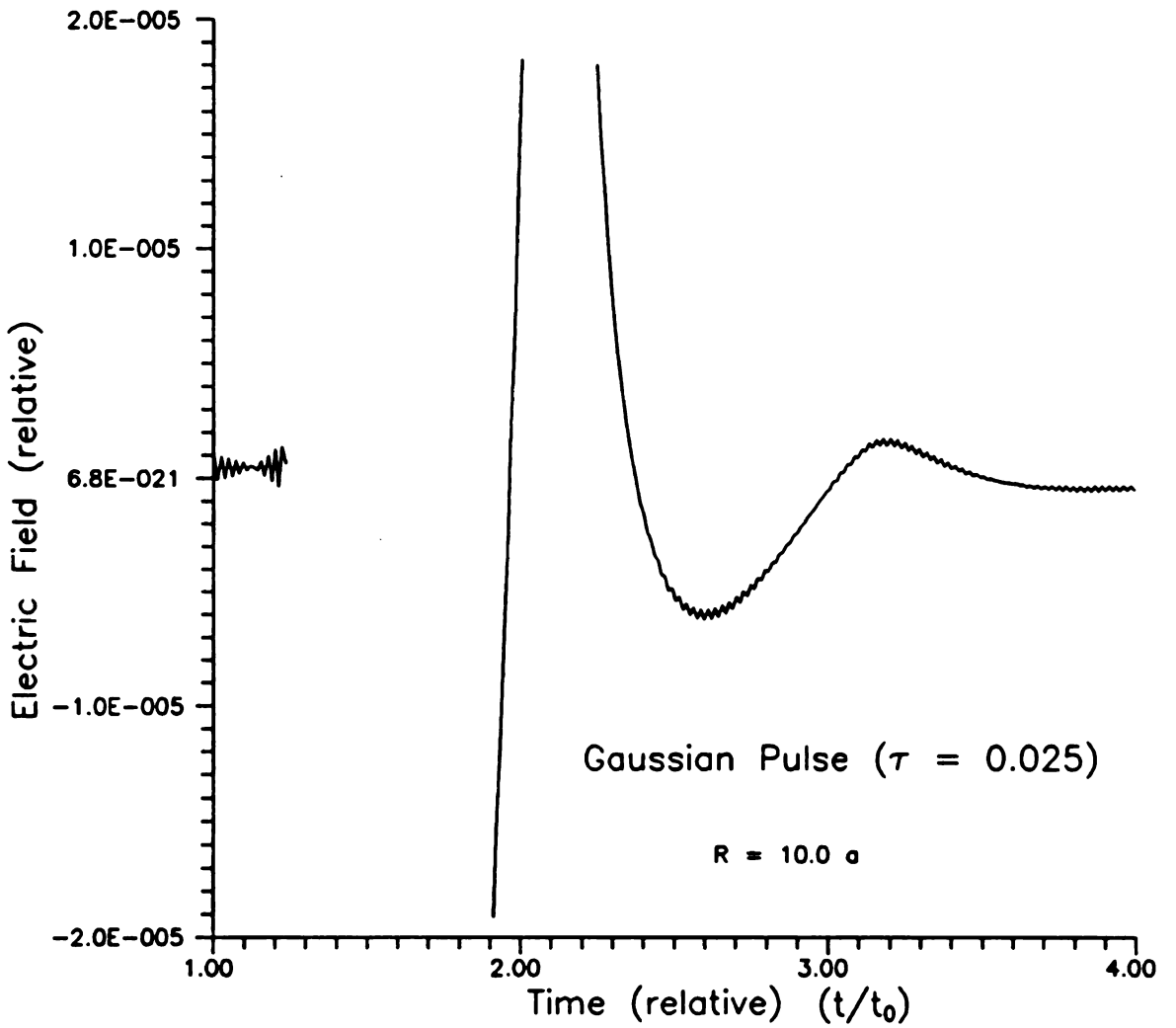

Figure 5.12 Gaussian pulse response of a perfectly conducting sphere showing second creeping wave.

discrepancies between the actual aspect angle and the angle used in the calculations cause errors in the deconvolution procedure. The problem of aspect dependency is not as severe for wires that are small with respect to a wavelength, but for long wires the errors can be considerable. Unfortunately, short wires do not provide a strong signal. The use of short wires for calibration then leads to a loss of signal-to-noise ratio in all measurements subsequent to deconvolution.

To illustrate the aspect dependency problem, a series of numerical simulations was performed. The spectral response of several different length wires was calculated for the anechoic chamber configuration used at Michigan State University. A frequency range of 0.400 to 4.400 Ghz was chosen for the calculations to coincide with the values usually used in the low band configuration for target measurements.

The calculations were done with the method-of-moments for various orientation angles. The configuration of the chamber modeling for these calculations is shown in Appendix C. Figure 5.13 shows the response of a stainless steel wire 2.0 inches long and 0.043 inches in diameter for various aspect angles. The response is only slightly different at the highest frequencies. As the wire length is increased to 4.0 inches, the variation with angular position is more pronounced as shown in Figure 5.14. Similar effects are observed for wires of length 6.0 and 8.0 inches as seen in Figure 5.15 and Figure 5.16.

It should be noted that calibration using the theoretical field values at a point is only valid if far-zone conditions are enforced in the measurement system. This requirement means that the variation of the transmitted field over the target should be small. Similarly, the variation of the scattered field over the aperture of the receive antenna should be small as well. The results in this dissertation were obtained by using

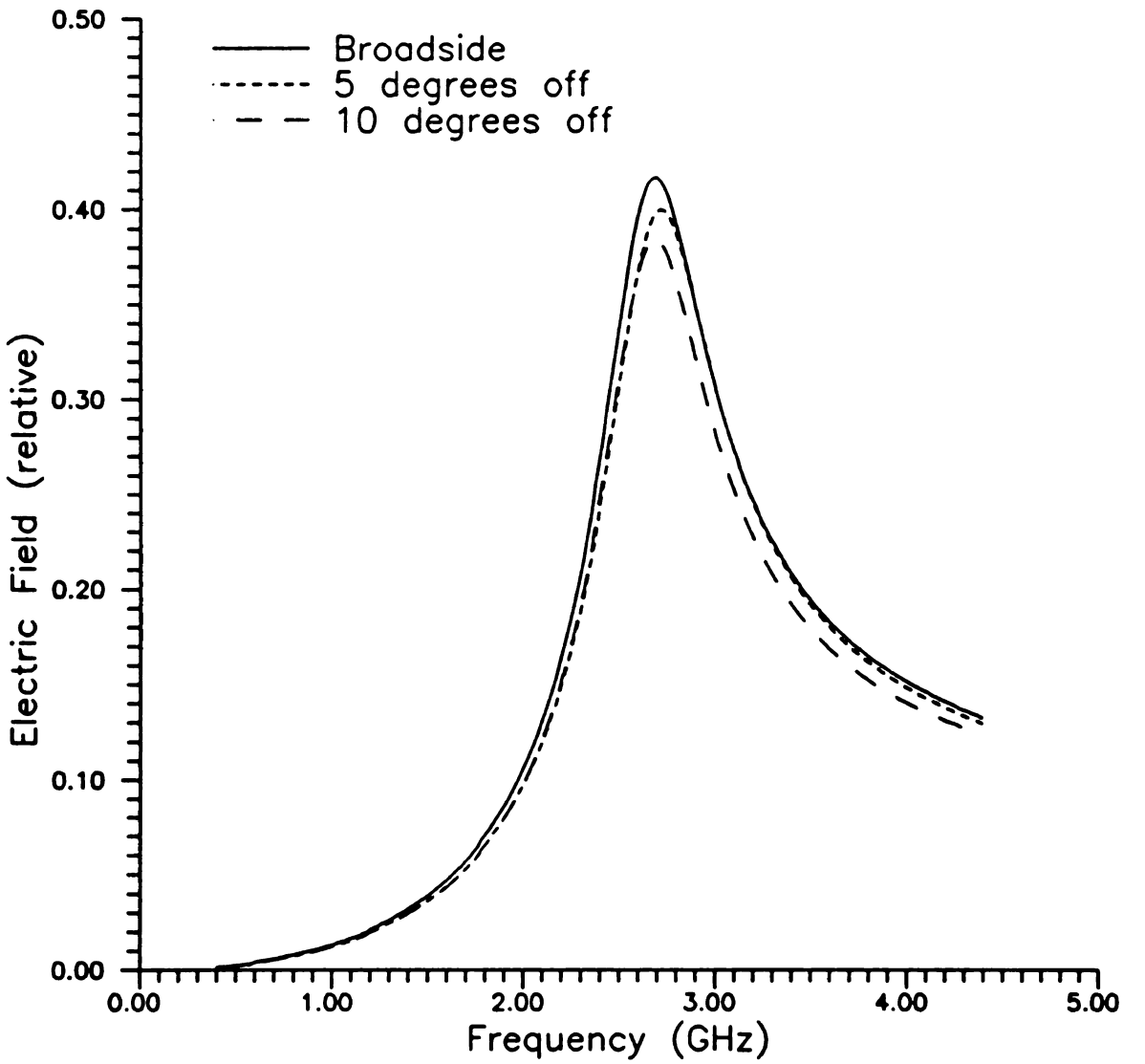

Figure 5.13 Scattered field amplitude vs aspect angle for wire (2.0 x 0.043 inches). Moment method results computed for MSU anechoic chamber geometry.

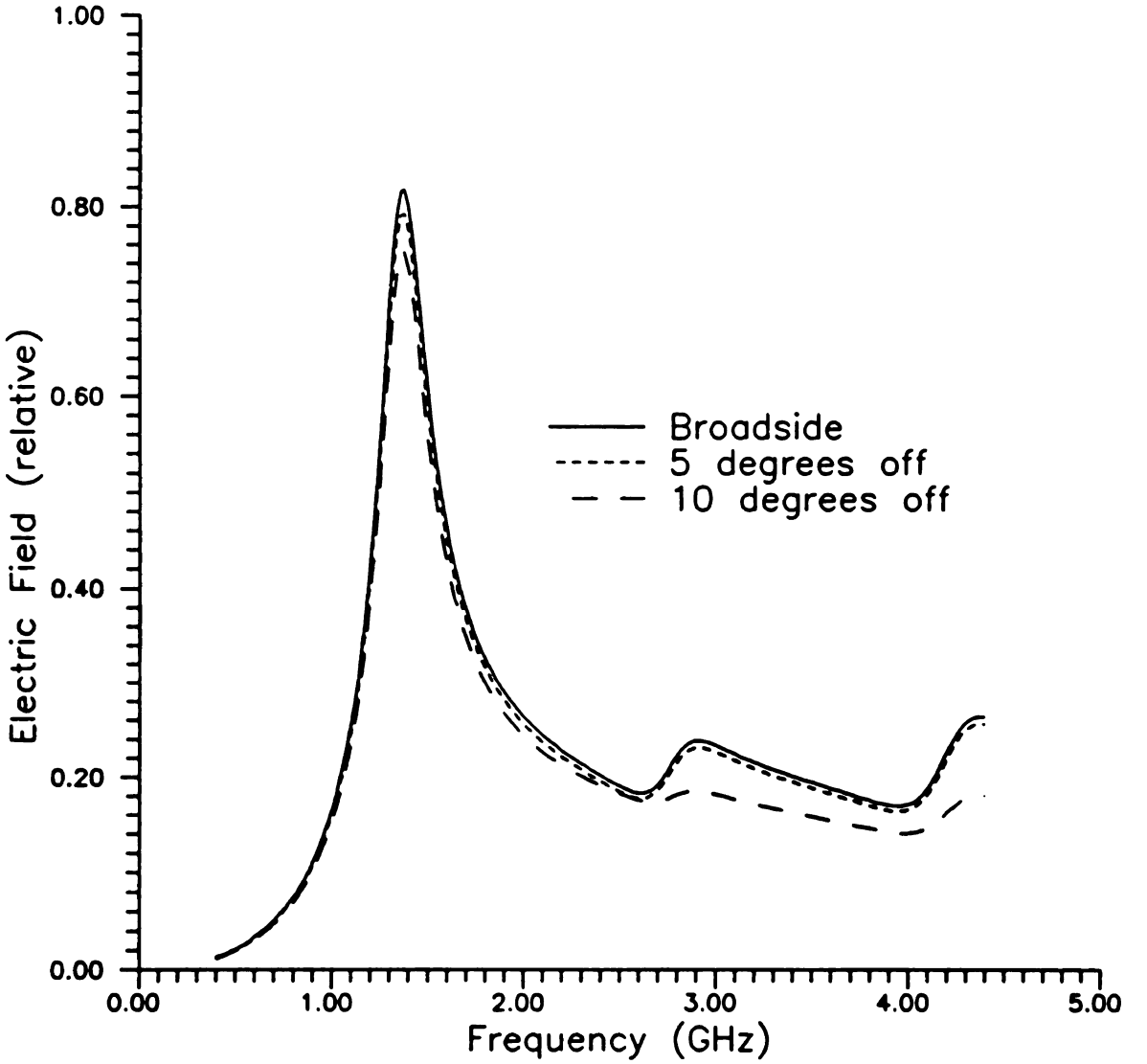

Figure 5.14 Scattered field amplitude vs aspect angle for wire (4.0 x 0.043 inches). Moment method results computed for MSU anechoic chamber geometry.

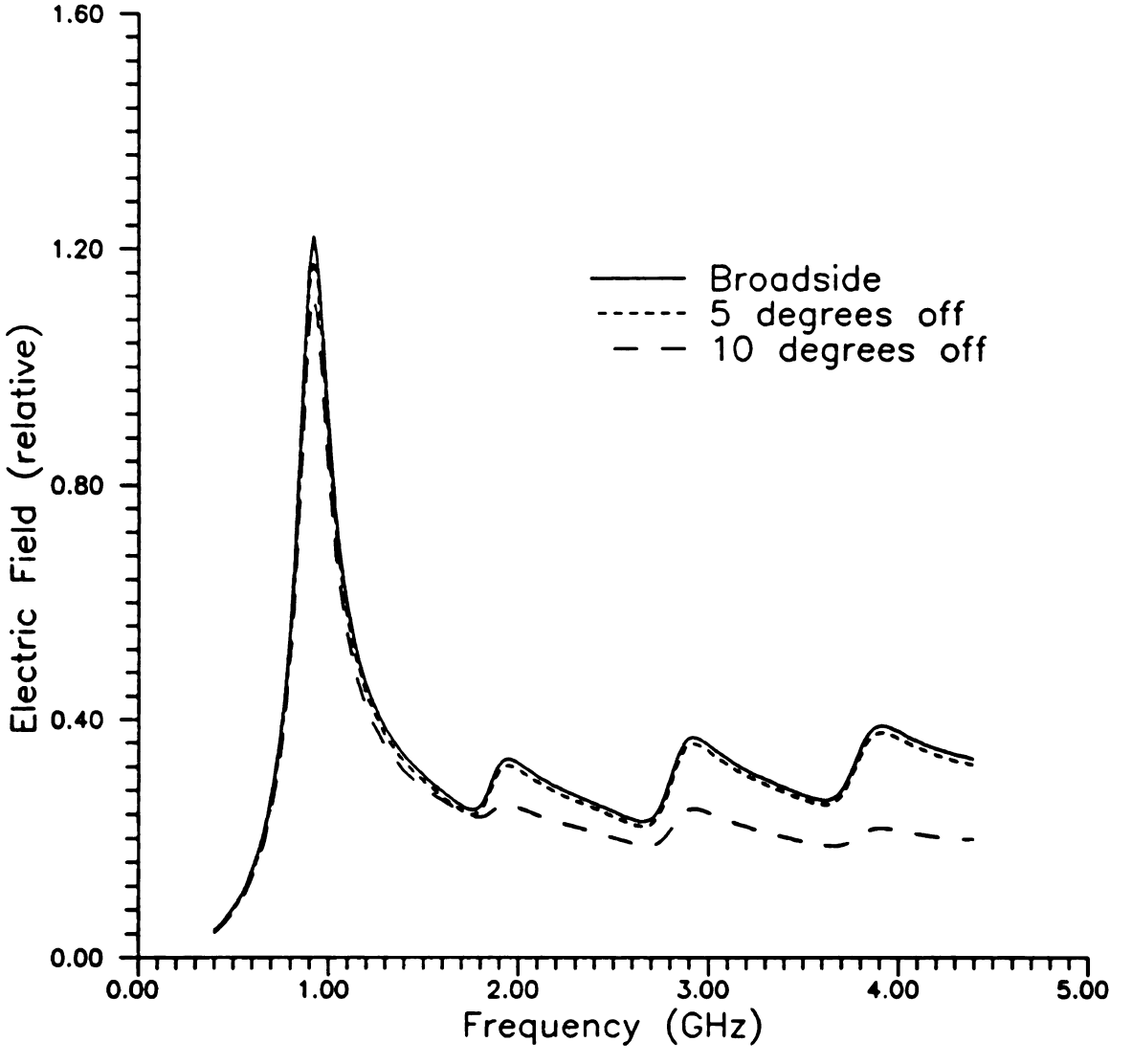

Figure 5.15 Scattered field amplitude vs aspect angle for wire (6.0 x 0.043 inches). Moment method results computed for MSU anechoic chamber geometry.

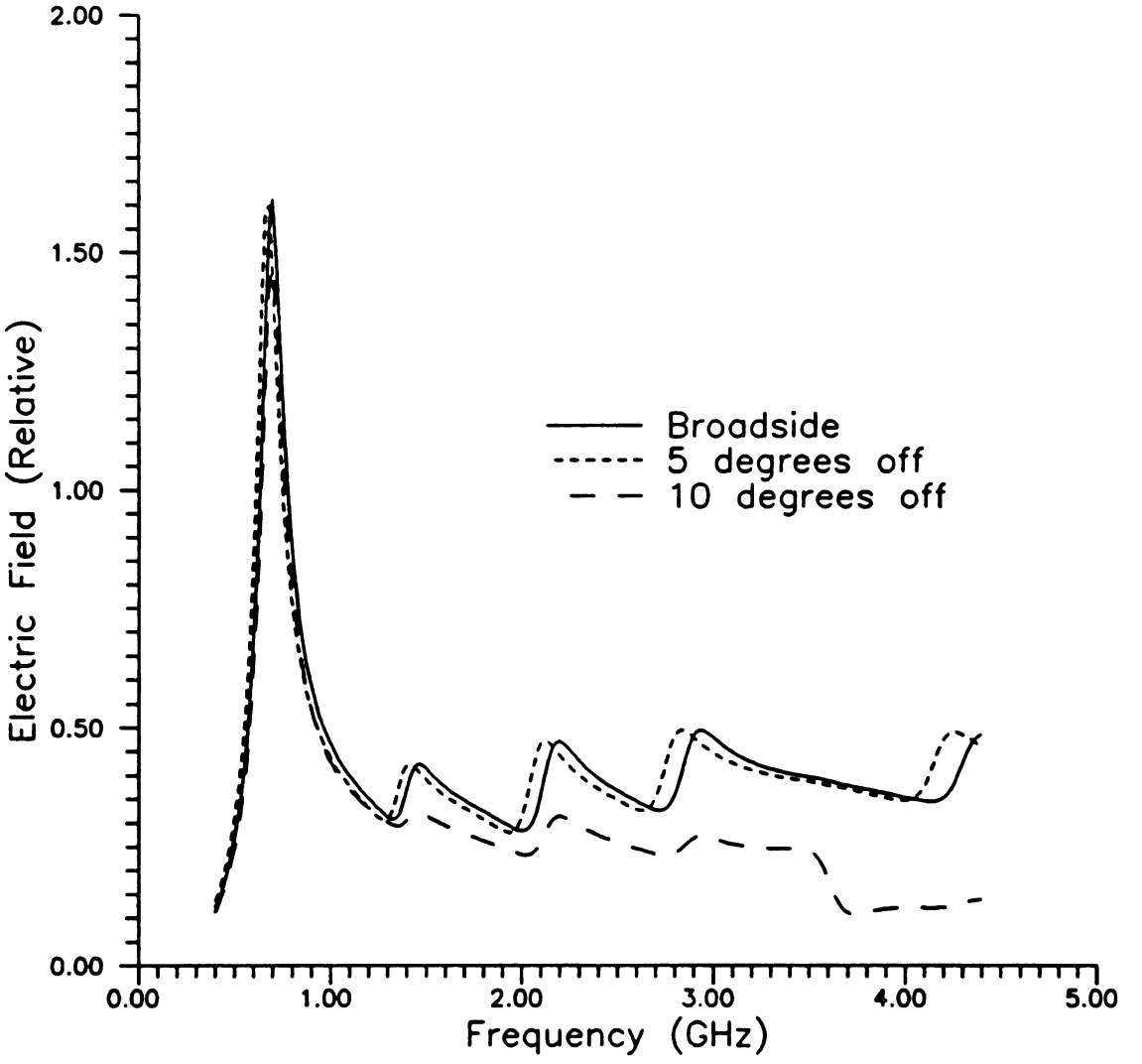

Figure 5.16 Scattered field amplitude vs aspect angle for wire (8.0 x 0.043 inches). Moment method results computed for MSU anechoic chamber geometry.

a field point near the throat of the TEM horn antennas.

5.7 Calibration Examples

This section presents experimental and theoretical results to demonstrate the calibration procedure described earlier. Examples of the various waveforms and spectra encountered in the measurement procedure are presented to provide a baseline of expectations for future workers. Significant characteristics of these waveforms and spectra are discussed.

The first step in the calibration procedure is to measure the background clutter. The background measurement can reveal problems with a measurement system. The spectral representation of the background measurement made with the HP8720B Network Analyzer inside the MSU Anechoic Chamber is shown in Figure 5.17. This measurement shows that coupling between transmit and receive antennas is strongest at the lower frequencies. A similar curve is obtained by taking the FFT of a background measurement using the time domain system. This result is shown in Figure 5.18. This curve should not be identical to the one obtained using the frequency domain system since the power spectral density of the pulse used in the time domain system is different from that generated by the frequency domain systems.

Strong coupling is indicative of both direct free space antenna-to antenna coupling and coupling via reflections from the chamber walls and antenna support structures. Coupling via the chamber walls is usually stronger at low frequencies since the efficiency of most absorber decreases as the frequency is decreased. Note, however, that absorber efficiency also decreases if the frequency is increased into the millimeter-wave regime.

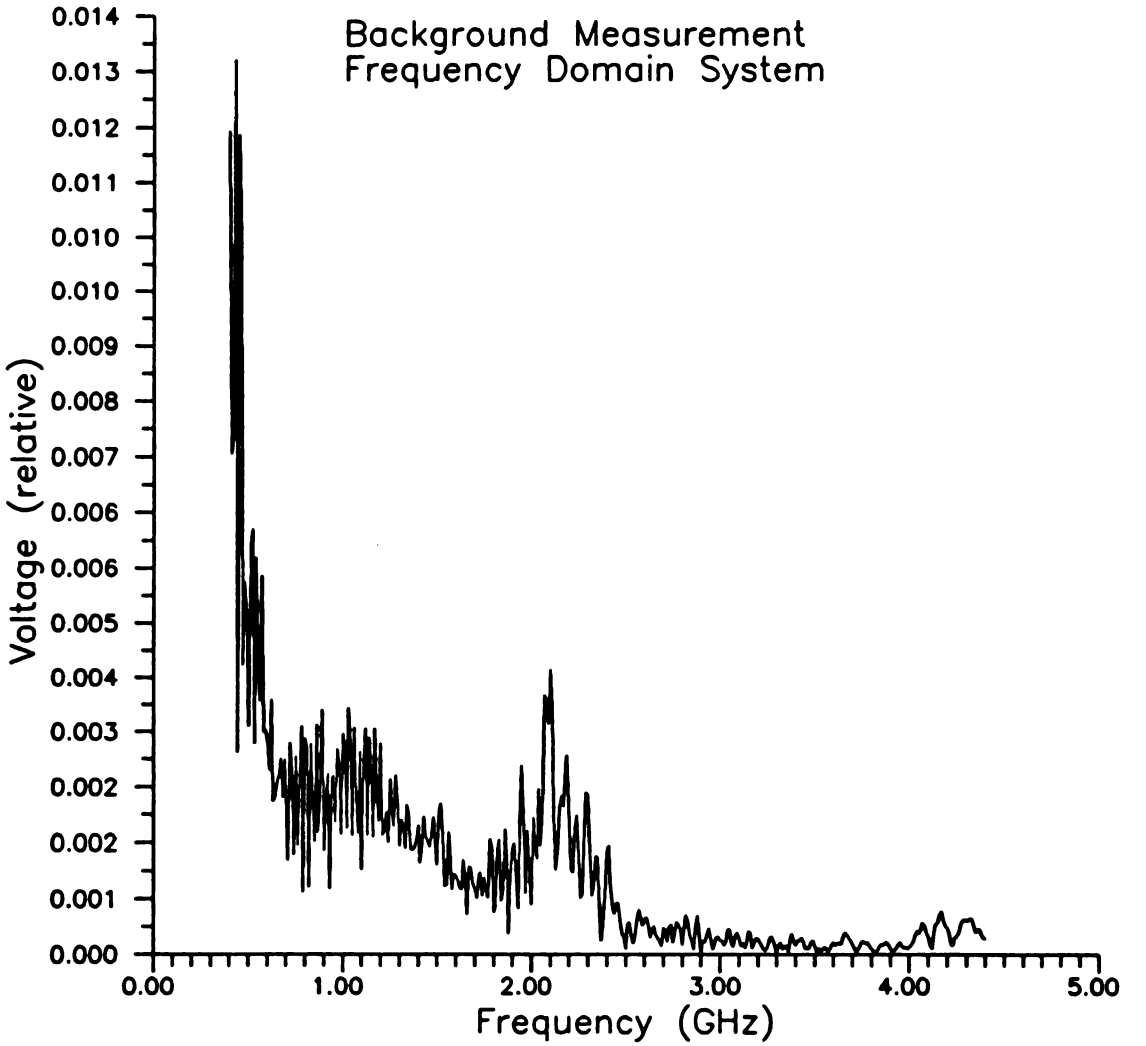

Figure 5.17 Spectral background measurement of MSU anechoic chamber using frequency domain system.

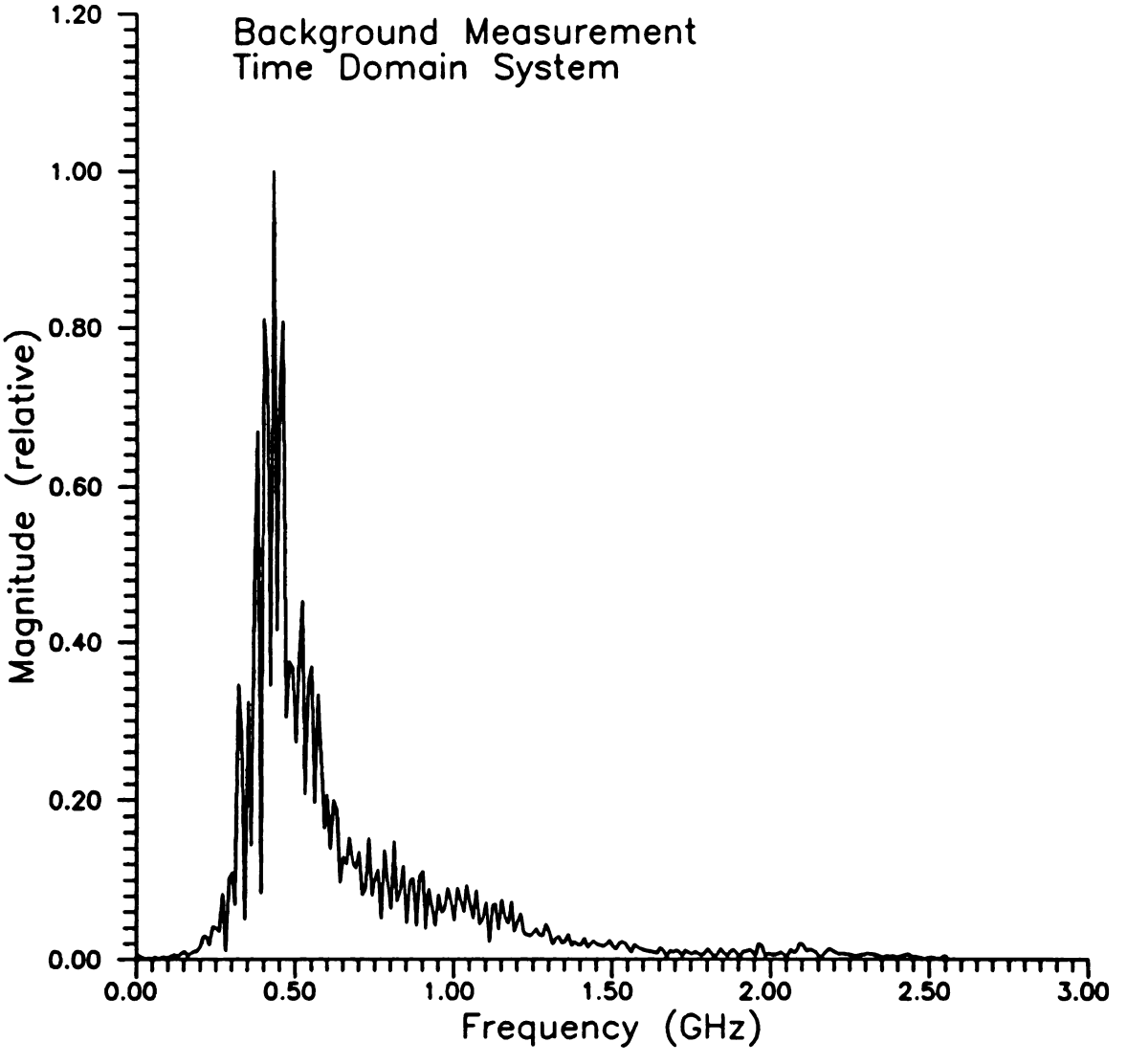

Figure 5.18 Spectral background measurement of MSU anechoic chamber using time domain system.

Higher quality absorber on the chamber walls, on the antenna supports and between the antennas can reduce the direct coupling. Reduction of direct coupling is probably the most efficient way to improve the quality of the scattering measurements. Ideally, the background response is very small as compared to the target response. Clutter subtraction is then only a minor correction. In practice, this is not the case and the clutter is of the same order or larger than the target response. A larger clutter signal limits the dynamic range of the measurement system when subtraction is necessary. Even though the network analyzer has a tremendous dynamic range, the ultimate accuracy of any measurement is no better than .01 dB in magnitude and .1 degree in phase. The same effect is present in time domain systems as well.

Another perspective on the background measurement is seen in the time domain. Figure 5.19 shows the temporal background measurement made using the time domain measurement system. The direct coupling is easily differentiated from the scatter of the anechoic chamber. Since the transmit and receive antennas are located close together the direct coupling occurs before the transmitted wave has time to interact with the chamber and return to the receive antenna. Thus, the first part of the signal is due to direct coupling while the scatter from the chamber walls starts at a later time. A similar result is obtained by Fourier transforming the result obtained from the frequency domain system as shown in Figure 5.20.

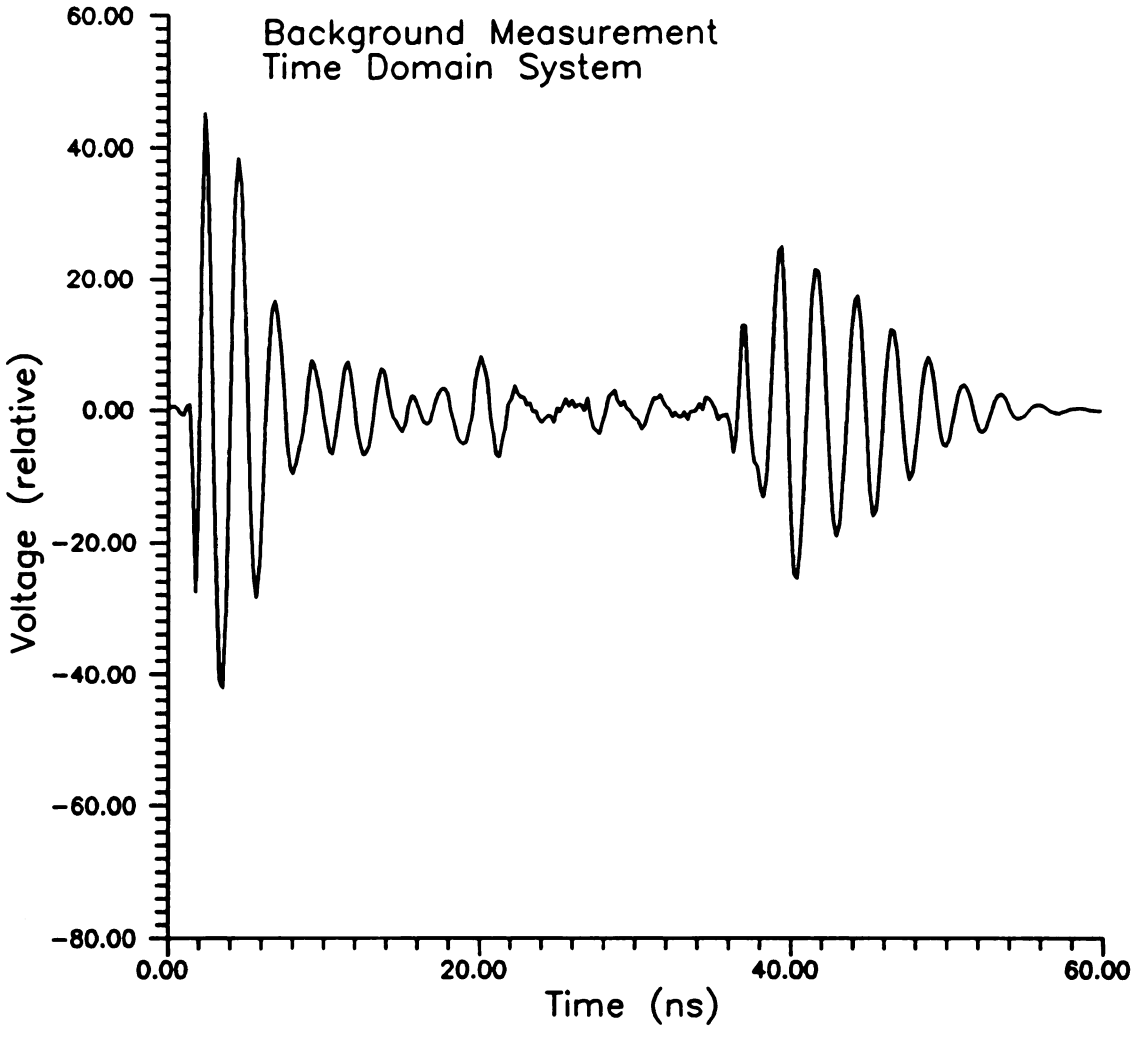

Figure 5.19 Temporal background measurement of MSU anechoic chamber using time domain system.

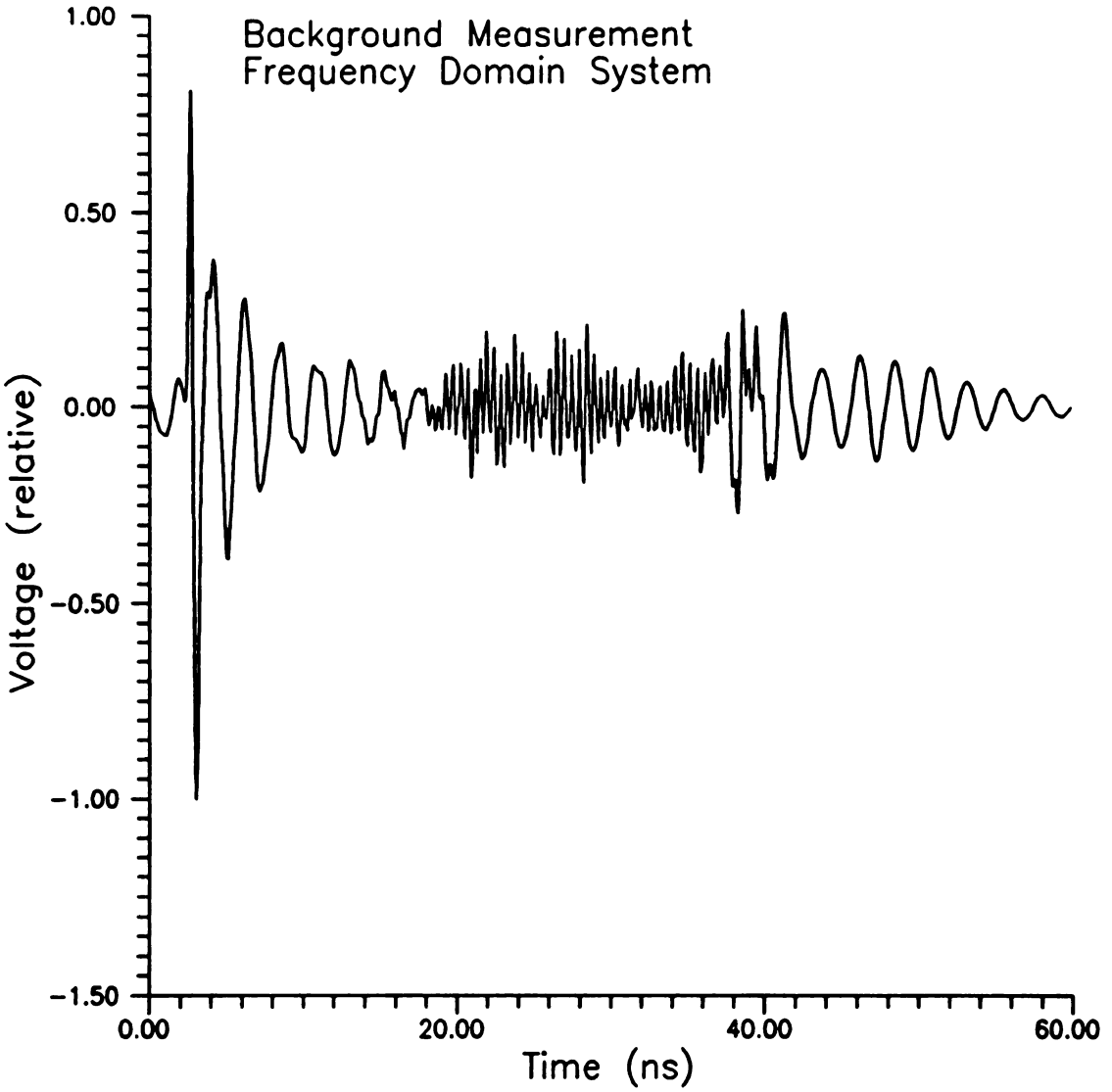

Figure 5.20 Temporal background measurement of MSU anechoic chamber using frequency domain system.

The next step is to measure the calibration standard. The spectral response of a 14 inch diameter metal calibration sphere measured using the frequency domain system is shown in Figure 5.21. The Inverse Fourier Transform of this measurement is shown in Figure 5.22. A direct time domain measurement of the same sphere is shown in Figure 5.23. The portion of the response due to the interaction of the target with the back wall is clearly identifiable at approximately 40 ns. The interaction term is windowed out of the time domain response and the Fourier Transform operation performed. The spectrum of the calibration sphere without the interaction term obtained from the frequency domain system is shown in Figure 5.24. Note that the frequencies outside the original measurement bandwidth must be discarded here to prevent introduction of extraneous noise. The spectrum of the windowed calibration sphere measurement obtained using the time domain system is shown in Figure 5.25.

The theoretical response of the 14 inch diameter sphere for the MSU anechoic chamber configuration is shown in Figure 5.26. These results were computed by numerical evaluation of the Mie series as outlined in the previous section. Note that for pure backscatter the sphere does not depolarize, however, for the bistatic configuration of the anechoic chamber there is some depolarization. In this case both components of scattered field must be used.

The system transfer function was computed using the theoretical sphere response and the windowed sphere measurement as shown in (5.15). The result is shown in Figure 5.27. The result has been normalized to a peak value of unity. Normalization is used since the waveshape, and not the wave amplitude, contains the desired information. A plot of the transfer function of the time domain system using the same procedure is

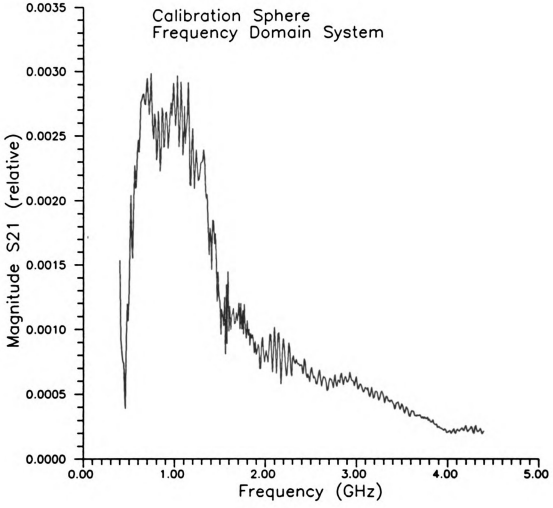

Figure 5.21 Spectral response of 14 inch metal calibration sphere measured using frequency domain system in MSU anechoic chamber.

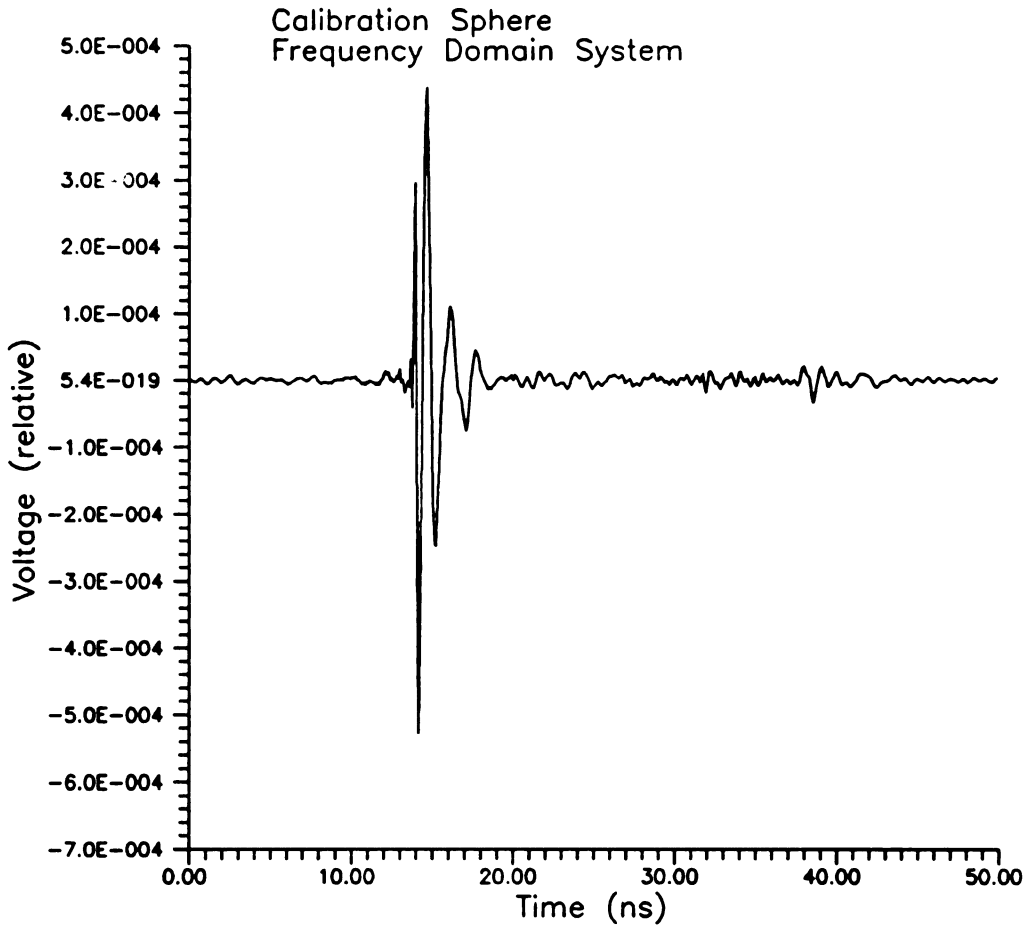

Figure 5.22 Temporal response of 14.0 inch diameter metal calibration sphere measured using frequency domain system in MSU anechoic chamber.

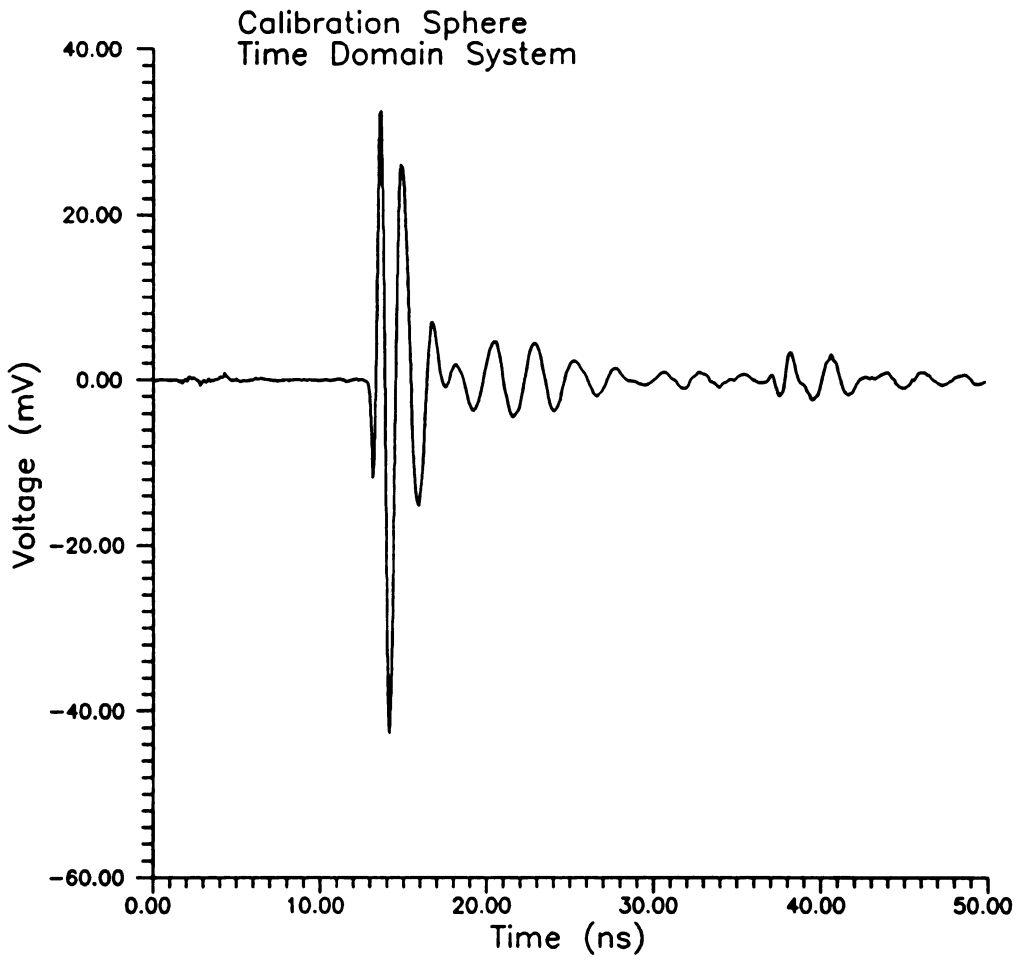

Figure 5.23 Temporal response of 14.0 inch metal calibration sphere measured using time domain system in MSU anechoic chamber.

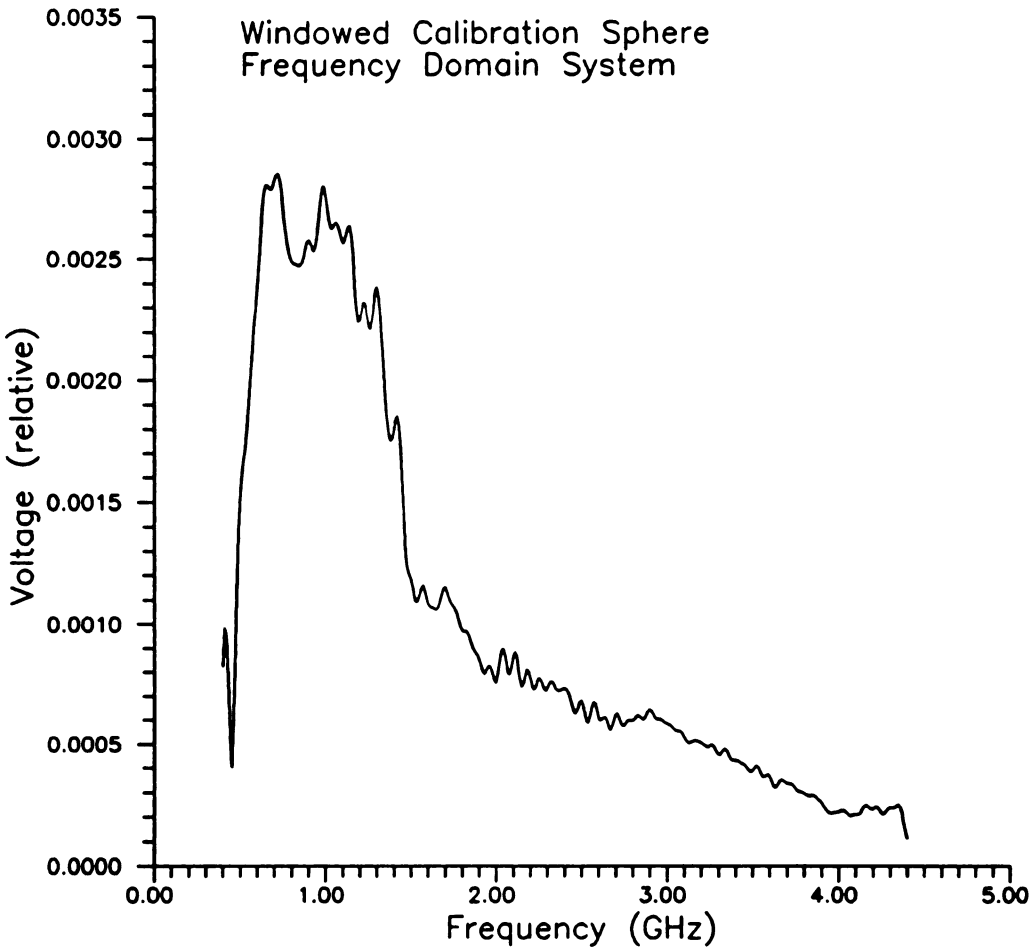

Figure 5.24 Spectral response of 14.0 inch calibration sphere after time domain filtering of chamber wall reflections. Measured using frequency domain system in MSU anechoic chamber.

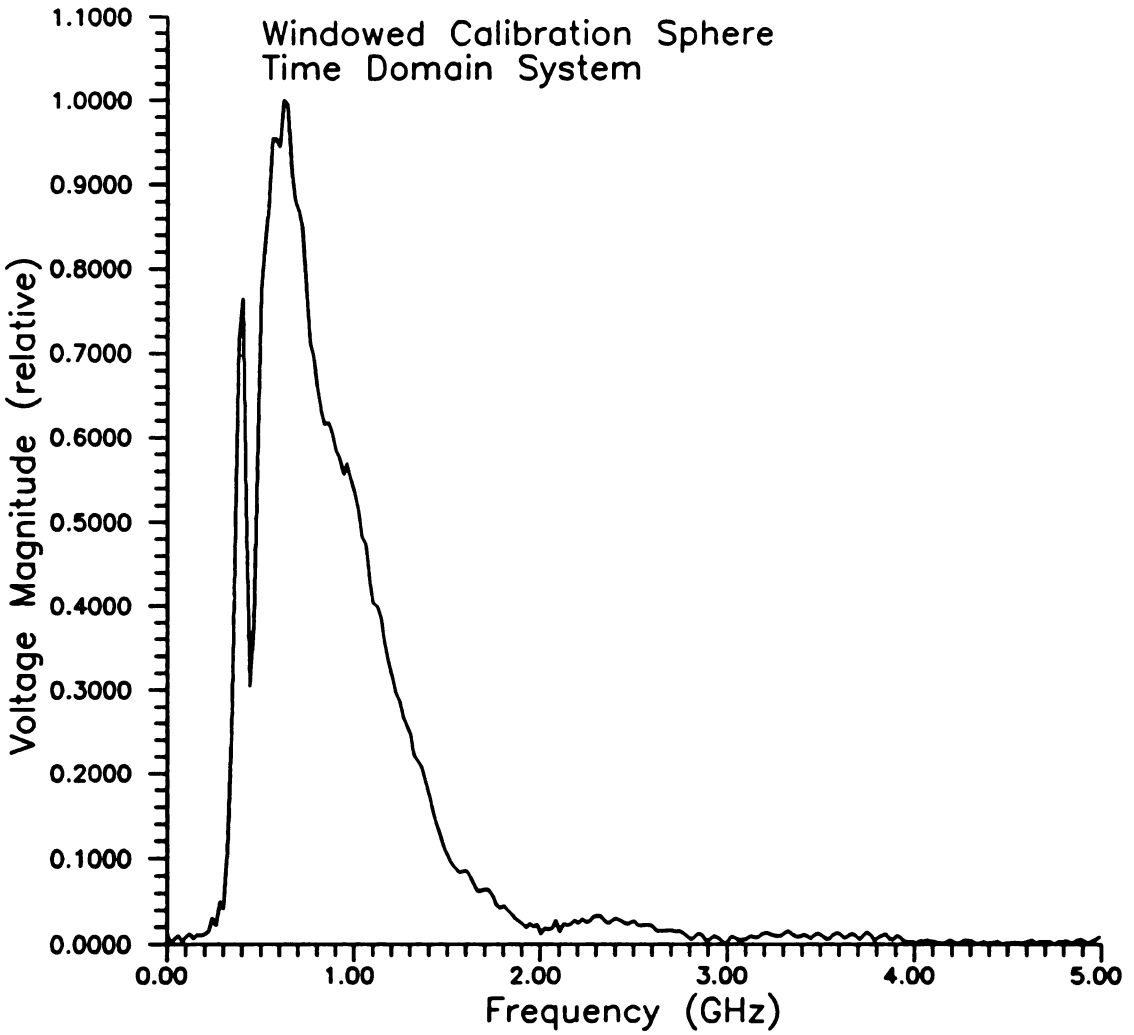

Figure 5.25 Spectral response of calibration sphere after time domain filtering of chamber wall reflections. Measured using time domain system in MSU anechoic chamber.

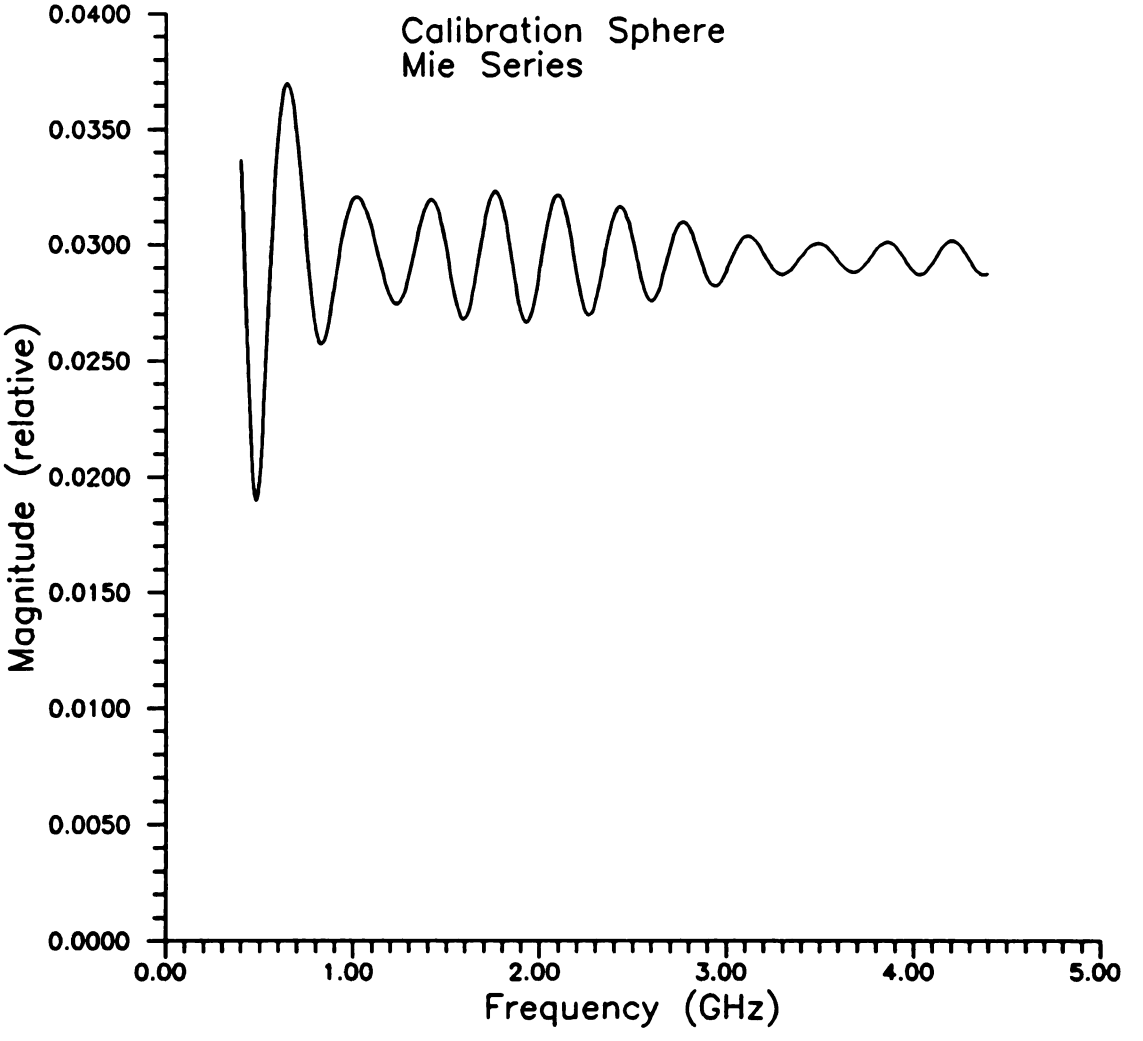

Figure 5.26 Theoretical response of 14.0 inch diameter metal calibration sphere calculated using Mie series for MSU anechoic chamber configuration.

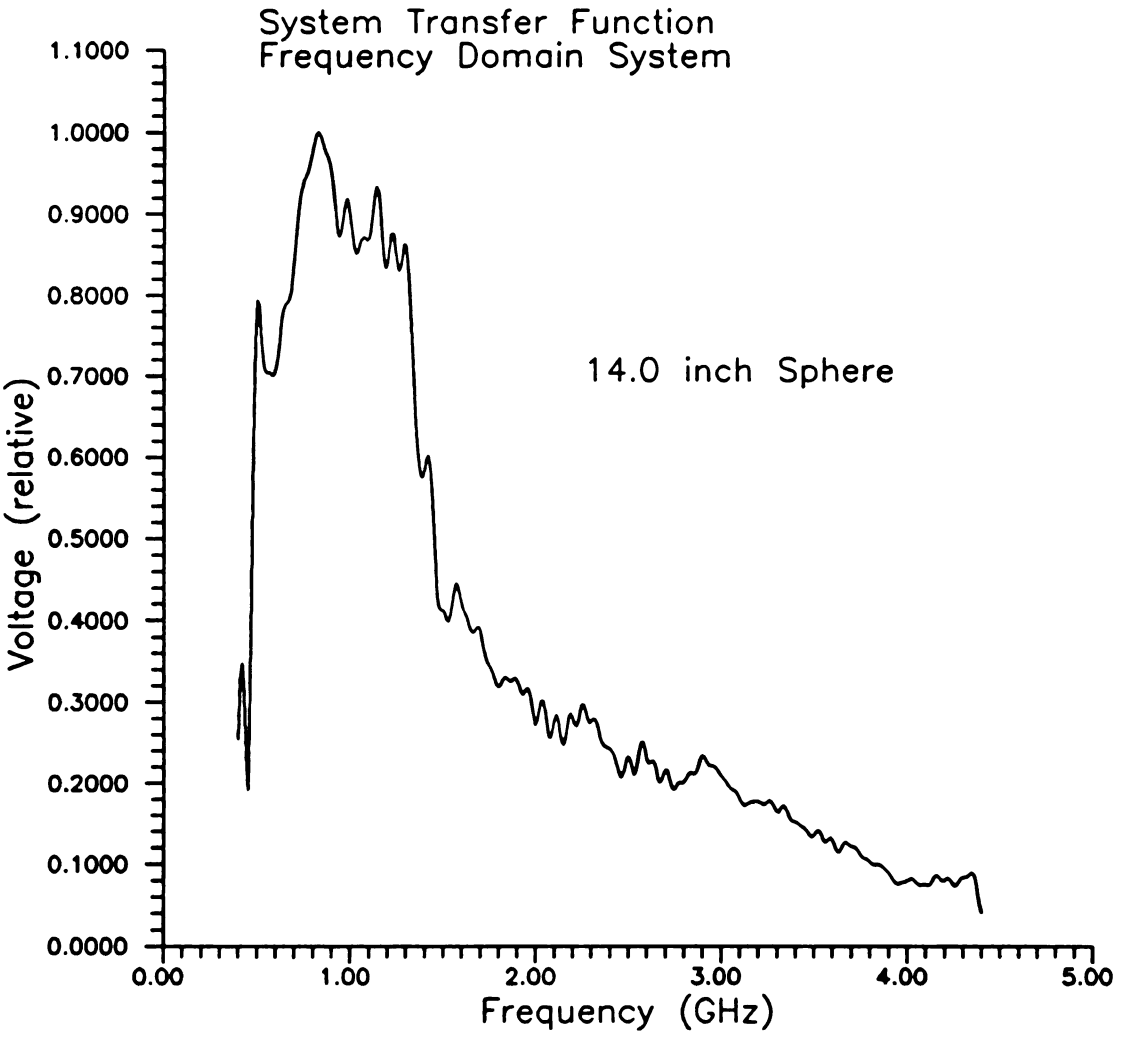

Figure 5.27 Transfer function of frequency domain system obtained using 14.0 inch diameter sphere as calibration standard. Results normalized to peak value of unity.

shown in Figure 5.28. Note that there are peaks in the spectrum. These peaks are most likely due to resonances of the individual horn antennas. The Inverse Fourier Transform of the system transfer function is known as the system impulse response. The band-limited system impulse response of the frequency domain measurement system is shown in Figure 5.29. It is clear that the extra oscillations that would be induced into an uncalibrated measurement are not negligible for mode extraction or early-time studies. The impulse response of time domain system is shown in Figure 5.30.

5.8 Measurements with Canonical Targets using Sphere Calibrator

With the system transfer function determined, other target measurements can be accurately performed. For validation purposes, the response of the targets must be known by either theoretically or through some different experimental procedure. This section presents measurements of canonical targets using a sphere as a calibrator.

A good verification target is another calibration sphere with a diameter different from the one used to perform the initial calibration. Unfortunately, other calibration spheres of known high quality were not available for this research. However, a small hollow brass sphere 3.0 inches in diameter was available. This sphere was originally intended for other purposes and had a 3/8 inch hole on its surface. A comparison of the corrected spectral response of this sphere obtained using the HP8720-B Network Analyzer with the theoretical Mie series solution is shown in Figure 5.31. The calibrated experimental results and the theory agree well. The uncalibrated sphere measurement is also shown to illustrate how calibration improves the accuracy of the measurement. The largest errors are present at the highest frequencies. This is probably due to the hole in

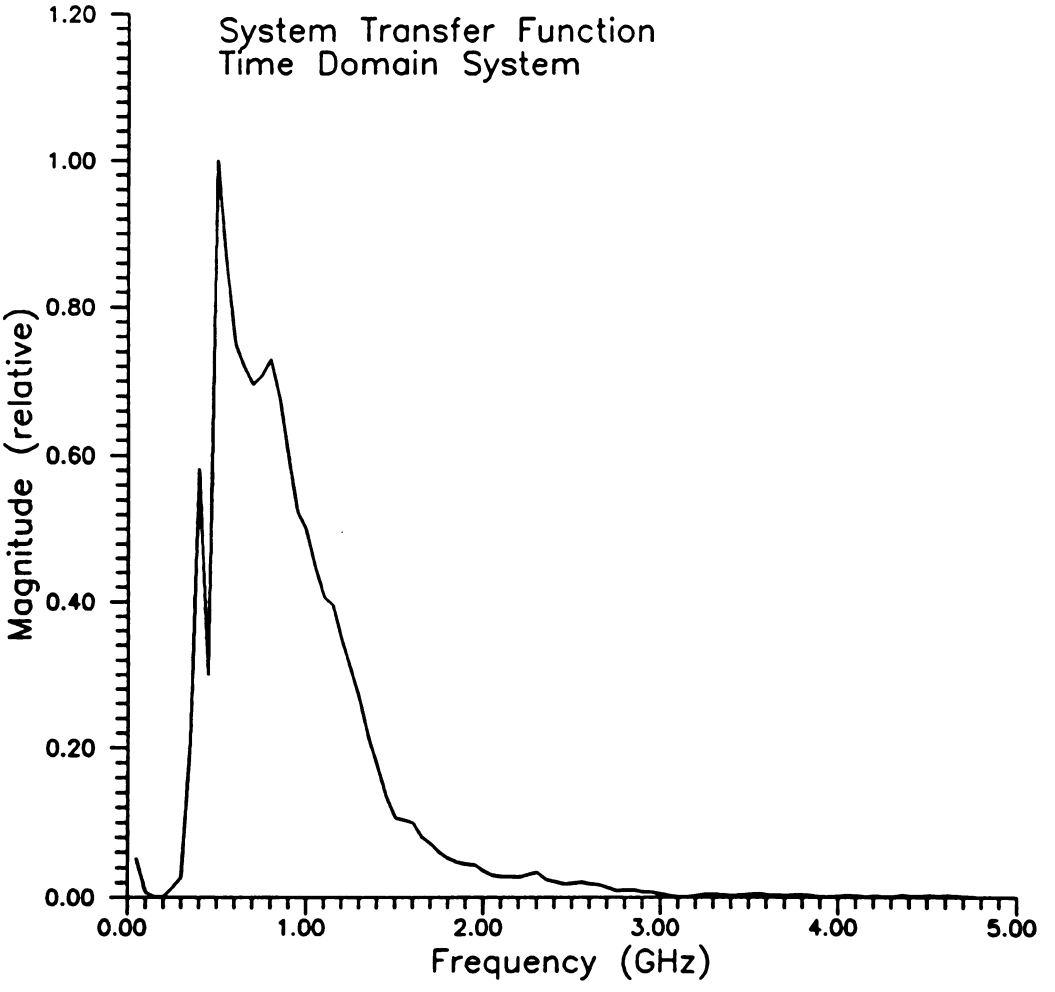

Figure 5.28 Transfer function of time domain system obtained using 14.0 inch diameter sphere as calibration standard. Results normalized to peak value of unity.

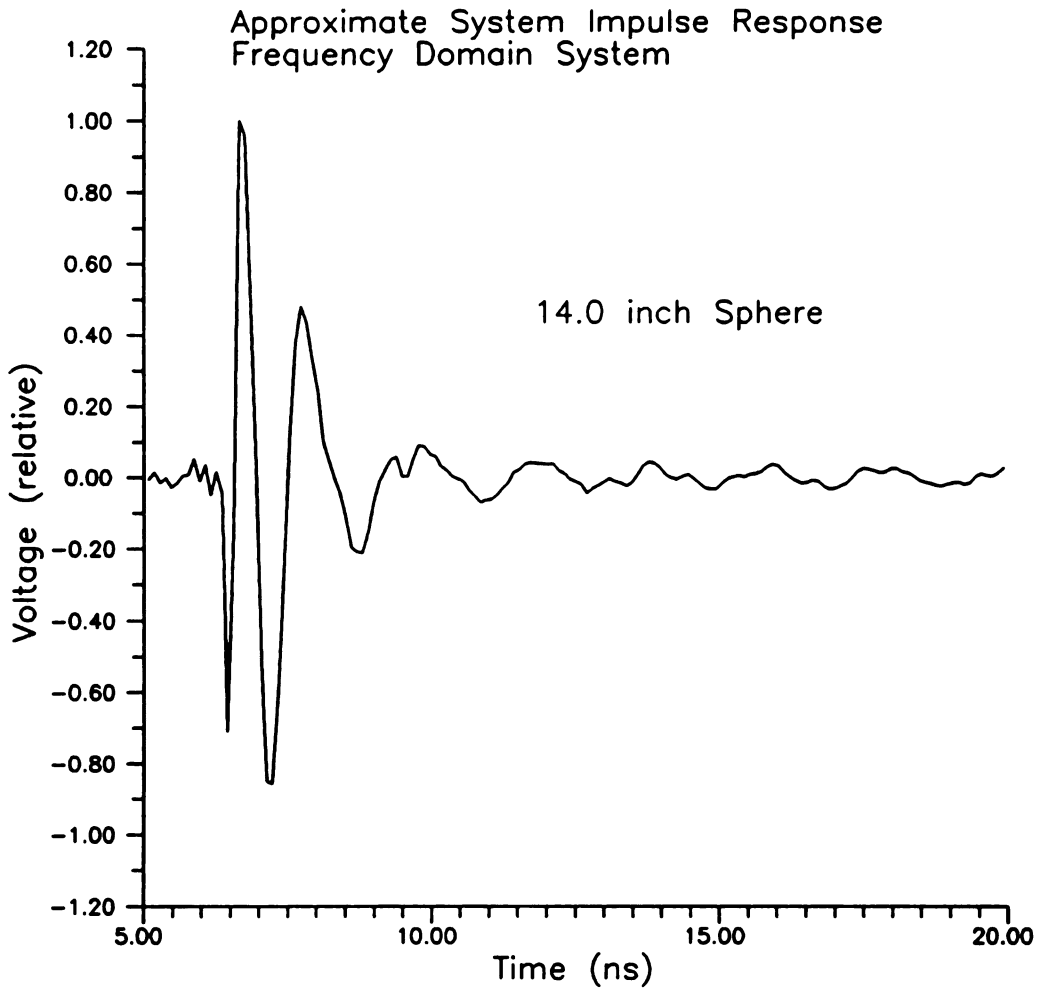

Figure 5.29 Impulse response of frequency domain system obtained using 14.0 inch diameter sphere as calibration standard. Results normalized to peak value of unity.

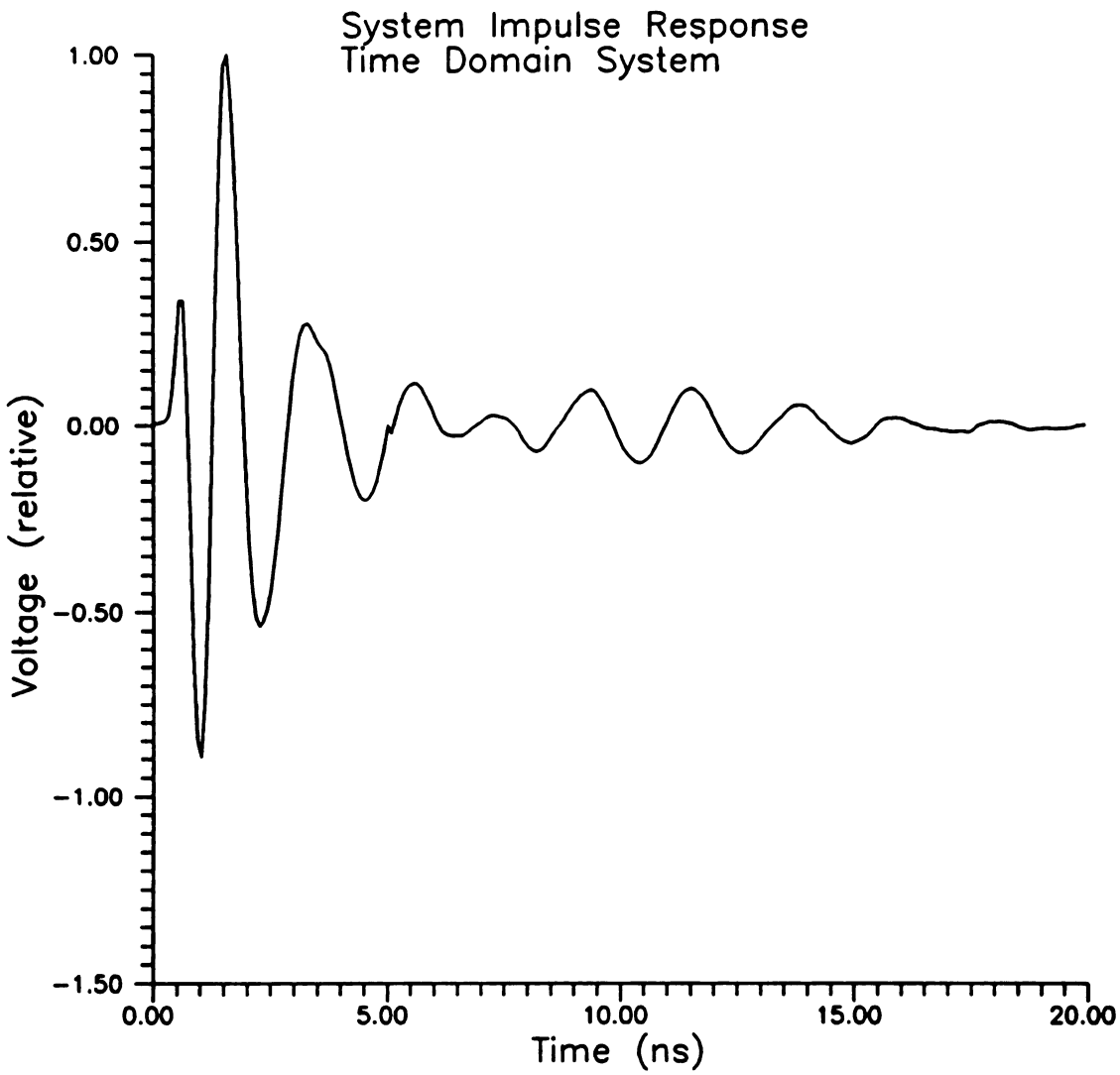

Figure 5.30 Impulse response of time domain system obtained using 14.0 inch diameter sphere as calibration standard. Result normalized to peak value of unity.

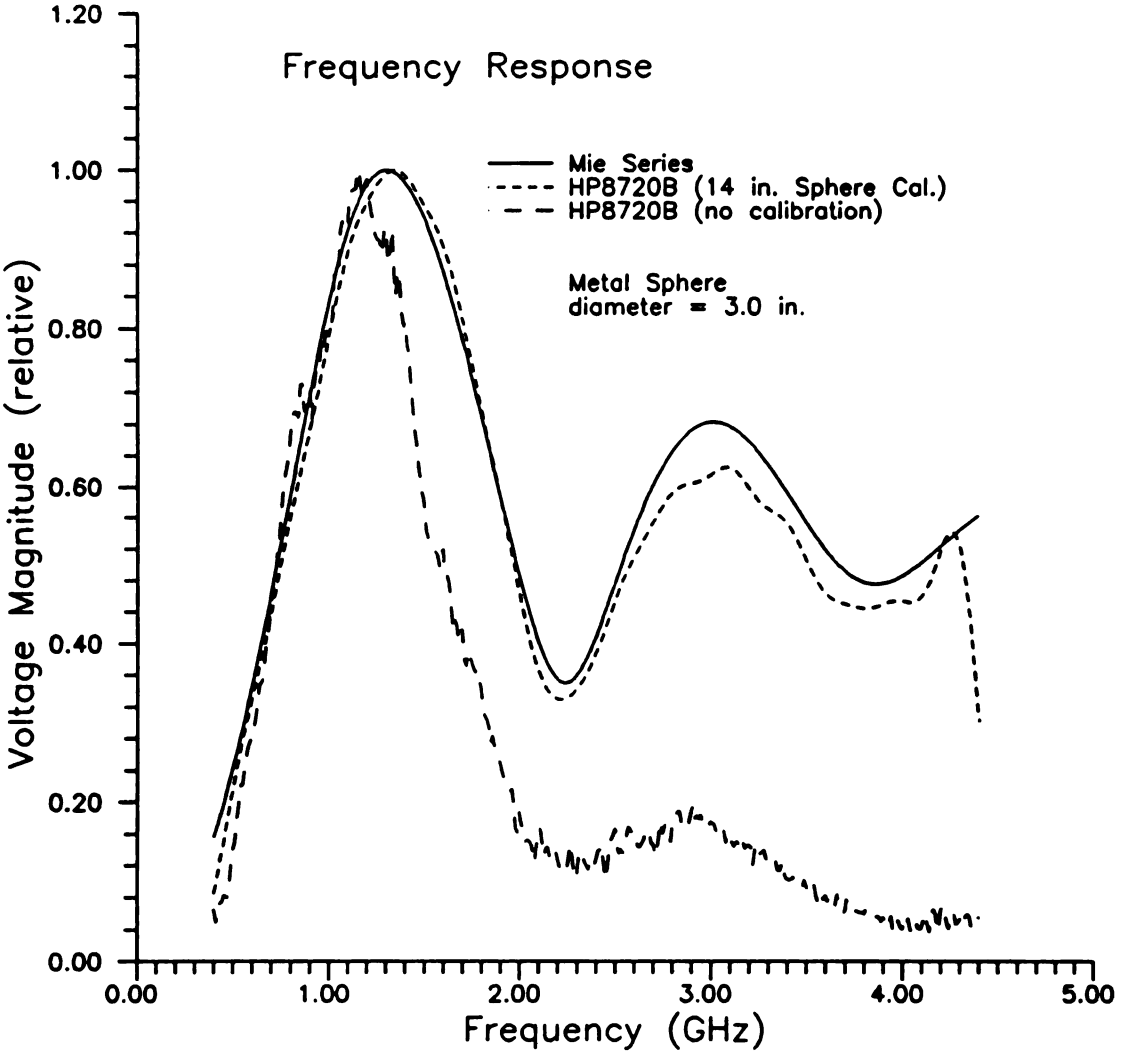

Figure 5.31 Comparison of theoretical and experimental frequency responses of a 3.0 inch diameter brass sphere. Measurements performed using frequency domain system in MSU anechoic chamber.

the sphere and the effects of windowing of extraneous system noise from the measured response. The transient response of the sphere to the DG waveform described previously in Figure 5.8 is shown in Figure 5.32. The agreement between theory and experiment is quite good.

Another good test target is the thin wire. As previously discussed, the theoretical response of these targets can be obtained via the method-of-moments and used to evaluate the usefulness of the calibration. A limited number of comparisons are shown here for single wires, while a large number of comparisons are made for the case of coupled wires in the next chapter.

The spectral response of a single stainless steel wire 6.0 inches long and 0.043 inches in diameter oriented at broadside is shown in Figure 5.33. There is excellent agreement between the theoretical model and the calibrated network analyzer measurement. Note that the response is dominated by the lowest order mode. The higher order modes, especially the even ones, are not excited as strongly in the broadside orientation. The even modes would not be excited at all except that there is a slight bi-static angle in the measurement apparatus. The bi-static angle was included in all theoretical calculations. The response of the wire measured using the time domain system is also shown on this plot. This measurement agrees well within the very limited bandwidth of the time domain measurement system. The transient response to the DG waveform of Figure 5.8 is shown in Figure 5.34. Again the agreement between theory and experiment is very good. The temporal response measured using the time domain measurement system is not shown since the DG waveform is unsuitable for the limited bandwidth of that system. The spectral response of the same wire oriented at 45 degrees

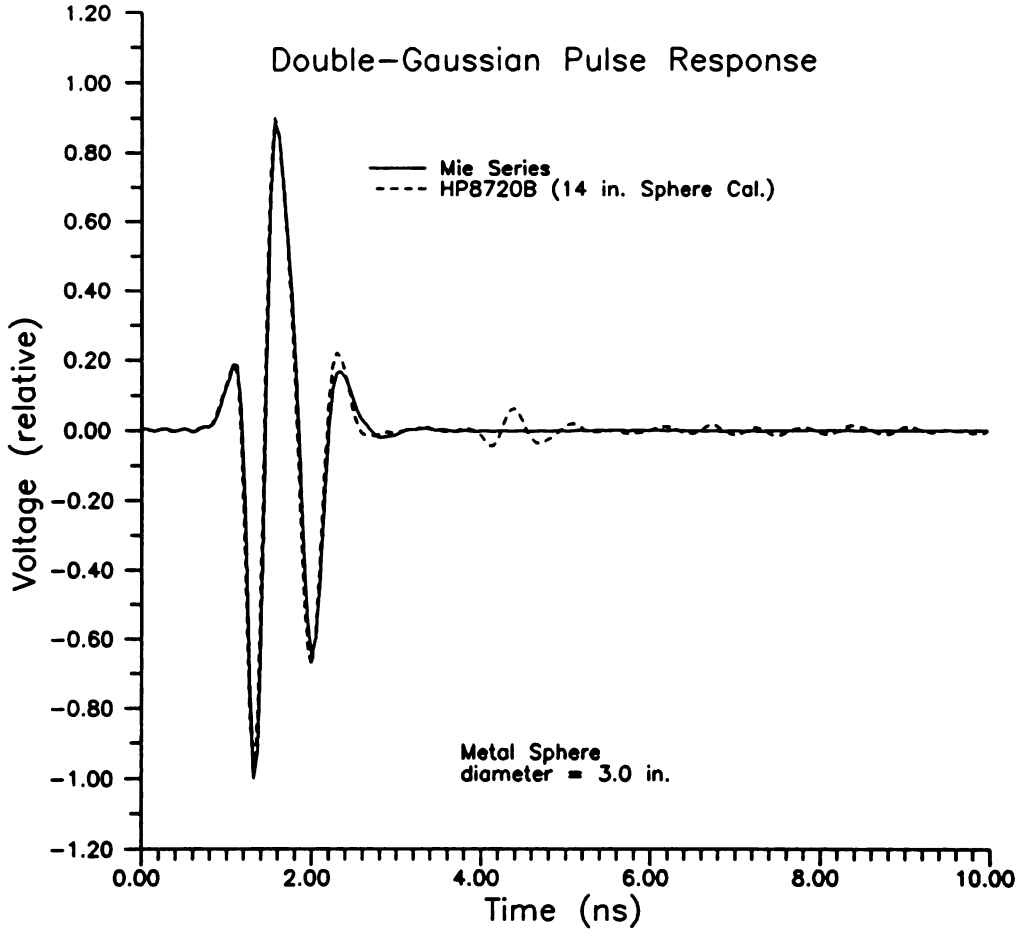

Figure 5.32 Comparison of theoretical and experimental transient responses of 3.0 inch diameter brass sphere. Measurements performed with frequency domain system in MSU anechoic chamber.

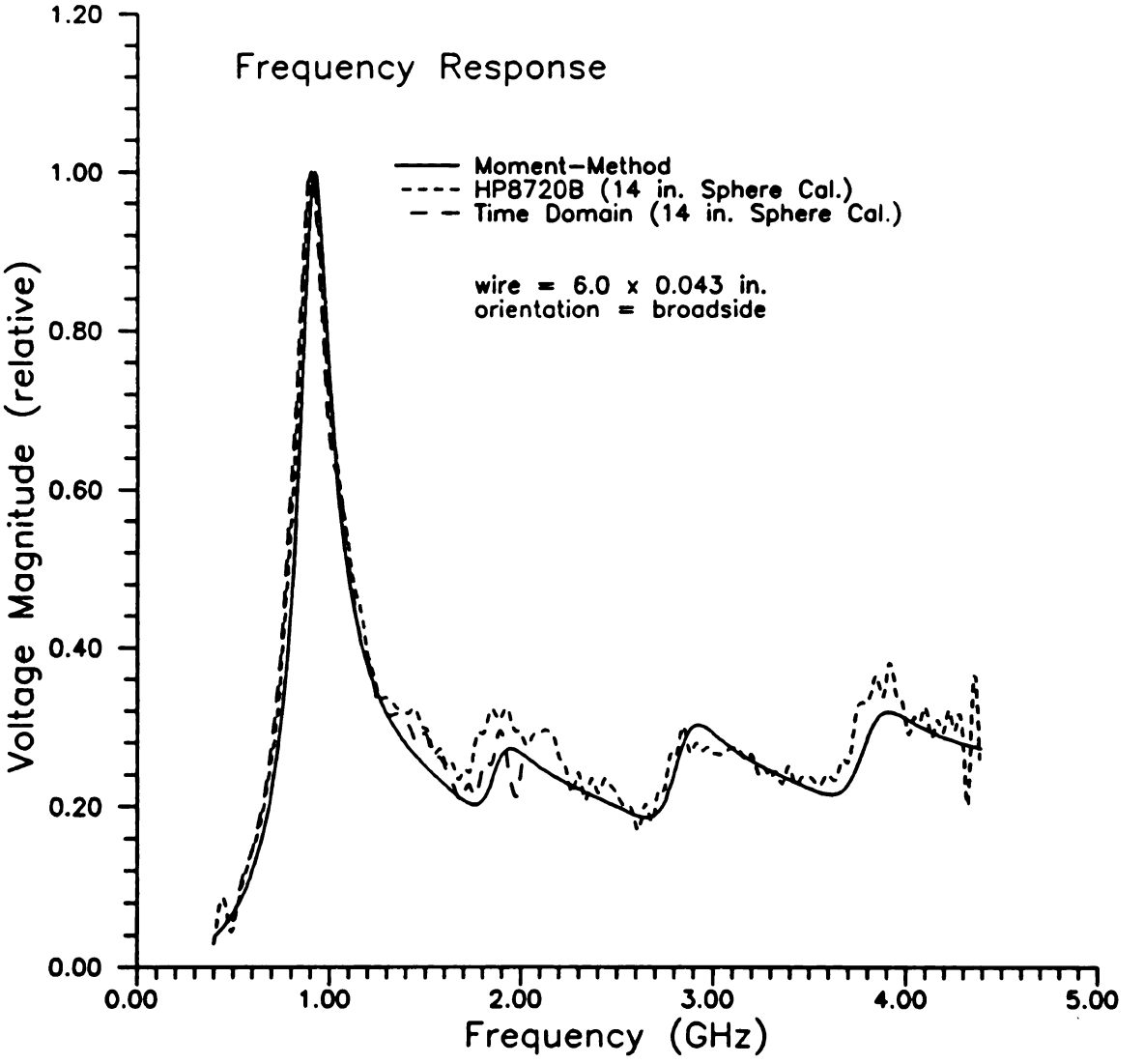

Figure 5.33 Comparison of theoretical and experimental results for the frequency response of a stainless steel wire 6.0 inches long and 0.043 inches in diameter. Measurements performed in MSU anechoic chamber.

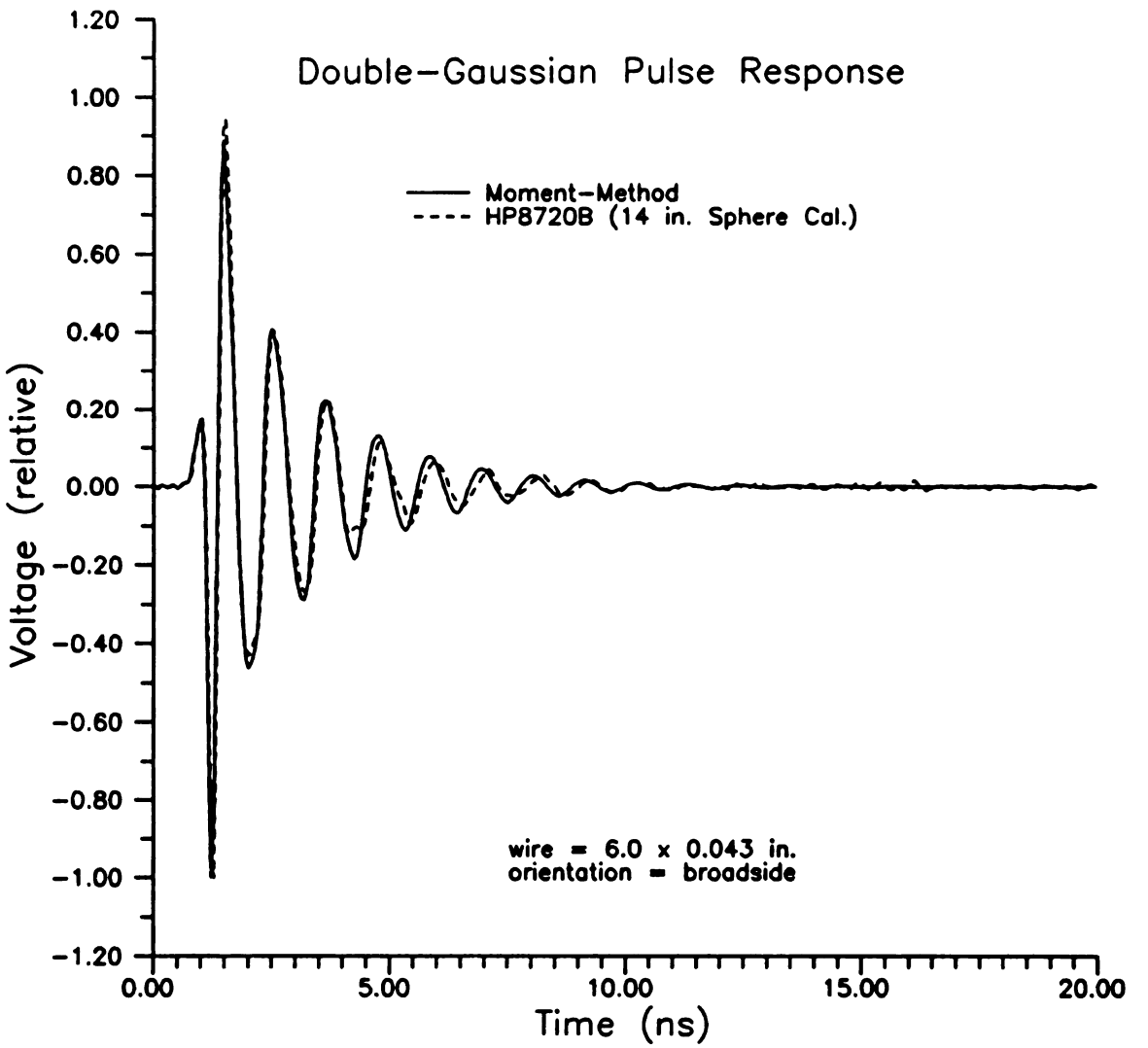

Figure 5.34 Transient scattering response of stainless steel wire 6.0 inches long and 0.043 inches in diameter oriented at broadside. Measurements performed using frequency domain system. Numerical results performed using moment method.

from broadside is shown in Figure 5.36. In this response, the second mode is more strongly excited than the first, while the third mode also has significant energy content. The transient response of the wire in the 45 degree orientation is shown in Figure 5.35. Again, the agreement between theory and experiment is good. Discrepancies between theory and experiment are most likely due to differences in the angle used in the experiment and the angle used in the theoretical model.

5.9 Measurement of Canonical Targets using Wire Calibrator

A thin wire can also be used as a calibration target. To demonstrate the use of a thin wire as a calibration target, the 6.0 x 0.043 inch wire was measured for broadside orientation. This response was taken as the calibration standard. Then, the response of the 3.0 inch sphere was computed using this calibration measurement. The frequency domain result is shown in Figure 5.37 while the time domain result is shown in Figure 5.38. Again, the agreement between theory and experiment is very good indicating that a thin wire is also a valid calibration target. Note that great care was used in placing the 6.0 x 0.043 inch wire in the broadside position so that angular effects previously discussed were minimized.

A thin wire can also be used as a calibrator for another wire target. In this case the broadside response from the 6.0 x 0.043 inch wire is used as a calibrator for the same wire oriented 45 degrees off broadside. The frequency domain result is shown in Figure 5.39 while the time domain result is shown in Figure 5.40. The theory and experiment agree very well except for the highest frequencies used in the measurement. These discrepancies are probably the result of a slight error from the assumed 45 degree

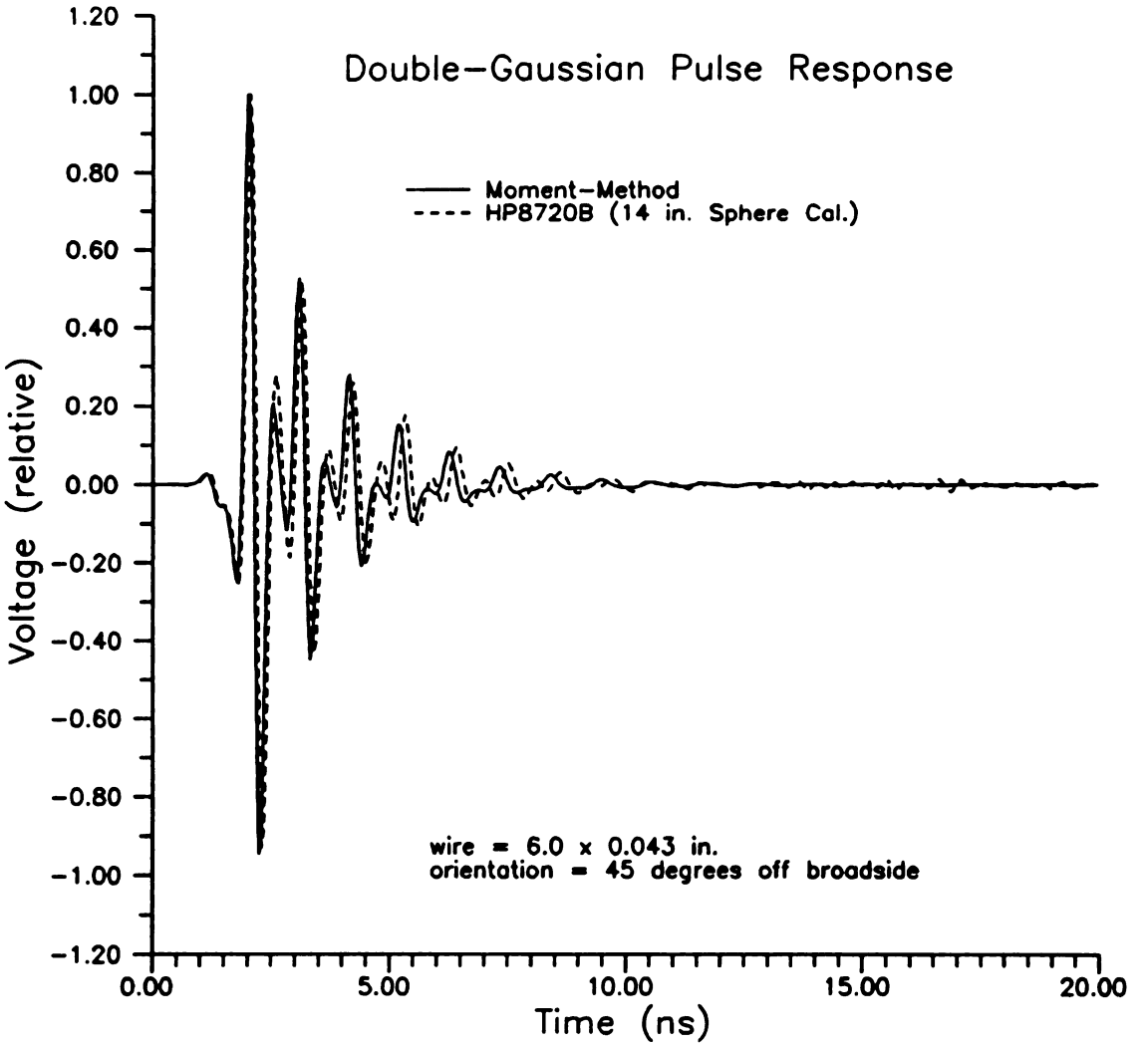

Figure 5.35 Comparison of theory and experiment for the transient response of a 6.0 x 0.043 inch stainless steel wire oriented at 45 degrees from broadside in the MSU anechoic chamber.

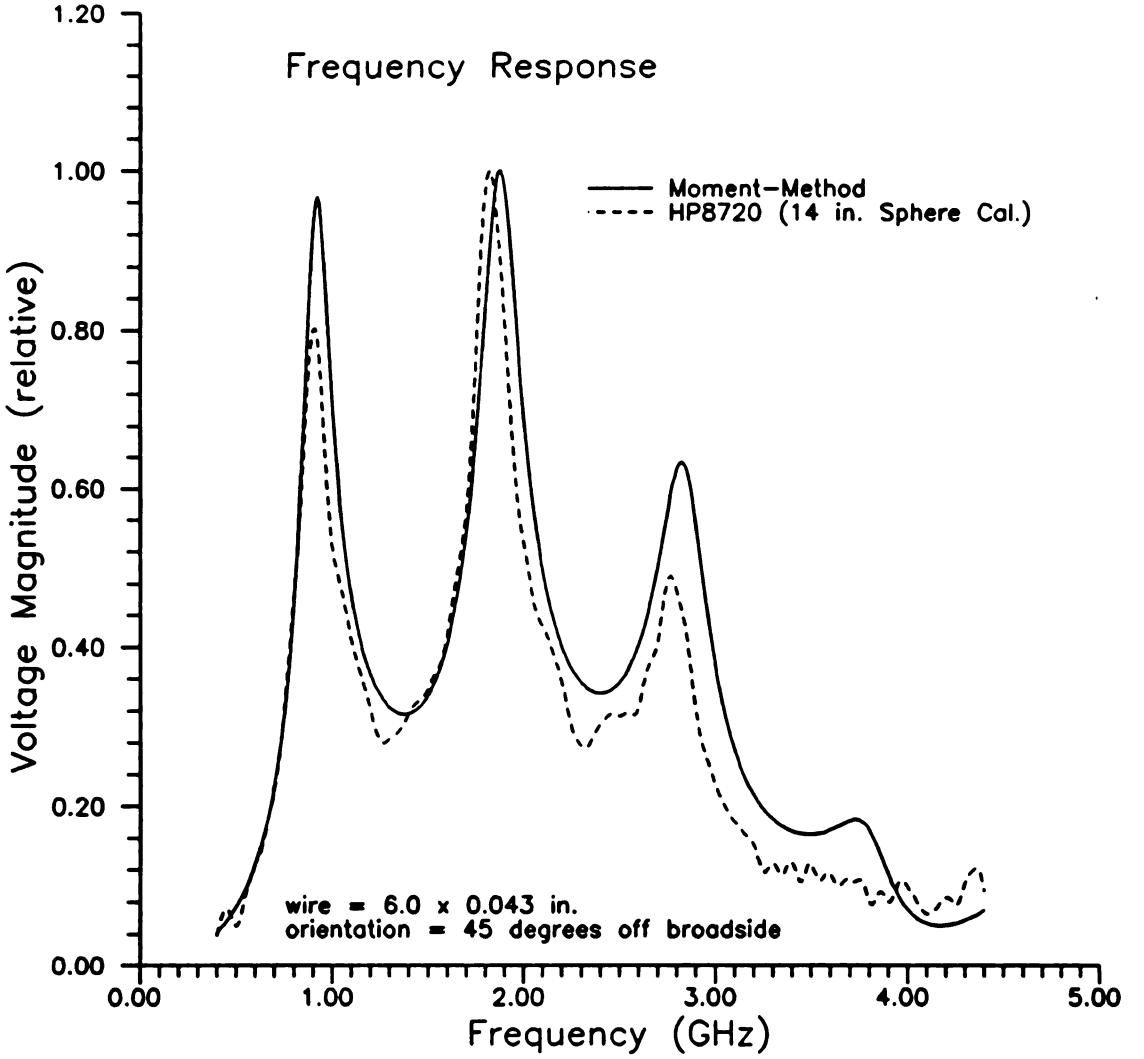

Figure 5.36 Scattering of stainless steel wire 6.0 inches long and 0.043 inches in diameter oriented at 45 degrees from broadside. Measurements performed using frequency domain system. Numerical results computed using moment method.

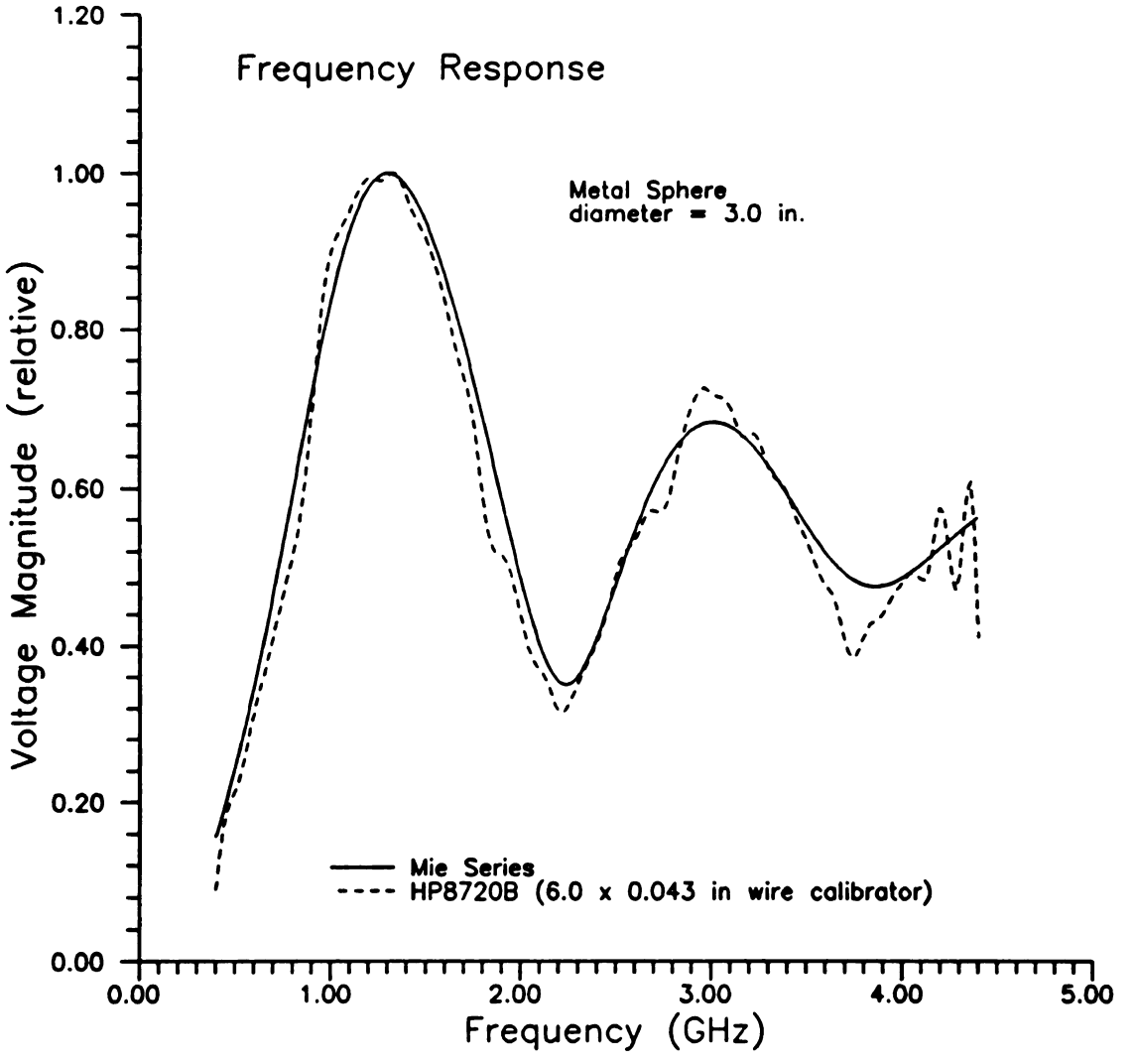

Figure 5.37 Comparison of theory and experiment for a metal sphere 3.0 inches in diameter. A wire of length 6.0 inches and 0.043 inches in diameter oriented at broadside was used as the calibrator for the measured results.

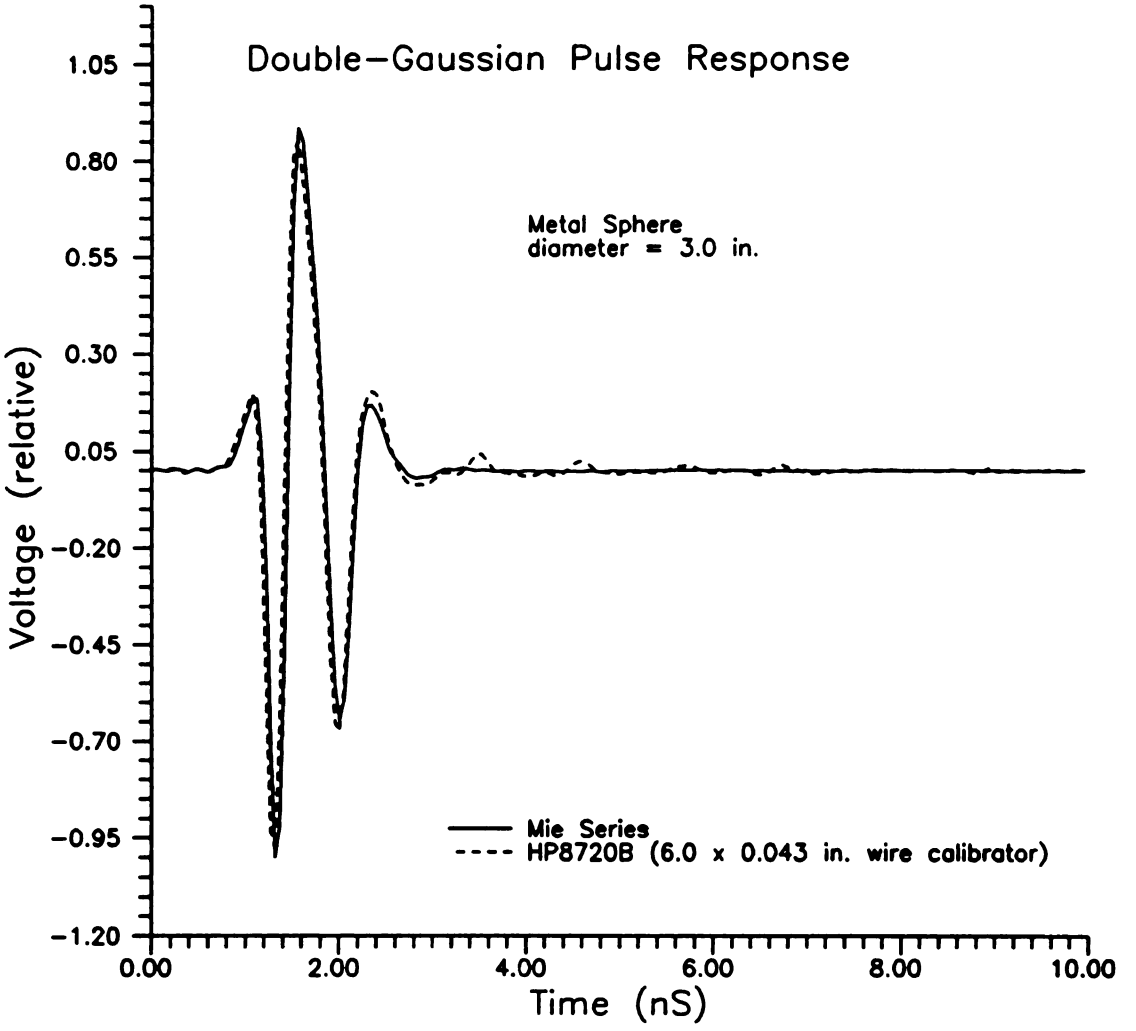

Figure 5.38 Comparison of theory and experiment for transient response of a 3.0 inch diameter metal sphere. A 6.0x0.043 inch wire oriented at broadside was used as the calibrator in the measurements.

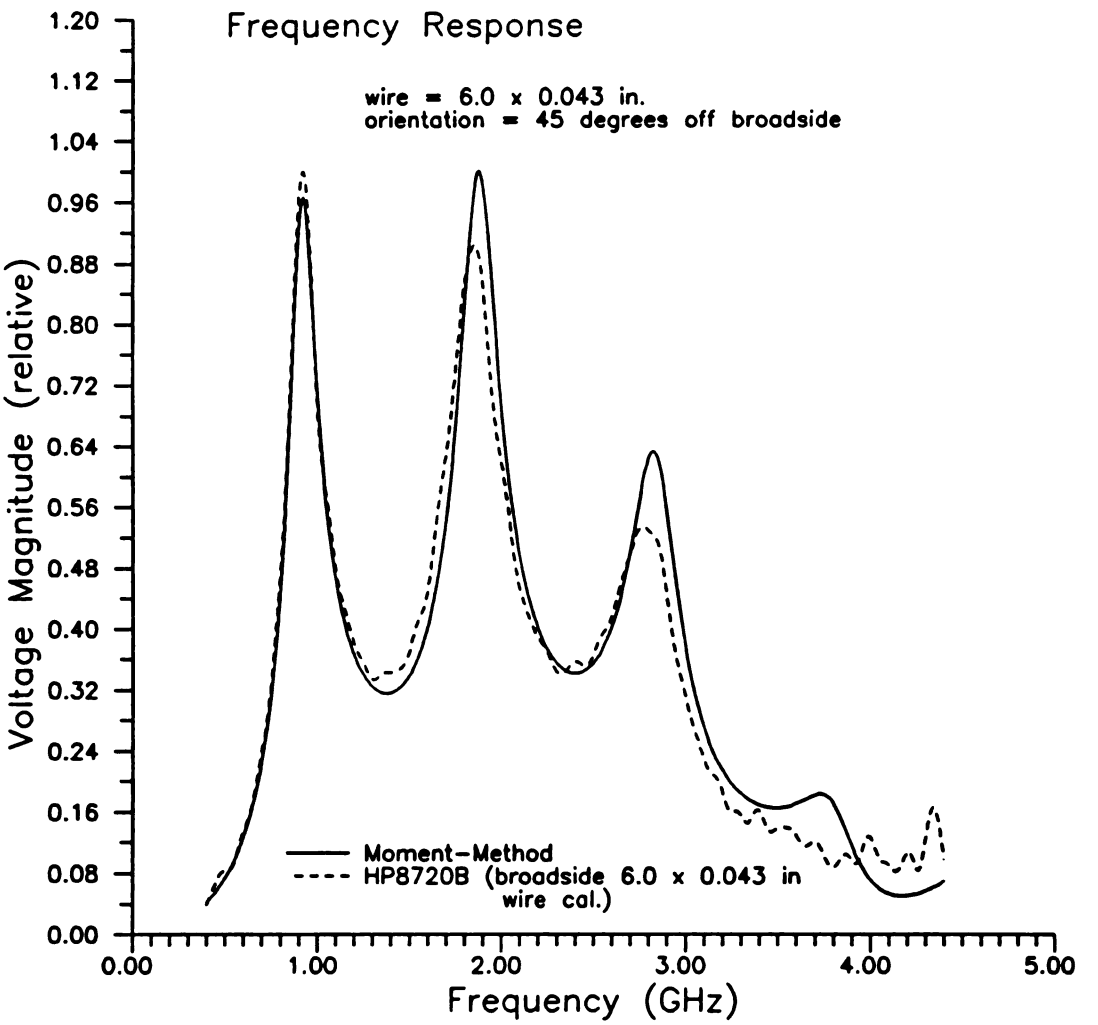

Figure 5.39 Comparison of theory and experiment for frequency response of a 6.0x0.043 inch wire oriented 45 degrees off broadside. Measurements performed using response of same wire oriented at broadside as a calibrator.

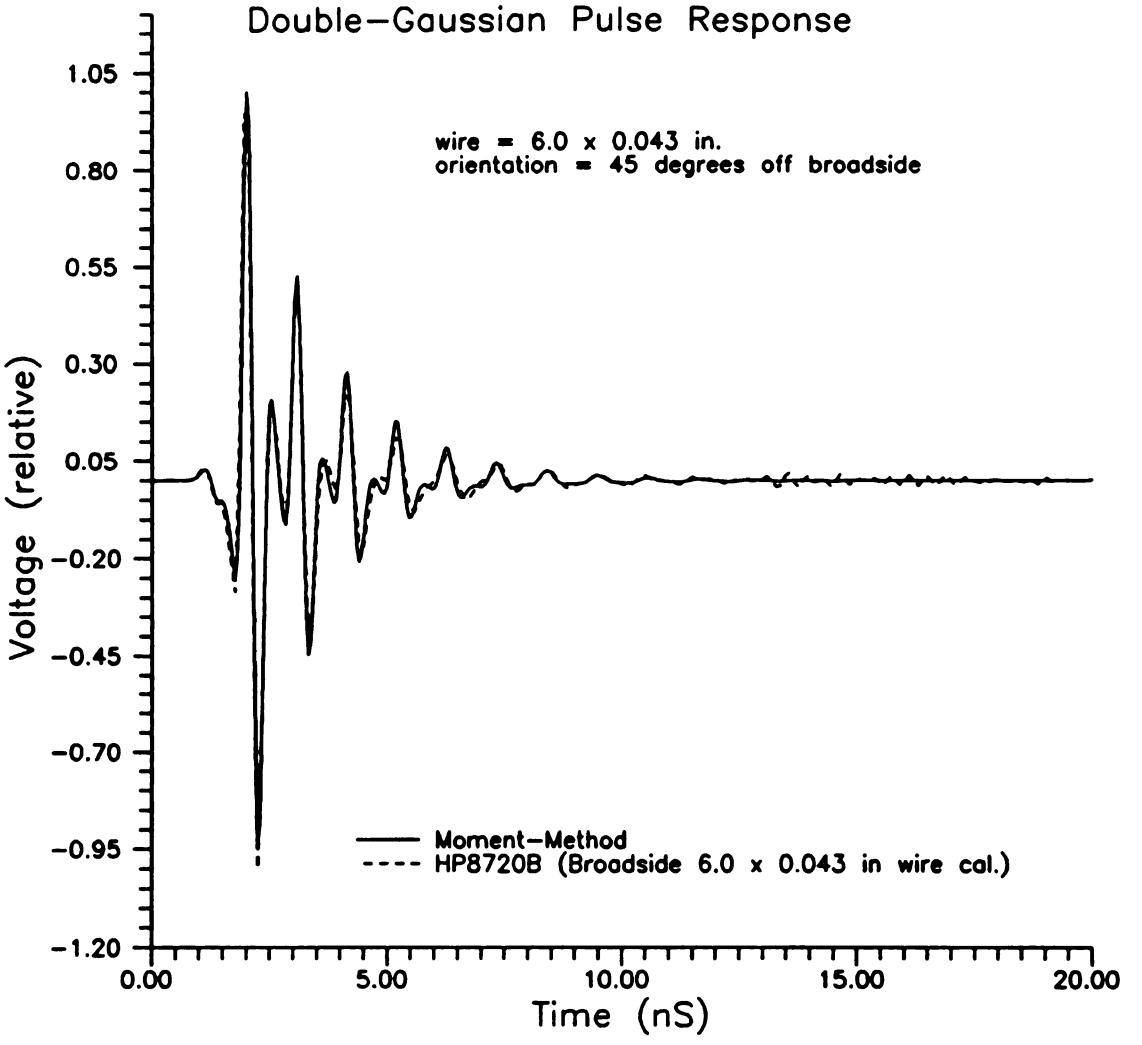

Figure 5.40 Comparison of theory and experiment for the transient response of a 6.0x0.043 inch wire oriented 45 degrees off broadside. Measurements performed using same wire oriented at broadside for calibrator.

angular orientation of the wire within the chamber.

5.10 High-Band Measurement Validation

All of the measurements shown previously were performed using the MSU "low-band" configuration. The "low-band" configuration uses a bandwidth of 0.400 to 4.400 GHz. The lower frequency limit is set by the antennas and anechoic chamber walls, while the upper limit is set by the bandwidth of a Picosecond Pulse Labs 10 dB Amplifier used on the output of the analyzer. A second "high-band" configuration is also available at MSU. This configuration uses a HP8349B microwave amplifier having a gain of approximately 20 dB over the 1.0 to 20.0 GHz band. This allows the measurement band of 1.0 to 7.0 GHz to be used with good success. In this case, the lower limit is set by the amplifier while the upper limit is set by limitations in the antennas and the feed cables. Several modifications were made to the MSU anechoic chamber in an attempt to increase the upper frequency limit beyond 7.0 GHz. The equipment and anechoic chamber configurations are described more fully in Appendix C. The measurements presented here were performed prior to the anechoic chamber upgrade of February 1992. Because of the higher power available in the high-band configuration, the results in the new configuration promise to be even better than the low band measurements previously presented.

As an example of the potential quality of the high-band configuration the 3.0 inch sphere was measured using the 14.0 inch sphere as a calibration standard. Figure 5.41 shows the transient response obtained by applying a 1/10 cosine taper weighing function to the measurements prior to the IFFT. The equivalent pulse of the 1/10 cosine window

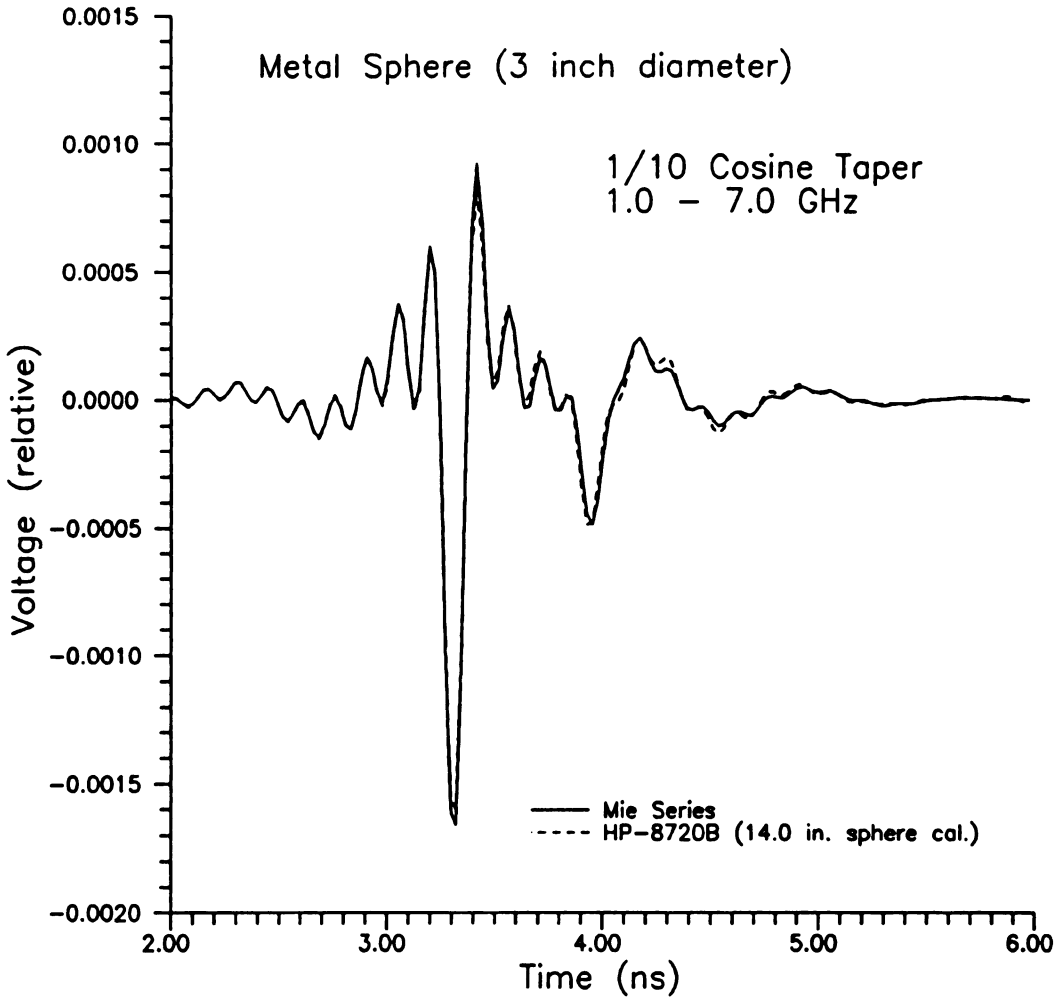

Figure 5.41 Comparison of theory and experiment transient response from a 3.0 inch diameter sphere. Measurements performed using 14 inch diameter sphere as a calibrator.

is shown in Figure 5.42. It should be noted that the data has not been normalized to the peak value in this case indicating that the measurements can be made very accurately relative to an absolute standard such as the 14 inch calibration sphere. The same conclusion holds true for the low-band configuration as well.

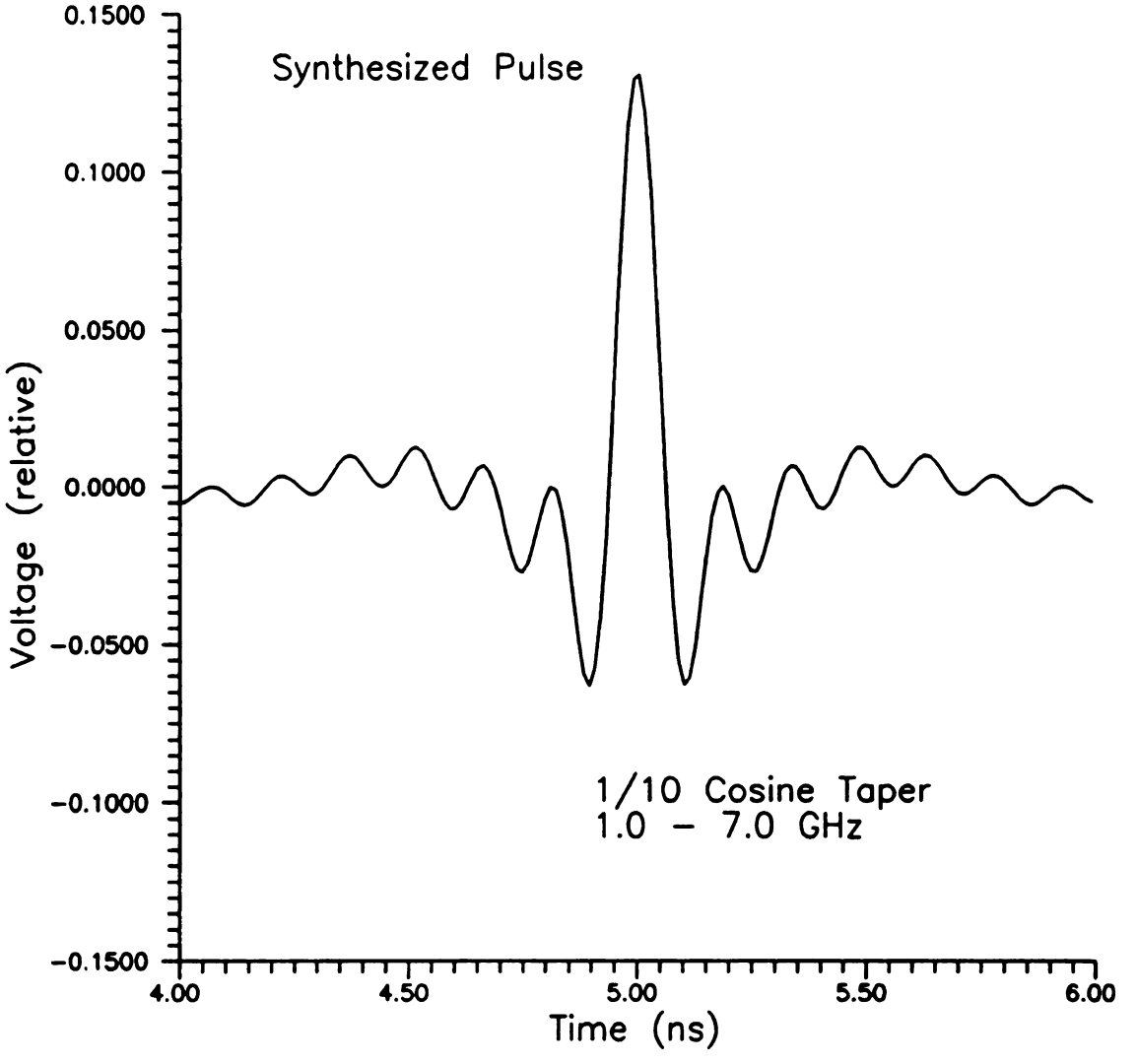

Figure 5.42 Pulse synthesized from 1/10 cosine taper over bandwidth 1.0-7.0 GHz.

Chapter 6

Experimental Results

6.1 Introduction

This chapter discusses experimental results obtained during the course of this research. The calibration method discussed in Chapter 5 is applied to make accurate measurements of the both the early-time and late-time responses of canonical targets as well as complicated aircraft models.

The results can be grouped into several categories. The first group of results is concerned with the topics discussed in Chapter 3. Specifically, the scattered fields and temporal currents of a system of two parallel wires are measured. The scattered field measurements compare favorably with those computed using the frequency domain moment method and thus validate conclusions of Chapter 3. The SEM mode frequencies were extracted from the late-time portion of the transient current response measured using a surface current probe. The extracted mode frequencies are seen to be in agreement with results predicted using the SEM formulation.

Some of the capabilities of the frequency domain measurement system are illustrated for the case of a wire stick airplane model. This is currently the most sophisticated target that can be easily and accurately modeled using available computer programs. In fact, the model measurements indicated areas of improvement in the computer program used for the theoretical calculations.

A third group of results is concerned with experimental determination of the effects of coupling on discrimination using the E-pulse method. To do this, the transient scattered field of isolated and coupled model aircraft are measured using the frequency domain measurement system.

Another group of results is concerned with the amount of energy contained in the late-time vs early-time portion of an aircraft response. Accurate frequency domain measurements are used to determine the fraction of the total energy in practical responses that can be used for target discrimination. Lastly, the measured early-time response of several scale model aircraft are shown and discussed.

6.2 Parallel Wire Systems

The SEM mode frequencies and currents of a system of two parallel wires have been extensively discussed and analyzed in Chapter 3. This section presents measurements supporting the theoretical calculations performed in Chapter 3 regarding the SEM mode frequencies, transient currents, and scattered fields of a coupled wire system. The measurements presented in this section represent, to the best of the author's knowledge, the first ever accurate measurements of transient coupling effects. The importance of measurements such as these should be apparent after the discussions of the theoretical difficulties presented in Chapter 3.

At the start of the investigation of transient coupling, the only way to obtain reliable transient measurements was to use the ground plane transient scattering range. To measure the effect, one monopole was constructed with a slot so that a loop type magnetic flux probe [56] could be attached. A second identical monopole was placed

the same distance from the transmitting antenna and the distance between the monopoles was varied in increments of 5 cm. For each value of separation distance the transient current was recorded. Then, the SEM mode frequencies were extracted from the measured transient current response using the Hybrid E-Pulse/Least Squares technique [21]. In the extraction process, great care was taken to avoid inclusion of any part of the response that occurred prior to the time when the wires could have interacted. The damping coefficient and radian frequencies obtained from this process for the first mode are plotted in Figures 6.1 and 6.2. Results obtained from the HALLEN formulation of the moment method discussed in Chapter 3 are shown for comparison. The accuracy of the results is quite good, especially for the damping coefficient which is typically very difficult to accurately extract from measured data.

To investigate the effects of coupling on the transient response of multiple wire systems several configurations were measured with the frequency domain measurement system which was discussed in Chapter 5. Two identical stainless steel wires were considered. The wire dimensions are 6.0 x 0.043 (diameter) inches. A 14 inch diameter metal sphere was used as a calibration standard. The measurements were performed in the old anechoic chamber configuration prior to February 1992 as shown in Appendix C. The "low band" (0.400-4.4 GHz) configuration was used throughout. The double gaussian weighting function described in Chapter 5 was used to smooth the impulse responses. For purposes of comparison between theory and experiment, all curves are normalized to a peak value of unity. This normalization is appropriate since the discrimination and detection schemes used in this thesis are dependent only on the spectral content and the shape of the waveform and not on the overall amplitude of the

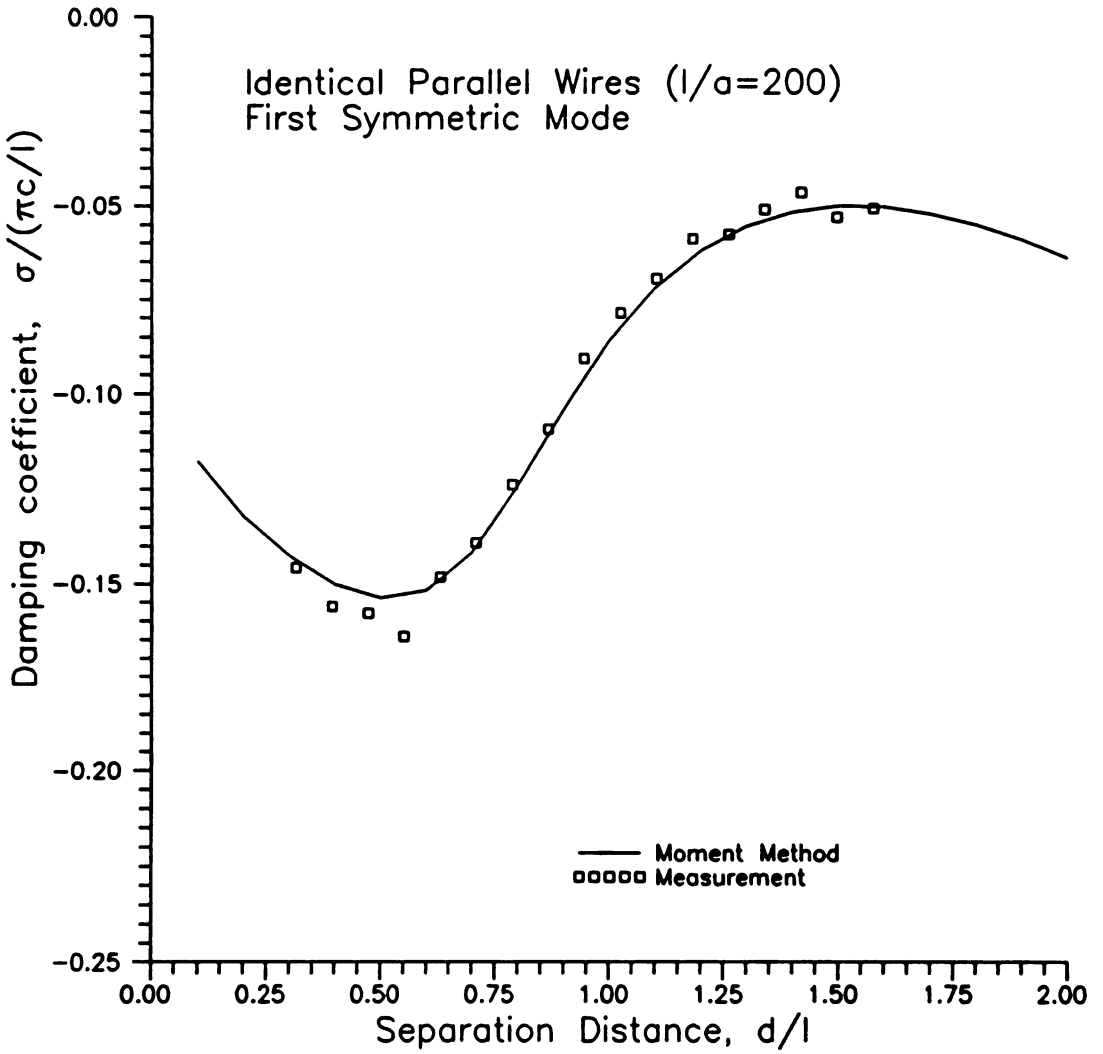

Figure 6.1 Damping coefficient of lowest order symmetric mode for two parallel wires (l/a = 200) extracted from surface current measurements.

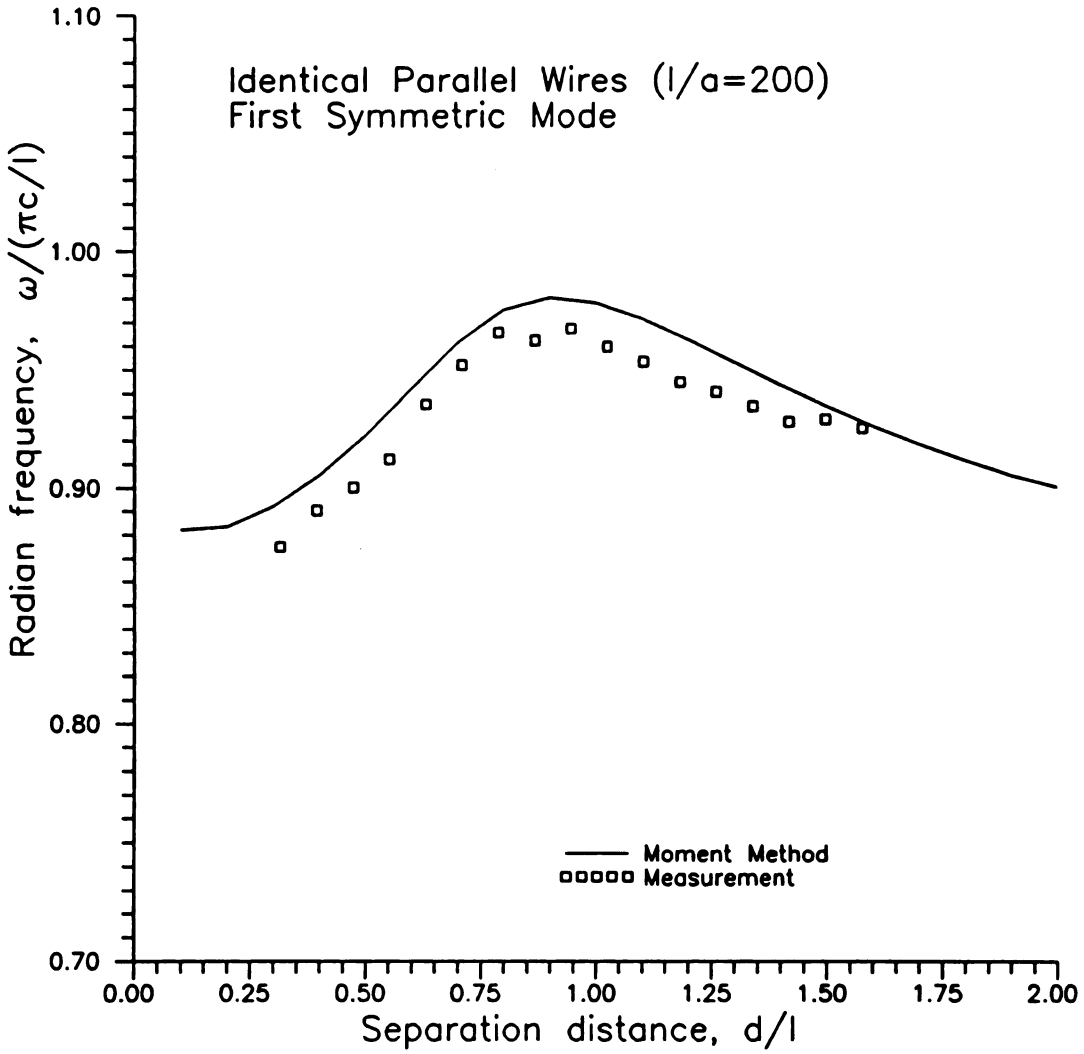

Figure 6.2 Radian frequency of lowest order symmetric mode of two parallel wires (l/a = 200) extracted from surface current measurements.

response.

Figures 6.3 and 6.4 show the near backscatter spectral and temporal responses of the two wire system when the wires are separated 8.0 inches in down range. The wires are in the broadside orientation. Several features are seen in the temporal response. The first response is the initial early-time specular reflection from the first wire. This impulse like response occurs at approximately 1.5 ns. This is followed by the late-time damped sinusoidal response of the first wire. The damped sinusoidal behavior is interrupted by the early-time specular reflection of the second wire. This is the impulse like response that occurs at approximately 2.8 ns. This response is followed by the late-time damped sinusoidal response of the system of wires.

The temporal components are represented in the spectral measurement in different ways. It is immediately obvious that the spectral response has a number of peaks and nulls that appear at approximately integer multiples of one another. This effect is caused by the presence of the two specular responses that are embedded in the temporal response. An approximate temporal representation of the early-time specular response is

$$v_e(t) = \{\delta(t) - \delta(t-\tau)\} * f_s(t) \tag{6.1}$$

where τ is the separation between the responses, and the convolution of $f_s(t)$ represents approximately the difference between a Dirac delta function and the actual specular response. The Fourier transform of this relation is

$$V_e(f) = W(f)\{1+e^{-j\omega\tau}\} = W(f)e^{-j\frac{\omega\tau}{2}}\{e^{j\frac{\omega\tau}{2}}+e^{-j\frac{\omega\tau}{2}}\} \tag{6.2}$$

The magnitude of this spectrum is

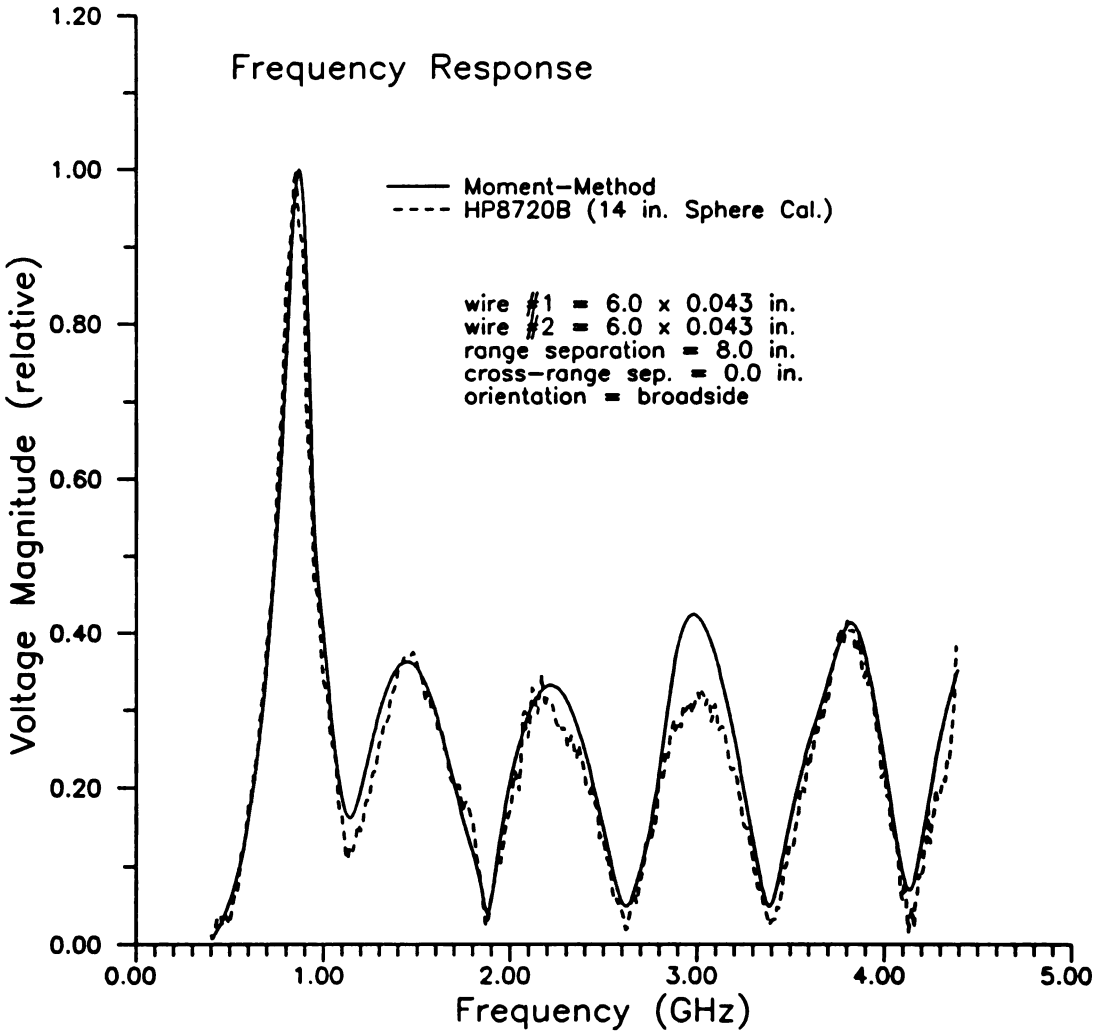

Figure 6.3 Spectral response of two parallel 6.0 x 0.043 inch wires separated by 8.0 inches in down range.

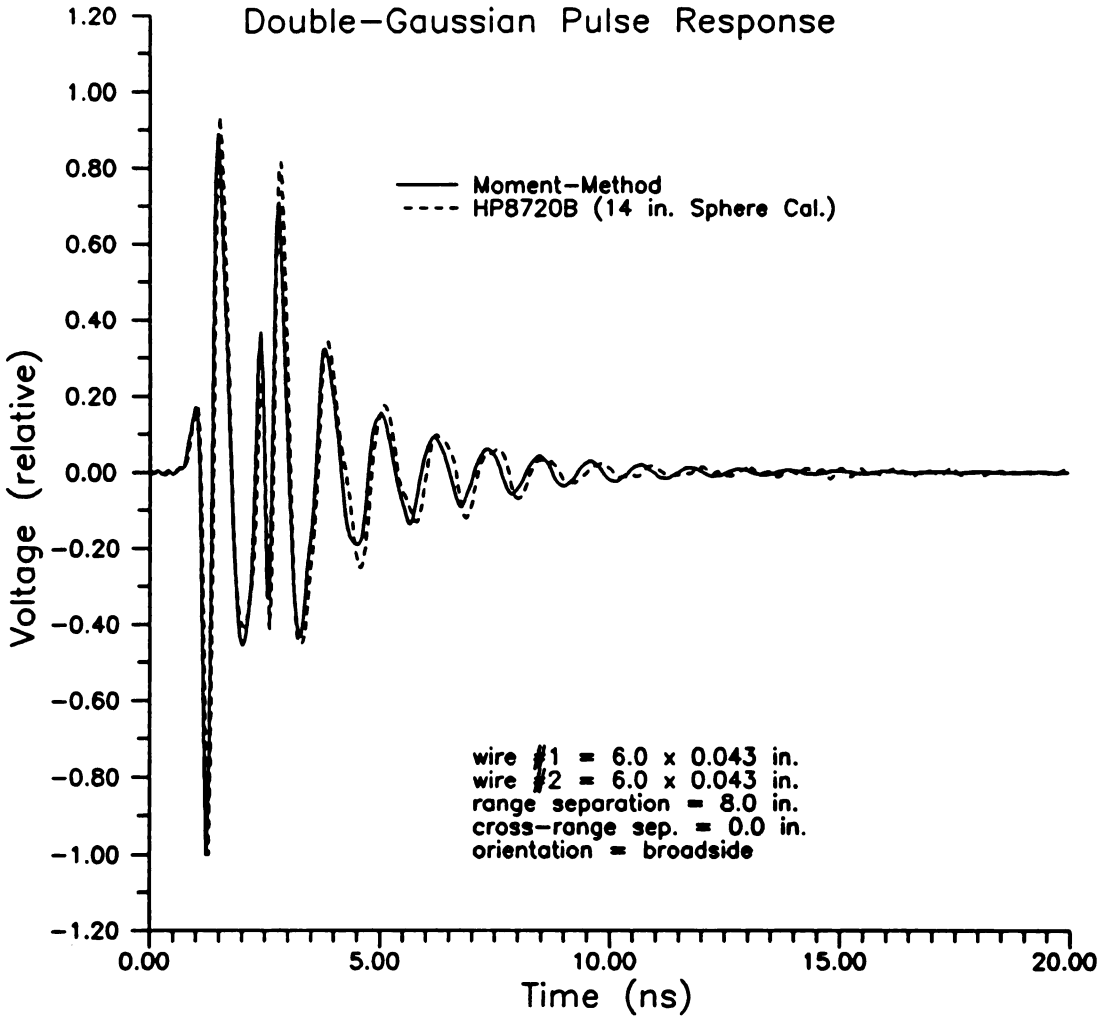

Figure 6.4 Double-Gaussian pulse response of two 6.0 x 0.043 inch wires separated by 8.0 inches in down range.

$$|V_e(f)| = |W(f)| 2 \cos\frac{\omega\tau}{2} \tag{6.3}$$

which has nulls and peaks separated by

$$\Delta f = \frac{1}{\tau} \tag{6.4}$$

For 8.0 inch down range separation this calculation gives 750 MHz between nulls or between peaks. This number is consistent with the measurements.

Also apparent in the spectral response are peaks associated with the late-time portions of the response. The peak at approximately 800 MHz is associated with the first principal mode of the system of wires as well as that of the first wire prior to interaction with the second wire. For close wire spacings however, the spectral response is dominated by the late-time response of the system. For down range separations, the wires currents are excited at different times. This leads to the antisymmetric system mode dominating the response. It is interesting to observe how the response changes as a function of down range separation. As the separation distance between the wires is decreased, the delay between the specular reflections decreases and the distance between the nulls in the spectral response is increased. This effect is clearly seen by comparing the previous results with those of Figures 6.5 and 6.6 where a separation distance of only 6 inches is used and those of Figures 6.7 and 6.8. Note also that the height of the peak associated with the first principal mode has increased relative to the rest of the spectrum, while the duration of the temporal response is correspondingly increased.

Finally, consider the case when the wires are separated in down range by only 2.0 inches. These results are shown in Figures 6.9 and 6.10. There are no nulls within the measurement bandwidth due to the specular reflections in the spectral response. It is seen

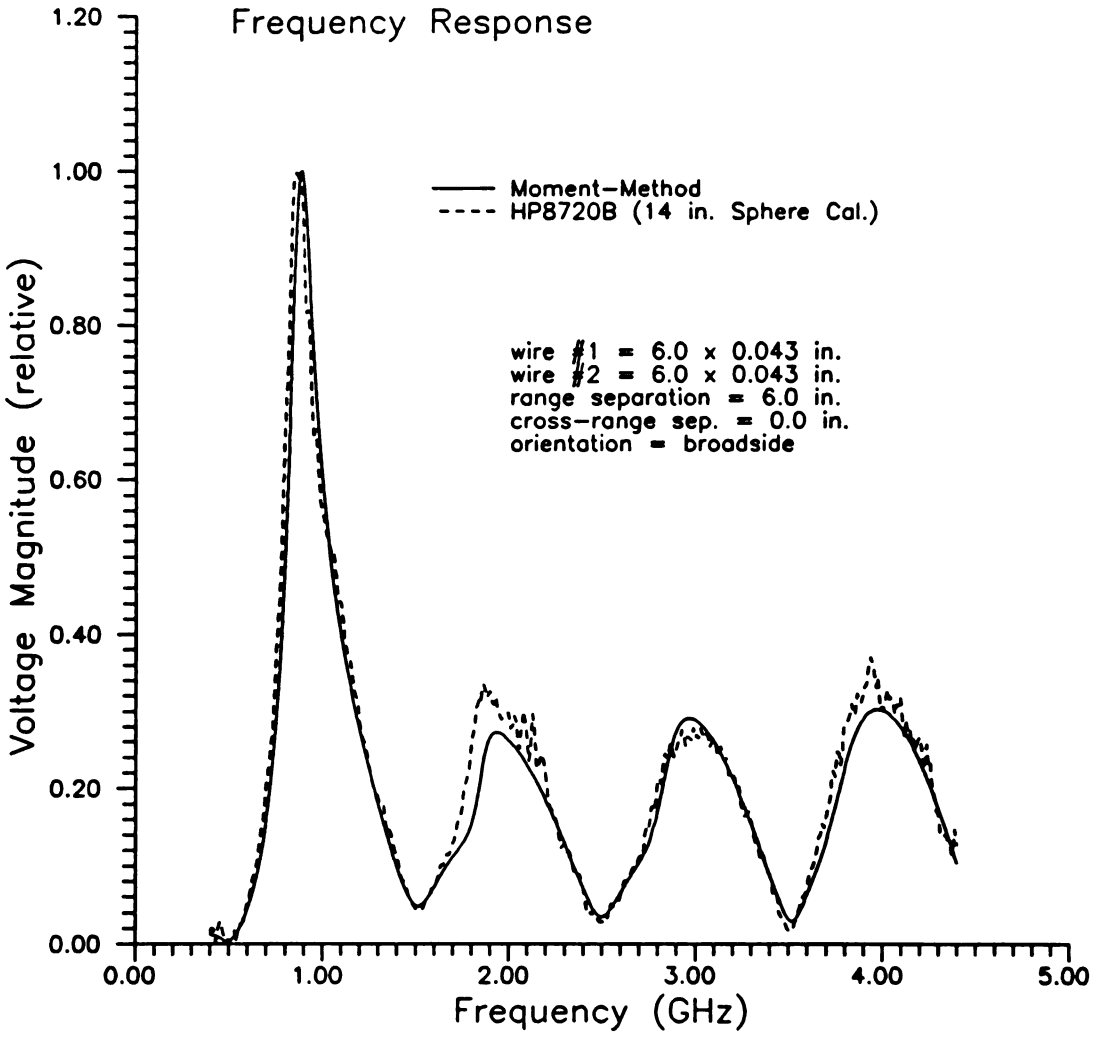

Figure 6.5 Spectral response of two parallel 6.0x0.043 inch wires separated by 6.0 inches in down range.

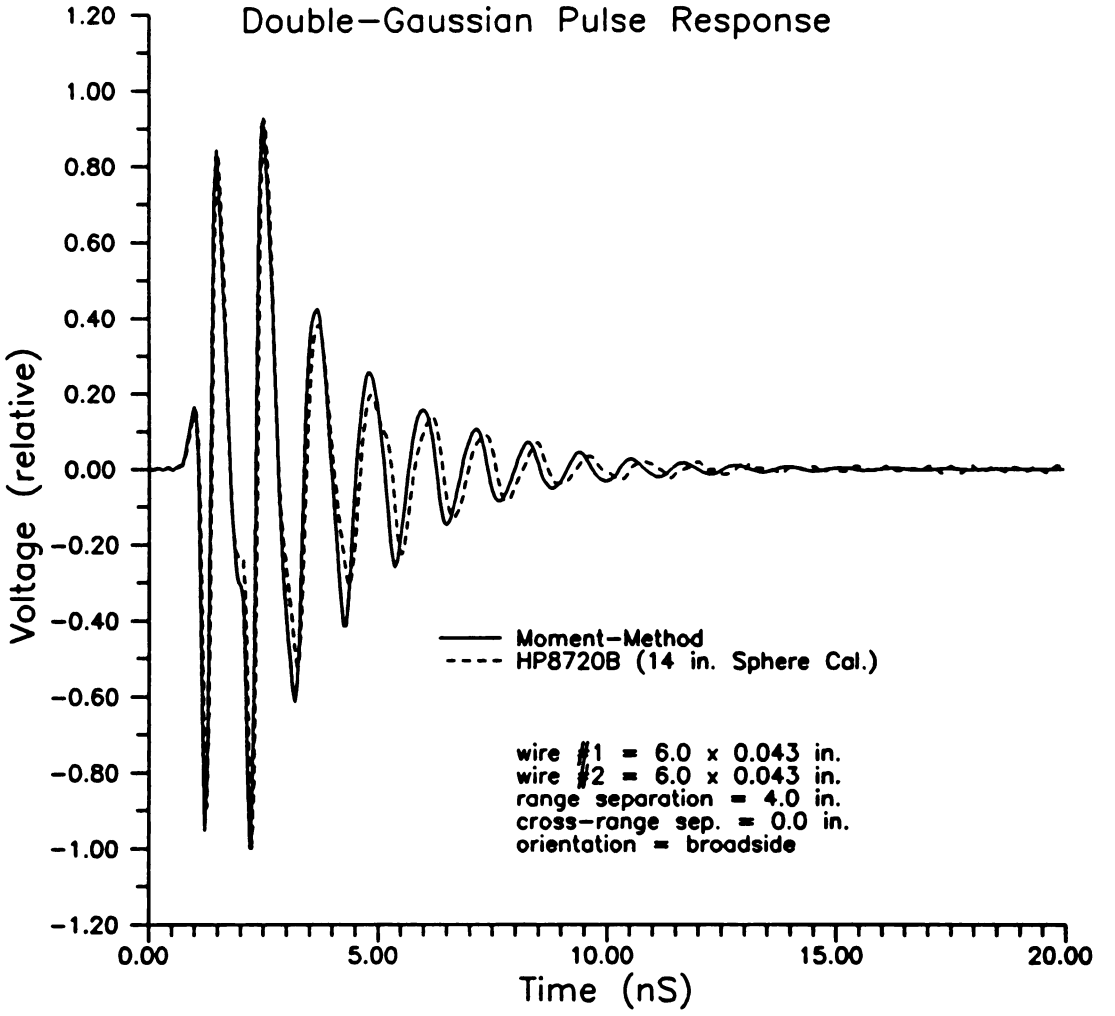

Figure 6.6 Double-Gaussian pulse response of two 6.0x0.043 inch wires separated by 6.0 inches in down range.

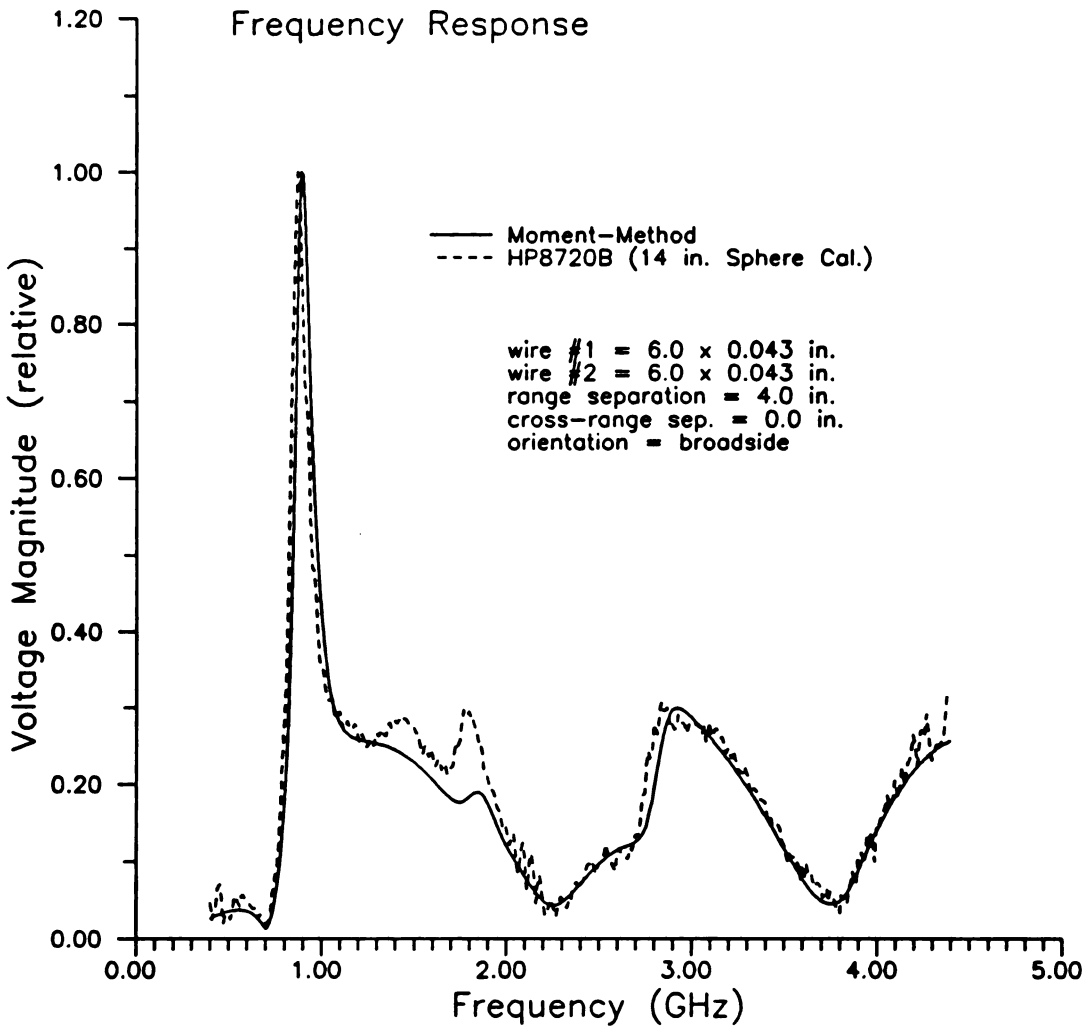

Figure 6.7 Spectral response of two 6.0x0.043 inch wires separated by 4.0 inches in down range.

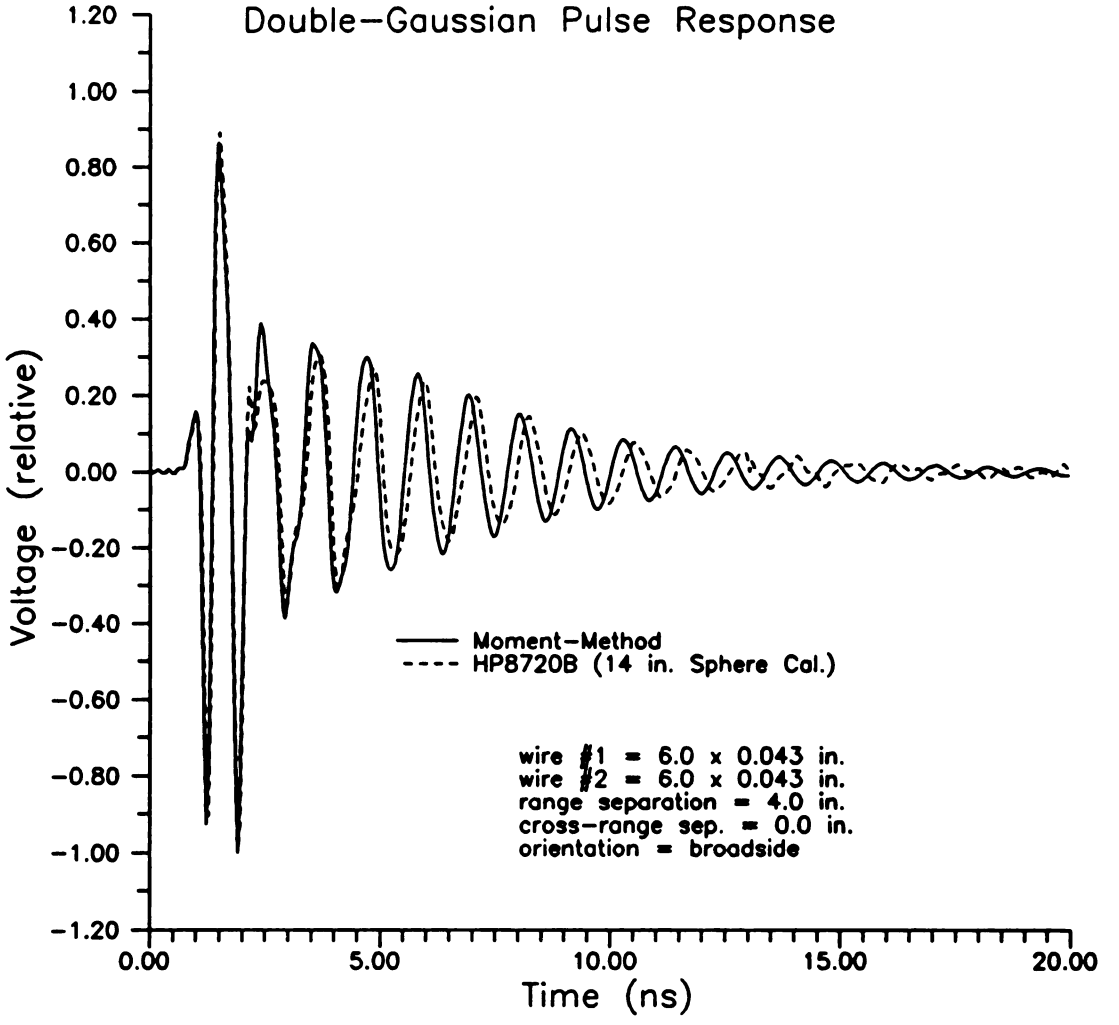

Figure 6.8 Double-Gaussian pulse response of two 6.0x0.043 inch wires separated by 4.0 inches in down range.

that the peak associated with the first resonance is very narrow, or equivalently, the temporal response rings for a long time at the first resonant frequency. The increase in Q of the antisymmetric mode is consistent with the calculations of Chapter 3 that show the antisymmetric mode pole moving very close to the $j\omega$-axis. Note that for this case the moment method predicts a narrower resonant peak than is measured. This is in contrast to the other measurements where the agreement is relatively good. It is believed that the difference between theory and experiment is primarily due to resistive losses in the stainless steel wires. These losses are not severe except when the Q of the resonance becomes very high. To test this conjecture, the moment method was modified to account for a distributed resistive loss and the scattering was recalculated for this case. The theory used to account for the loss is well known and is detailed in Appendix A. Since the actual conductivity of the stainless steel wires was unknown, the calculations were performed for several different values that correspond to readily available materials. The resulting curves are shown in Figure 6.11. It is apparent from the figure that resistive losses affect primarily the response at resonance while the off resonance response is not strongly affected. The radian frequency of the peak is relatively unaffected, but as expected, the resistive losses alter the damping coefficient of the mode. Figure 6.12 shows a comparison of the measurements to the curve obtained using $\sigma = 1.57\text{x}10^7$ S/m. The agreement is much better than for the case of a perfect conductor.

Now, consider the case of the same two wires separated in cross range. In this situation, the specular responses from the wires arrive at the receiver at the same time. Since the currents on the wires are excited in unison by the incident electric field, the dominant system resonances are of the symmetric type. From Chapter 3 it was observed

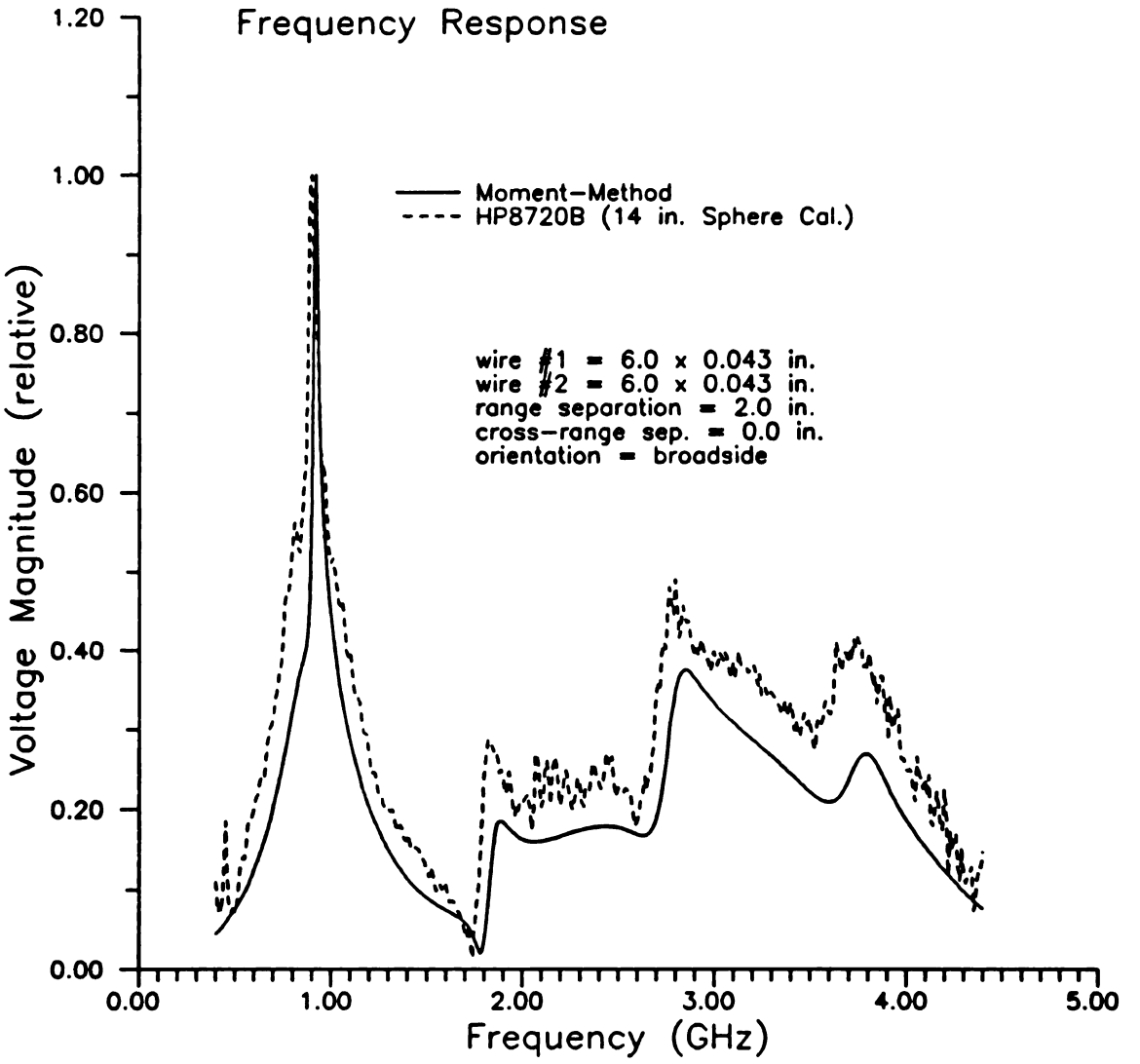

Figure 6.9 Spectral response of two 6.0x0.043 inch wires separated by 2.0 inches in down range.

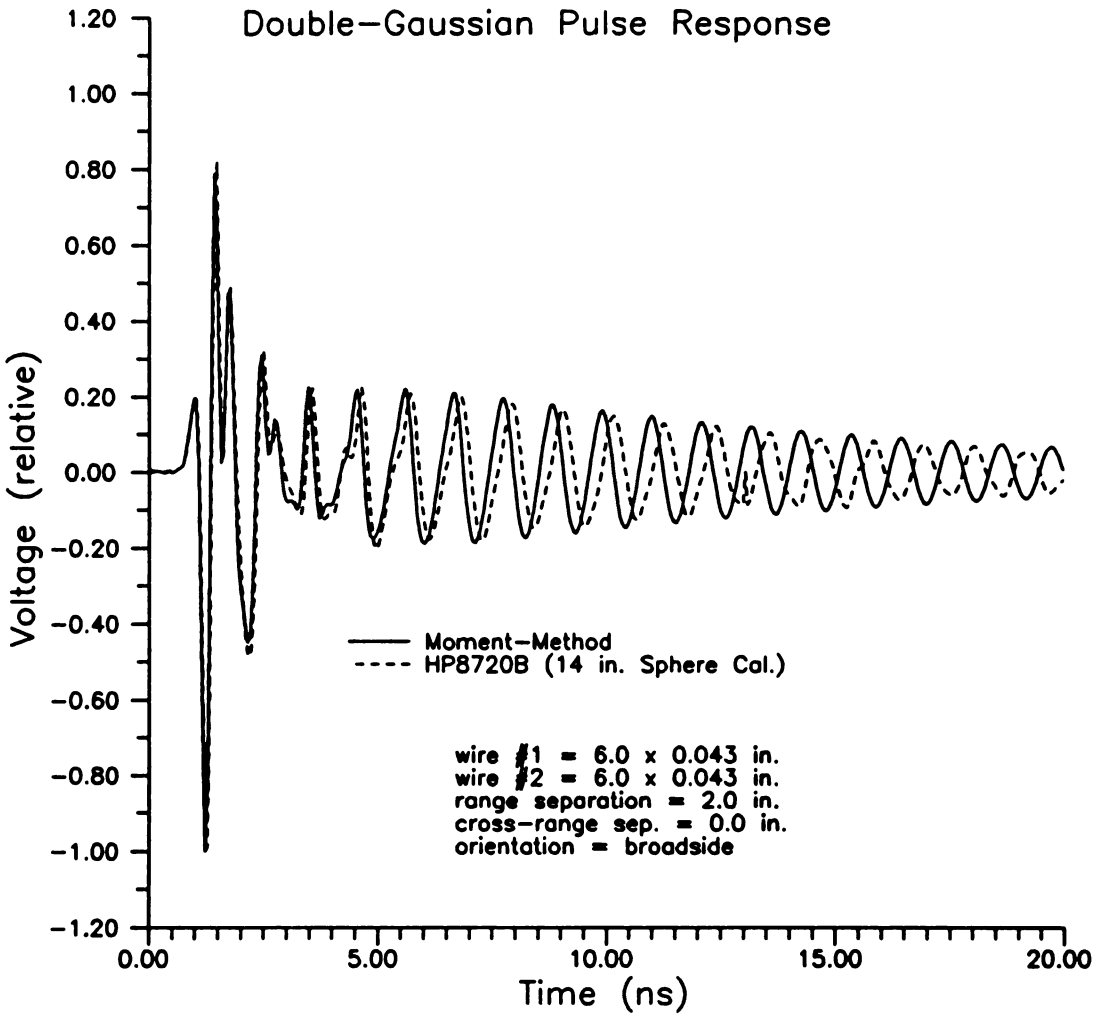

Figure 6.10 Double-Gaussian pulse response of two 6.0x0.043 inch wires separated by 2.0 inches in down range.

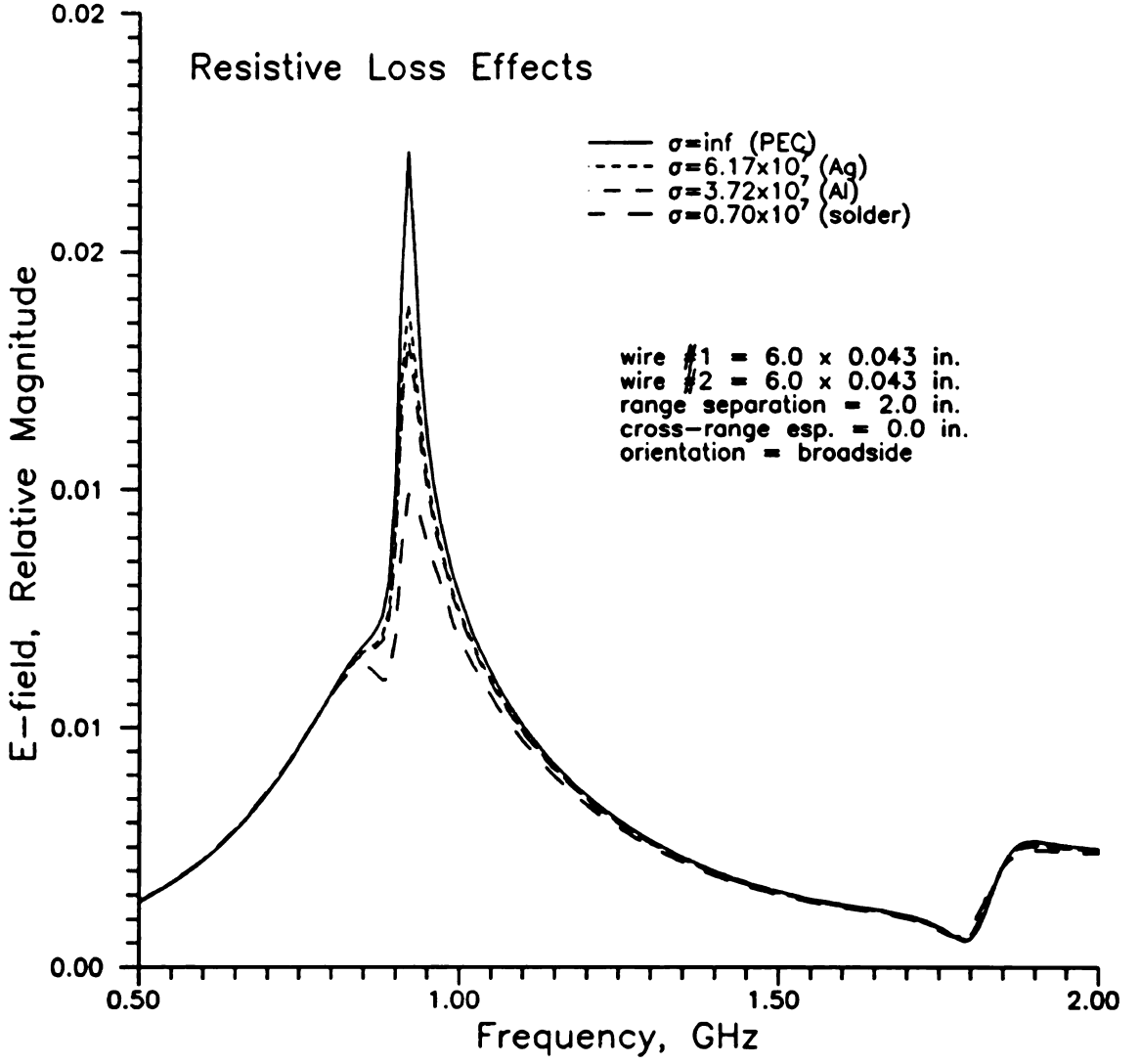

Figure 6.11 Effects of resistive loss on wire scattering - moment method calculations.

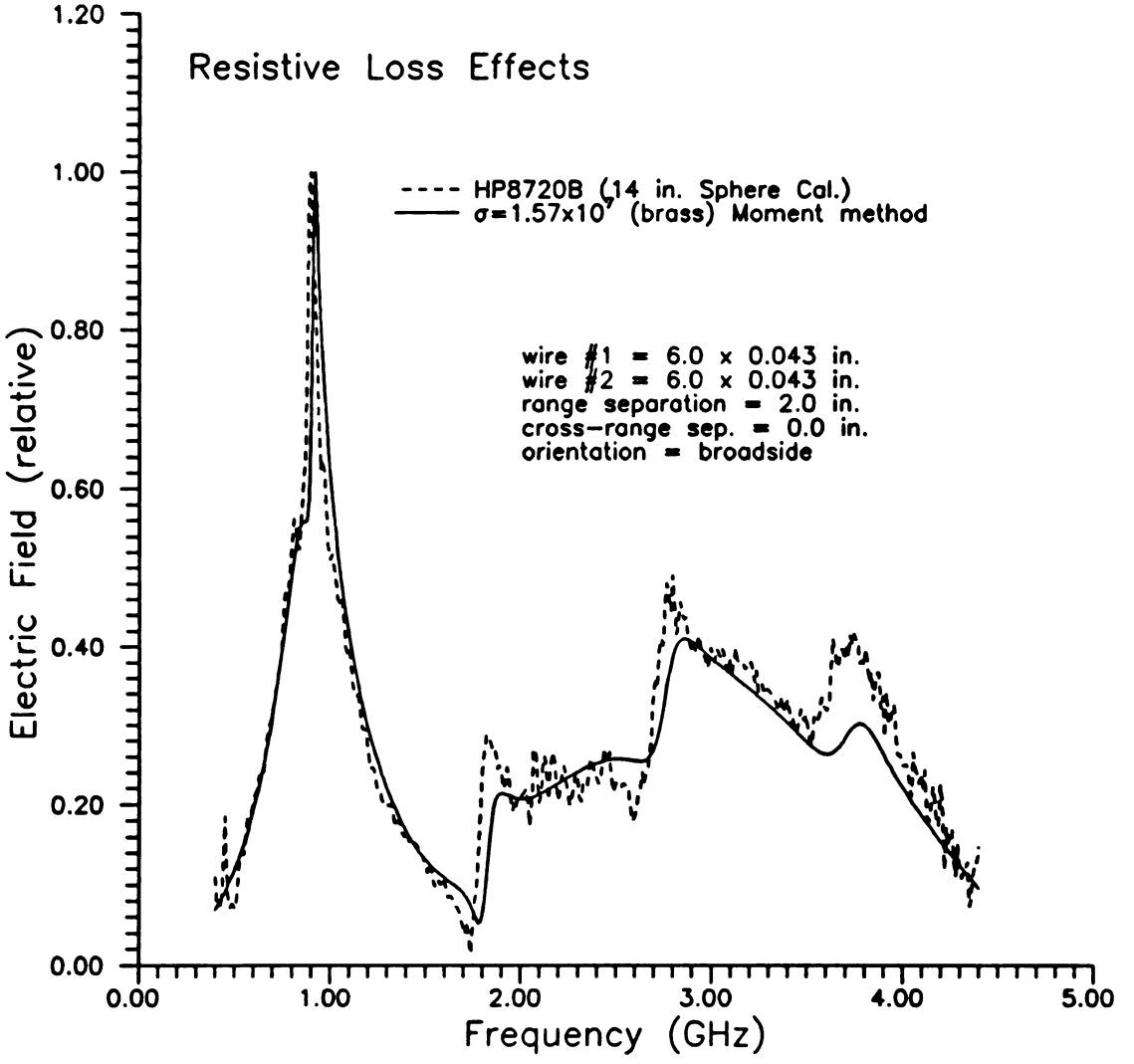

Figure 6.12 Comparison of measurements and theory including resistive losses.

that for close spacing, the dominant symmetric mode has a large negative damping coefficient. This is easily seen in Figures 6.13 and 6.14 which show the spectral and temporal response when the wires are separated by 2 inches in cross range. The difference between this case and the case of 2 inch down range separation is impressive and illustrates the need for detection and discrimination schemes that are insensitive to the shape of the response waveform. As the cross range separation distance is increased, the Q of the symmetric modes is increased and the response is dominated more and more by the early-time response of the system which is characteristic of the response of the isolated wires. These properties are illustrated in the responses for cross range separation of 4.0 inches which are shown in Figures 6.15 and 6.16 and those with a cross range separation of 8.0 inches which are shown in Figures 6.17 and 6.18.

Figure

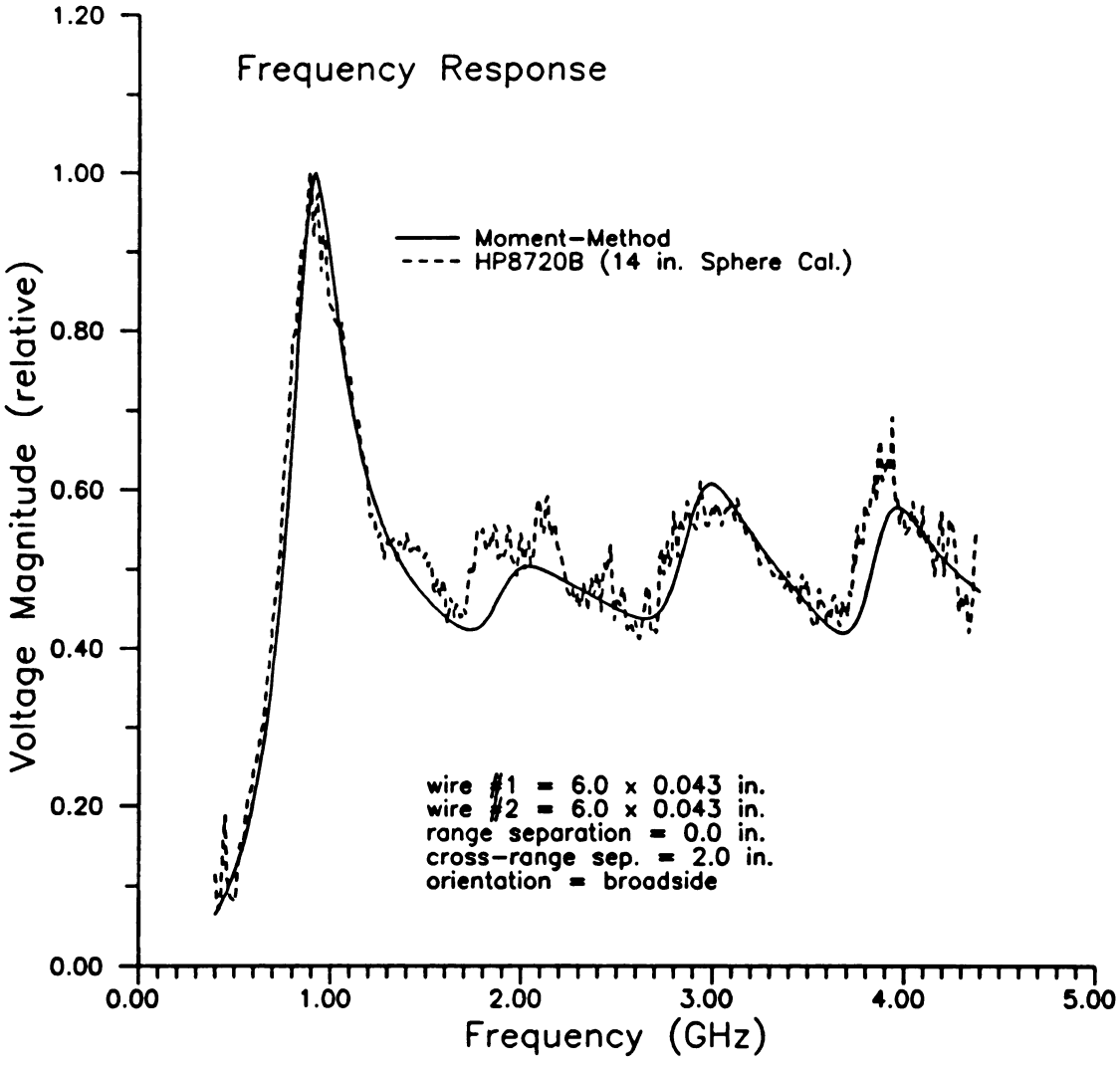

Figure 6.13 Spectral response of two 6.0x0.043 inch wires separated by 2.0 inches in cross range.

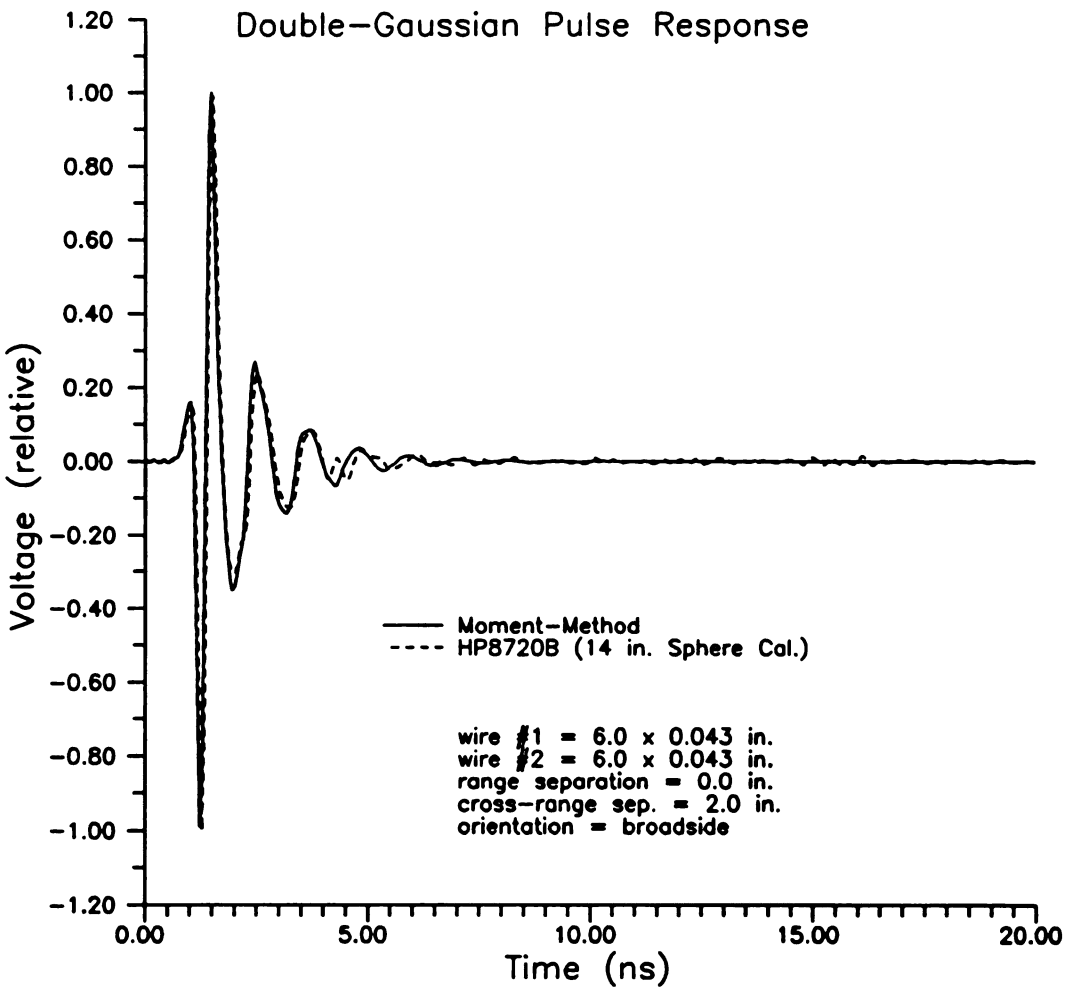

Figure 6.14 Double-Gaussian pulse response of two 6.0x0.043 inch wires separated by 2.0 inches in cross range.

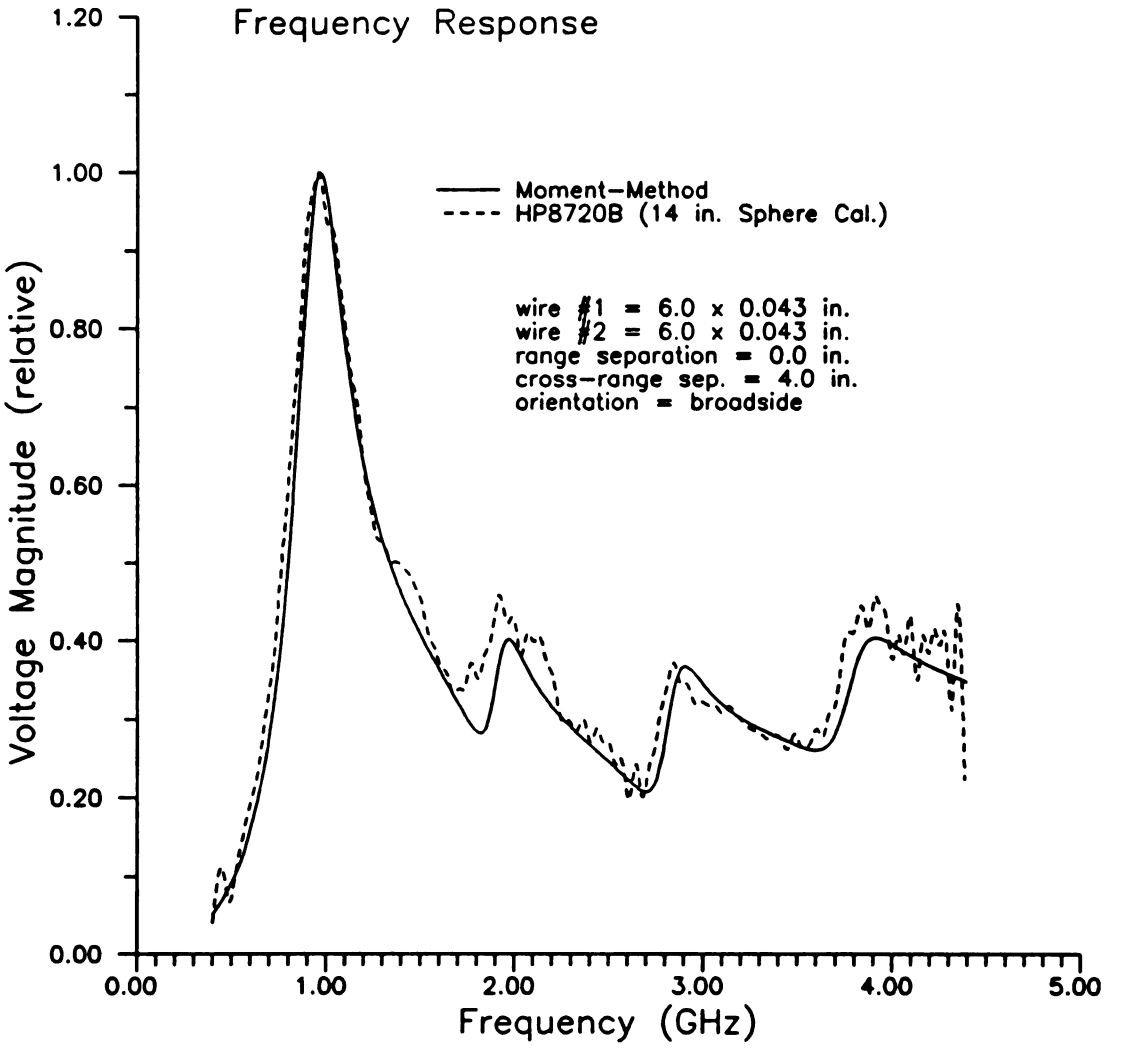

Figure 6.15 Spectral response of two 6.0x0.043 inch wires separated by 4.0 inches in cross range.

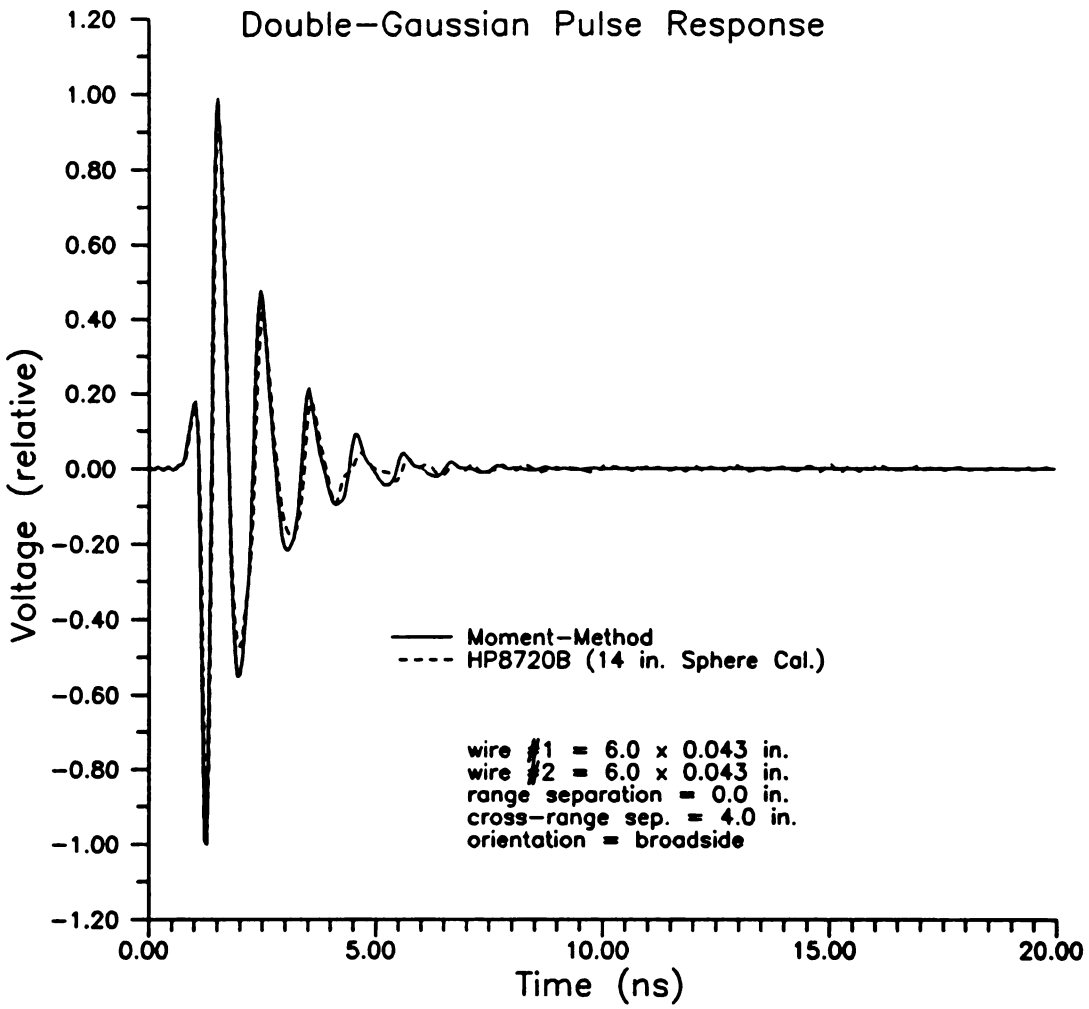

Figure 6.16 Double-Gaussian pulse response of two 6.0x0.043 inch wires separated by 4.0 inches in cross range.

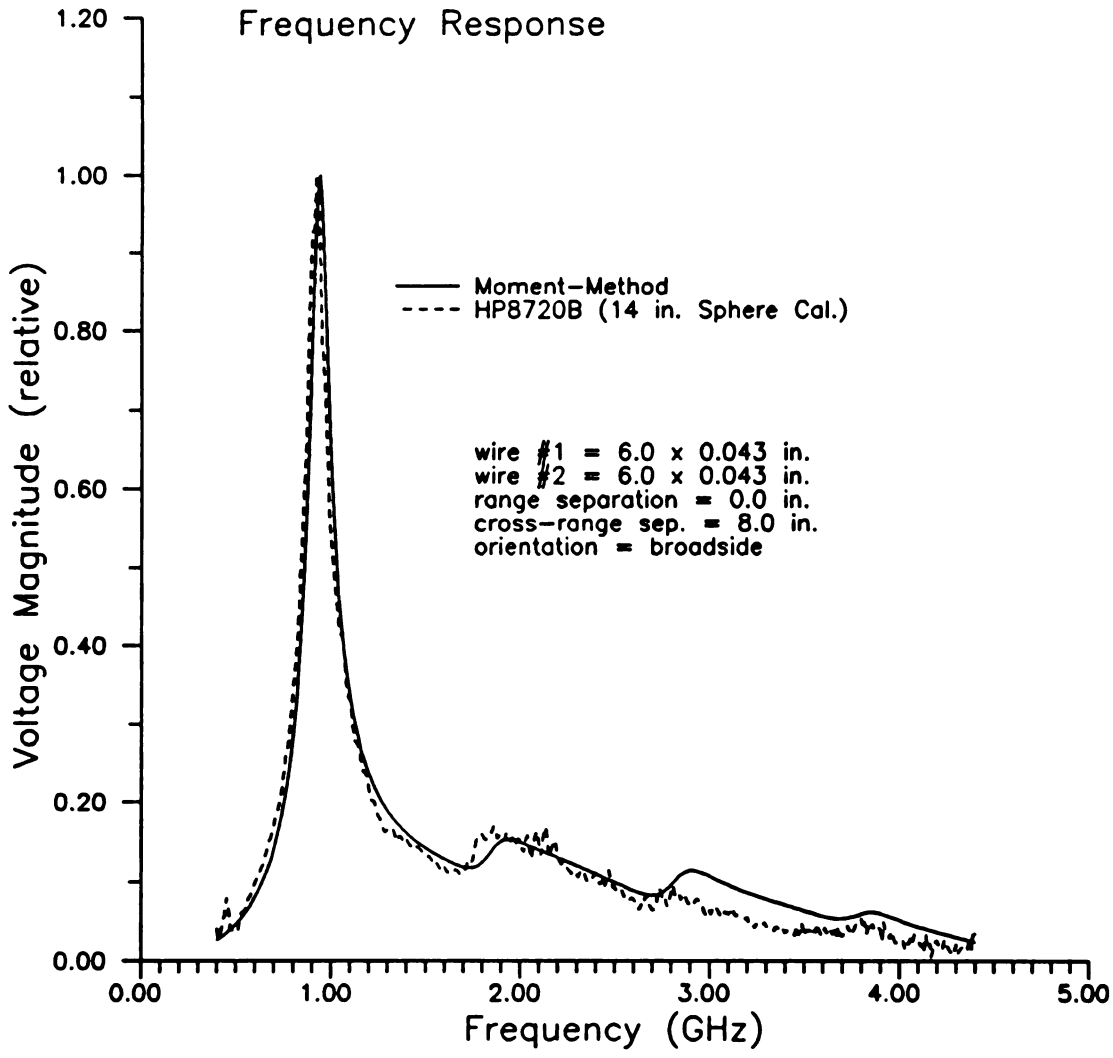

Figure 6.17 Spectral response of two 6.0x0.043 inch wires separated by 8.0 inches in cross range.

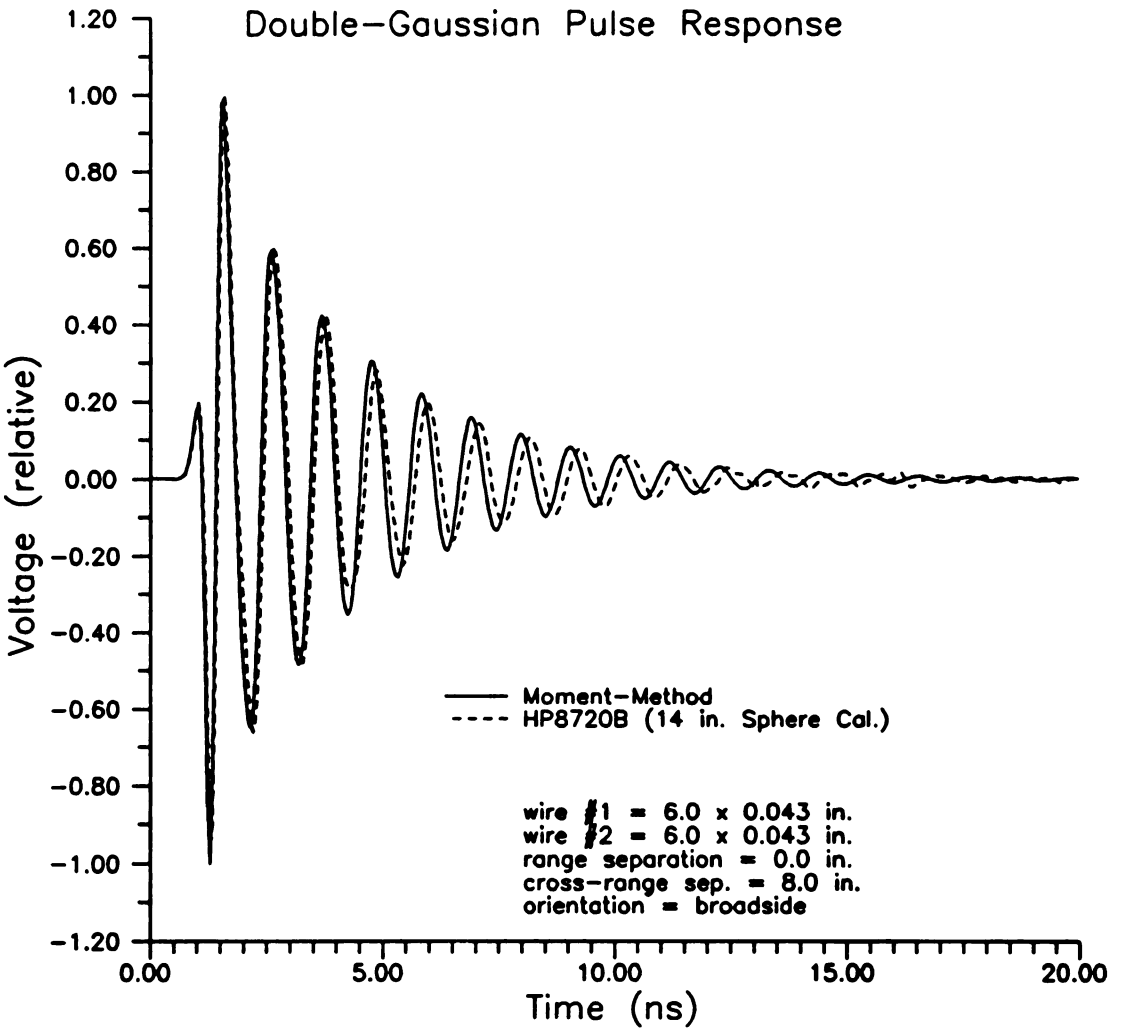

Figure 6.18 Double-Gaussian pulse response of two 6.0x0.043 inch wires separated by 8.0 inches in cross range.

6.3 Wire Stick Airplane Model

This section presents a comparison of theory and measurement for a wire stick airplane model. The wire stick model is diagramed in Figure 6.19. The model was made from solid copper wire that was pre-stressed to increase stiffness by stretching it beyond the plastic limit. The wires were attached using tin-lead solder. The size of the joints was kept small by filing away the excess solder. The joints were made as small as possible while maintaining the physical and electrical integrity of the contact.

The wire model was measured in the anechoic chamber using the frequency domain scattering measurement system. The low-band measurement (0.4-4.4 GHz) configuration was used for all measurements. It was anticipated that the measurements would be repeated for the high-band configuration but this was not possible due to the timing of equipment malfunctions and the anechoic chamber upgrade. The measurements were verified by comparison to results obtained from a frequency domain moment method calculation. Unlike other results in this thesis, the theoretical calculations in this section were obtained using a computer program developed by Dr. E.J. Rothwell. This program uses piecewise sinusoidal basis functions and testing functions as previously discussed. The program is general and can handle arbitrarily oriented wires and junctions between wires. The junction is accounted for by placing a half segment on each wire at the junction. Kirchoff's current law is enforced at the junction.

The incident field is assumed to be a plane wave and the scattered field is computed according to the geometry of the anechoic chamber prior to February 1992. The aircraft model was measured for five aspect angles between nose-on and tail-on.

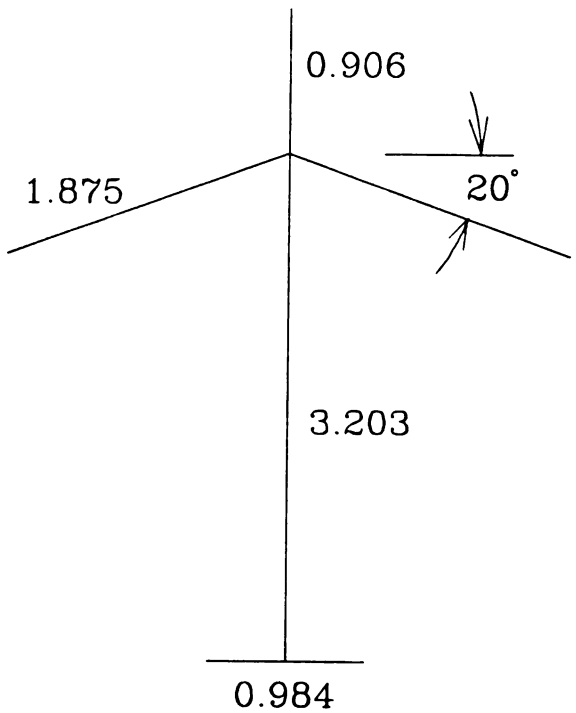

Figure 6.19 Wire stick airplane model.

This series of measurements is presented in this section. The spectral and temporal responses of the nose-on response are shown in Figures 6.20 and Figure 6.21. As before, the theoretical and experimental results are normalized to a peak value of unity. The double gaussian pulse is also used as before. Again, the theoretical and experimental results are in excellent agreement for both the spectral and temporal responses. The spectral response indicates that nose-on response is dominated by the SEM modes of the wing and tail.

When the airplane model is illuminated 45 degrees from nose-on, the response becomes more complicated as shown in Figures 6.22 and 6.23. When the fuselage is parallel to the incident field, the response is dominated by the lower frequency fuselage and wing-fuselage modes. The broadside (90 degree) case is shown in Figures 6.24 and 6.25. For an orientation angle of 135 degrees from nose-on, the response is again more complicated. The responses for this orientation are shown in Figures 6.26 and 6.27. For tail-on incidence, the response is similar to the nose-on incidence. The response is dominated by the wing mode as shown in Figures 6.28 and 6.29.

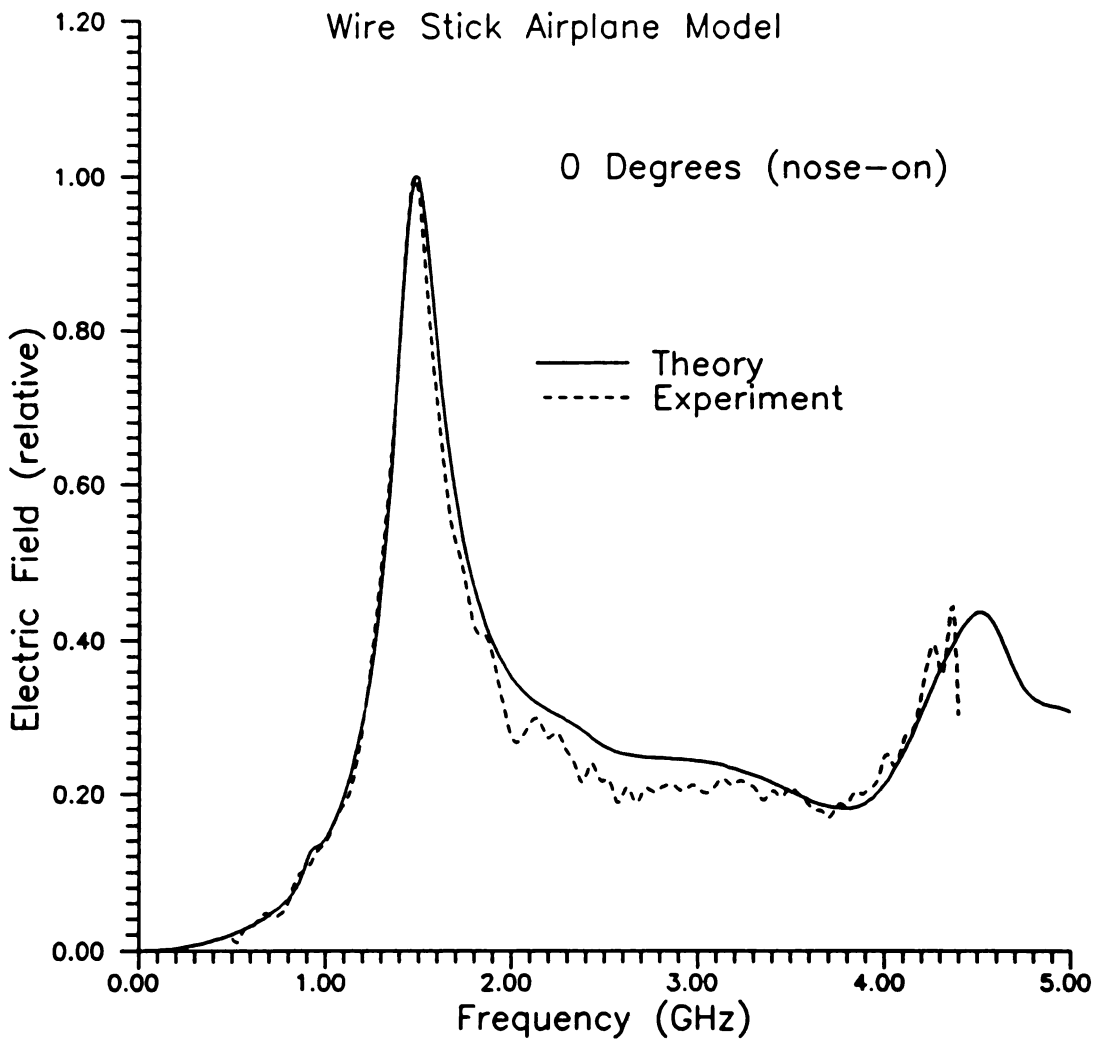

Figure 6.20 Spectral response of wire stick airplane model for nose-on (0 degrees) incidence.

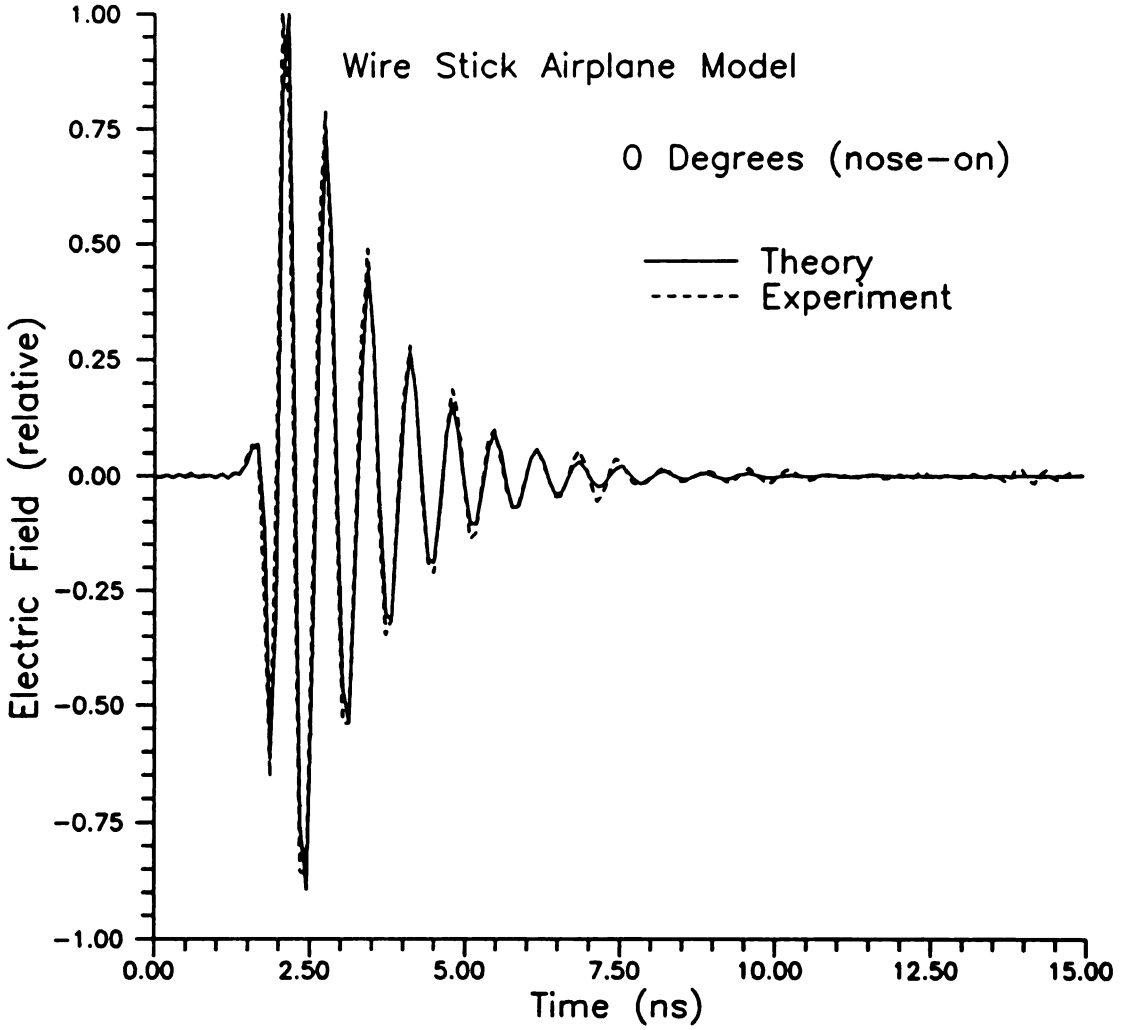

Figure 6.21 Temporal response of wire stick airplane model for nose-on incidence.

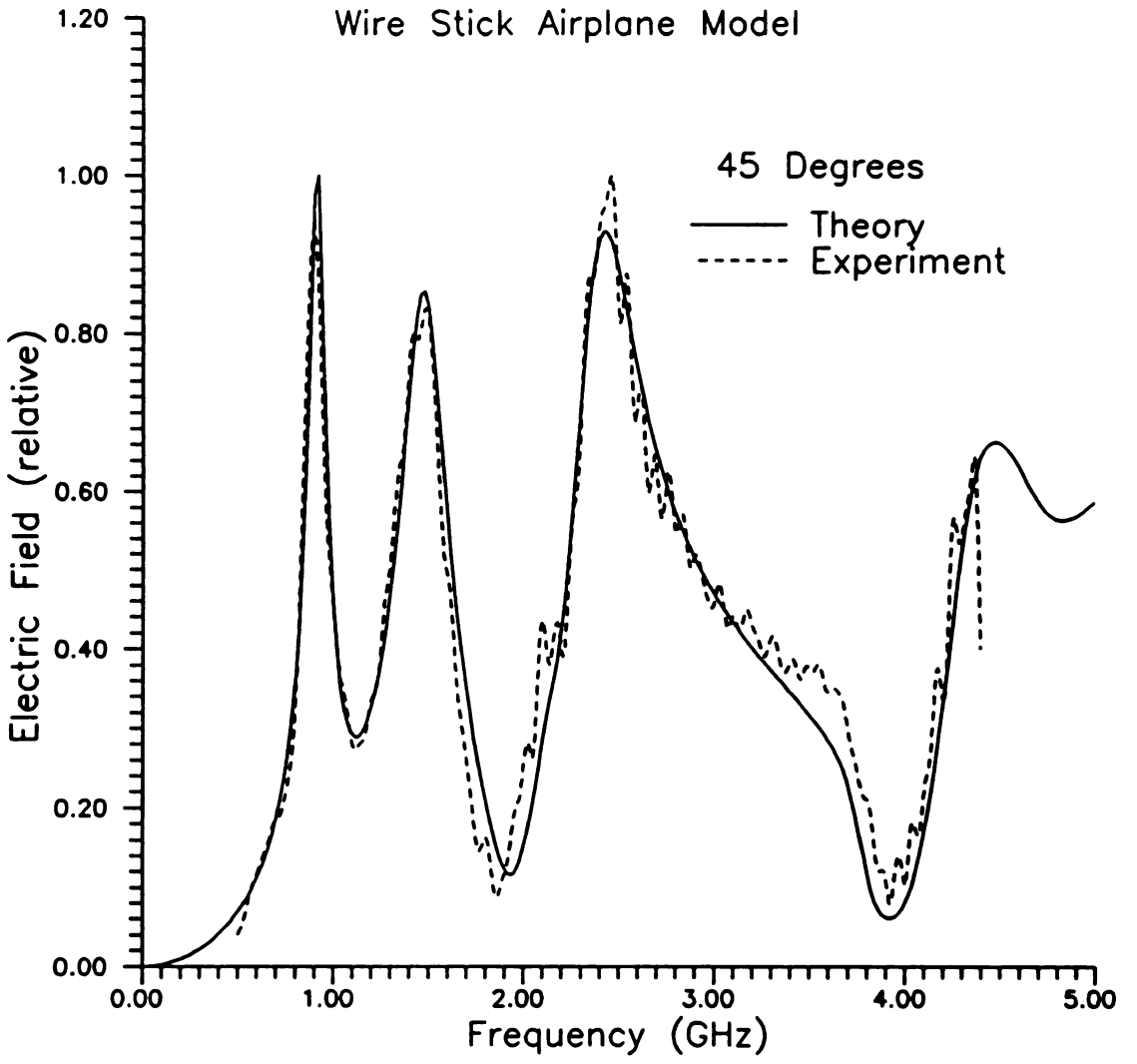

Figure 6.22 Spectral response of wire stick airplane model for 45 degree orientation.

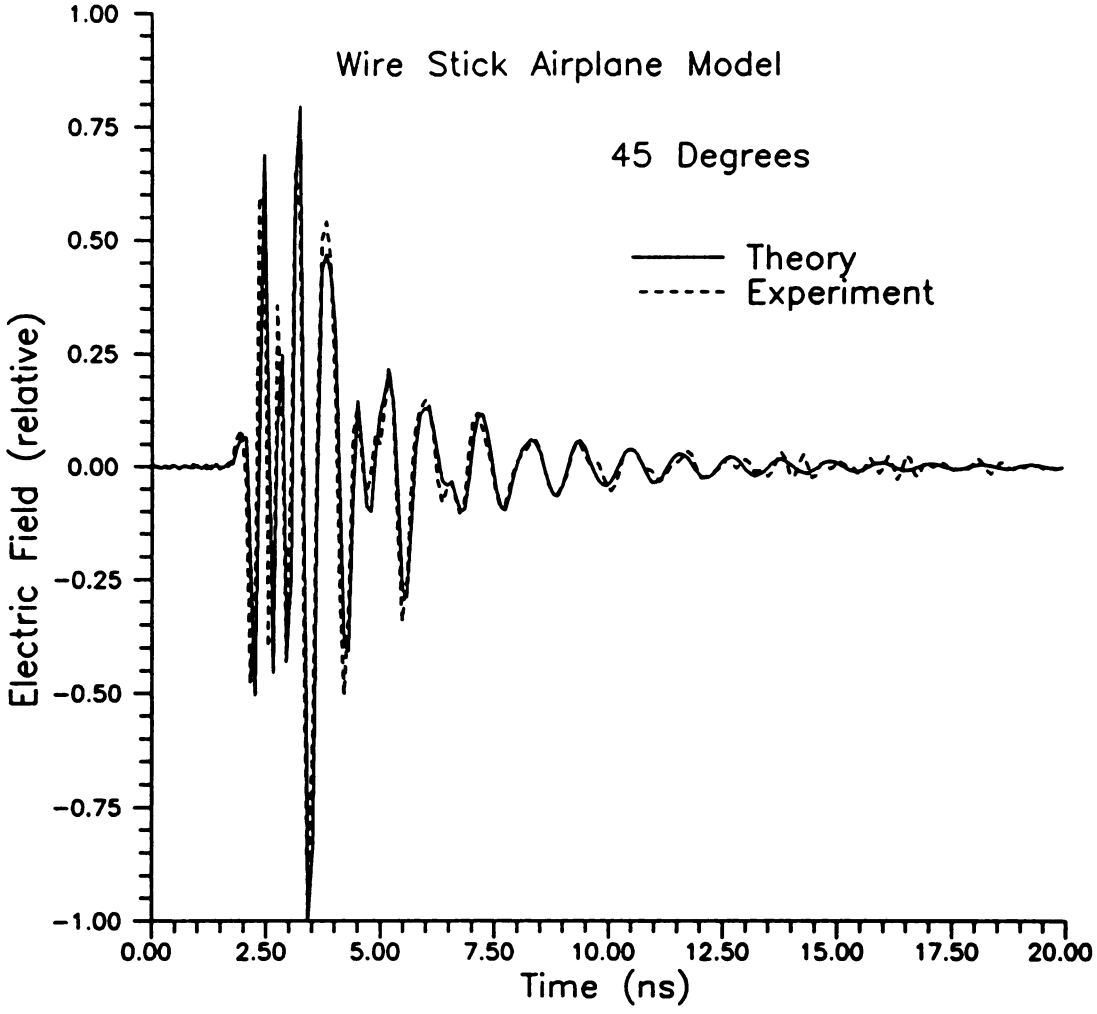

Figure 6.23 Temporal response of wire stick airplane model for 45 degree orientation.

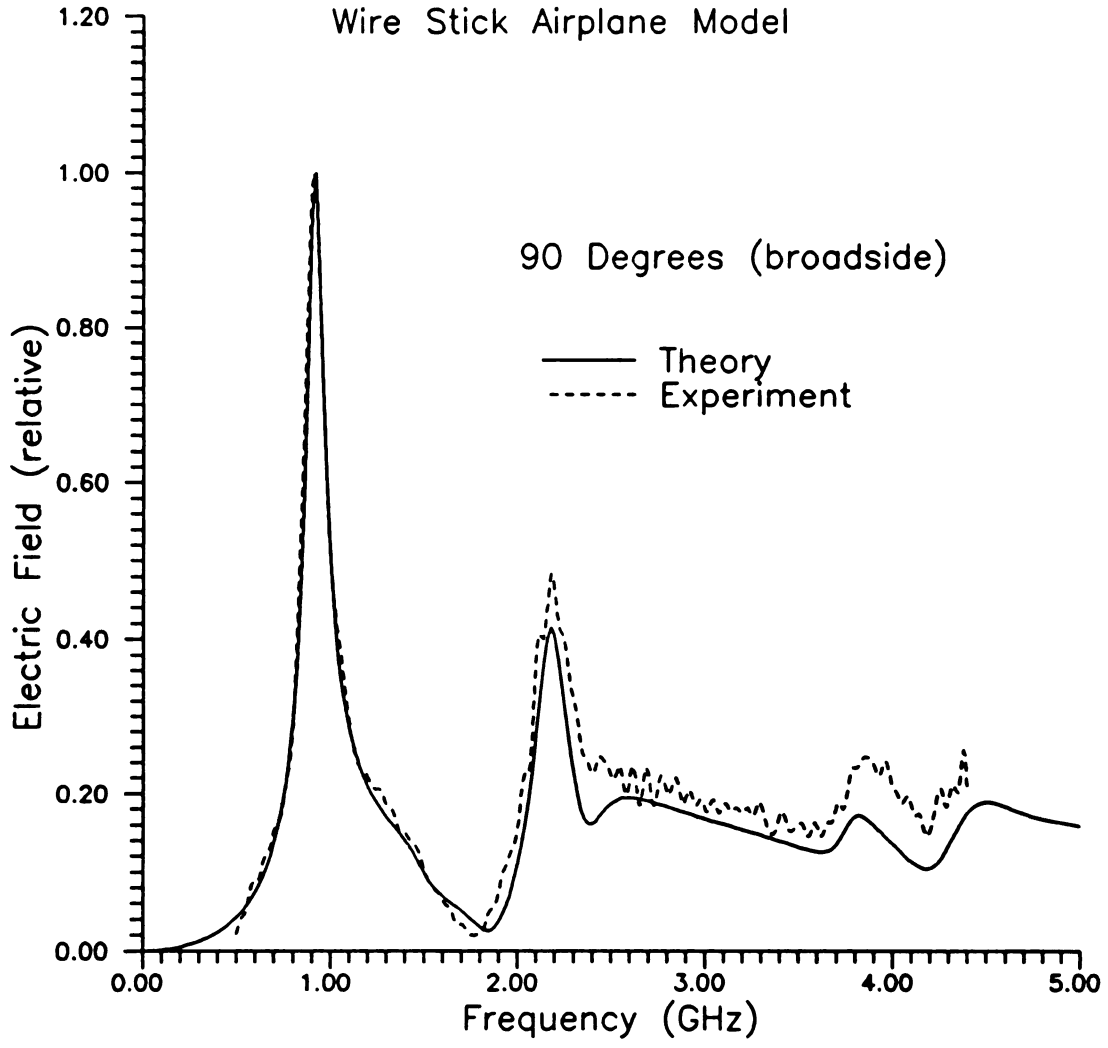

Figure 6.24 Spectral response of wire stick airplane model for broadside (90 degree) orientation.

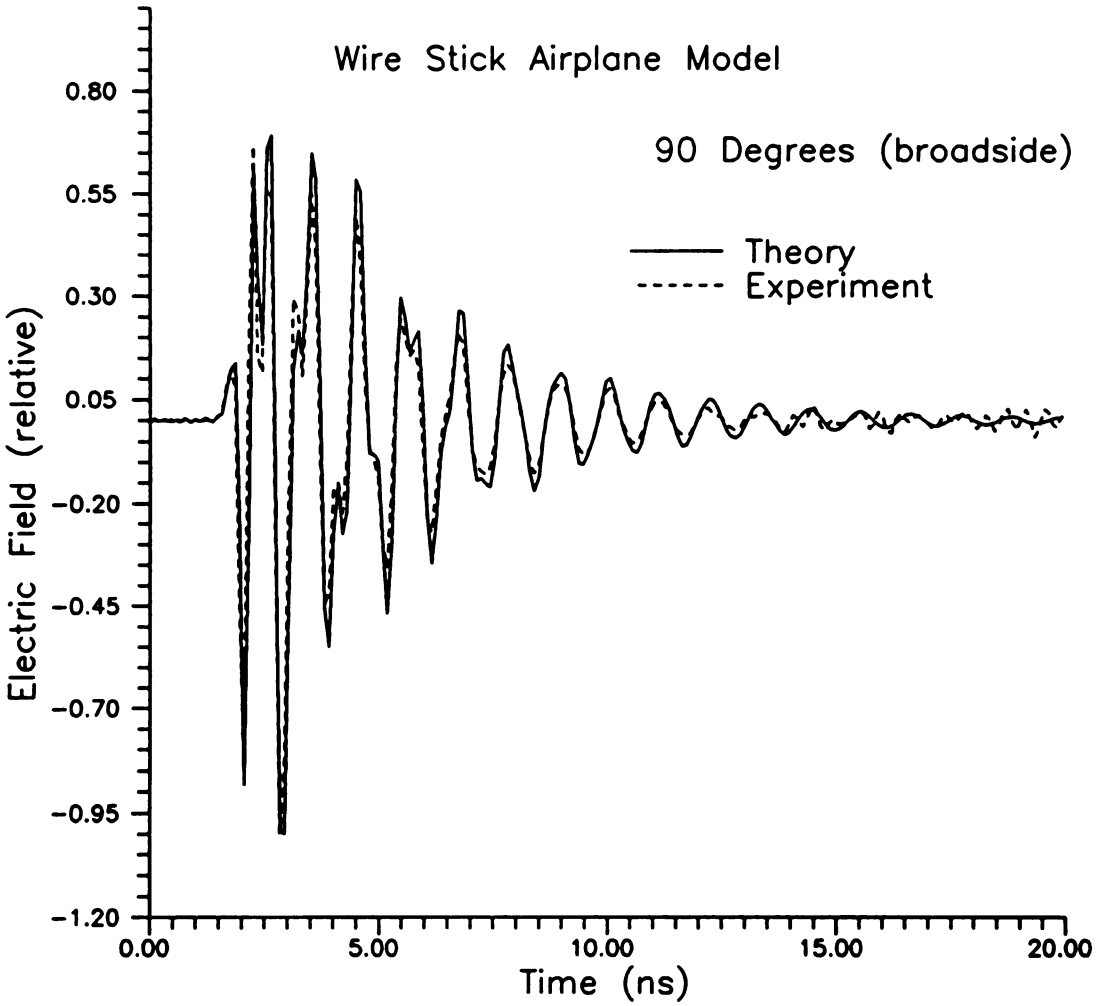

Figure 6.25 Temporal response of wire stick airplane model for broadside (90 degree) orientation.

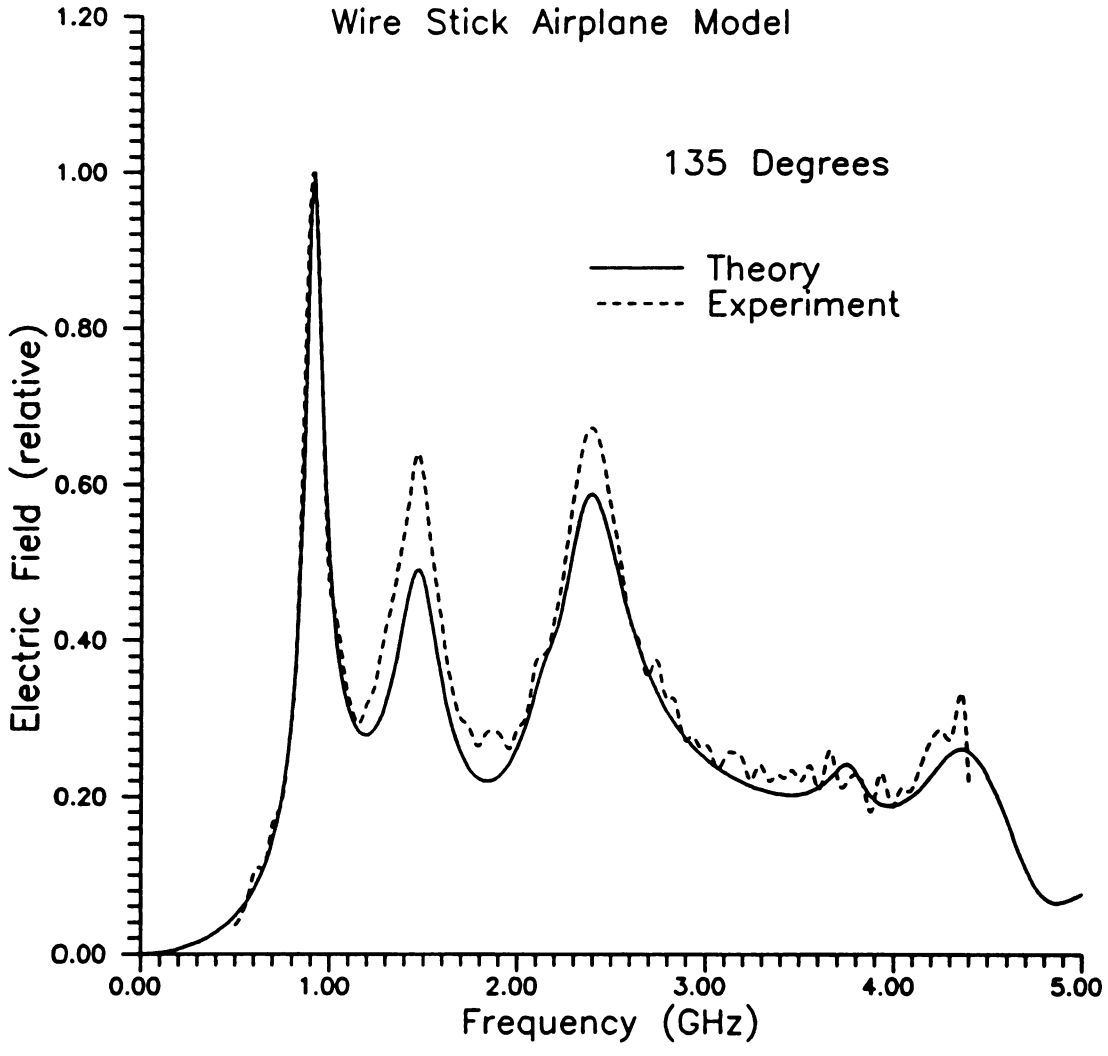

Figure 6.26 Spectral response of wire stick airplane model for 135 degree orientation.

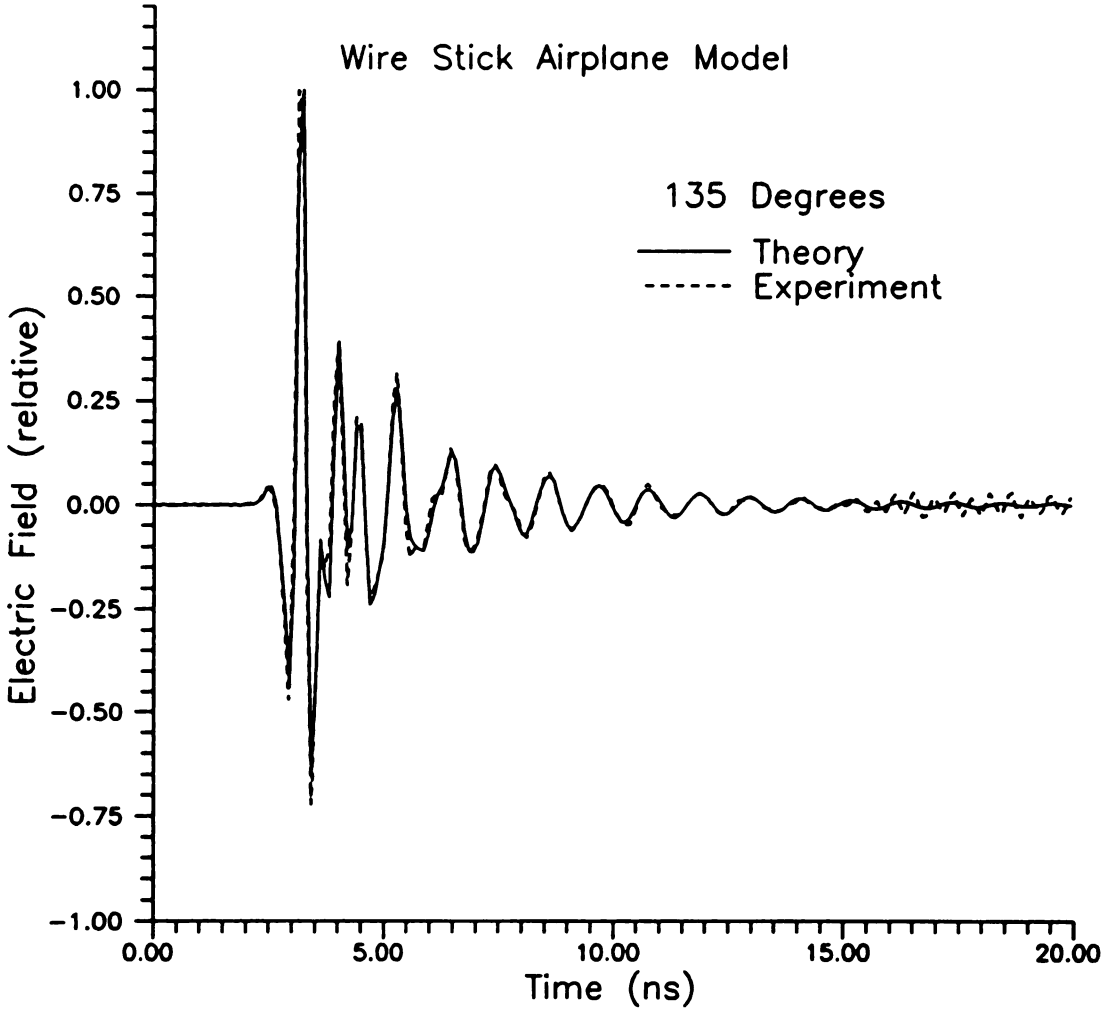

Figure 6.27 Temporal response of wire stick airplane model for 135 degree orientation.

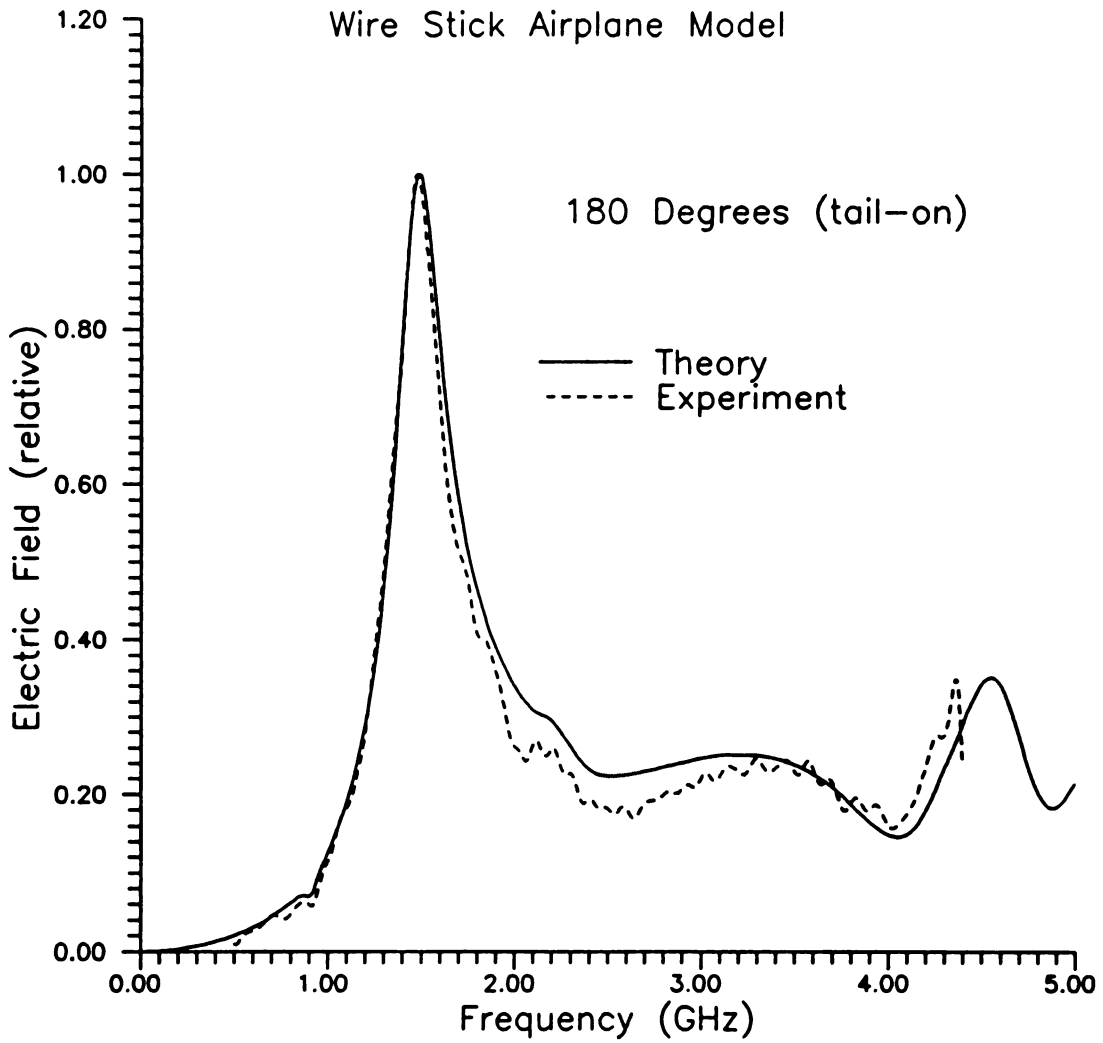

Figure 6.28 Spectral response of wire stick airplane model for tail-on incidence.

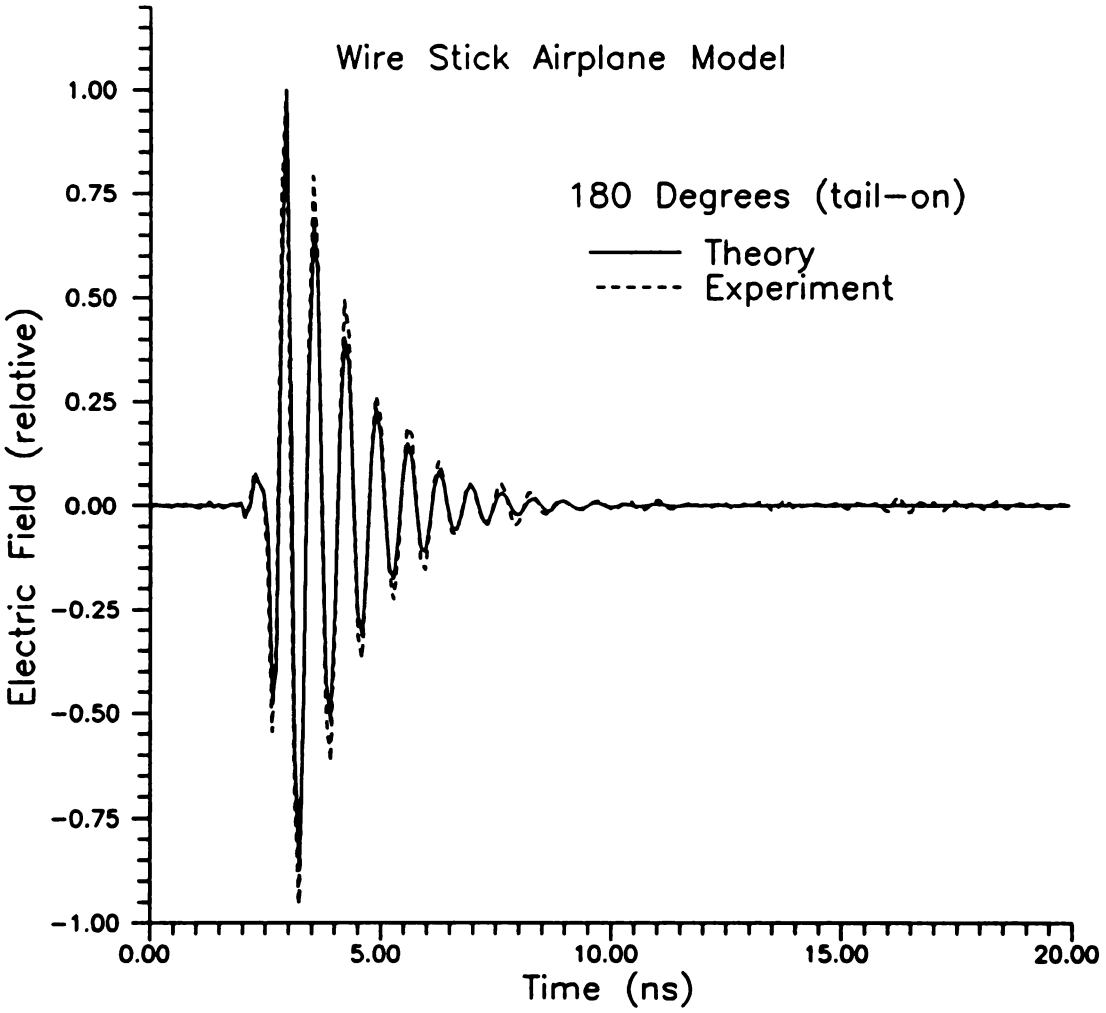

Figure 6.29 Temporal response of wire stick airplane model for tail-on incidence.

6.4 Early-Time vs Late-time Energy

The E-pulse and S-pulse discrimination schemes are based on the late-time response of the target. Thus, it is of great importance to determine how much of the received signal energy is contained in the late-time for practical targets. This section presents results of an experimental study which examines this question.

To quantify the amount of energy in the late-time response of the target, the ratio of the energy in the late-time to energy in the received waveform is defined as

$$R_{lte} = \frac{\int_{late\ time}^{\infty} v_r(t)^2 dt}{\int_{-\infty}^{\infty} v_r(t)^2 dt} \qquad (6.5)$$

where $v_r(t)$ is the received signal.

This ratio is expected to be a function of the bandwidth of the pulse that is used to excite the target. For purposes of this study, only pulses whose spectrum includes the lower target resonances were considered.

For the experimental study, three aircraft models were used. They are:

(1) U.S. Air Force A10 Thunderbolt (6.75 inch wing span)

(2) U.S. Air Force F15 E (7.5 inch nose-to-tail length)

(3) U.S. Air Force F16 (6.375 inch nose-to-tail length)

The response of these models was obtained using the frequency domain measurement system described in Chapter 5. The low-band (0.4-4.4 GHz) configuration was used and a 14 inch diameter sphere used as the calibration standard.

An example of the spectral response of the A10 model for three different incidence angles is shown in Figure 6.30. The resonant nature of the response is clearly

demonstrated in the lower half of the measured spectrum. An example of the double gaussian pulse response of this model is shown in Figure 6.31. It is clear that for both nose-on and broadside responses the response in late-time is very small while the 45 degree response has more significant late-time oscillations.

The energy available for target discrimination is a function of the aspect angle. This means that the ability to discriminate based on natural resonances is aspect dependent whereas the natural resonance frequencies are aspect independent. Similar observations can be made for the case of the F15 model. The frequency response is shown in Figure 6.32 while the double-gaussian pulse response is shown in Figure 6.33.

To provide a measure of the amount of energy available for discrimination, the R_{tt} values are calculated for the three models for 5 different aspect angles. The results are shown in Table 6.1. It is clear from this table that the fraction of total signal energy present in the late-time varies greatly with aspect angle. There are however clearly cases when the late-time response contains a significant percentage of the total received energy. Unfortunately, there are also cases where the late-time energy is very small in comparison to the total received energy. This leaves some worries about the ability of the E-pulse and S-pulse schemes to provide good discrimination for these aspect angles.

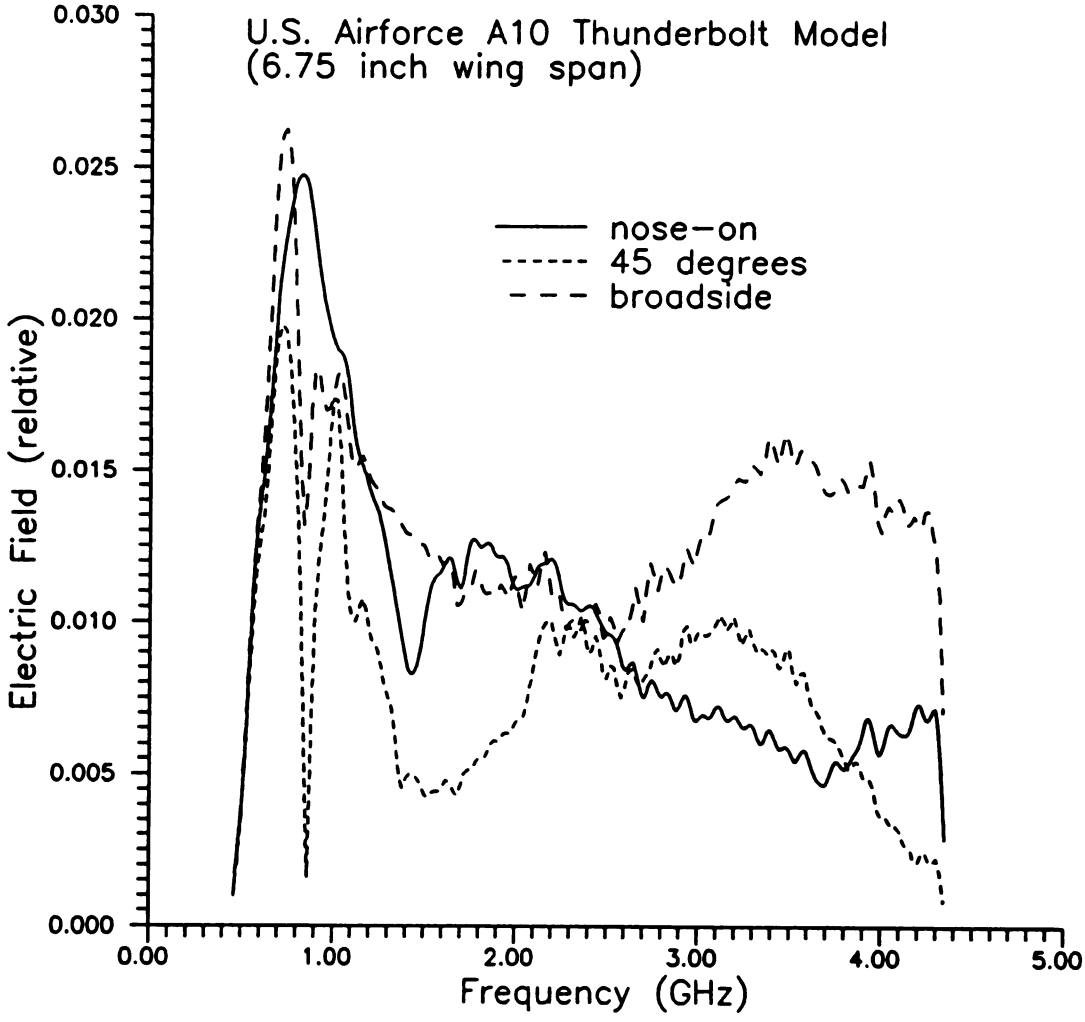

Figure 6.30 Spectral response of A10 model.

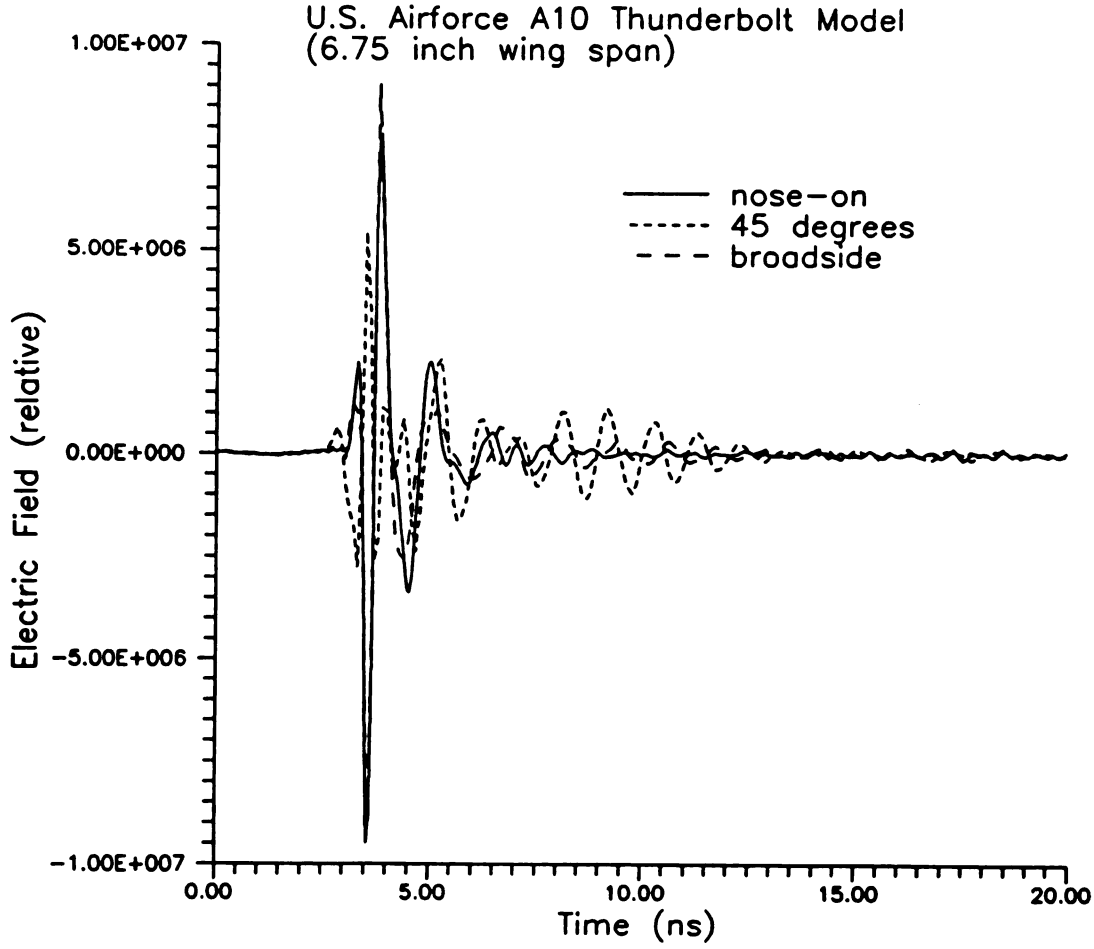

Figure 6.31 Double-gaussian pulse response of A10 model.

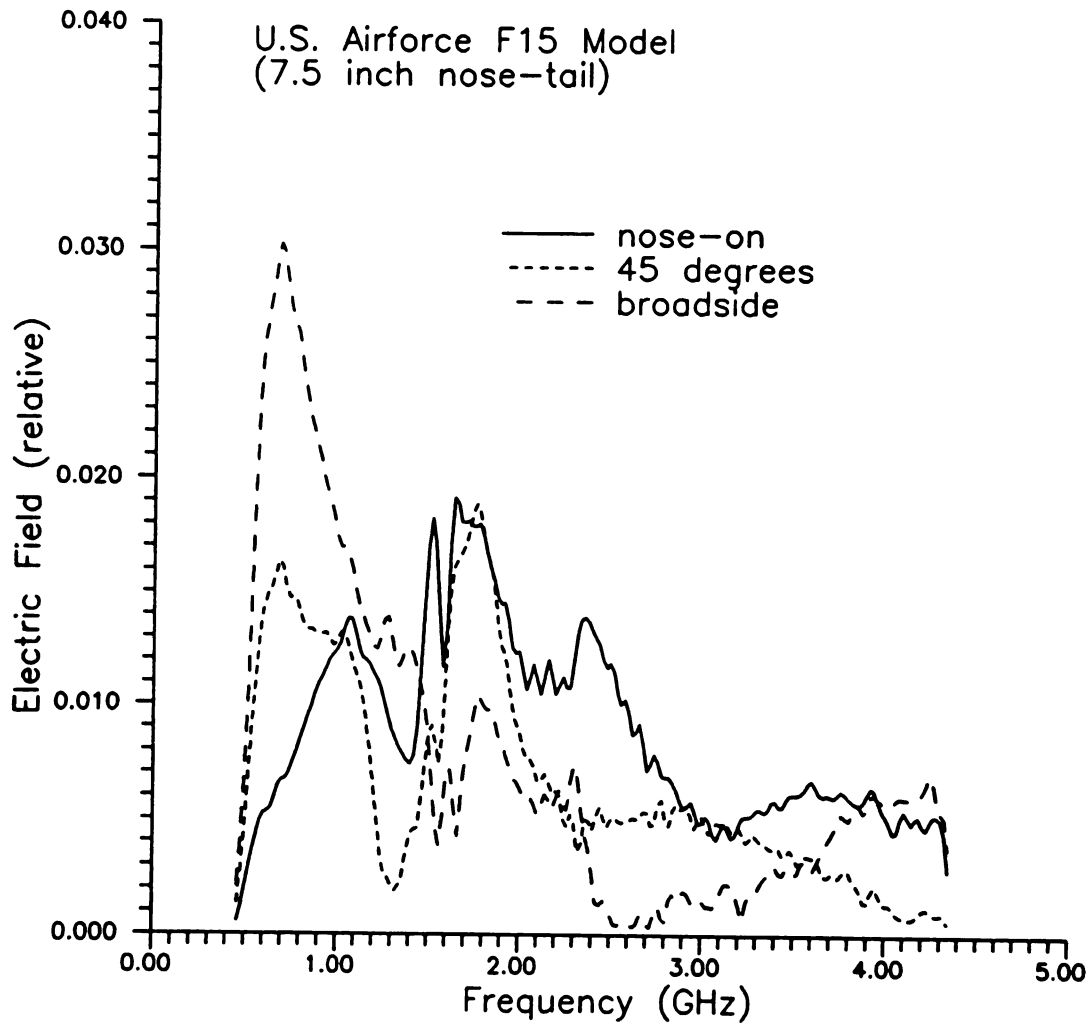

Figure 6.32 Spectral response of F15 model.

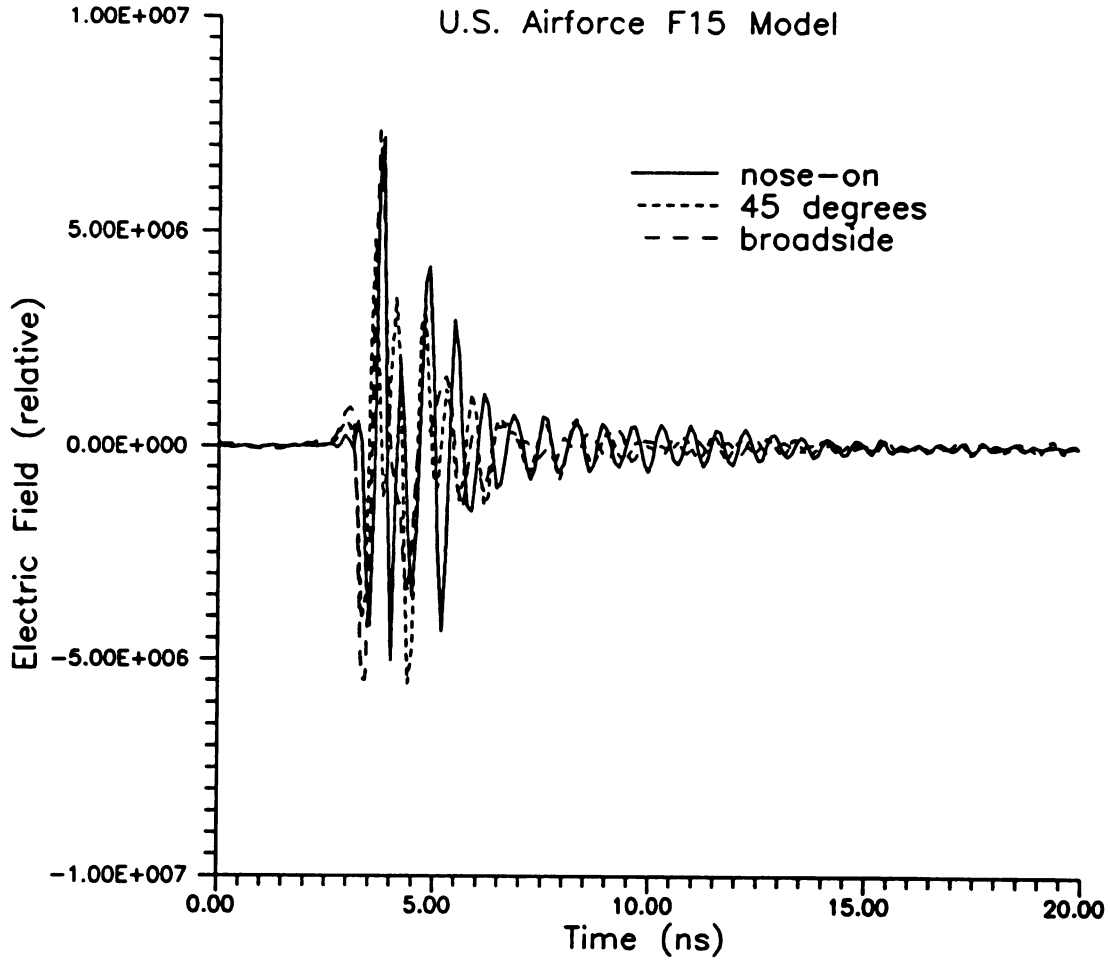

Figure 6.33 Double-gaussian pulse response of F15 model.

Table 6.1 R_{hc} values for model aircraft.

Angle (degrees)	F15 Model	A10 Model	F16 Model
0 (nose-on)	0.32	0.05	0.05
22.5	0.20	0.18	0.10
45.0	0.11	0.35	0.17
67.5	0.12	0.15	0.02
90.0	0.08	0.04	0.03

6.5 Effects of Coupling on Aircraft Model Discrimination

This section extends the discussion of Chapter 4 to investigate the effect of coupling on E-pulse and S-pulse discrimination schemes for the case of realistic aircraft models separated in cross range. Since realistic aircraft models are difficult to model theoretically, the evaluation is made using experimentally derived data.

For this study, two identical A10 models, an F16 model, and an F15 model are used. These models are the same as those used in the previous section. The individual models were measured using the same technique as previously described. The constrained E-pulse technique (CET) developed by Ilavarasan [?] was used to extract the natural frequencies of the A10, F15 and F16 models from the measured transient responses. The extraction was performed using responses from three aspect angles for each target.

Due to limitations on the early version of the CET computer program a maximum of 9 modes could be reliable extracted from measured data. The aircraft models are very

complicated structures and the transient data apparently contained more than 9 modes over the measured bandwidth from 0.4 to 4.4 GHz. To allow use of the CET program, the data was filtered using a GMC weighting function with parameters θ = 1.3 ns, ω = 1.3 GHz. This window function reduces the effects of spectral truncation on the transient response and eliminates enough modes so that the CET program can be used. The natural frequencies extracted for the F15 model are shown in Table 6.2, while those of the A10 are shown in Table 6.3, and the F16 results are listed in Table 6.4. Note that the lowest frequency mode common to all targets is most likely the result of low frequency truncation of the frequency spectrum.

Table 6.2 Natural frequencies of A10 model extracted using CET method.

Mode	σ x 10^9 np/s	ω x 10^9 rad/s
1	-0.4184	9.8037
2	-4.586×10^{-7}	9.4300
3	-0.2728	8.2461
4	-0.0207	7.0993
5	-0.2727	6.0708
6	-0.1275	5.1669
7	-8.2958×10^{-7}	4.7827
8	-0.3552	4.0202
9	-0.0477	3.2012

Table 6.3 Natural frequencies of F15 model extracted using CET method.

Mode	σ x 10^9 np/s	ω x 10^9 rad/s
1	-0.4413	9.6503
2	-0.1673	9.8805
3	-0.2944	8.3826
4	-0.1734	7.7460
5	-0.0398	6.8470
6	-0.0300	5.3380
7	-0.0520	5.1525
8	-0.2831	4.2018
9	-0.0003	3.1904

Originally, it was anticipated that the E-pulse method would be used to demonstrate the effects of coupling for measured data from realistic aircraft. However, after much effort it was found that the S-pulse method provides better discrimination than the E-pulse method. Apparently, measured data from complicated targets contains more modes than can currently be used effectively. Also, there are also unavoidable errors in the extracted natural frequencies due to underestimating the number of modes, noise, and systematic errors in the measurements due to slight inaccuracies in the deconvolution procedure. Since the E-pulse attempts to extinguish all modes, any errors in the natural dominant mode natural frequencies results in slight variations from the idealized zero

result. Unfortunately, these slight variations drastically affect the discrimination ability of the E-pulse.

In the case of S-pulse discrimination, the dominant mode of the response is usually chosen for discrimination. Thus, the convolution operation results in a waveform that is dominated by a single mode signal. For the S-pulse, however, errors in the natural frequencies cause incomplete cancellation of only the weaker modes and hence a smaller overall deviation of the convolution from the expected single mode spectrum. It is conjectured that this may be a real and significant advantage of the S-pulse in actual applications where measured data must be used.

Table 6.4 Natural frequencies of F16 model extracted using CET method.

Mode	σ x 10^9 np/s	ω x 10^9 rad/s
1	-0.2919	10.158
2	-0.3460	9.2589
3	-0.4020	8.3495
4	-2.47×10^{-6}	7.4621
5	-0.0744	6.4881
6	-0.3020	5.6535
7	-0.1046	4.9759
8	-0.3473	3.9691
9	-0.0784	3.2080

To evaluate the effect of coupling on discrimination, the S-pulse discrimination scheme was applied to the targets individually and to the coupled A10 targets. For the F15 model an S-pulse was constructed for mode 3, while for the A10 model mode 5 was used, and mode 3 was used for the F16. Note that mode 3 of the F15 and F16 are very similar. This similarity prevented the S-pulse method from providing good single target discrimination results when all three models were included in the discrimination process. Thus, a binary discrimination problem was evaluated. The first binary discrimination problem performed used the F16 and the A10 model responses and S-pulses. The discrimination results for single aircraft are shown in Table 6.5. Here it is seen that

Table 6.5 SDR values computed for single targets using S-pulses for F16 and A10.

Target	Orientation	F16 (dB)	A10 (dB)
F16	nose-on	0.0	17.42
F16	45 degrees	0.0	16.37
F16	broadside	0.0	4.38
A10 #2	nose-on	0.0	4.73
A10 #2	45 degrees	15.07	0.0
A10 #2	broadside	13.49	0.0
A10 #2 *	30 degrees	4.84	0.0
A10 #2 *	60 degrees	20.23	0.0
A10 #1 *	30 degrees	7.89	0.0
A10 #1 *	45 degrees	13.34	0.0

discrimination is very good for most aspect angles. The waveforms denoted with * are independent of the mode extraction procedure. Discrimination with these waveforms confirm the validity of the extracted modes and the overall results. This is important to prevent a circular argument that is possible when using the same waveforms for both mode extraction and demonstration of discrimination.

The discrimination process using the same two S-pulses was applied to measured responses of two A10 models separated vertically in cross range. (In this configuration one model appears to be flying directly above the other with an aspect of approximately 45 degrees from nose-on.) The results of this study are shown in Table 6.6. It is seen that the SDR values are significantly lower than those obtained when only a single A10 aircraft is present at a 45 degree orientation.

Table 6.6 SDR values computed for coupled A10 models using S-pulses for F16 and A10.

Target	Separation	F16 (dB)	A10 (dB)
2 - A10's	1.75"	4.19	0.0
2 - A10's	3.00"	3.18	0.0
2 - A10's	4.25"	0.0	0.17
2 - A10's	5.50"	0.16	0.0
2 - A10's	6.25"	1.41	0.0

The second binary discrimination problem considered the case of the F15 and A10 S-pulses. The results of this study for single targets are shown in Table 6.7. It is clear that excellent discrimination is possible for single targets in this binary case. Finally, the discrimination process was performed using measured data for two coupled A10 aircraft as before. The results of this study are shown in Table 6.8. The results in this case indicate that discrimination while still possible is significantly degraded as compared to the single target scenario.

The results of this section demonstrates using realistic aircraft models that coupling can degrade the discrimination performance of the S-pulse method. It is

Table 6.7 SDR values computed for single targets using S-pulses for F15 and A10.

Target	Orientation	F15 (dB)	A10 (dB)
F15	nose-on	0.0	3.75
F15	45 degrees	0.0	12.50
F15	broadside	0.0	4.68
A10 #2	nose-on	0.0	1.40
A10 #2	45 degrees	18.32	0.0
A10 #2	broadside	17.57	0.0
A10 #2 *	30 degrees	10.72	0.0
A10 #2 *	60 degrees	22.23	0.0
A10 #1 *	30 degrees	10.91	0.0
A10 #1 *	60 degrees	16.47	0.0

Table 6.8 SDR values computed for coupled A10 models using S-pulses for F15 and A10.

Target	Separation	F15 (dB)	A10 (dB)
2 - A10's	1.75"	7.24	0.0
2 - A10's	3.00"	7.49	0.0
2 - A10's	4.25"	3.47	0.0
2 - A10's	5.50"	4.91	0.0
2 - A10's	6.25"	4.36	0.0

expected that coupling will also degrade the performance of the E-pulse method. Of course, the amount of degradation is a function of the number and types of targets to be discriminated. Because of these complexities, the results of this section can only be interpreted as a demonstration that coupling affects discrimination results and not as a general quantitative measure of the amount of degradation to be expected.

6.6 Early-time Scattering from Scale Model Aircraft

This section discusses the use of early-time scattering phenomena in target detection and discrimination. The measured responses of several 1/48 scale aircraft models are used to illustrate early-time scattering mechanisms. The measurements were performed in the MSU anechoic chamber using the vector network analyzer in the frequency band from 1.0 to 7.0 Ghz. The calibration procedure of Chapter 5 was used to correct the raw measurements for systematic errors introduced by the measurement

system. A metal calibration sphere 14 inches in diameter was used as a calibrator in all measurements. To achieve a narrow pulse without introducing excessive windowing effects into the transient data a 1/10 cosine taper weighting function was used. The effective pulse for this weighing function was shown previously in Chapter 5 and is not be repeated here.

The scale model targets were constructed from plastic model kits that are widely available in hobby shops and department stores. Since models are constructed of plastic, they were carefully coated by hand with aluminum foil to more closely simulate the actual conducting aircraft. The foil was attached using a cyanoacrylate adhesive commonly available as "super glue" in the department stores. The models were simplified by omitting certain features such as some externally attached weapon systems and missiles and by leaving all landing gear in the up positions. All flaps and movable wing parts were permanently fixed into position to eliminate any chance that the electrical properties of the models would change during or between measurements. The models used in this chapter include: N.A.S.A. Lockheed TR1 (atmospheric research plane - updated version of U2 spy plane) and a U.S.A.F. B58 Hustler (obsolete supersonic strategic bomber).

One of the most obvious and interesting phenomena associated with early-time scattering is the fact that response can be seen to be caused by specific localized "scattering centers" at distinct locations on the aircraft. This is in marked contrast to the late-time scattering response which is of a global nature. This can clearly be seen in Figure 6.34 which shows the synthesized transient response of the Lockheed TR1 model for nearly "wing-on" incidence. Note that the size of the aircraft drawing has been scaled

to the time axis so that the association between the response peaks and the physical locations on the aircraft model are more evident. The incident wave is applied from the left for this interpretation. From this figure it is clear the that response is dominated by two strong reflections. One reflection is from the vicinity of the left electronics pod and left edge of the tail wing. The other strong reflection is from the main fuselage of the aircraft. A smaller reflection occurs when the pulse strikes the edge of the wing from the left. It should be pointed out that there is little late-time energy associated with this target response. This due primarily to the fact that the lowest frequency and hence highest Q natural resonances of this aircraft model are well below the 1.0 GHz lower limit used in the measurement and are not excited. Unfortunately, even use of the low-band measurement configuration does not resolve this problem since the low frequency limit is set by the anechoic chamber performance.

As a further illustration of the scattering center phenomena, consider the wing-on response of the B58 Hustler model shown in Figure 6.35. Again, the scattering centers are clearly associated with the engines and main fuselage of the aircraft. Note that the scattering centers on the right hand side of the aircraft are not as distinct as those on the left hand side. This is most likely due to a shadowing of these discontinuities by the engines on the left and the main fuselage.

The aspect dependency of the early-time scattering can be seen by examining the nose-on response of the same B58 Hustler model as shown in Figure 6.36. Here, the scattering centers appear to be associated primarily with the current discontinuities the engine mounting junctions.

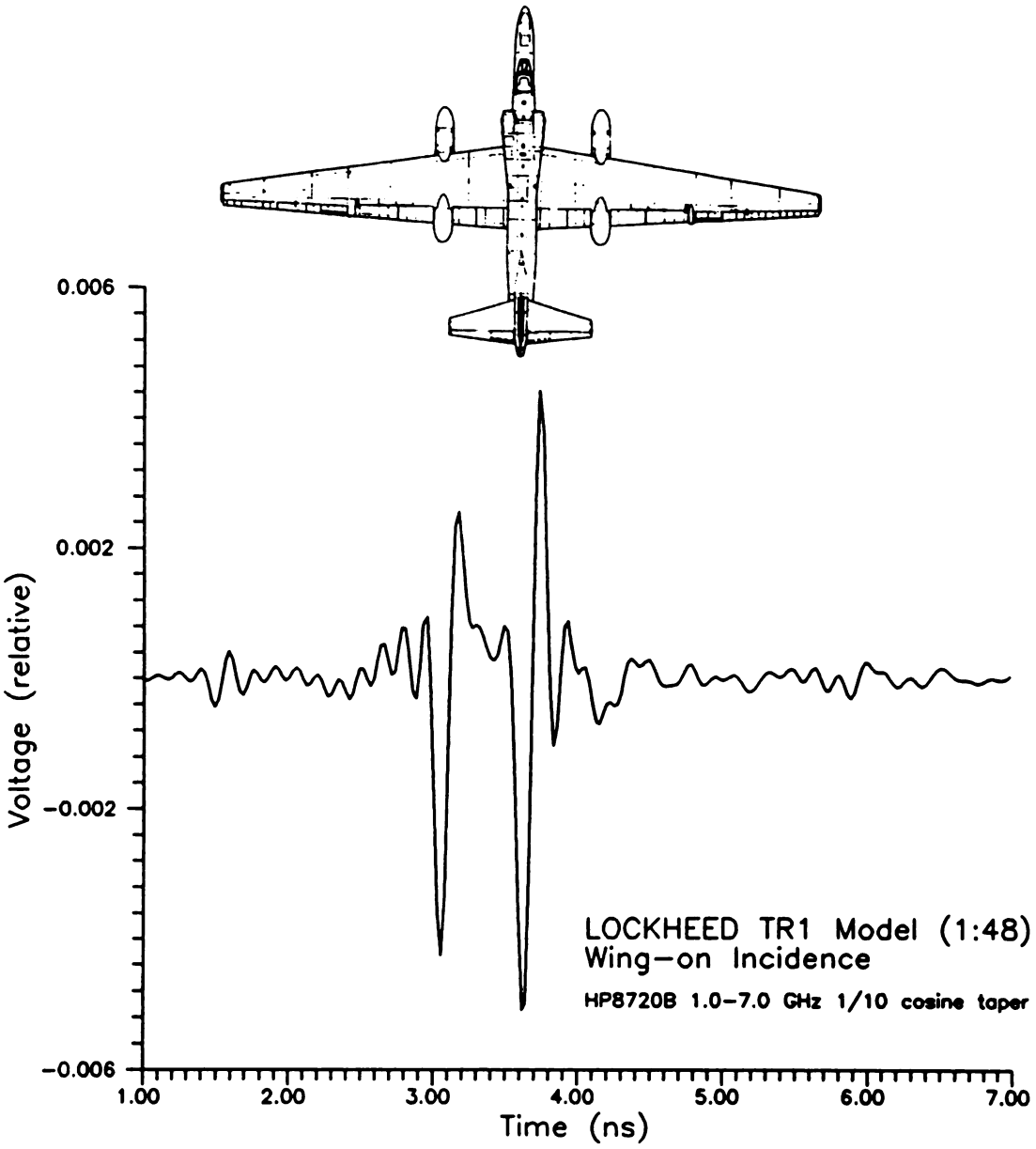

Figure 6.34 Early time scattering by Lockheed TR1A for wing-on incidence.

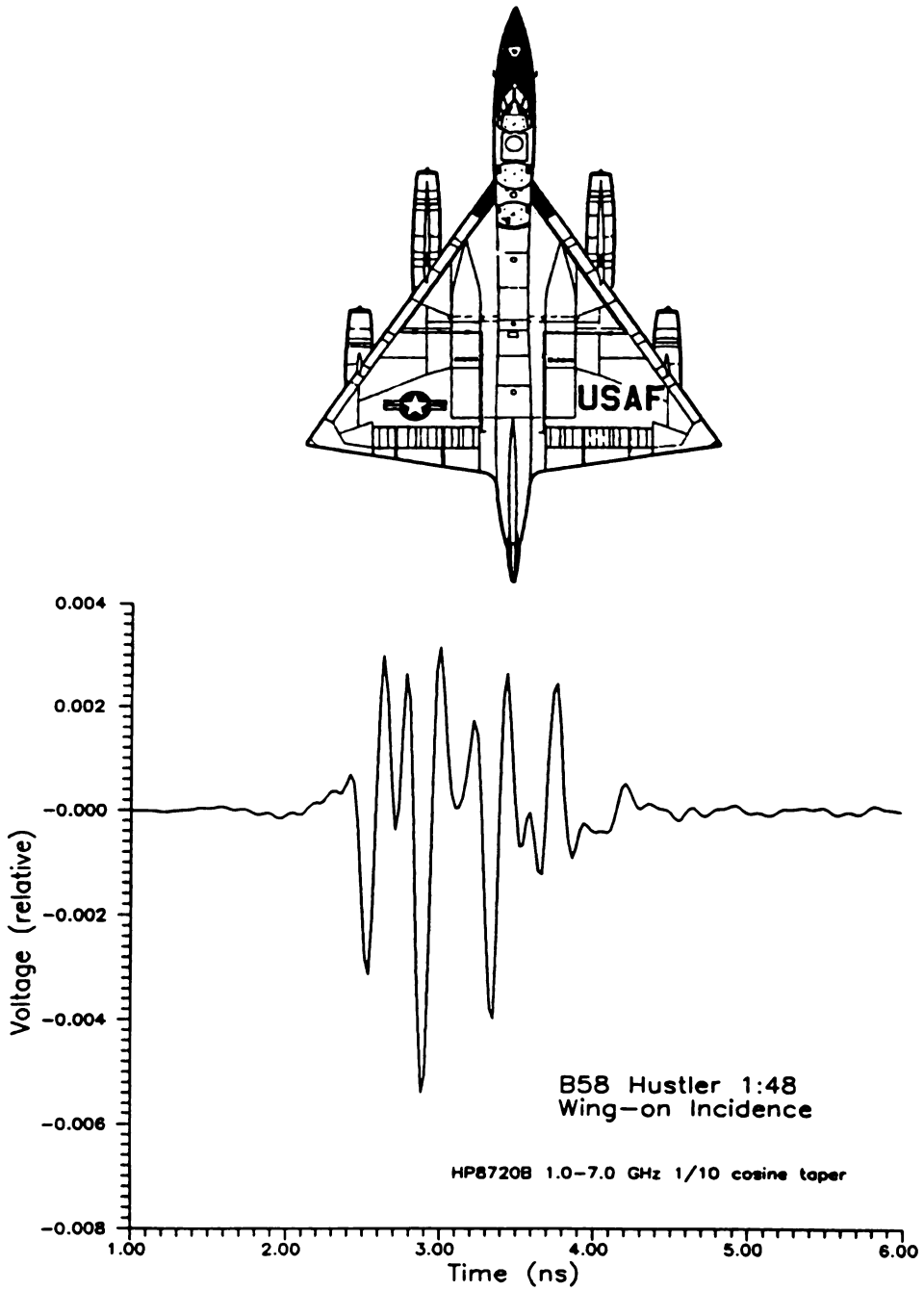

Figure 6.35 Early-time response of B58 Hustler for wing-on incidence.

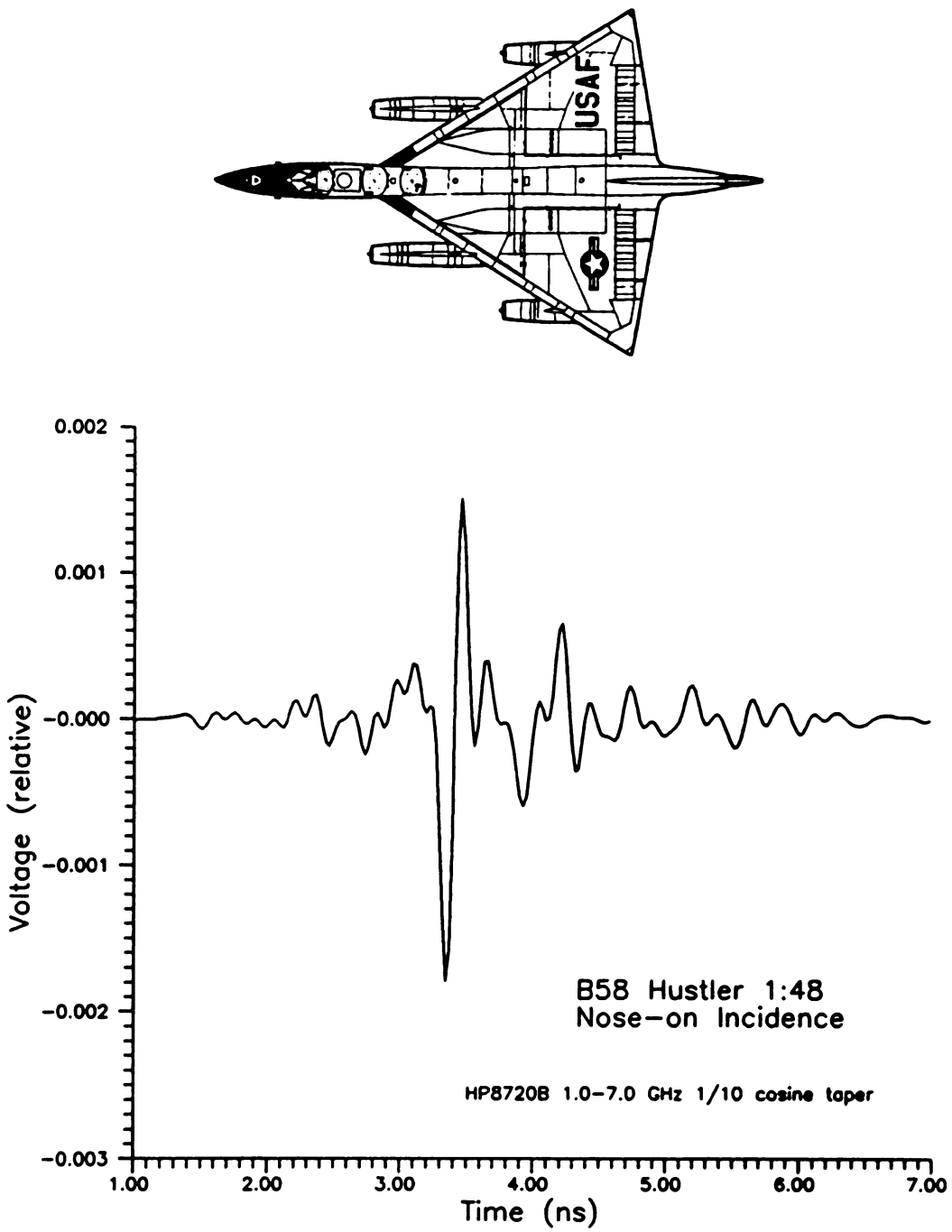

Figure 6.36 Early-time response of B58 Hustler for nose-on incidence.

Chapter 7

Conclusions

This dissertation has presented a number of topics and ideas related to the application of UWB radar to the detection and discrimination of targets. In Chapter 2, the performance of an automated discrimination scheme using the E-pulse and S-pulse method is evaluated using transient scattering data for thin-wire targets in the presence of varying amounts of additive random gaussian noise. The results of this analysis serve as a baseline for comparison of other discrimination methods as well as the effects of multiple targets on the effectiveness of the discrimination. Some initial considerations for applying the discrimination scheme in a multiple target environment are discussed in the last section of Chapter 2. In examining the multiple target environment, questions arise concerning the effects of interactions on the SEM mode frequencies of the target. To attempt to answer these questions, the detailed examination of the SEM analysis of a system of coupled thin wire targets was undertaken. Several methods of varying accuracy and computational requirements were used to calculate the SEM mode frequencies of the coupled wire system. The behavior of the SEM modes of the system of wires is very complicated. The physical significance of the system modes had not been previously published. Chapter 3 attempts to provide an increased understanding of the transient coupling phenomena and provide the correct physical picture for interpretation of the SEM formulation. In Chapter 4 this new physical picture is used as a guide to interpret

the results from an empirical study of the performance of the E-pulse and S-pulse discrimination scheme as applied to analytically generated scattering data for a system of two identical thin wire targets. Specifically, it is seen that the discrimination scheme is adversely affected when two thin wire targets are in close proximity. It is found that for cross range separation that the principle mechanism for degrading the discrimination is the shift of the natural frequencies due to the target interactions. In the case of down range separations, the principle degrading mechanism is the large early-time response of the second target.

A great deal of effort was expended during the course of this research in attempts to improve the transient measurement capability at the Michigan State University Electromagnetics Laboratory. This improvement was motivated by the need to have accurate transient scattering data from complex targets such as aircraft that cannot be modeled theoretically. In particular, the application of the E-pulse and S-pulse methods require that the natural frequencies of the targets be measured in a laboratory setting prior to implementing the discrimination scheme. Since the extraction algorithms in current use are sensitive to noise as well as systematic errors induced by the measurement systems, the transient measurements must be made as accurately and carefully as possible. Further, efforts are currently underway to use the early-time portion of the transient response of the target to enhance detection as well as for target discrimination and imaging applications. Thus, acquiring high quality measurements of the early-time response of complicated targets is essential for proof of concept applications and for use in verifying the accuracy of theoretical models. Chapter 5 presents a method for making accurate transient scattering measurements using a

frequency stepping vector network analyzer. The accuracy of the measurements is due both to the inherent advantages of the network analyzer such as high stability and wide dynamic range and to the use of a robust procedure for removing clutter and deconvolving the effects of the measurement system from the raw measurements. It is seen that the deconvolution process also improves the results obtained using direct time domain measurements. The accuracy of the measurements is demonstrated using several canonical targets such as the sphere and the thin wire.

Chapter 6 presents further demonstration of the quality of the measurement system as applied to measurement of the scattering from a system of coupled thin wires. These measurements are of sufficient quality to verify the theoretical calculations and physical pictures associated with the transient coupling phenomena. The SEM modes extracted from measurements of the transient surface current on a system of coupled wires further demonstrates the coupling phenomena. It is believed that the measurements of coupled wires presented here are accurate and are possibly the first such measurements published. Chapter 6 also presents comparisons of the measurements of a wire stick aircraft model to theoretical calculations to further demonstrate the measurement capability.

It has been widely accepted in the literature and EM community that the early-time portion of the response contains most of the energy in the scattered waveform. Measurements performed at Michigan State University have for a number of years suggested that this may not be the case in actual measurements of realistic targets excited in the resonance region. Chapter 6 settles this issue by making use of the accuracy of the transient measurements to calculate the amount of energy that is present for scale models of realistic aircraft. For the targets considered, it is demonstrated that the early-time does

indeed contain the larger fraction of total backscattered signal energy, but that there are instances when the late-time energy content is significant and useful for discrimination via the E-pulse and S-pulse.

The measurement capabilities are also used to illustrate early-time scattering measurements of practical 1/48 scale model aircraft. It is seen that the early-time response is composed of responses from distinct scattering centers along the fuselage of the aircraft. These scattering centers are generally associated with discontinuities and sharp bends. It is seen from measurements that the early-time response is also very aspect dependent. This aspect dependency places constraints on potential discrimination and detection schemes using the early-time response.

In summary, this dissertation has addressed a number of topics pertinent to the application of UWB radar to target discrimination and should serve to enhance the understanding of the transient scattering phenomena. In particular, the improved measurement schemes should continue to pay large dividends in future research at Michigan State University.

Though a number of problems associated with resonance based target discrimination have been addressed in this dissertation, many interesting and useful problems associated with UWB radar remain. Specifically, an SEM formulation that makes use of substructure resonances to describe the early-time response should be investigated further. Effective implementation of the E-pulse and S-pulse schemes will also require more exhaustive studies of aircraft responses and characterization of these responses using SEM. It would also be useful to translate the EDR and SDR numbers into a measure of confidence in the discrimination results. This could be extended to the

problem of confidence that the indicated target is contained in the library of E-pulses and S-pulses.

Detection is also a very important aspect of UWB radar. It is anticipated that a study of transient polarimetrics would be useful for reduction of sea and ground clutter in relation to the target response. Of course, a study of this sort would require accurate measurements of the polarimetric response of both targets and typical clutter mechanisms such as sea surfaces and vegetation.

Appendix A

Appendix A

Frequency Domain Moment Method Formulation

A.1 Piecewise Sinusoidal Basis Functions

Many results in this dissertation were generated using a moment method formulation based on the EFIE and piecewise sinusoidal basis functions. As such, it is appropriate to provide a summary of this formulation.

The geometry of a thin wire segment with half length Δ and radius a is shown in Figure A.1. Assume the current distribution on the wire is

$$I(z) = I_m \sin k(\Delta - |z|) \tag{A.1}$$

where $I_m \sin k\Delta$ is the amplitude of the current at the center of the wire and $k=\omega/c$ is the wavenumber. Note that it is common practice to normalize the current by the constant factor $\sin k\Delta$. To simplify notation, this factor is suppressed throughout this Appendix. It is well known that the fields of the thin wire with a sinusoidal current distribution have an analytic expression [57]. The $\hat{\phi}$ component of magnetic field is

$$B_\phi(\rho,z) = -\frac{\mu I_m}{j4\pi\rho}\left\{e^{-jkR_1} + e^{-jkR_2} - (2\cos k\Delta)e^{-jkr}\right\} \tag{A.2}$$

where

$$\rho = \sqrt{x^2+y^2} \qquad r = \sqrt{\rho^2+z^2} \tag{A.3}$$

and

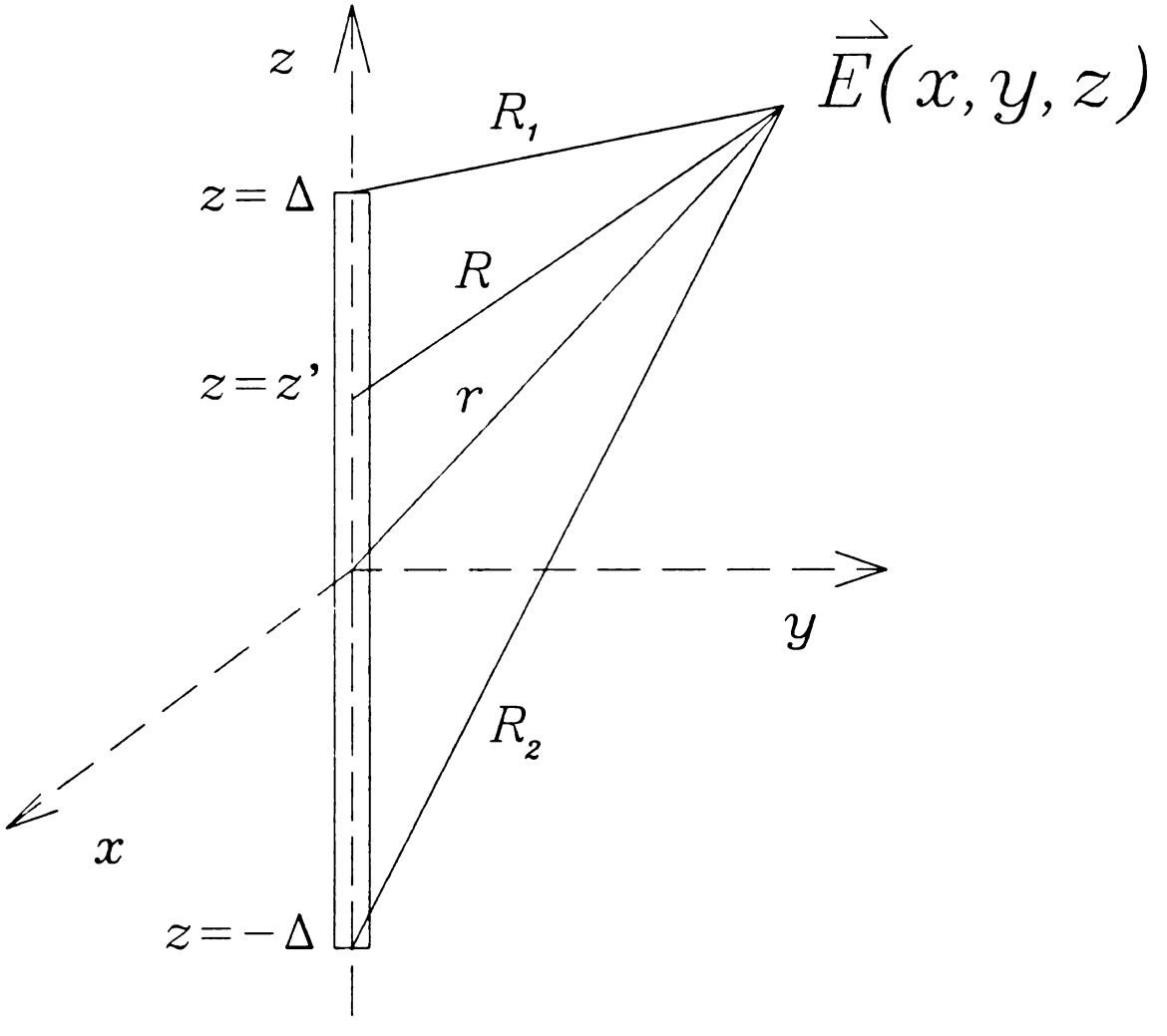

Figure A.1 Geometry of thin-wire scatterer.

$$R_1 = \sqrt{\rho^2+(z-\Delta)^2} \qquad R_2 = \sqrt{\rho^2+(z+\Delta)^2} \tag{A.4}$$

The $\hat{\rho}$ component of electric field is obtained from

$$E_\rho(\rho,z) = -\frac{1}{j\omega\mu\epsilon}\frac{\partial B_\phi}{\partial z} \tag{A.5}$$

which yields

$$E_\rho(\rho,z) = j\eta\frac{I_m}{4\pi}\left\{\frac{z-\Delta}{\rho}\frac{e^{-jkR_1}}{R_1} + \frac{z+\Delta}{\rho}\frac{e^{-jkR_2}}{R_2} - 2\cos k\Delta\frac{z}{\Delta}\frac{e^{-jkr}}{r}\right\} \tag{A.6}$$

where $\eta = \sqrt{\frac{\epsilon_0}{\mu_0}}$ is the impedance of free space. The $\hat{z}$ component of electric field is

obtained from

$$E_z(\rho,z) = \frac{1}{j\omega\mu\epsilon\rho}\frac{\partial(\rho B_\phi)}{\partial\rho} \tag{A.7}$$

which yields

$$E_z(\rho,z) = \frac{-j\eta I_m}{4\pi}\left\{\frac{e^{-jkR_1}}{R_1} + \frac{e^{-jkR_2}}{R_2} - 2\cos k\Delta\frac{e^{-jkr}}{r}\right\} \tag{A.8}$$

The boundary condition on the tangential electric field at the surface of a perfect conductor is

$$\hat{t}\cdot\vec{E}^s(\vec{r}) = -\hat{t}\cdot\vec{E}^i(\vec{r}) \tag{A.9}$$

If a structure is modeled by a number of thin wire segments then the scattered field can be written as

$$\vec{E}^s(\vec{r}) = \sum_{n=1}^{N} \vec{E}_n^s(\vec{r}) \tag{A.10}$$

where $\vec{E}_n^s(\vec{r})$ is the field scattered by the n^{th} wire segment. This field can be calculated from the previous expressions and can be extended to segments that are not parallel to the z-axis by appropriate vector transformations. If all segments are parallel to the z-axis, the EFIE can be converted to matrix form by applying the Galerkin testing function

$$\int_{seg\ m} \sin k(\Delta - |z - z_m|)\,\hat{z}\cdot\{...\}dz \tag{A.11}$$

where z_m is the center of the m^{th} segment. The resulting matrix equation has the form

$$AI = E \tag{A.12}$$

where I is the column vector containing the amplitudes of the current basis functions, the entries in the A matrix have the form

$$A_{mn} = \int_{seg\ m} \sin(\Delta - |z - z_m|)\,\hat{z}\cdot\vec{E}_n^s(\vec{r})dz \tag{A.13}$$

and the column vector E has entries of the form

$$E_m = -\int_{seg\ m} \sin k(\Delta - |z - z_m|)\,\hat{z}\cdot\vec{E}^i(\vec{r})dz \tag{A.14}$$

A.2 Finite Conductivity Effects

The finite conductivity of the wire is accounted for by using the boundary condition

$$\hat{t}\cdot\vec{E}^i(\vec{r}) + \hat{t}\cdot\vec{E}^s(\vec{r}) + Z^i J(\vec{r}) = 0 \tag{A.15}$$

where the impedance of the wire Z^i can be approximated by the skin effect resistance from [58] as

$$Z^i = \frac{TJ_0(Ta)}{2\pi a\sigma J_0'(Ta)}; \qquad T = (j)^{-\frac{1}{2}}\sqrt{\omega\mu\sigma} \tag{A.16}$$

where J_0 is the Bessel function of order 0 and J_0' is the derivative of J_0 with respect to the argument, a is the radius of the wire, σ is the conductivity, and μ is the permeability. Using the previous piecewise sinusoidal weighting function, the matrix elements for the case when the weighting function and basis functions overlap ($m=n$) are augmented with

$$t_s = Z^i \int_{-\Delta}^{\Delta} \sin^2 k(\Delta - |z|)dz \tag{A.17}$$

The integral can be rewritten as

$$\int_{-\Delta}^{\Delta} \sin^2 k(\Delta - |z|)dz = \int_{0}^{\Delta} \sin^2 k(\Delta - z)dz + \int_{-\Delta}^{0} \sin^2 k(\Delta + z)dz \tag{A.18}$$

Making the change of variables $z=-z$ in the second integral results in

$$\int_{-\Delta}^{\Delta} \sin^2 k(\Delta - |z|)dz = 2\int_{0}^{\Delta} \sin^2 k(\Delta - z)dz \tag{A.19}$$

After a further change of variables $u=\frac{\Delta}{2}-z$, this integral is in tabulated form [59]. The resulting additive term is

$$t_s = Z^i\left\{\Delta - \frac{1}{2k}\sin k2\Delta\right\} \tag{A.20}$$

For the cases when the weighting function only overlaps half of the basis function, the matrix elements are augmented by

$$t_c = \int_0^{\Delta} \sin k(\Delta - |z|) \sin k(\Delta - |z-\Delta|)\, dz \tag{A.21}$$

which can be rewritten as

$$t_c = \int_0^{\Delta} \sin k(\Delta - z) \sin kz\, dz \tag{A.22}$$

then using $\sin\alpha\sin\beta = \frac{1}{2}\cos(\alpha-\beta) - \frac{1}{2}\cos(\alpha+\beta)$ this becomes

$$t_c = \frac{1}{2}\int_0^{\Delta} \cos k(\Delta - 2z)\, dz - \frac{1}{2}\int_0^{\Delta} \cos k\Delta\, dz \tag{A.23}$$

Evaluating the integrals gives the following result

$$t_c = Z^i\left\{-\frac{\Delta}{2}\cos k\Delta + \frac{1}{2k}\sin k\Delta\right\} \tag{A.24}$$

Appendix B

Appendix B

SEM Formulations

B.1 Piecewise Sinusoidal Basis Functions

For the computations of the SEM mode frequencies, currents and scattered fields, the piecewise sinusoidal basis function as presented in Appendix A can be used. The formulation must be generalized to complex frequency. This is easily accomplished by substituting ω with $-js$ in the expressions for the current and scattered fields.

B.2 Hallen Equation for Array of Parallel Wires

An electric field integral equation for the special case of an array of P wires parallel to the z-axis and centered at $z=0$ can be written as [60],

$$\sum_{p=1}^{P} \int_{-\frac{l_p}{2}}^{\frac{l_p}{2}} \left\{ \frac{\partial}{\partial z'} I_p(z') \frac{\partial}{\partial z} - \gamma^2 I_p(z') \right\} g_{pq}(z,z',s) dz' = \gamma \frac{4\pi}{\eta} E^i_{qz}(z,s) \qquad \text{(B.1)}$$

where l_p is the length of the p^{th} wire, I_p is the axial current on the p^{th} wire, γ is the complex wavenumber, η is the impedance of free space, $E^i_{qz}(z,s)$ is the $\hat{z}$ component of the impressed field on the q^{th} wire, and g_{pq} is the scalar Green's function under the thin wire approximations which is given by

$$g_{pq}(z,z',s) = \frac{e^{-\gamma R_{pq}}}{R_{pq}} \qquad \text{(B.2)}$$

where under the thin wire approximations

$$R_{pq} = \sqrt{(z-z')^2 + d_{pq}^2} \tag{B.3}$$

where d_{pq} is the radius of the pth wire for $p=q$, and d_{pq} is the axial spacing between wires for $p \neq q$. For the purpose of computing the SEM mode frequencies and currents only the homogenous form is required. The equation can be written as

$$\left(\frac{\partial^2}{\partial z^2} - \gamma^2\right) \sum_{p=1}^{P} \int_{-\frac{l_p}{2}}^{\frac{l_p}{2}} I_p(z') g_{pq}(z,z',s)\, dz' = 0 \tag{B.4}$$

To avoid the numerical differentiation, the previous expression is rewritten in the Hallen form as

$$\sum_{p=1}^{P} \int_{-\frac{l_p}{2}}^{\frac{l_p}{2}} I_p(z') g_{pq}(\vec{r},\vec{r}',s)\, dz' = A_q \sinh\gamma z + B_q \cosh\gamma z \qquad q=1,2,\ldots,P \tag{B.5}$$

By specializing to the case of P monopoles above and perpendicular to a perfectly conducting ground plane ($z=0$) with their bases at $z=0$, the homogenous equation becomes

$$\sum_{p=1}^{P} \int_{0}^{\frac{l_p}{2}} I_p(z') \bar{g}_{pq}(z,z',s)\, dz' = B_q \cosh\gamma z \qquad q=1,2,\ldots,P \tag{B.6}$$

where

$$\bar{g}_{pq}(z,z',s) = g_{pq}(z,z',s) + g_{pq}(z,-z',s) \tag{B.7}$$

accounts for the image of the monopoles. Since I_p and $\bar{G}(\vec{r},\vec{r}',s)$ are even functions of z, the unknown coefficient A_q must be zero. A moment method solution can be implemented by expressing the current on each monopole in a pulse function expansion

$$I_p(z) = \sum_{m=1}^{M_p} c_{pm} \Pi_{pm}(z) \tag{B.8}$$

where M_p is the number of basis functions on the pth monopole and the pulse functions are defined as

$$\Pi_{pm}(z) = \begin{cases} 1 & \text{if } (z_{pm}-\Delta_p) \le z \le (z_{pm}+\Delta_p) \\ 0 & \text{otherwise} \end{cases} \tag{B.9}$$

where z_{pm} is the center of the mth basis function on the pth wire, and Δ_p is the half width of the pulses on the pth wire. The centers of the pulses are usually chosen as

$$z_{pm} = (2m-1)\Delta_p; \qquad \Delta_p = \frac{1}{2M_p}\frac{l_p}{2} \tag{B.10}$$

Then substituting the current expansion in to the integral equation and applying the weighting function

$$\int_0^{\frac{l_q}{2}} w_{qn}(z)\{...\}dz \qquad q=1,2,...,P \quad n=1,2,...,M_q \tag{B.11}$$

results in the equations

$$\int_0^{\frac{l_q}{2}} w_{qn}(z) \sum_{p=1}^{P} \sum_{m=1}^{M_p} c_{pm} \int_0^{\frac{l_p}{2}} \Pi_{pm}(z') \bar{g}_{pq}(\vec{r},\vec{r}',s) dz' dz = B_q \int_0^{\frac{l_q}{2}} w_{qn}(z) \cosh\gamma z dz \tag{B.12}$$

Passing the testing function through the sums and integrations results in

$$\sum_{p=1}^{P}\sum_{m=1}^{M_p} c_{pm}\int_0^{\frac{l_p}{2}} \Pi_{pm}(z')\int_0^{\frac{l_q}{2}} w_{qn}(z)\bar{g}_{pq}(z,z',s)\,dz\,dz' = B_q\int_0^{\frac{l_q}{2}} w_{qn}(z)\cosh\gamma z\,dz \qquad \text{(B.13)}$$

If point matching is used then, $w_{qn}(z)=\delta(z-z_{qn})$ where the match points are chosen to be at the center of the pulse basis functions. Then using the sifting property of the Dirac delta function,

$$\sum_{p=1}^{P}\sum_{m=1}^{M_p} c_{pm}\int_0^{\frac{l_p}{2}} \Pi_{pm}(z')\bar{g}_{pq}(z_{qn},z',s)\,dz' - B_q\cosh\gamma z_{qn} = 0 \qquad \begin{matrix} q=1,2,\ldots,P \\ n=1,2,\ldots,M_q \end{matrix} \qquad \text{(B.14)}$$

The above choice of testing functions results in the same number of testing points (equations) as basis functions per monopole. There must then be P additional equations to solve the problem due to the presence of the B_q. These constraints are obtained by using the boundary condition on the current at the ends of the monopoles

$$I_p(z=l_p) = 0 \qquad p=1,2,\ldots,P \qquad \text{(B.15)}$$

Thus, for the case of pulse basis functions $c_{p,Mp} = 0$. Hence, the number of unknowns is reduced by P and the resulting square matrix has zero determinant for $s=s_n$. A numerical procedure is used to locate these zeros as discussed in Chapter 3.

B.3 Approximate Green's Function Solution with Sinusoidal Current

This section contains details of the formulation of the approximate Green's function method of Chapter 3 for the case of two identical parallel wires. The formulation follows that used by Chuang and Nyquist [61]. Recall from Chapter 3 that for the special case of two identical scatterers, one need only calculate two constants to evaluate the shift in the natural frequency.

$$s = s_n^o \pm \delta \qquad \delta = \frac{a_{12}}{\bar{a}_{11}} \tag{B.16}$$

where s_n^o is nth natural mode frequency of the isolated scatterer. From Chapter 3,

$$a_{12} = \int_{S_1} \vec{K}_n^o(\vec{r}) \cdot \int_{S_2} \ddot{G}(\vec{r},\vec{r}',s_n^o) \cdot \vec{K}_n^o(\vec{r}')\, dS'\, dS \tag{B.17}$$

where $\vec{K}_n^o$ is the nth natural mode current of the isolated scatterer. This can be specialized for the case of two identical wires parallel to the z-axis as

$$a_{12} = \int_0^l I_n^o(z) \int_0^l G_{12}(z,z',s_n^o) I_n^o(z')\, dz'\, dz \tag{B.18}$$

where l is the length of the wire, G_{12} is given by

$$G_{12}(z,z',s_n^o) = \left\{ \frac{\partial^2}{\partial z \partial z'} + (\gamma_n^o)^2 \right\} g_{12}(z,z',s_n^o) \tag{B.19}$$

and

$$g_{12}(z,z',s_n^o) = \frac{e^{-\gamma_n^o R_{12}}}{R_{12}} \qquad R_{12} = \sqrt{(z-z')^2 + d_{12}^2} \tag{B.20}$$

where d_{12} is the axial distance between the wires. Then,

$$a_{12} = \int_0^l \int_0^l I_n^o(z) I_n^o(z') \frac{\partial^2}{\partial z \partial z'} g_{12}(z,z',s_n^o)\, dz'\, dz + \int_0^l \int_0^l I_n^o(z) I_n^o(z') (\gamma_n^o)^2 g_{12}(z,z',s_n^o)\, dz'\, dz \tag{B.21}$$

The first term is integrated by parts twice, once on z' and once on z, to remove the spatial derivatives from $g_{12}(z,z',s_n^o)$. Note that $I_n^o(z=0,l) = 0$ so that

$$\int_0^l\int_0^l I_n^o(z')I_n^o(z)\frac{\partial^2}{\partial z\partial z'}g_{12}(z,z',s_n^o)dz'dz = \int_0^l\int_0^l I_n^{o'}(z')I_n^{o'}(z)g_{12}(z,z',s_n^o)dz'dz \quad \text{(B.22)}$$

where the prime on the currents denotes a derivative with respect to the argument. Hence,

$$a_{12} = \int_0^l\int_0^l \left\{I_n^{o'}(z')I_n^{o'}(z) + (\gamma_n^o)^2 I_n^o(z')I_n^o(z)\right\}g_{12}(z,z',s_n^o)dz'dz \quad \text{(B.23)}$$

The second constant has the general form

$$\bar{a}_{11} = \int_{S_1}\vec{K}_n^o(\vec{r})\cdot\int_{S_1}\frac{\partial}{\partial s}\vec{\vec{G}}(\vec{r},\vec{r}',s)|_{s=s_n^o}\cdot\vec{K}_n^o(\vec{r}')dS'dS \quad \text{(B.24)}$$

which can be written as

$$\bar{a}_{11} = \int_0^l\int_0^l I_n^o(z)I_n^o(z')\frac{\partial}{\partial s}G_{11}(z,z',s)|_{s=s_n^o}dz'dz \quad \text{(B.25)}$$

where

$$G_{11}(z,z',s) = \left\{\frac{\partial^2}{\partial z'\partial z} + \gamma^2\right\}g_{11}(z,z',s) \quad \text{(B.26)}$$

with

$$g_{11}(z,z',s) = \frac{e^{-\gamma R_{11}}}{R_{11}} \qquad R_{11} = \sqrt{(z-z')^2 + a^2} \quad \text{(B.27)}$$

where a is the wire radius. Then,

$$\begin{aligned}\bar{a}_{11} = &\int_0^l\int_0^l I_n^o(z)I_n^o(z')\frac{\partial^2}{\partial z\partial z'}\frac{\partial}{\partial s}g_{11}(z,z',s)|_{s=s_n^o}dz'dz + \\ &\int_0^l\int_0^l I_n^o(z)I_n^o(z')\frac{\partial}{\partial s}(\gamma_n^o)^2 g_{11}(z,z',s)|_{s=s_n^o}dz'dz\end{aligned} \quad \text{(B.28)}$$

The first integral can be integrated by parts as before to obtain

$$\int_0^l\int_0^l I_n^{o\prime}(z')I_n^{o\prime}(z)\frac{\partial}{\partial s}g_{11}(z,z',s)|_{s=s_n^o}dz'dz \tag{B.29}$$

The second integral can be expanded to obtain

$$\int_0^l\int_0^l I_n^o(z)I_n^o(z')\gamma_n^o(\frac{2}{R}-\gamma_0)\frac{\partial}{\partial s}g_{11}(z,z',s)|_{s=s_n^o}dz'dz \tag{B.30}$$

Noting that $\frac{\partial}{\partial s}g_{11}(z,z',s)|_{s=s_n^o} = -\frac{e^{-\gamma_n^o R_{11}}}{c}$ and combining terms gives

$$\bar{a}_{11} = \int_0^l\int_0^l\left\{I_n^{o\prime}(z)I_n^{o\prime}(z') + \gamma_n^o(\frac{2}{R}-\gamma_n^o)I_n^o(z)I_n^o(z')\right\}\frac{e^{-\gamma_n^o R}}{c}dz'dz \tag{B.31}$$

If the current on the wires is assumed to be sinusoidal,

$$I_n^o(z) = \sin\frac{n\pi z}{l}; \qquad 0\le z\le l;\ n\in \mathbf{I} \tag{B.32}$$

then the derivatives on the current can be performed analytically to yield

$$a_{12} = \int_0^l\int_0^l\left\{\sin\frac{n\pi z}{l}\sin\frac{n\pi z'}{l}(\gamma_n^o)^2 + (\frac{n\pi}{l})^2\cos\frac{n\pi z}{l}\cos\frac{n\pi z}{l}\right\}g_{11}(z,z',s_n^o)dz'dz \tag{B.33}$$

$$\bar{a}_{11} = \int_0^l\int_0^l\left\{(\frac{n\pi}{l})^2\cos\frac{n\pi z}{l}\cos\frac{n\pi z'}{l} + \gamma_n^o(\frac{2}{R}-\gamma_n^o)\sin\frac{n\pi z}{l}\sin\frac{n\pi z'}{l}\right\}\frac{e^{-\gamma_n^o R_{11}}}{c}dz'dz \tag{B.34}$$

B.4 Coupling Coefficient and Normalization Constant Calculations

This section describes some details associated with calculation of the coupling coefficient a_n and normalization constant c_n. The Pocklington form of the EFIE for wires parallel to the z-axis can be written as

$$\int_{\Gamma} I_n(z')\bar{G}(\vec{r},\vec{r}',s)\,dz' = \gamma\frac{4\pi}{\eta}E_z^i(\vec{r},s) \tag{B.35}$$

where $\bar{G}(\vec{r},\vec{r}',s)$ is the Pocklington form of the Green's function under the thin wire approximations

$$\bar{G}(\vec{r},\vec{r}',s) = \left\{\frac{\partial^2}{\partial z^2} - \gamma^2\right\}\frac{e^{-\gamma R}}{R} \tag{B.36}$$

and R is the distance between the source point and field point. Using the thin wire approximations

$$R(z,z') = \sqrt{(z-z')^2 + d^2} \tag{B.37}$$

where and d is the wire radius when the source point and field point are on the same wire and d is the axial spacing between the wires when the source point and field point are on different wires. Then, the expression for c_n of Chapter 3 is written as

$$c_n = \int_{\Gamma} I_n(z)\int_{\Gamma}\frac{\partial\bar{G}(\vec{r},\vec{r}',s)}{\partial s}I_n(z')\,dz'\,dz \tag{B.38}$$

where the $\frac{\partial}{\partial s}$ operator has been passed through the surface integrations. Here, I_n is the current distribution of the n^{th} mode. Numerical differentiation is avoided by analytically evaluating $\frac{\partial}{\partial s}\bar{G}(z,z',s)$.

$$\frac{\partial}{\partial s}G(z,z',s) = \frac{1}{4\pi}\left\{\frac{\partial^2}{\partial z^2}\frac{\partial}{\partial s}\frac{e^{-\gamma R}}{R} - \frac{\partial}{\partial s}\left(\gamma^2\frac{e^{-\gamma R}}{R}\right)\right\} \tag{B.39}$$

Note that $\frac{\partial}{\partial s}\frac{e^{-\gamma R}}{R} = -\frac{e^{-\gamma R}}{c}$. Then, the first term in braces is

$$T_1 = \frac{\partial^2}{\partial z^2}\frac{\partial}{\partial s}\frac{e^{-\gamma R}}{R} = \frac{1}{c}\frac{\partial}{\partial z}\frac{\partial}{\partial z}\frac{e^{-\gamma R}}{R} \tag{B.40}$$

Note that $\frac{d}{dz}R = \frac{z-z'}{R}$ and $\frac{\partial}{\partial z}e^{-\gamma R} = -\frac{\gamma(z-z')}{R}e^{-\gamma R}$. Thus,

$$T_1 = \frac{1}{c}\frac{\partial}{\partial z}\left\{\frac{-\gamma(z-z')}{R}e^{-\gamma R}\right\} \tag{B.41}$$

Expanding using the product rule and the relation $\frac{\partial}{\partial z}(\frac{1}{R}) = -\frac{z-z'}{R^3}$ gives

$$T_1 = -\frac{\gamma}{c}\left\{\frac{\partial}{\partial z}(\frac{z-z'}{R})e^{-\gamma R} + \frac{z-z'}{R}\frac{d}{dz}e^{-\gamma R}\right\} \tag{B.42}$$

$$T_1 = -\gamma\frac{e^{-\gamma R}}{c}\left\{\frac{1}{R} + (z-z')\frac{d}{dz}(\frac{1}{R}) - \frac{(z-z')^2}{R^2}\gamma\right\} \tag{B.43}$$

$$T_1 = -\gamma\frac{e^{-\gamma R}}{c}\left\{\frac{1}{R} - \frac{(z-z')^2}{R^3} + \gamma\frac{(z-z')^2}{R^2}\right\} \tag{B.44}$$

The second term in braces from (B.39) is

$$T_2 = \frac{\partial}{\partial s}\left\{\gamma^2\frac{e^{-\gamma R}}{R}\right\} = \left\{\frac{2\gamma}{cR} - \frac{\gamma^2}{c}\right\}e^{-\gamma R} \tag{B.45}$$

Then after further manipulation,

$$\frac{\partial}{\partial s}\bar{G}(z,z',s) = \gamma\frac{e^{-\gamma R}}{c}\left\{\frac{1}{R} + \frac{(z-z')^2}{R^3} + \frac{\gamma(z-z')^2}{R^2} - \gamma\right\} \tag{B.46}$$

This result is useful for computation of the normalization constants. Due to the formulation used here, the coupling coefficient of Chapter 3 must be modified by the factor of γ/η is given by

$$a_n = -\frac{1}{c_n}\frac{\gamma_n}{\eta}\int_{\Gamma} I_n(z')E_z^i(\vec{r},s_n)\,dz \qquad \text{(B.47)}$$

Appendix C

Appendix C

Experimental Apparatus

This appendix summarizes the equipment used for the experimental portion of the research. The equipment used in the frequency domain scattering measurements is listed in Table C.0. There were two different configurations used in the frequency domain scattering measurements. In both cases, the dual antenna configuration of ? was used. The "low-band" configuration used the PPL 5812 amplifier to amplify the signal from port 1 of the network analyzer. The pertinent network analyzer parameters used in this configuration are shown in Table C.0. The "high-band" configuration used the HP8349B amplifier to amplify the signal from port 1 of the network analyzer. The parameters used in this configuration are given in Table C.0. The equipment used in the time domain scattering measurements are summarized in Table C.0.

Table C.1 Equipment used for frequency domain scattering measurements.

(1)	Hewlett-Packard HP8720B Vector Network Analyzer
(1)	Hewlett-Packard HP8349B Microwave Amplifier
(1)	Picosecond Pulse Labs PPL 5812 10dB Broadband Amplifier
(2)	American Electronics Laboratory AEL H-1734 Wideband TEM Horn Antennas
(1)	23.5 foot RG-9B cable with N-Type Connector
(1)	22.5 foot RG-9B cable with N-Type Connector
(1)	B&K Precision D.C. Power Supply 1610 (for PPL Amplifier)
(1)	IBM PC/AT compatible microcomputer
(1)	HP-82335 HPIB interface and software library

Table C.2 Network analyzer parameters for low band measurements.

Measurement Parameter:	S21
Frequency Sweep:	0.4 - 4.4 GHz
Number of points:	401
IF Bandwidth:	100 Hz
Number of Averages:	10
Sweep Time:	30 seconds

Table C.3 Network analyzer parameters for high band measurements.

Measurement Parameter:	S21
Frequency Sweep:	1.0 - 9.0 GHz
Number of points:	801
IF Bandwidth:	100 Hz
Number of Averages:	10
Sweep Time:	60 seconds

Table C.4 Equipment used for time domain scattering measurements.

(1) Tektronix 7854 Digital Sampling Oscilloscope
(1) Picosecond Pulse Labs PPL 1000B Pulse Generator
(1) Tektronix Type 113 Delay Cable
(1) 23.5 foot RG-9B cable with N-type connectors
(1) 22.5 foot RG-9B cable with N-type connectors
(2) American Electronics Laboratory AEL H-1734 Wideband TEM Horn Antennas
(1) IBM PC/AT compatible microcomputer
(1) HP-82335 HPIB interface and software library

An anechoic chamber was used extensively throughout the research and is essential for performing frequency domain scattering measurements. The Michigan State University anechoic chamber is constructed of wood with 6 inch pyramidal foam absorbers covering the inside walls. The dimensions of the chamber and approximate locations of targets and antennas for the configuration used throughout most of this research is shown in Figure C.1. A new configuration was implemented near the completion of this research in an attempt to reduce the direct coupling of antennas, scattering from the antenna supports, and cable losses. This new configuration is shown in Figure C.2.

To accurately characterize the measurement system, the network analyzer was used to measure the gain of the amplifiers and attenuation of the cables over a wide range of frequencies. The results of these measurements are provided here to indicate the limitations of the measurement system, areas for possible improvement, and baseline measurements to assess future equipment changes. The small signal gain of the HP8349B amplifier is shown in Figure C.4. The gain of the PPL 5812 amplifier gain is shown in Figure C.5. Cable losses for the system prior to February 1992 are shown in Figure C.3. The new chamber configuration makes use of the old receive cable after being cut into two sections. Thus, the total cable losses in the new system are effectively those of the old receive cable.

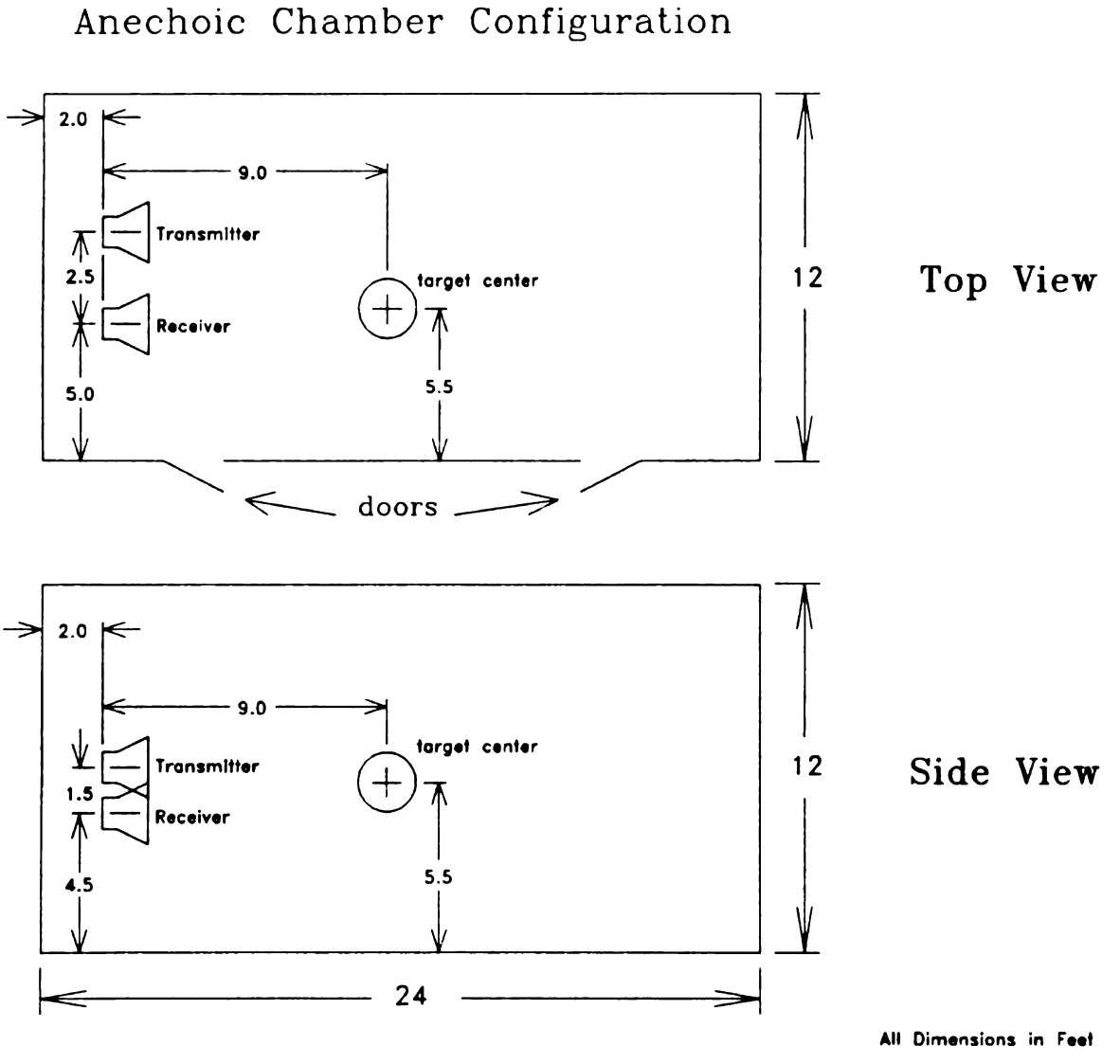

Figure C.1 Michigan State University anechoic chamber configuration prior to February 1992.

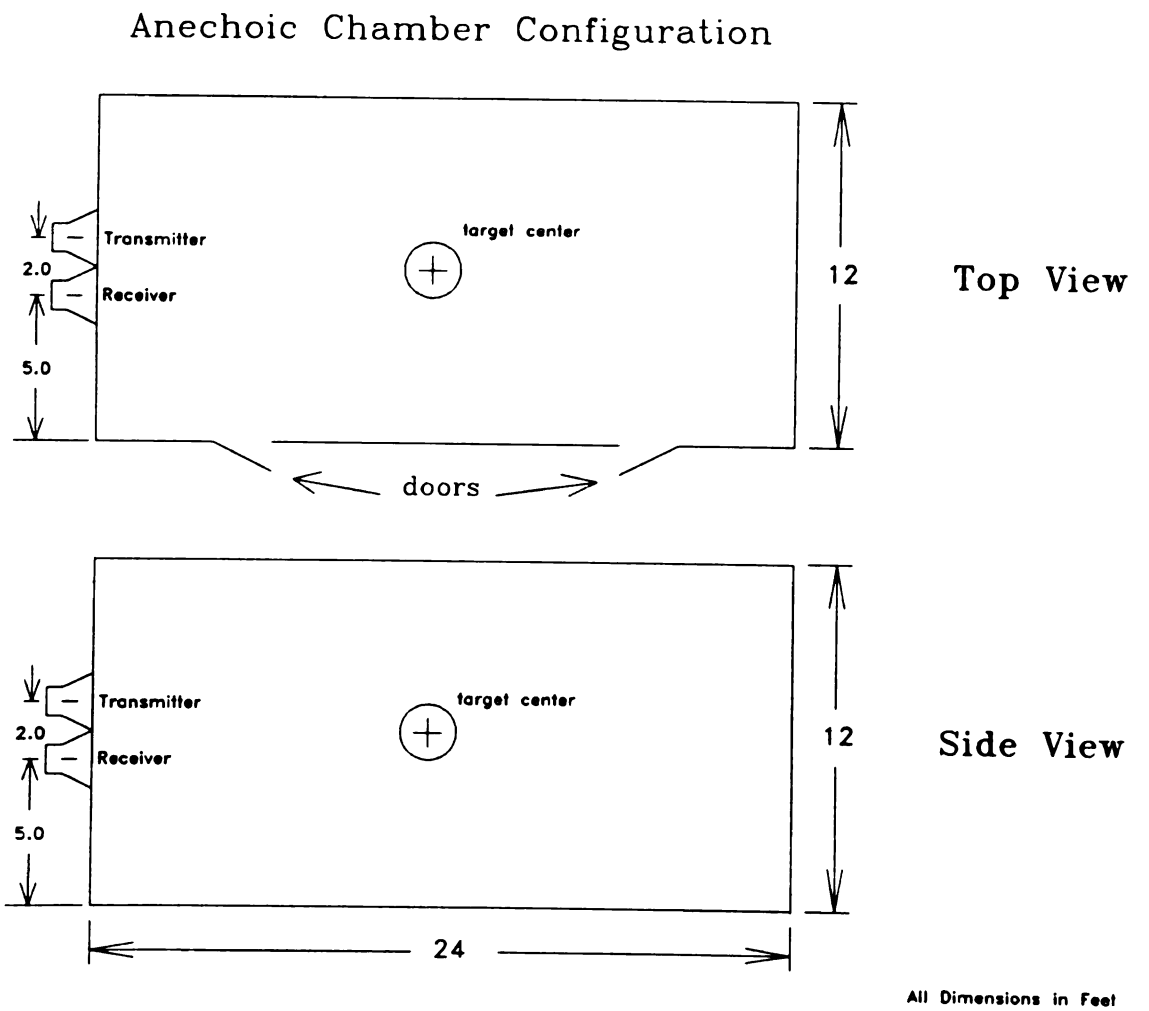

Figure C.2 Michigan State University anechoic chamber after February 1992.

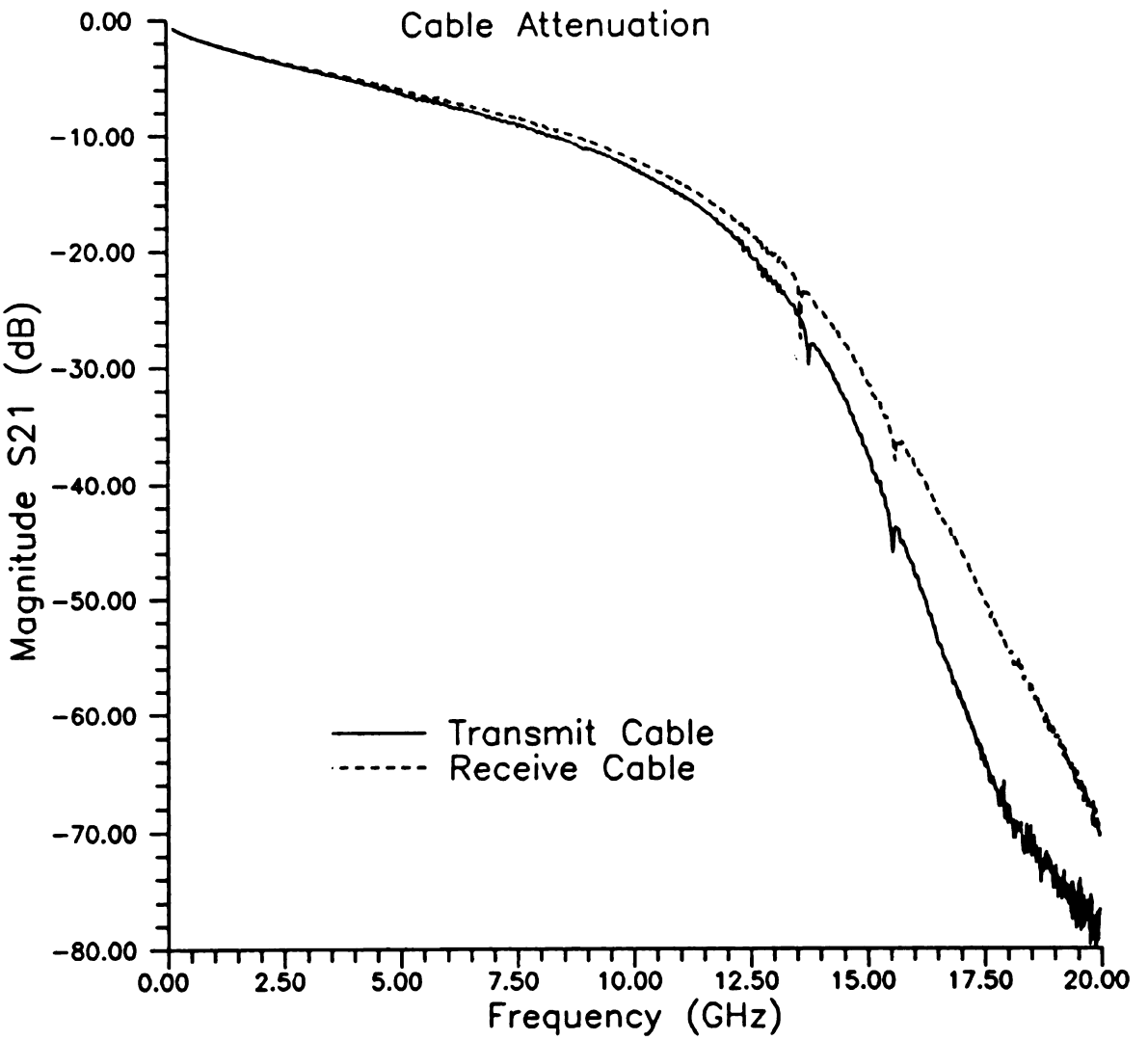

Figure C.3 Measured cable attenuation.

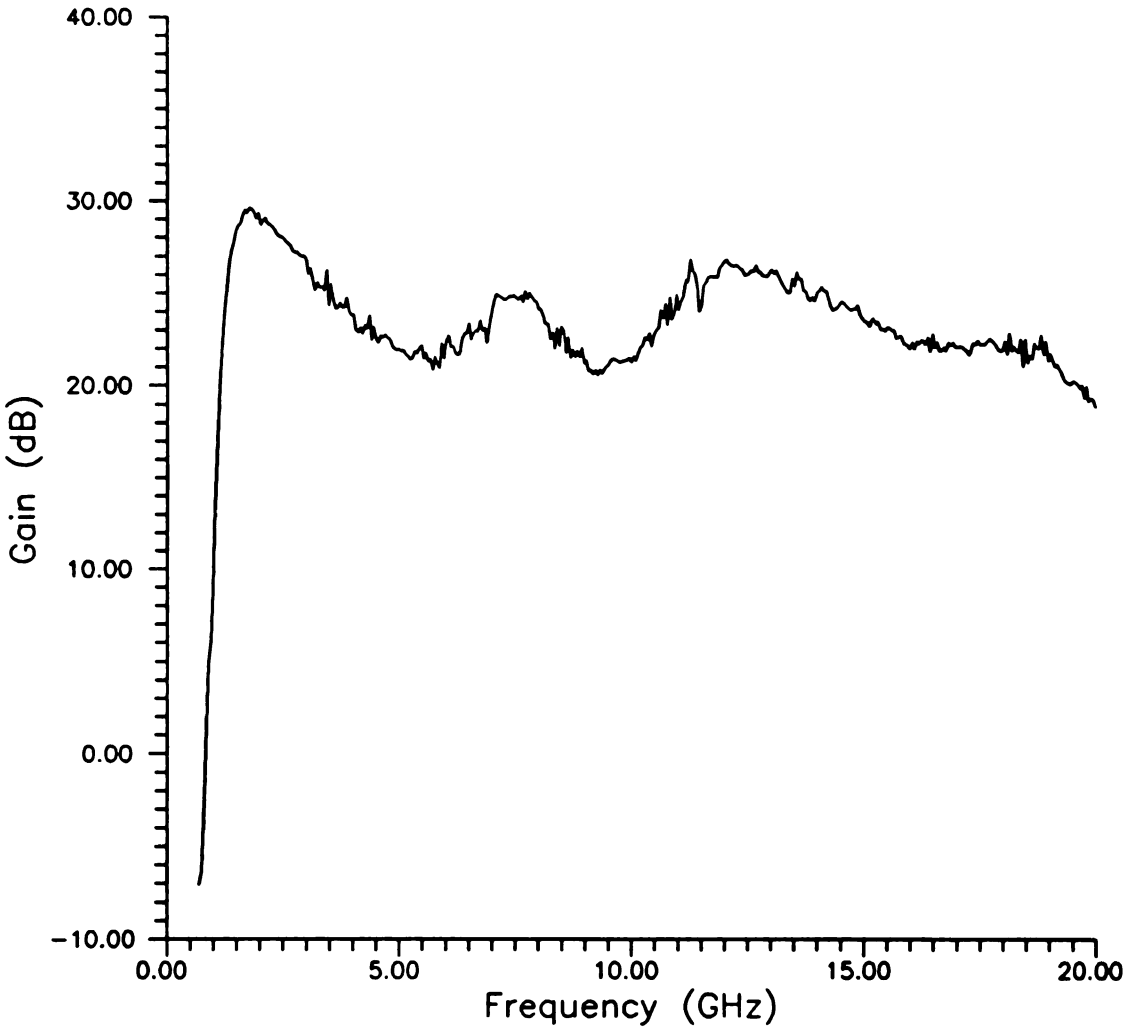

Figure C.4 Gain of HP8349B Microwave Amplifier measured using HP-8720B network analyzer. Amplifier input power = -30 dBm.

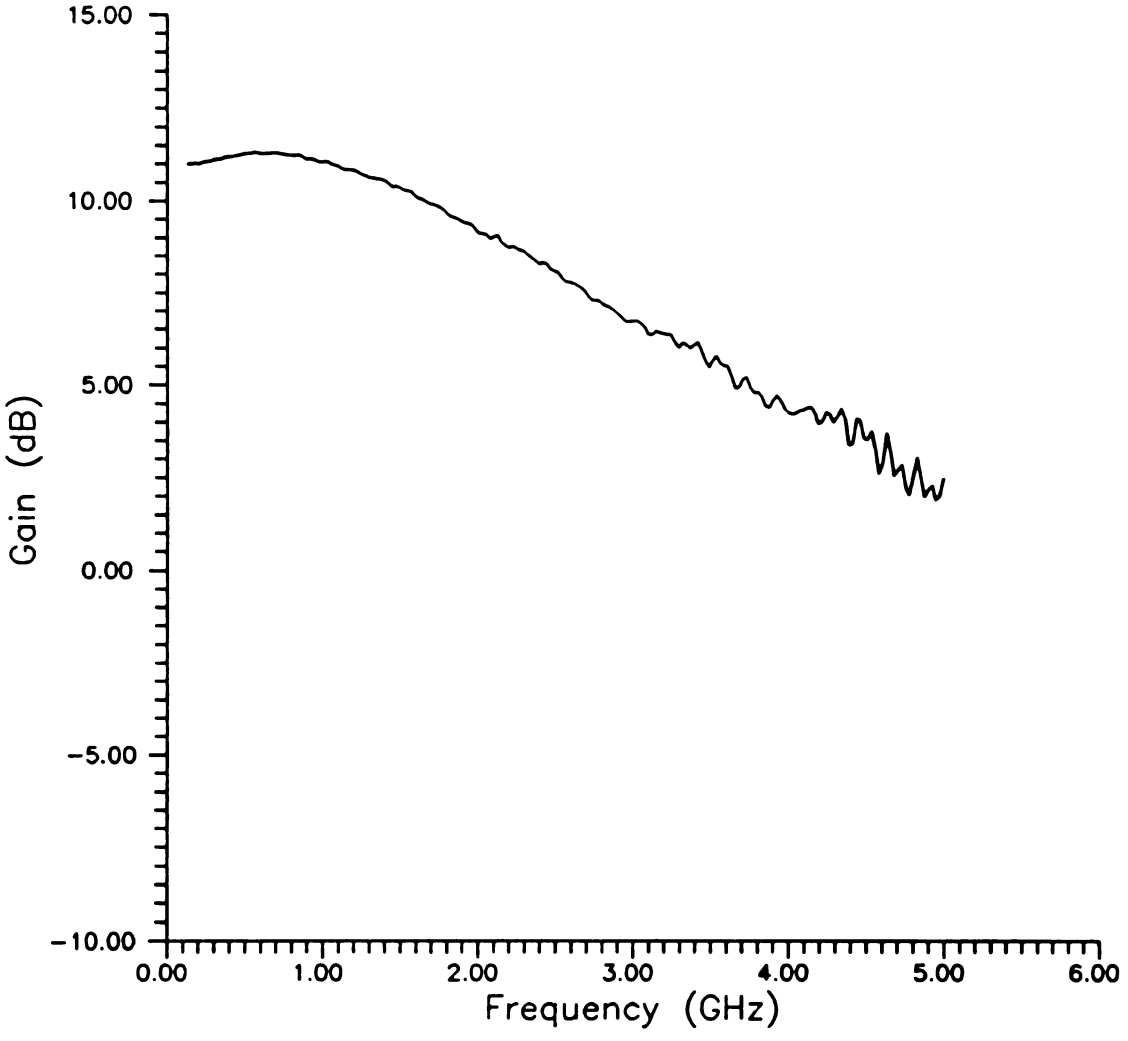

Figure C.5 Gain of PPL 5812 wide band amplifier measured using HP-8720B network analyzer. Amplifier input power = -10 dBm.

Bibliography

Bibliography

1. J.D. Taylor, "Introduction to Ultrawideband Radar Technology," Draft of notes presented at the First Ultrawideband Radar Symposium, Los Alamos National Laboratory, March 1990.

2. C.W. Davis, III, N.M. Tomljanovich, J.D.R. Kramer, Jr. and J.L. Poirer, "Characteristics of Ultra Wide Band Radars Pertinent to Air Defense," Los Alamos Symposium on Ultra-Wideband Radar, 1990.

3. I. LaHaie, R. Harger, S. Robinson, and J. Miller, "An Evaluation of Nonsinusoidal Radar Techniques," Report to U.S. Government from Environmental Research Institute of Michigan, June, 1985.

4. M.L. Skolnik, Introduction to Radar Systems, New York: McGraw-Hill, 1980.

5. 1992 IEEE International Microwave Symposium Program Guide, Albuquerque, NM, June 1992.

6. 1992 Joint Symposia, IEEE APS International Symposia, URSI Radio Science Meeting, Nuclear EMP Meeting - Call for Papers.

7. Alfonso Farina and Flavio A. Studer, "Detection with High Resolution Radar: Great Promise, Big Challenge," Microwave Journal, pp. 263-273, May 1991.

8. L. Webb, "Radar Target Discrimination Using K-pulses from a 'Fast' Prony's Method, " Doctoral dissertation, Michigan State University, May 1984.

9. E.J. Rothwell, "Radar Target Discrimination Using the Extinction-Pulse Technique," Doctoral dissertation, Michigan State University, 1985.

10. W. Sun, "Scattering of Electromagnetic Waves and Radar Target Discrimination," Doctoral dissertation, Michigan State University, 1989.

11. P. Ilavarasan, E. Rothwell, K.M. Chen, and D.P. Nyquist, "Natural Resonance Extraction with Physical Constraints," to be presented at the 1992 National Radio Science Meeting in Chicago, IL, June 1992.

12. K.M. Chen, D.P. Nyquist, E.J. Rothwell, L.L. Webb and B. Drachman, "Radar Target Discrimination by Convolution of Radar Returns with Extinction-Pulses and Single-Mode Extraction Signals," *IEEE Transactions on Antennas and Propagation*, vol. AP-34, no. 7, pp. 896-904, July 1986.

13. E.J. Rothwell, D.P. Nyquist, K.M. Chen and B. Drachman, "Radar Target Discrimination Using the Extinction-Pulse Technique," *IEEE Transactions on Antennas and Propagation*, vol. AP-33, no. 9, pp. 929-937, September 1985.

14. E.J. Rothwell, K.M. Chen, D.P. Nyquist and W. Sun, "Frequency Domain E-Pulse Synthesis and Target Discrimination," *IEEE Transactions on Antennas and Propagation*, vol. AP-35, no. 4, pp. 426-434, April 1987.

15. C.E. Baum, "On The Singularity Expansion Method For The Solution of Electromagnetic Interaction Problems," *Interaction Notes*, Note 88, December 1971.

16. L. Marin, "Representation of Transient Scattered Fields in Terms of Free Oscillations of Bodies," *Proceedings of the IEEE*, pp. 640-641, May 1972.

17. P. Ilavarasan, E. Rothwell, J. Ross, D. Nyquist and K.M. Chen, "Time Domain Radar Target Discrimination Using S-Pulse Waveforms," presented at the 1991 North American Radio Science Meeting, London, Ontario, Canada, June 22-25, 1991.

18. P. Ilavarasan, J.E. Ross, E.J. Rothwell, D.P. Nyquist and K.M. Chen, "Performance of an Automated Radar Discrimination Scheme using E-Pulses and S-Pulses," submitted for review, *IEEE Transactions on Antennas and Propagation.*

19. P. Ilavarasan, "Automated Radar Target Discrimination Using E-Pulse and S-Pulse", Doctoral Dissertation, Michigan State University, 1992.

20. E.J. Rothwell, K.M. Chen, and D.P. Nyquist, "Extraction of the Natural Frequencies of A Radar Target from A Measured Response Using E-Pulse Techniques," *IEEE Transactions on Antennas and Propagation,* vol. AP-35, no. 6, pp. 715-720, June 1987.

21. E.J. Rothwell and K.M. Chen, "A Hybrid E-Pulse/Least Squares Technique for Natural Resonance Extraction," *Proceedings of the IEEE*, pp. 296-298, vol. 76, no. 3, March 1988.

22. W. Sun, "Scattering of Transient Electromagnetic Waves and Radar Target Discrimination," Ph.D. Dissertation, Michigan State University, 1989.

23. F.M. Tesche, "On the Analysis of Scattering and Antenna Problems Using the Singularity Expansion Technique," *IEEE Transactions on Antennas and Propagation*, vol. AP-21, no. 1, pp. 53-62, January 1973.

24. F.M. Tesche, "The Far-Field Response of a Step-Excited Linear Antenna Using SEM," *IEEE Transactions on Antennas and Propagation*, vol. AP-23, no. 6, pp. 834-838, November 1975.

25. K.R. Umashankar, T.H. Shumpert and D.R. Wilton, "Scattering by a Thin Wire Parallel to a Ground Plane Using the Singularity Expansion Method," *IEEE Transactions on Antennas and Propagation*, vol. AP-23, no. 2, pp. 178-184, March 1975.

26. T.H. Shumpert and D.J. Galloway, "Finite Length Cylindrical Scatterer Near Perfectly Conducting Ground. A Transmission Line Mode Approximation," *IEEE Transaction on Antennas and Propagation*, vol. AP-26, no. 1, pp. 145-151, January 1978.

27. L.S. Riggs and T.H. Shumpert, "Trajectories of the Singularities of a Thin Wire Scatterer Parallel to Lossy Ground," *IEEE Transactions on Antennas and Propagation*, vol. AP-27, no. 6, pp. 864-868, November 1979.

28. Che-I Chuang, "Transient Waveform Synthesis For Radar Target Discrimination," Doctoral Dissertation, Michigan State University, 1983.

29. C.E. Baum, T.H. Shumpert and L.S. Riggs, "Perturbation of the SEM-Pole Parameters of an object by a mirror object," *Electromagnetics*, 8:169-186, 1989.

30. J. Nitch, C.E. Baum and R. Sturm, "Splitting of Degenerate Natural Frequencies in Coupled Two-Conductor Lines by Distance Variation," Interaction Note 477, July 1989.

31. D.J. Riley, W.A. Davis and I.M. Besieris, "The singularity expansion method and multiple scattering," *Radio Science*, vol. 20, no. 1, pp. 20-24, January-February 1985.

32. J. Ross, E. Rothwell, D.P. Nyquist and K.M. Chen, "Multiple Target Discrimination using E-pulse Techniques," 1990 IEEE/APS Symposium Digest, Dallas, TX, June 1990.

33. M.A. Morgan, "Singularity Expansion Representations of Fields and Currents in Transient Scattering," *IEEE Transactions on Antennas and Propagation*, vol. AP-32, no. 5, pp. 466-473, May 1984.

34. M.A. Morgan, "Response to Comments Regarding SEM Representations," *IEEE Transactions on Antennas and Propagation*, vol. AP-33, no. 1, p. 120, January 1985.

35. L.W. Pearson, "A Note on the Representation of Scattered Fields as a Singularity Expansion," *IEEE Transactions on Antennas and Propagation*, vol. AP-32, no. 5, pp. 520-524, May 1984.

36. L.B. Felson, "Comments on Early Time SEM," *IEEE Transactions on Antennas and Propagation*, vol. AP-33, no. 1, pp. 118-119, January 1985.

37. D.G. Dudley, "Comments on SEM and the Parametric Inverse Problem," *IEEE Transactions on Antennas and Propagation*, vol. AP-33, no. 1, pp. 119-120, January 1985.

38. C.E. Baum, "Representation of Surface Current Density and Far Scattering in EEM and SEM With Entire Functions," *Interaction Notes*, Note 486, February 1992.

39. C.E. Baum, "On the Singularity Expansion Method for the Solution of Electromagnetic Interaction Problems," *Interaction Notes*, Note 88, 1971.

40. A.D. Yaghjian, "Electric Dyadic Green's Functions in the Source Region," *Proceedings of the IEEE*, vol. 68, no. 2, pp. 248-262, February 1980.

41. B.K. Singaraju, D.V. Giri and C.E. Baum, "Further Developments in the Application of Contour Integration to the Evaluation of the Zeroes of Analytic Functions and Relevant Computer Programs," *Mathematics Notes*, Note 42, March 1976.

42. G.W. Hanson, "The Singularity Expansion Method for Integrated Electronic Circuits," Ph.D. Dissertation, Michigan State University, 1991.

43. C.L. Bennett, "The Numerical Solution of Transient Electromagnetic Scattering Problems," in Electromagnetic Scattering, ed. by P.L.E. Uslenghi, Academic Press, 1978, pp. 393-428.

44. Morgan M.A., "Time-Domain Scattering Measurements," *IEEE Antennas and Propagation Newsletter*, vol. 6, pp. 5-9, August 1984.

45. M.A. Morgan and B.W. McDaniel, "Transient Electromagnetic Scattering: Data Acquisition & Signal Processing," *IEEE Transactions on Instrumentation and Measurement*, vol. 37, no. 2, pp. 263-267, June 1988.

46. M.A. Morgan and N.J. Walsh, "Ultra-Wide-Band Transient Electromagnetic Scattering Laboratory," *IEEE Transactions on Antennas and Propagation*, vol. AP-39, no. 8, pp. 1230-1234, August 1991.

47. F.T. Ulaby, T.F. Haddock, J. East, and M. Whitt, "A millimeter-wave newtork analyzer based scatterometer," *IEEE Transactions on Geoscience and Remote Sensing*, vol. GE-26, no. 1, pp. 75-81 January 1988.

48. B. Drachman, "Two Methods to Deconvolve: L_1-Method Using Simplex Algorithm and L_2-Method Using Least Squares and a Parameter," *IEEE Transactions on Antennas and Propagation*, vol. AP-32, no. 3, pp. 219-225, March 1984.

49. E.J. Rothwell and W.E. Sun "Time Domain Deconvolution of Transient Radar Data," *IEEE Transactions on Antennas and Propagation,* vol. AP-38, no. 4, pp. 470-475, April 1989.

50. Radar Reflectivity Measurement - Techniques and Applications, ed. Nicolas C. Currie, Artech House, 1989.

51. Mie, *Ann. Physik*, **25**, 377, 1908.

52. J.A. Stratton, Electromagnetic Theory, New York and London: McGraw-Hill, 1941, pp. 563-573.

53. R.F. Harrington, Time Harmonic Electromagnetic Fields, New York: McGraw Hill, 1961.

54. K.M. Chen, EE836-Electromagnetic Waves I; Course Notes, Michigan State University, 1989.

55. D. Deirmedjian, Electromagnetic Scattering on Spherical Polydispersions, USAF Project Rand Report R-456-PR, April 1969.

56. N. Gharsallah, "Measurements of Transient Electromagnetic Fields with Surface Probes," Master's Thesis, Michigan State University, 1987.

57. R.S. Elliot, Antenna Theory and Design, New York: Prentice Hall, 1981.

58. S. Ramo, J.R. Whinnery and T. Van Duzer, Fields and Waves in Communication Electronics, 2nd ed.; New York: Wiley, 1984.

59. CRC STANDARD MATHEMATICAL TABLES, ed. by W.H. Beyer, 25th ed.; Boca Ratan, Florida: CRC Press, 1980.

60. D.P. Nyquist, EE926&927 - Antenna Theory Course Notes, Michigan State University, 1989.

61. C.I. Chuang and D.P. Nyquist, "Perturbational formulation for nearly degenerate coupling," 1984 National Radio Science Meeting, Boulder, CO.